UNIVERSITY OF CALIFORNIA,
IRVINE

Measurement of the θ_{13} Neutrino Mixing Angle at Daya Bay via Neutron Capture on Hydrogen

DISSERTATION

submitted in partial satisfaction of the requirements
for the degree of

DOCTOR OF PHILOSOPHY

in Physics

by

Olivia Noonan Dalager

Dissertation Committee:
Professor Juan Pedro Ochoa-Ricoux, Chair
Professor Henry Sobel
Professor Jianming Bian

2024

DEDICATION

To my parents, Sandy and Myron, and brother, Andrew:
Thank you for your constant love and support!

TABLE OF CONTENTS

LIST OF FIGURES

LIST OF TABLES

ACKNOWLEDGMENTS

Many people have my deep gratitude for their guidance and support over the years. This is by no means a fully comprehensive list, so to those who were there for me during this process not specifically named here: thank you!

Firstly, I am extremely grateful to Professor Juan Pedro Ochoa-Ricoux. Thank you for your perpetual guidance, your support throughout the intricacies of this project, and your mentorship through this project and in my development as a physicist!

Secondly, to Bedřich Roskovec: Beda, thank you for your indispensable contributions to this analysis and our research group! You were always prepared with your insights and commentary, willing to get into detailed discussions any time it was needed, literally and figuratively. Thank you for your support and encouragement to make this analysis the best it could be.

To the rest of the research group, namely Dr. Sindhujha Kumaran, Roberto Mandujano Bejarano, and Katherine Dugas: I am infinitely grateful for all of you and your immense impact on my life. Thank you for your friendship and for fostering a close-knit research environment which extended past the boundaries of academia! Your unwavering support, shared insights, and mutual encouragement have transformed the challenges of research into shared triumphs and cultivated a sense of belonging and friendship that I deeply treasure.

To the Daya Bay Collaboration, especially the US-Czech-Hong Kong group: Thank you for the many thorough discussions and valuable input to this truly collaborative effort. Deep thanks to Kam-Biu Luk for your mentorship over the years.

To my thesis committee, Hank Sobel and Jianming Bian: Thank you for sharing your insights and expertise with me through the years, the weekly neutrino meetings, and through the thesis/defense process!

And to my family – Mom, Dad, and Andrew: thank you for your unceasing love and support since day one! Thank you for your encouragement to explore my curiosities of the world, as well as my other interests, which led me to where I am today. Thank you for being my support crew, my full-fledged cheering section, and the utmost best family I could possibly ask for!

VITA

Olivia Noonan Dalager

EDUCATION

Doctor of Philosophy in Physics **2024**
University of California, Irvine *Irvine, California*

Bachelor of Science in Physics **2017**
University of California, Davis *Davis, California*

RESEARCH EXPERIENCE

Graduate Research Assistant **2018–2023**
University of California, Irvine *Irvine, California*

- Regents Fellow
- PMT Gain Calibration for Daya Bay
- Measurement of the θ_{13} Neutrino Mixing Angle at Daya Bay via Neutron Capture on Hydrogen

Undergraduate Research Assistant **2014–2017**
University of California, Davis *Davis, California*

- Operated local experiment to determine the optimal thickness of wavelength-shifting organic compound for light detection by Silicon photomultipliers (SiPMs)
- Built a test-bench dual-phase xenon time projection chamber using both PMTs and SiPMs

TEACHING EXPERIENCE

Teaching Assistant **2017–2021**
University of California, Irvine *Irvine, California*

- Instructed 2 quarters of physics labs and 7 quarters of physics discussions to physics, engineering, biology and pre-med students

CONFERENCES AND ACADEMIC EVENTS

June 2023 — **International School of Subnuclear Physics** (Erice, Sicily, Italy)
- Talk: "Measurement of the θ_{13} Neutrino Mixing Angle at Daya Bay"

June 2022 — **Neutrino 2022** (online)
- Poster: "Daya Bay Neutrino Oscillation Analysis Using Neutron Capture on Hydrogen"

April 2022 — **American Physical Society April Meeting 2022** (online)
- Talk: "Recent Results from the Daya Bay Experiment"

July 2021 — **European Physical Society Conference on High Energy Physics 2021** (online)
- Poster: "Sterile Neutrino Search from Daya Bay"

June–July 2021 — **INFN International School on Underground Physics** (online)
- Introduction to neutrino and dark matter phenomenology, detection techniques, and analysis methods

April 2021 — **American Physical Society April Meeting 2021** (online)
- Talk: "Recent Results from the Daya Bay Experiement"

June–July 2020 — **Neutrino 2020** (online)
- Poster: "Daya Bay's Latest Oscillation Results Using Neutron Capture on Gadolinium"

April 2020 — **American Physical Society April Meeting 2020** (online)
- Talk: "Latest Oscillation Results from Daya Bay"

August 2019 — **International Neutrino Summer School 2019** (Fermilab, IL)
- Focused exploration of the theoretical, experimental, and phenomenological aspects of neutrino physics and detection
- Toured several experiments on Fermilab's campus

ABSTRACT OF THE DISSERTATION

Measurement of the θ_{13} Neutrino Mixing Angle at Daya Bay via Neutron Capture on Hydrogen

By

Olivia Noonan Dalager

Doctor of Philosophy in Physics

University of California, Irvine, 2024

Professor Juan Pedro Ochoa-Ricoux, Chair

Neutrinos exhibit a unique behavior compared to other Standard Model particles: neutrino oscillations. This phenomenon is the periodic change of probability to interact with certain lepton flavors as they propagate. Measuring the oscillation parameters accurately is crucial to exploring the unanswered questions related to neutrino physics, most notably the possibility that these particles violate the CP symmetry or that there are more than three generations of them.

The Daya Bay Reactor Neutrino Experiment is known for making the first unambiguous determination of the non-zero value of the θ_{13} mixing angle and producing the most precise measurements of this parameter ever since. Located in Southern China, Daya Bay utilizes eight strategically placed identically-designed detectors to measure the disappearance of electron antineutrinos from six nuclear reactor cores. The antineutrino interactions are identified through the double coincidence signature of the inverse beta decay. The neutron from this interaction can get captured on a nucleus of either gadolinium (nGd) or hydrogen (nH). Given that the statistical samples are entirely separate and the systematics largely decoupled, the nH and nGd measurements are virtually independent of one another. This makes the nH analysis valuable as a precise cross-check to the nGd analysis.

Daya Bay's world-leading measurement of θ_{13} is the result of analyzing the former. The measurement of the latter sample is presented in this thesis, including the event selection, removal of background events, evaluation of the systematic uncertainties, and fitting procedure, ultimately leading to the best fit results of $\sin^2 2\theta_{13} = 0.0776 \pm 0.0053$ and $\Delta m^2_{ee} = (2.80 \pm 0.14) \times 10^{-3}$ eV^2. This measurement is among the second most precise measurements of θ_{13} globally.

Chapter 1

Neutrino Oscillation

The study of neutrinos has presented many unexpected results over the years. Originally theorized to account for missing energy in beta decay, neutrinos have captivated the scientific community with properties that defy the confines of the Standard Model of particle physics. Neutrinos provide us with directly verifiable experimental evidence of physics beyond the Standard Model. This chapter provides a overview of the discovery of the neutrino and its properties as expressed within the Standard Model (Sec. 1.1) and beyond (Sec. 1.2), the framework with which we currently understand neutrino oscillation (Sec. 1.3), and a discussion on measuring oscillation parameters, with an emphasis on θ_{13} (Sec. 1.4).

1.1 Early Understanding of Neutrinos

The first evidence of neutrinos came from inconsistencies between the data and theoretical predictions in the energy of electrons released in nuclear beta decays (Sec. 1.1.1). Following the first detection of neutrino interactions (Sec. 1.1.2), many important observations were made (Sec. 1.1.3), including the existence of antineutrinos ($\overline{\nu}_e$) and the three flavor genera-

tions (e, μ, and τ). These discoveries led to the understanding of neutrinos in the Standard Model (Sec. 1.1.4).

1.1.1 Initial Theory of Neutrinos

As with many physics discoveries, the history of neutrino physics can be traced back to an experimental puzzle. In the case of neutrinos, this was the unexpected 1914 result from Chadwick of the energy spectrum of β particles observed from the nuclear decay process [1]. As understood at the time, nuclear beta decay of a nucleus N, with atomic mass A and charge Z, was simply a 2-body process:

$$N(A, Z) \rightarrow N(A, Z + 1) + \beta^{-}. \tag{1.1}$$

Conservation of energy and momentum dictated that this process would result in emitted β particles with a single, specific energy. However, Chadwick's observations, which were confirmed by others in the subsequent decade, contradicted this prediction. Instead of a single discrete energy, a continuous spectrum was observed. Furthermore, the spectrum resided exclusively below the expected energy of the two-body assumption, such that the electrons were always emitted with lower energies. This discrepancy implied that either conservation of energy or the prevailing understanding of the nuclear decay process was flawed. In 1931, Pauli offered a solution to maintain conservation of energy and explain the continuous β energy spectrum: a new, light and neutrally charged particle [2]. Originally, Pauli named these particles "neutrons," but the name was given to the particle later discovered by Chadwick which could not be Pauli's theorized particle. Based on Pauli's theory, Fermi theorized the beta decay process where this particle escapes detection due to a small interaction cross section:

$$N(A, Z) \rightarrow N(A, Z + 1) + \beta^{-} + \nu. \tag{1.2}$$

Now recognized as the neutrino, this additional particle takes away a portion of the energy which would otherwise go to the electron, thus explaining the observed energy spectrum.

1.1.2 Discovering Neutrinos

Based on Fermi's predictions, the approximate value of the neutrino cross-section was already established, and it was merely a matter of time before experimental evidence would validate these predictions. In 1956, Reines and Cowan made such history by detecting the particle we now identify as the electron antineutrino. Stationed near a reactor in the Savannah River Plant, their experiment utilized a detector composed of five alternating layers of liquid scintillator and target volumes filled with $CdCl_2$-doped water [3]. The reactor produced antineutrinos, which interacted with hydrogen nuclei in the target volume composed of $CdCl_2$ dissolved in water, thereby undergoing the inverse beta decay (IBD) process:

$$\overline{\nu}_e + p \rightarrow e^+ + n. \tag{1.3}$$

This process resulted in the creation of a double coincidence signature consisting of two events: one prompt and one delayed. In Reines and Cowen's experimental setup, the prompt event consisted of the near-immediate annihilation between the positron and an electron in the target volume, producing two γs, which were then detected in the liquid scintillator. Unlike the positron, the neutron scattered within the target volume for $\sim$5 μs before being captured by a Cd nucleus, producing a characteristic 9 MeV delayed signal. Reines and Cowan reported an IBD rate of 2.88 ± 0.22 neutrinos per hour, exclusively when the nuclear reactor was running. The fact that IBDs were not detected when the reactor was off confirmed its role as the source of the antineutrinos.

1.1.3 Key Experimental Observations

As more experimental efforts confirmed the existence of Pauli's proposed particle, an image of neutrinos in the Standard Model (SM) was developing. Following Pauli's theory, neutrinos were found to be light and neutrally-charged particles, with further observations rounding out the understanding of neutrinos in the SM.

The first additional neutrino property was the observation of antineutrinos as independent from neutrinos. In 1954, Davis attempted to detect neutrinos using the Brookhaven nuclear reactor as a source for his experiment searching for

$$^{37}\mathrm{Cl} + \overline{\nu} \rightarrow {}^{37}\mathrm{Ar} + \beta^{-}, \tag{1.4}$$

a process which would only occur if $\nu = \overline{\nu}$ [4]. This would also violate what we now know as lepton number conservation, though this was not an established concept yet. Davis observed no additional decays above the background rate, so after Reines and Cowan's results, Davis concluded that neutrinos and antineutrinos must be entirely different particles.

Later, Goldhaber, Grodzins, and Sunyar determined that neutrinos are left-handed particles and the antineutrinos are right-handed [5, 6]. This described the direction of the intrinsic angular momentum with respect to the momentum of the particle: aligned for right-handed and opposite for left-handed. The experiment measured the helicity of neutrinos by observing the helicity of the corresponding γs produced in the following chain reaction:

$$\begin{aligned} e^{-} + {}^{152m}\mathrm{Eu}(0^{-}) &\rightarrow \nu_e + {}^{152}\mathrm{Sm}^{*}(1^{-}) \\ {}^{152}\mathrm{Sm}^{*}(1^{-}) &\rightarrow {}^{152}\mathrm{Sm}(0^{+}) + \gamma. \end{aligned} \tag{1.5}$$

When the ν_e and the γ are emitted in exact opposite directions, the helicities must be the same. Firstly, Goldhaber, Grodzins, and Sunyar selected the γ's originating from this

process by measuring only the highest energy γs, which were Doppler-boosted by the recoil of $^{152}\mathrm{Sm}^{*}(1^{-})$ and which did not scatter. Secondly, an electromagnet surrounding the ^{152m}Eu source was instrumented to measure the helicity of the γs, utilizing the fact that only those with opposite polarization to the e^{-} in the magnet would Compton-scatter. Then comparing the rates of events from both polarizations of the electromagnet determined that the helicity of the γs, and therefore the ν, to be –1.

The next development in the understanding of neutrinos was the discovery of neutrino flavors. The first experiment to explore different flavors was also the first acclerator neutrino experiment. It was conducted using a ν_{μ} beam originating from the Brookhaven Alternating Gradient Synchrotron (AGS) by Danby *et al.* in 1962 [7]. The neutrino beam was created by aiming the 15 GeV proton beam at a fixed beryllium target and therefore producing pions which decay according to:

$$\pi^{\pm} \rightarrow \mu^{\pm} + \nu(\overline{\nu}). \tag{1.6}$$

The detector consisted of a series of spark chambers positioned behind 13.5 m of steel to shield from non-neutrino beam products. If only one flavor of neutrinos existed, e^{-} and μ^{-} interactions within the target would occur in equal proportions as they would interact equally with all lepton generations. With a count of ν_{μ} events $\sim$7 times higher than that of ν_{e}, the findings verified a difference in behavior between e and μ neutrino flavors.

As for the third and final flavor, the discovery of the τ lepton in 1975 prompted the search of a corresponding neutrino [8]. In an attempt to determine whether it was a third independent flavor or a superposition of the other two, experiments began searching for τ production in ν_{e} and ν_{μ} beams in 1978 [9, 10, 11]. Due to an absence of such events by 1982, the Particle Data Group concluded that ν_{τ} was independent from the other flavors [12]. Finally in 2001, the DONuT experiment reported first direct observation of four ν_{τ} interactions, with an additional five events in 2008 [13, 14].

1.1.4 Neutrinos in the Standard Model

Alongside the experimental breakthroughs, huge strides were also being made in the theory side of particle physics. Most notably, in the 1960s, Glashow [15], Salam [16], and Weinberg [17] developed unified electroweak theories, which became the foundation of the Standard Model (SM) of particle physics.

The SM concisely summarizes the most elementary particles and how they interact with one another. The particles are first organized based on their characteristic spin states: bosons for integer spins and fermions for half-integer spins. The fermions consist of the particles which make up matter: quarks (up, down, charm, strange, top, and bottom) and leptons (three charged leptons, electron e, muon μ, and tau τ, and the three massless and neutrally charged neutrinos corresponding flavors ν_e, ν_μ, and ν_τ). In contrast, the bosons are the mediators of the fundamental forces. Gluons and photons mediate the strong nuclear force and the electromagnetic force, respectively, while the weak nuclear force is mediated by the W (charged) and Z (neutral) bosons. The final boson, the Higgs boson, gives mass to the other particles in the SM.

Neutrinos only interact via the W and Z bosons through charged current (CC) and neutral current (NC) interactions, respectively. The CC neutrino interactions had been observed by neutrino experiments previously, while the NC neutrino interactions were not seen until the 1970s by the Gargamelle neutrino experiment at CERN [18, 19, 20]. The signature of the NC interactions would be only the detection of the other particle involved in the scattering, with no visible incoming particle and no additional charged lepton.

1.2 Beyond the Standard Model

While Pauli was correct about the existence of neutrinos, experiments observed that neutrinos didn't entirely match the SM description. Primarily, the observed neutrinos were not massless, therefore allowing for the neutrino oscillation phenomenon. The first evidence of neutrino oscillations came from experiments observing fewer neutrinos than predicted. The observed deficits are discussed in Sec. 1.2.1, followed by Sec. 1.2.2 which summarizes the results attributing this to neutrino oscillation.

1.2.1 Missing Neutrinos

Through the understood neutrino producing processes, particularly nuclear fusion for solar neutrinos and cosmic ray collisions creating atmospheric neutrinos, theory was able to calculate expected neutrino rates. However, in early neutrino experiments, the data revealed rates significantly lower than predicted.

Solar Neutrinos

The Solar Standard Model (SSM) predicts nuclear fusion, a neutrino producing process, as the mechanism powering the Sun [21]. Therefore, detecting neutrinos originating from the Sun would serve as validation of the SSM. Being the first to measure the rate of solar neutrinos, Davis built an experiment in South Dakota's Homestake gold mine [22]. The detector was a 610 t tank of CCl_4 as a target which utilized the reaction

$$^{37}\mathrm{Cl} + \nu_e \rightarrow {}^{37}\mathrm{Ar} + \beta^- \tag{1.7}$$

to measure the amount of ^{37}Ar and determine the number of neutrino interactions.

Compared to the SSM's prediction, the experiment observed a significant deficit of solar neutrino events. Using solar neutrino units (SNU), defined as 1 interaction per second per 10^{36} target nuclei, the experiment originally reported a maximal limit of 3 SNU observed compared to the predicted (20 ± 12) SNU [23], though after more than a decade of data, the results were updated to (2.1 ± 0.03) SNU compared to the predicted (5.8 ± 2.2) SNU [21]. This discrepancy, which would become known as "the solar neutrino problem," had at least two possible explanations: either the SSM was incorrect or neutrinos decay and/or oscillate in the journey between production and detection.

Atmospheric Neutrinos

Similarly to solar neutrinos, neutrinos originating from within the atmosphere ("atmospheric neutrinos") were detected at a significantly lower rate than expected. When cosmic rays (predominantly protons) collide with nuclei in the atmosphere, particles (mainly $\pi^{\pm}$) are created then decay producing neutrinos. For example, in the case of π^+:

$$\begin{aligned} \pi^+ &\rightarrow \mu^+ + \nu_\mu \\ \mu^+ &\rightarrow \overline{\nu}_\mu + e^+ + \nu_e. \end{aligned} \tag{1.8}$$

With low enough energy such that all the muons decay before reaching the ground, the predicted ν_μ rate was expected to be twice the ν_e rate. To include atmospheric data and kinematics of pion, kaon, and muon decays, Monte Carlo simulation was used to provide more precise predictions for experiments to compare to [24].

In 1963, Reines heard of experimental observations demonstrating that placing experiments deep underground, such as in mines, signficantly reduced the flux of secondary cosmic rays, which would allow for the detection of atmospheric neutrinos. Following discussions with the group at the Tata Institue of the University of Bombay, Reines instigated a collaboration

with Case Institute of Technology and the University of Witwatersrand. Together, they built the CASE-WITS experiment in a gold mine in South Africa. This 20 t liquid scintillator detector was designed as a crude hodoscope to determine the zenith direction of through-going muons. The experiment observed approximately 170 events, resulting in the neutrino flux measurement roughly 40% less than predicted [25]. With large uncertainties, the results were considered to be consistent with expectation.

Later, in the 1980s, experiments were rushing to detect proton decay. The largest such experiment was the Irvine-Michigan-Brookhaven (IMB) 8 kt water Cherenkov detector. By not observing the proton decay, the collaboration ruled out the Grand Unified (SU(5)) Theory it set out to test. As a major background to this search, atmospheric neutrinos were observed at a rate lower than predicted: $(26 \pm 3)\%$ vs $(34 \pm 1)\%$ [26]. As with the CASE-WITS experiment, these rates, reported in 1986, had large systematic uncertainties, and therefore, conclusive disagreement was not claimed.

The Kamiokande experiment was a another water Cherenkov experiment which set out to observe proton decays. In the 1988 results, the experiment reported the measured neutrino flux of both electron and muon flavors. The flux of electron-type neutrinos matched expectation, however the measured muon-type neutrino flux was only $(59 \pm 7)\%$ of the prediction [27]. With the earlier observations by CASE-WITS and IMB, Kamiokande reported confirmation of the deficit [28].

1.2.2 Resolution of the Deficits

For the solar neutrino problem, two experiments made history for resolving the deficit: Super-Kamiokande in Japan and Sudbury Neutrino Observatory (SNO) in Canada. The Super-Kamiokande experiment, a 50 kt water Cherenkov detector, measured the solar neutrino rates through CC elastic scattering [29]. SNO, another Cherenkov detector with a 1 kt

target of heavy water (D_2O), measured the NC channel of detecting solar neutrinos [30]. The CC interaction rate indicated a deficit of neutrinos from prediction, as seen by previous experiments, whereas the rate of NC interactions, which were produced by all flavors of neutrinos, did not. The combination of the two precise rate measurements were consistent with the hypothesis of neutrino oscillations.

In the following year, the KamLAND experiment published results of electron anti-neutrino disappearance from Japan's nuclear reactors [31]. Their measurements revealed a significant distortion of the $\overline{\nu}_e$ energy spectrum. The results were consistent with the L/E dependence of the three-flavor oscillation theory. The results from both SNO and KamLAND confirmed both the SSM's ability to accurately model the Sun's processes and the oscillation of neutrino flavors.

As for the atmospheric neutrino case, Super-Kamiokande, the successor to Kamiokande, provided the results for resolving the deficits in 1998 [28]. The experiment measured atmospheric neutrino flux with PMTs surrounding a 50 kt target of ultrapure water and compared the the ν_μ flux dependence on the neutrino direction as a proxy for the distance between production and detection. While the downward-going neutrinos were produced in the atmosphere above the experiment, the upward-going neutrinos were produced on the other side of the Earth and had traveled a much greater distance. The data revealed a deficit in the flux of upward-going neutrinos compared to the downward-going neutrinos, attributed to the larger probability of oscillation to other flavors.

The results of these experiments and many others solidified flavor oscillations as a behavior of neutrinos, indicating physics beyond the SM: The oscillations between flavors require that neutrinos are not massless particles, as specified by the SM. This is explained more in Sec. 1.3.

1.3 Neutrino Mixing and Oscillation

To mathematically explain the phenomenon, Sec. 1.3.1 presents the derivation of the theory behind neutrino oscillations in the general case, while Sec. 1.3.2 and Sec. 1.3.3 present the phenomenology for neutrino oscillations within the two- and three-flavor frameworks, respectively.

1.3.1 Oscillation Theory

Presented here is the derivation for a generic neutrino oscillation theory, as shown in [24] and [32]. Following a standard choice of units in particle theory, let $c = \hbar = 1$ in this section, unless otherwise noted.

For the theory with n leptonic flavors, a neutrino ν_α exists for each charged lepton l_α^-, as demanded by the charged current (CC) interaction vertex between W, l_α, and ν_α. The interaction is governed by the α flavor eigenstate of the neutrino, written as $|\nu_\alpha\rangle$. The flavor eigenstates, however, are not necessarily equal to the eigenstates of the Hamiltonian, $|\nu_i\rangle$, which are known as the energy, or mass, eigenstates. A unitary matrix U, known as the mixing matrix, relates the energy and flavor eigenstates:

$$\begin{aligned} |\nu_\alpha\rangle &= \sum_{i=1}^{n} U_{\alpha i}^* \, |\nu_i\rangle \\ |\nu_i\rangle &= \sum_{\alpha \in \{\text{flavors}\}} U_{\alpha i} \, |\nu_\alpha\rangle \, , \end{aligned} \tag{1.9}$$

where the elements of this equation must adhere to the unitarity relations:

$$\begin{aligned} \langle \nu_\alpha \mid \nu_\beta \rangle &= \delta_{\alpha\beta}, \\ \langle \nu_i \mid \nu_j \rangle &= \delta_{ij}, \\ U^\dagger U &= \mathbf{1}. \end{aligned} \tag{1.10}$$

Given that the mass eigenstates are eigenstates of the Hamiltonian, Schrödinger's equation, $\hat{H} \left|\nu_i(t)\right\rangle = E_i \left|\nu_i(t)\right\rangle$, simplifies to:

$$E_i \left|\nu_i(t)\right\rangle = i\frac{d}{dt} \left|\nu_i(t)\right\rangle . \tag{1.11}$$

The propagation of neutrinos states can be described as plane waves, and therefore, Eq. 1.11 becomes

$$\left|\nu_i(t)\right\rangle = e^{-iE_i t} \left|\nu_i(0)\right\rangle . \tag{1.12}$$

Defining $\left|\nu_\alpha\right\rangle = \left|\nu_\alpha(0)\right\rangle$, Eq. 1.12 with Eq. 1.9 describe the flavor eigenstate evolution:

$$\begin{aligned} \left|\nu_\alpha(t)\right\rangle &= \sum_{i=1}^{n} U^*_{\alpha i} e^{-iE_i t} \left|\nu_i\right\rangle \\ &= \sum_{i=1}^{n} U^*_{\alpha i} e^{-iE_i t} \left(\sum_{\rho \in \{\text{flavors}\}} U_{\rho i} \left|\nu_\rho\right\rangle \right) \\ &= \sum_i \sum_\rho U^*_{\alpha i} U_{\rho i} e^{-iE_i t} \left|\nu_\rho\right\rangle . \end{aligned} \tag{1.13}$$

Therefore, it follows that at time t, the amplitude $A_{\alpha\to\beta}(t)$ for observing the state $\left|\nu_\beta\right\rangle$ after

a neutrino produced as $|\nu_\alpha\rangle$ also evolves:

$$\begin{aligned} A_{\alpha\to\beta}(t) = \langle \nu_\beta \mid \nu_\alpha(t)\rangle &= \left\langle \nu_\beta \left| \sum_i \sum_\rho U^*_{\alpha i} U_{\rho i} e^{-iE_i t} \right| \nu_\rho \right\rangle \\ &= \sum_i U^*_{\alpha i} U_{\beta i} e^{-iE_i t}. \end{aligned} \tag{1.14}$$

The square of the amplitude returns the probability for observing $|\nu_\alpha(t)\rangle$ in state $|\nu_\beta\rangle$:

$$\begin{aligned} P_{\alpha\to\beta}(t) = |A_{\alpha\to\beta}(t)|^2 &= \left| \sum_i U^*_{\alpha i} U_{\beta i} e^{-iE_i t} \right|^2 \\ &= \left(\sum_i U_{\alpha i} U^*_{\beta i} e^{iE_i t} \right) \left(\sum_j U^*_{\alpha j} U_{\beta j} e^{-iE_j t} \right) \\ &= \sum_i \sum_j U^*_{\alpha j} U^*_{\beta i} U_{\alpha i} U_{\beta j} e^{-i(E_j - E_i)t}. \end{aligned} \tag{1.15}$$

Further simplifications can be imposed given that, currently, all experimentally-accessible neutrinos are ultrarelativistic ($p \gg m$). Thus the energy E of a massless neutrino with momentum p can be approximated as

$$\begin{aligned} E_i = \sqrt{p^2 + m_i^2} &= p\sqrt{1 + \frac{m_i^2}{p^2}} \\ &\approx p\left(1 + \frac{m_i^2}{2p^2}\right) = p + \frac{m_i^2}{2p} \\ &\approx E + \frac{m_i^2}{2E}, \end{aligned} \tag{1.16}$$

yielding

$$E_j - E_i \approx \frac{m_j^2 - m_i^2}{2E}. \tag{1.17}$$

Furthermore, the ultrarelativistic approximation leads to the additional approximation that

$t \approx L$, thus by defining $\Delta m^2_{ij} = m^2_i - m^2_j$, Eq. 1.15 and Eq. 1.16 become

$$P_{a\to\beta}(L) = \sum_{ij} U^*_{\alpha j} U^*_{\beta i} U_{\alpha i} U_{\beta j} e^{i\frac{\Delta m^2_{ij}}{2E}L} \tag{1.18}$$

For the case when $i = j$, $\Delta m^2_{ij} = 0$. Alternatively, for $i \neq j$, the matrix elements and phase term can be broken into the real and imaginary components and multiplied on a term-by-term basis, giving rise to the entirely real probability:

$$\begin{aligned} P_{\alpha\to\beta}(L) =& \sum_i |U_{\alpha i}|^2 |U_{\beta i}|^2 \\ &+ 2\sum_{i\gg j} \mathfrak{Re}\left[U^*_{\alpha j} U^*_{\beta i} U_{\alpha i} U_{\beta j}\right] \cos\left(\Delta m^2_{ij}\frac{L}{2E}\right) \\ &+ 2\sum_{i\gg j} \mathfrak{Im}\left[U^*_{\alpha j} U^*_{\beta i} U_{\alpha i} U_{\beta j}\right] \sin\left(\Delta m^2_{ij}\frac{L}{2E}\right) \end{aligned} \tag{1.19}$$

where the real and imaginary contributions are denoted by $\mathfrak{Re}$ and $\mathfrak{Im}$, respectively. By incorporating the unitarity relation, the leading term can be expressed as:

$$\begin{aligned} \delta_{\alpha\beta} &= \left(U^\dagger U\right)^2_{\alpha\beta} \\ &= \sum_{ij} U^*_{\alpha j} U^*_{\beta i} U_{\alpha i} U_{\beta j} \\ &= \sum_i |U_{\alpha i}|^2 |U_{\beta i}|^2 + 2\sum_{i>j} \mathfrak{Re}\left[U^*_{\alpha j} U^*_{\beta i} U_{\alpha i} U_{\beta j}\right] \end{aligned} \tag{1.20}$$

Substituting this back into Eq. 1.19, the full oscillation probability for n neutrino flavors becomes:

$$\begin{aligned} P_{\alpha\to\beta}(L) =& \delta_{\alpha\beta} \\ &- 4\sum_{i>j} \mathfrak{Re}\left[U^*_{\alpha j} U^*_{\beta i} U_{\alpha i} U_{\beta j}\right] \sin^2\left(\Delta m^2_{ij}\frac{L}{4E}\right) \\ &+ 2\sum_{i>j} \mathfrak{Im}\left[U^*_{\alpha j} U^*_{\beta i} U_{\alpha i} U_{\beta j}\right] \sin\left(\Delta m^2_{ij}\frac{L}{2E}\right) \end{aligned} \tag{1.21}$$

In the case where $\alpha = \beta$, the probability is known as the survival probability. The product of matrix elements $U^*_{\alpha j} U^*_{\beta i} U_{\alpha i} U_{\beta j}$ becomes entirely real, and therefore, the general formula for survival probability is:

$$P_{\text{sur}} = P_{\alpha\to\alpha}(L) = 1 - 4\sum_{i>j} |U_{\alpha i}|^2 |U_{\alpha j}|^2 \sin^2\left(\Delta m^2_{ij}\frac{L}{4E}\right) \tag{1.22}$$

Setting c and $\hbar$ to their physical units, the phase of the oscillation (Δ_{ij}) becomes:

$$\Delta_{ij} = \Delta m^2_{ij}\frac{L}{4E} \to \Delta m^2_{ij} c^4 \frac{L}{4\hbar c E} \approx 1.267 \frac{\Delta m^2_{ij}}{(1\text{eV}/c^2)^2}\frac{L}{1\text{ m}}\frac{1\text{MeV}}{E} \tag{1.23}$$

The derivation is identical for the case of antineutrinos oscillating from $\overline{\alpha}$ flavor to $\overline{\beta}$ flavor, except for the use of the complex conjugate of the unitary mixing matrix. This leaves the survival probability unchanged, and only slightly alters the form of the general case:

$$\begin{aligned} P_{\overline{a}\to\overline{\beta}}(L) =& \delta_{\alpha\beta} \\ &- 4\sum_{i>j} \mathfrak{Re}\left[U^*_{\alpha j} U^*_{\beta i} U_{\alpha i} U_{\beta j}\right] \sin^2\left(\Delta m^2_{ij}\frac{L}{4E}\right) \\ &- 2\sum_{i>j} \mathfrak{Im}\left[U^*_{\alpha j} U^*_{\beta i} U_{\alpha i} U_{\beta j}\right] \sin\left(\Delta m^2_{ij}\frac{L}{2E}\right), \end{aligned} \tag{1.24}$$

where the complex conjugate merely changes the sign of the imaginary part.

1.3.2 Oscillations in the Two-Neutrino Framework

As a precursor to the phenomenology of three-flavor neutrino oscillation, this section will discuss the two-flavor case in order to simplify the explanation. Additionally, this is applicable in experiments where primarily only two flavors are involved, i.e. atmospheric neutrino experiments.

To start, the 2×2 mixing matrix is constructed with only one mixing angle, θ:

$$U_{2\times 2} = \begin{pmatrix} \cos\theta & \sin\theta \\ -\sin\theta & \cos\theta \end{pmatrix} \tag{1.25}$$

Defining $\Delta m^2 = m_2^2 - m_1^2$ with 1 and 2 indicating the mass state, the probability of a neutrino produced in the α flavor state oscillating to the β flavor becomes

$$P_{\alpha\to\beta} = 4\cos^2\theta\sin^2\theta\sin^2\left(\Delta m^2\frac{L}{4E}\right) = \sin^2 2\theta\sin^2\left(\Delta m^2\frac{L}{4E}\right), \tag{1.26}$$

and therefore, the survival probability is

$$P_{\alpha\to\alpha} = 1 - \sin^2 2\theta\sin^2\left(\Delta m^2\frac{L}{4E}\right). \tag{1.27}$$

It is worthwhile to note that the sum of Eq. 1.26 and Eq. 1.27 is identically 1, as the neutrino either remained in the α flavor state or oscillated into the β state.

The amplitude of neutrino oscillations is described entirely by the value of θ. The extreme cases of Eq. 1.26 come from $\theta = 0$ and $\pi/4$. For the former, oscillations will never occur, regardless of distance traveled or energy of the particle. Alternatively, for the latter, at the oscillation maximum where $\sin^2\left(\Delta m^2\frac{L}{4E}\right) = 1$, the probability of oscillation is 100%.

Until this point, the oscillations described were the "vacuum oscillations" where the influences of matter have been ignored. However, matter does affect the propagation of neutrinos by the Mikheyev-Smirnov-Wolfenstein (MSW) effect, as experienced by solar neutrino oscillations due to the density of the Sun [24]. The MSW effect exists as a result of the flavors interacting differently within matter. As the neutrinos pass through matter, all flavors experience NC interactions, though only e-flavored (anti)neutrinos can interact via CC.

It can be shown [33] that neutrino oscillation in matter can be modeled with the same equations but with modified parameters. Using a "tilde" to denote the mixing parameters in matter, the mixing angles are related by:

$$\cos 2\tilde{\theta} = \frac{\cos 2\theta - \zeta}{(\cos 2\theta - \zeta)^2 + \sin^2 2\theta}, \tag{1.28}$$

where ζ accounts for the neutrino's energy (E_ν), the Fermi coupling constant (G_F), the local electron density along the neutrino's path (n_e):

$$\zeta = \frac{2\sqrt{2} G_F n_e E_\nu}{\Delta m^2}, \tag{1.29}$$

The mass splitting term in matter $\Delta\tilde{m}^2$ is related to the vacuum mass splitting by:

$$\Delta\tilde{m}^2 = \Delta m^2 \sqrt{\sin^2 2\theta + (\cos 2\theta - \zeta)^2}. \tag{1.30}$$

1.3.3 Oscillations in the Three-Neutrino Framework

To extend to three-flavors, additional degrees of freedom are required to build the the 3×3 mixing matrix. Named after Pontecorvo, Maki, Nakagawa, and Sakata, the PMNS matrix describes three-neutrino mixing and takes the form:

$$U_{\text{PMNS}} = \begin{pmatrix} 1 & 0 & 0 \\ 0 & c_{23} & s_{23} \\ 0 & -s_{23} & c_{23} \end{pmatrix} \begin{pmatrix} c_{13} & 0 & s_{13}e^{-i\delta} \\ 0 & 1 & 0 \\ -s_{13}e^{i\delta} & 0 & c_{13} \end{pmatrix} \begin{pmatrix} c_{12} & s_{12} & 0 \\ -s_{12} & c_{12} & 0 \\ 0 & 0 & 1 \end{pmatrix} \tag{1.31}$$

where $s_{ij} = \sin\theta_{ij}$ and $c_{ij} = \cos\theta_{ij}$ for the three real mixing angles θ_{12}, θ_{23}, and θ_{13}. The remaining parameter, δ, is the phase, which if $\delta \notin \{0, \pi\}$, the PMNS matrix becomes complex and allows for CP violation. Historically, δ is inserted in the second term as θ_{13} was the final

mixing angle to be measured.

Each of these mixing angles corresponds primarily to a different oscillation regime for experiments to explore. Atmospheric neutrinos, with energies of a few GeV traveling over baselines of tens to thousands of km, are largely influenced by the first term of Eq. 1.31. The second term dominates for low energies on the order of a few MeV and distances of ∼1 km, which makes reactor neutrinos ideal for measuring θ_{13}. Finally, the third term is associated with the oscillation of solar neutrinos, which have low energy and long baselines.

The disappearance of electron antineutrinos is of particular relevance to the analysis presented in this thesis, which takes the form:

$$P_{e\to e} = 1 - \sin^2 2\theta_{12}\cos^4\theta_{13}\sin^2\Delta_{21} - \sin^2 2\theta_{13}(\cos^2\theta_{12}\sin^2\Delta_{31} + \sin^2\theta_{12}\sin^2\Delta_{32}) \quad (1.32)$$

where Δ_{ji} is defined by Eq. 1.23. As the Daya Bay experiment, whose data is analyzed in this thesis, is not sensitive to the difference between Δm^2_{32} and Δm^2_{31}, the survival probability can be approximated as:

$$P_{e\to e} \approx 1 - \sin^2 2\theta_{12}\cos^4\theta_{13}\sin^2\Delta_{21} - \sin^2 2\theta_{13}\sin^2\Delta m_{ee} \quad (1.33)$$

1.4 Measurements of Oscillation Parameters

In the past two decades, significant progress has been achieved in the field of neutrino physics, particularly in measuring the oscillation parameters. Through the studying the three neutrino flavors with diverse detection technologies and various baselines, many experiments have led to precise measurements, with each oscillation parameter now known to a few percent precision. Furthermore, with only a few exceptions, all neutrino data to date can be explained with the three-neutrino model. Tab. 1.1 summarizes the current measured values.

Table 1.1: The current measured values for all mixing parameters as reported in Ref. [34]. The convention of reporting $\sin^2\theta_{ij}$ rather than $\sin^2 2\theta_{ij}$ is maintained here so to emphasize in which octant θ_{23} resides (whether it is greater than or less than 45°).

Parameter	Measured Value
$\sin^2\theta_{12}$	0.307 ± 0.013
$\sin^2\theta_{23}$	0.546 ± 0.021 (NO) 0.539 ± 0.022 (IO)
$\sin^2\theta_{13}$	$(2.20 \pm 0.007) \times 10^{-2}$
Δm^2_{21}	$(7.53 \pm 0.18) \times 10^{-5}$ eV^2
Δm^2_{32}	$(2.453 \pm 0.033) \times 10^{-3}$ eV^2 (NO) $(-2.536 \pm 0.034) \times 10^{-3}$ eV^2 (IO)
δ_{CP}	$(1.36^{+0.20}_{-0.16}) \times \pi$ rad (NO)

Firstly, the θ_{12} mixing angle and Δm^2_{21} mass splitting term require low energy neutrinos over long baselines. For this reason, many experiments measuring these parameters utilize solar neutrinos, including the Homestake and SNO experiments, which observed and resolved the solar neutrino problem, respectively (Sec. 1.2). Additionally, long-baseline reactor neutrino experiments, such as KamLAND, are also suitable for these measurements. Currently, the most precise estimates were obtained by KamLAND, Super-Kamiokande, and SNO [35].

Next, the θ_{23} and Δm^2_{32} parameters require neutrinos with GeV-neutrinos measured with baselines ranging from tens to thousands of km. Many of the experiments studying these parameters use atmospheric neutrinos as their source, while others use accelerators to produce the neutrinos. For the former, the experiments compare neutrinos produced in the atmosphere above the experiment to those produced in the atmosphere on the other side of the Earth. Alternatively, accelerator experiments collide beams of protons into targets, such as beryllium, to produce pions whose decays produce (anti-)neutrinos. The most precise estimates have been made by T2K, Super-Kamiokande, NOvA, IceCube, and MINOS+ [35].

Finally, θ_{13}, the last mixing angle measured in the PMNS matrix, is especially accessible

by reactor neutrino experiments since the first oscillation maximum resides within a couple of kilometers from the nuclear reactors. Therefore, relatively small neutrino detectors can obtain highly precise results. Sec. 1.4.1 discusses reactor neutrino experiments and the measurements of θ_{13} further.

1.4.1 Measurements of θ_{13}

For L/E scales of $\sim$0.5 km/MeV, the θ_{13} mixing angle dominates the oscillation effects observed for ν_e appearance and $\overline{\nu}_e$ disappearance. For these cases, Earth-based neutrino sources (nuclear reactors and accelerators) are the most convenient as they are well understood and controllable. Experiments measure θ_{13} by observing neutrino appearance ($\nu_\mu \rightarrow \nu_e$) or disappearance ($\nu_e \rightarrow \nu_{\mu/\tau}$). Accelerator neutrino experiments usually observe the neutrino appearance channel since the neutrino beams they produce consist of primarily ν_μ or $\overline{\nu}_\mu$. On the other hand, nuclear reactors produce low energy (few MeV) electron antineutrinos via β^- decay. Even after oscillating to other flavors, these neutrinos only have enough energy to produce e^+s, but not μ^+ or τ^+ leptons. Therefore, reactor neutrino experiments are ideal for the $\overline{\nu}_e$ disappearance channel. This section will focus primarily on the θ_{13} measurements made by reactor experiments.

The very first reactor $\overline{\nu}_e$ experiment attempting to observe $\overline{\nu}_e$ disappearance was the Savannah River Experiment, orchestrated by University of California, Irvine in 1996, followed by the Chooz and Palo Verde reactor $\overline{\nu}_e$ experiments [36, 37, 38]. However, the reactor $\overline{\nu}_e$ models, detector response, and detection efficiency systematic uncertainties restricted these experiments from successfully measuring θ_{13}, though they did constrain the value of $\sin^2 2\theta_{13} \lesssim 0.1$.

Accelerator experiments, T2K and MINOS, observed evidence for a nonzero value of θ_{13} using the ν_e appearance channel in as early as 2011 but only at the level of 2σ to 3σ

significance [39, 40].

The next generation of reactor experiments aimed to reduce the reactor systematics by introducing antineutrino detectors at multiple distances from the reactor cores and measure the relative difference [41]. The near detectors constrain the $\overline{\nu}_e$ flux prediction while the far detectors measure the $\overline{\nu}_e$ rate after oscillation to determine the disappearance due to θ_{13}. These experiments, namely Double Chooz, Reno, and Daya Bay, proved much more successful. In early 2021, Double Chooz published results at the 3σ value when combined with T2K and MINOS [42]. In April 2012, Daya Bay published the first measurement of θ_{13} with a significance $\geq 5\sigma$ [43], with other experiments reporting measurements soon after.

Since Daya Bay's first measurement, consistent results have been published from other reactor and accelerator neutrino experiments, such as RENO [44], Double CHOOZ [45], T2K [46], and NOvA [47]. The published results for $\sin^2 2\theta_{13}$ and Δm^2_{32} (assuming normal mass ordering) are shown in Fig. 1.1 [48]. Currently, Daya Bay still holds the most precise measurement of θ_{13} with a value of $\sin^2 2\theta_{13} = 0.0851 \pm 0.0024$ [49]. This thesis will discuss a new measurement of θ_{13} at Daya Bay and the analysis behind it.

1.4.2 Open Questions

In the century since the first experimental indications of neutrinos, many experiments have observed neutrinos and contributed significantly to our current understanding. However, not all the neutrinos properties and behaviors have been measured yet, including their nature as Dirac or Majorana particles. Furthermore, some discoveries have raised additional questions, such as those surrounding the absolute masses, mass ordering/hierarchy, and if neutrinos violate CP conservation.

The question of whether neutrinos are their own antiparticles has existed since the early

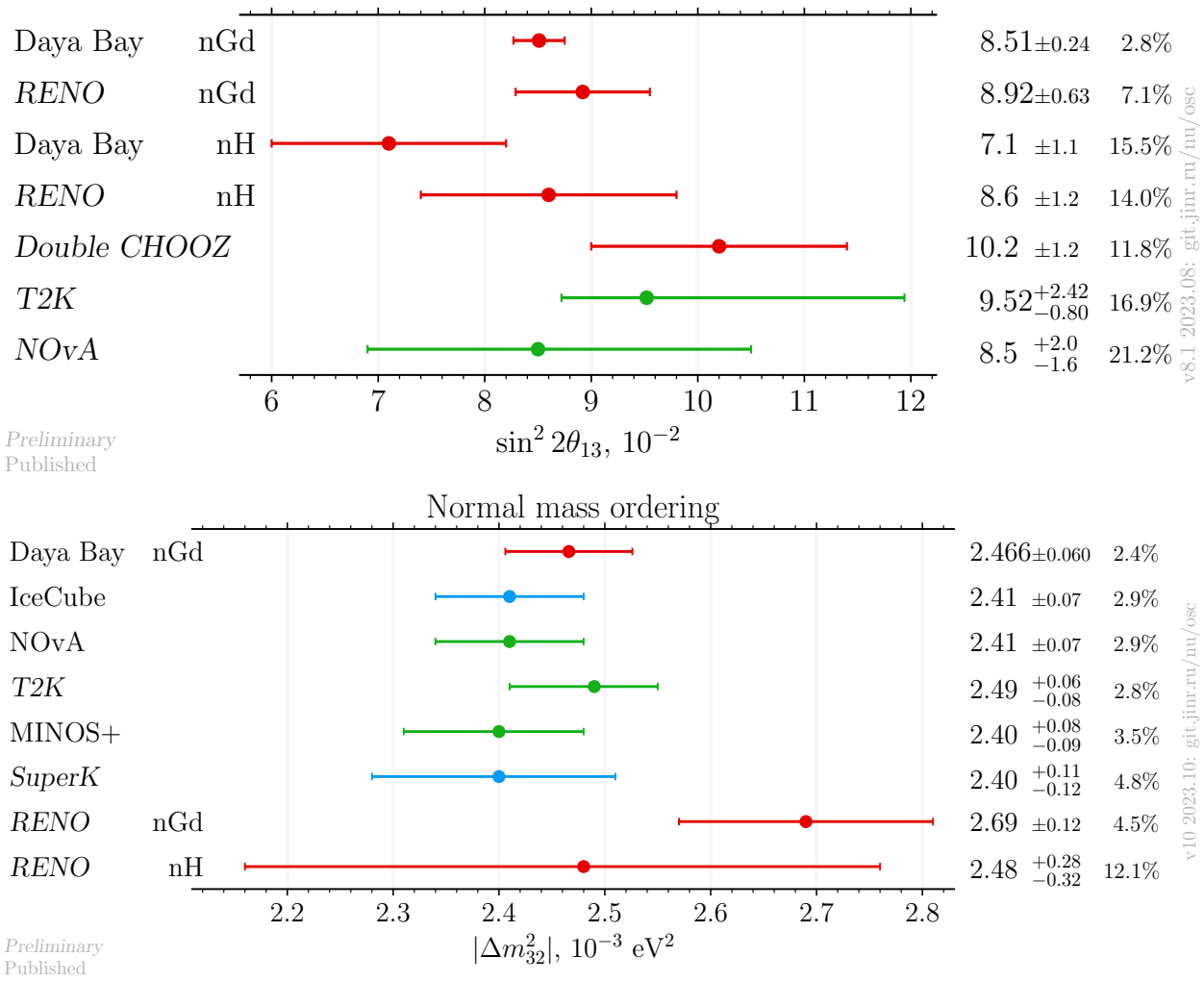

Figure 1.1: Published results for $\sin^2 2\theta_{13}$ (top) and Δm^2_{32} assuming normal mass ordering (bottom) [48].

days of neutrino studies. If neutrinos and antineutrinos are distinct entities, characterized as Dirac particles, the number of leptons in a particle interaction would adhere to the current conservation principle, remaining constant. However, if neutrinos and antineutrinos are the same particle, known as Majorana particles, this postulated lepton number conservation would be violated. Importantly, the mechanism governing neutrino mass is intricately linked to whether they are Dirac or Majorana particles, a determination that also sets the scale for permissible neutrino masses. Evidence of Majorana neutrinos could come from detecting neutrinoless double beta decays, where the neutrinos of the simultaneous decays annihilate

with one another.

Secondly, neutrino oscillations can only occur with non-zero differences between the three neutrino masses, indicating that neutrinos are not massless. However, to date, only the mass splitting terms, Δm^2_{21} and Δm^2_{32}, have been measured; the absolute masses and the mass ordering/hierarchy remain unknown. These measurements depend on precise values of the other oscillation parameters, such as θ_{13}. Currently, accelerator experiments report a slight preference for the normal mass ordering (NO), where $m^2_3 > m^2_2 > m^2_1$, as opposed to the inverted mass ordering (IO), where $m^2_2 > m^2_1 > m^2_3$ [35].

Finally, the determination that all three mixing angles are non-zero, with θ_{13} being the last of the three, mathematically allows for the potential violation of leptonic CP (charge parity) conservation. The violation of CP conservation could explain the observed matter-antimatter asymmetry in the universe, as the Big Bang Theory suggest that matter and antimatter should have been produced in equal amounts. The CP phase angle δ_{CP} dictates the extent of CP violation in the neutrino sector and its measurement depends on precision measurements of θ_{13}. Recently, the T2K accelerator neutrino experiment reported evidence of $\delta_{CP} \neq 0$ at 3σ confidence [50].

The possibility for leptonic CP violation and the ability to determine the neutrino mass ordering relied on the non-zero value of θ_{13}. This, in turn, incentivized new multi-billion dollar experimental programs, such as DUNE [51] and Hyper-Kamiokande [52]. DUNE, for example, will be the principal experiment in the US for the next several decades. As shown in Fig. 1.2, its sensitivity to δ_{CP} is enhanced by the prior from reactor experiments, which is dominated by the measurement from Daya Bay.

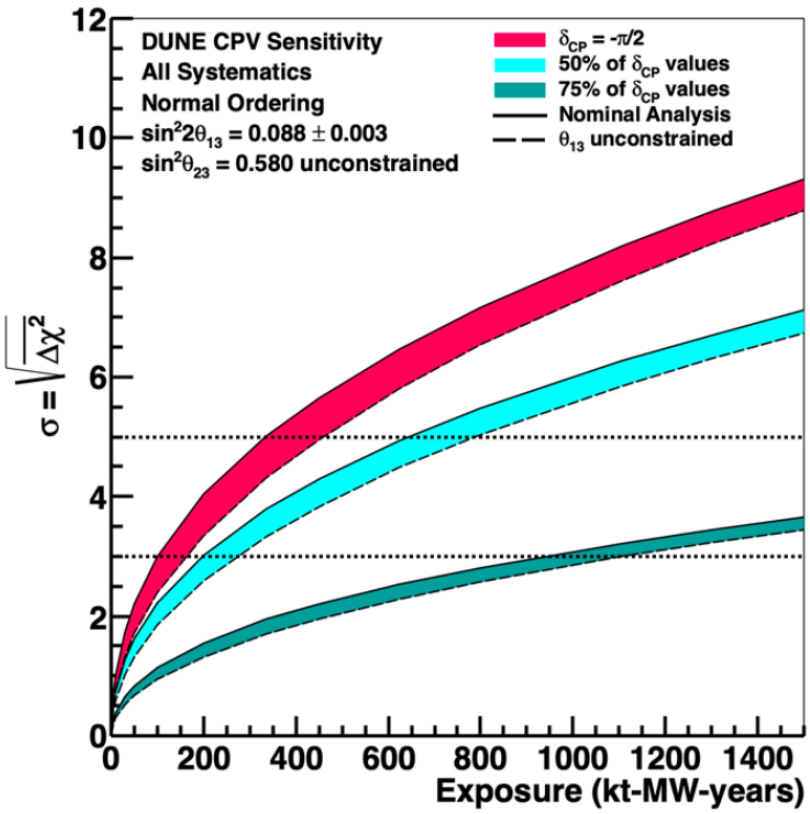

Figure 1.2: Projected δ_{CP} sensitivity by DUNE in terms of exposure in kt-MW-years [53]. The solid lines indicate the improved sensitivity due to constraints on θ_{13} provided by reactor neutrino experiments compared to the dashed lines without these constraints.

Chapter 2

The Daya Bay Reactor Neutrino Experiment

The Daya Bay Reactor Neutrino Experiment was specifically designed to measure the θ_{13} neutrino mixing parameter by doing a relative measurement of the $\overline{\nu}_e$ fluxes at near and far experimental halls (EHs) [54]. As mentioned in Sec. 1.4, the near and far antineutrino detectors (ADs) measured the essentially-unoscillated and oscillated $\overline{\nu}_e$ rates, respectively, and by comparing the two, the uncertainties associated with the reactor prediction and the absolute detection efficiency were almost fully cancelled, therefore allowing θ_{13} to be precisely measured.

Built on the campus of the Daya Bay and Ling Ao Nuclear Power Plants in southeastern China, the location was ideal for this task: The six nuclear reactors act as one of the most intense sources of $\overline{\nu}_e$ on Earth, while the nearby mountains provide shielding from cosmic-ray muons with easy-access tunnels [55]. Construction began in October 2007 and lasted until 2011: the first near experimental hall (EH1) was completed in August, EH2 in November, and finally the far hall, EH3, was ready in December [56]. Data-taking began on the 24th of

December, 2011 and with just 55 days of data, Daya Bay published results of the first definite measurement of θ_{13} with $\geq 5\sigma$ significance [43]. Data collection continued for just under 9 years, with only brief interruptions, and on the 12th of December, 2020, the experiment concluded data-taking.

2.1 Overview

The nuclear reactor complex which acts as the $\overline{\nu}_e$ source consists of three pairs of nuclear reactors, called Daya Bay, Ling Ao, and Ling Ao II. The nuclear fissions within each 2.9 $\mathrm{GW_{th}}$ reactor produce $\sim 5.8 \times 10^{20}$ $\overline{\nu}_e/\mathrm{s/GW_{th}}$ [57].

The EHs were strategically placed such that EH1 was nearest to the Daya Bay cores, EH2 was closest to the Ling Ao and Ling Ao II cores, and EH3 was significantly further from the complex. Fig. 2.1 shows the locations of the EHs with relation to the nuclear reactors, while Tab. 2.1 provides the baselines for each reactor-AD pair as measured by two GPS surveys which agreed to within 4 mm of each other. The uncertainty in the baseline measurement was less than 18 mm and was deemed to have negligible impact on the θ_{13} measurement [55].

All three EHs were built under the nearby mountain to reduce the cosmic-ray muon rates

Table 2.1: Baselines from each reactor core (columns) to each AD (rows) [m] [57].

Detector	D1	D2	L1	L2	L3	L4
EH1-AD1	362.38	371.76	903.47	817.16	1653.62	1265.32
EH1-AD2	357.94	368.41	903.35	816.90	1354.23	1265.89
EH2-AD1	1332.48	1362.88	472.97	489.58	557.58	499.21
EH2-AD2	1337.43	1362.88	472.97	495.35	558.71	501.07
EH3-AD1	1919.63	1894.34	1533.18	1533.63	1551.18	1524.94
EH3-AD2	1917.52	1891.98	1534.92	1535.03	1554.77	1528.05
EH3-AD3	1925.26	1899.86	1538.93	1539.47	1556.34	1530.08
EH3-AD4	1923.15	1897.51	1540.67	1540.87	1559.72	1533.18

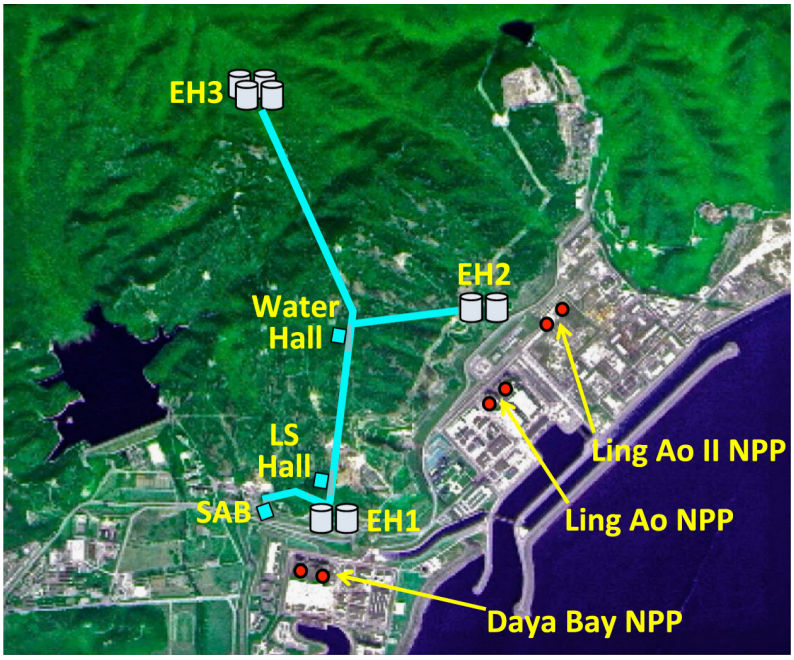

Figure 2.1: The layout of Daya Bay's three experimental halls and six nuclear reactors [57].

observed by the detectors. The overburden for each EH provided by the mountain and the corresponding muon flux and average muon energies are listed in Tab. 2.2. Additionally, each EH was equipped with a water pool surrounding the detectors to veto any muons that survived the overburden, as well as shield against natural radioactivity from the surrounding rock and neutrons from cosmic ray muons [58]. See Sec. 2.2 for more details.

Each of the near halls (EH1 and EH2) contained two ADs and were used to determine the $\overline{\nu}_e$ flux produced by the reactors. EH3, also known as the far hall, housed 4 ADs $\sim$ 2 km

Table 2.2: Overburden, simulated muon flux and average energy for each experimental hall. The uncertainty of the simulated flux is $\sim$10%. Table from [58].

Hall	Overburden		Muon Flux	Average Energy
	[m]	[mwe]	[Hz/m^2]	[GeV]
EH1	93	250	1.27	57
EH2	100	265	0.95	58
EH3	324	860	0.056	137

from the Daya Bay cores and $\sim$ 1.5 km from the Ling Ao cores, corresponding rougly to the location of the first oscillation minimum primarily determined by Δm^2_{32}. This location makes Daya Bay particularly sensitive to θ_{13}, through comparison of the $\overline{\nu}_e$ measurements at EH3 to prediction with no oscillation effects, as computed by the near halls. For the specifics of the ADs, see Sec. 2.3.

2.2 Water Pools

To surround the ADs with at least 2.5 m of shielding, the water pools were 10 m deep, 16 m long, and 10 m wide for the near halls, 16-m wide for the far hall [58]. Each water pool was comprised of an inner water shield (IWS) and an outer water shield (OWS) which were separated via Tyvek sheets, making them optically isolated from one another. Both regions were instrumented with photomultiper tubes (PMTs) to detect the muon-induced Cherenkov radiation within the water pools. Of the 960 PMTs used in the water pools, 341 were donated by the MACRO experiment. These 8-in PMTs were models 9350KA and D642KB, manufactured by EMI. The other 619 PMTs were brand new Hamamatsu PMTs, model R5912. All the PMTs in the IWS are directed towards the ADs (inward), though for the OWS, PMTs are placed in both orientations, see Tab. 2.3.

In addition to the water pools, a resistive plate chamber (RPC) array was built to provide additional muon tagging efficiency. However, the RPC data was not used for this analysis.

Table 2.3: Water pool PMT populations. Table from [58].

Hall	IWS	OWS (inward/outward)	Total
EH1	121	167 (103/64)	288
EH2	121	167 (103/64)	288
EH3	160	224 (128/96)	384

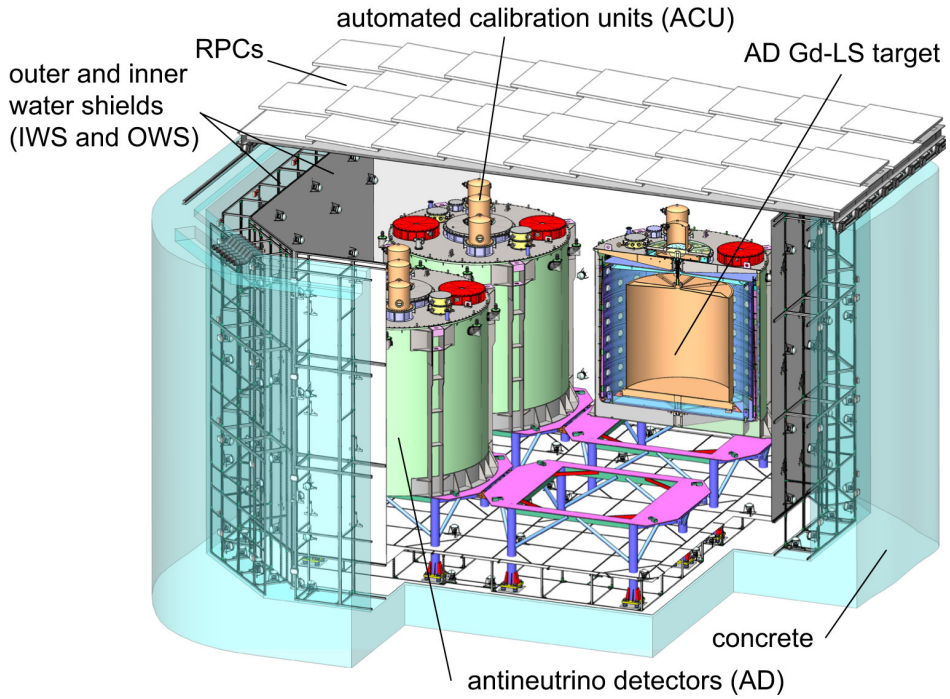

Figure 2.2: Schematic of the Water Pools and Antineutrino Detectors in the Far Hall. Figure taken from Ref. [55].

For details on this system, refer to Ref. [58].

Alongside the schematic of EH3 (Fig. 2.2), Fig. 2.3 shows a picture of the far hall during the filling of the IWS, prior to the RPCs (seen in the background) being positioned to cover the detectors and water pool.

2.3 Antineutrino Detectors

As mentioned in Sec. 2.1, eight identically designed ADs were divided into the three EHs: Each of the near halls housed two identically-designed ADs each, with four in the far hall.

The experiment's data-taking timeline can be divided into three periods: the 6-, 8-, and 7-AD periods. Initially, only six were installed and operated, allowing for the experiment to begin taking data earlier. In the 6-AD period, which lasted from December 24, 2011 to

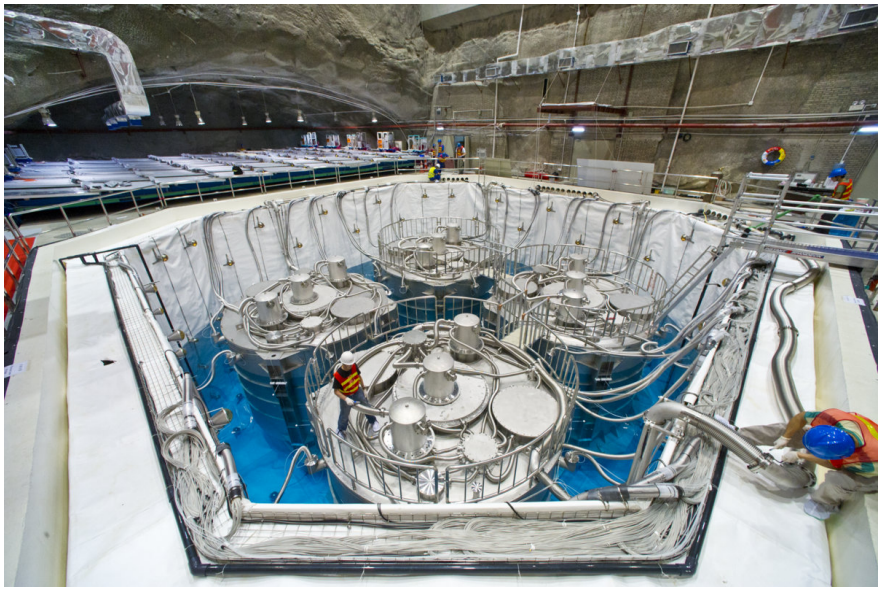

Figure 2.3: Picture of the Far Hall after the installation of the final Far AD.

July 28, 2012, both EH2 and EH3 operated with the absence of one detector. The final two ADs were installed during the next few months while the experiment was shut down. After coming back online on October 19, 2012, all eight ADs were in operation until December 20, 2016. At this time, another shut down occurred such that one AD in EH1 could be repurposed for the JUNO experiment to conduct liquid scintillator studies [59]. Finally, the 7-AD period spanned from January 26, 2017 to December 12, 2020, when the experiment ended data-taking.

Each AD had three concentric cylindrical volumes: gadolinium-doped liquid scintillator (GdLS) in the inner most, followed by liquid scintillator (LS), and finally mineral oil (MO). Both the LS and GdLS regions were used as target volumes for the antineutrinos. Sec. 2.3.1 describes the antineutrino interactions in the detectors and Sec. 2.3.2 details the design of the ADs.

2.3.1 Detection of Antineutrinos: Inverse Beta Decays

The interaction between the reactor antineutrino and the protons within the detection volume of the ADs occurs via the Inverse Beta Decay (IBD): $\overline{\nu}_e + p \rightarrow e^+ + n$. This process creates a two-event signature, called a "double coincidence", which allows for effective selection against many other events of radiogenic and cosmogenic origin. The first event, called the prompt event, arises from the positron's loss of kinetic energy and annihilation with an electron, the latter part releasing two 0.511 MeV γ-rays. The second event, called the delayed event, comes from the neutron capture on a nucleus within the target volume, illustrated in Fig. 2.4.

The total prompt energy is associated with the incoming antineutrino energy due to conser-

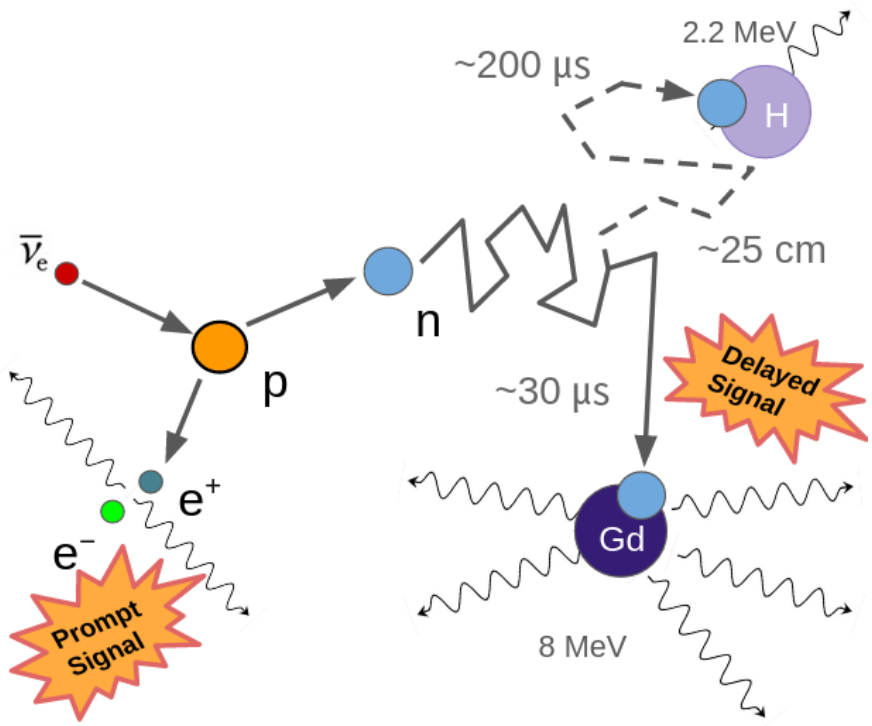

Figure 2.4: Diagram of IBD process within the AD target volume.

vation of mass-energy, such that:

$$E_p \approx E_\nu - \delta m_{pn} + m_e \approx E_\nu - 0.78\ MeV. \tag{2.1}$$

Here $\delta m_p n$ is used to denote the difference in mass between the neutron and proton. This relation allows for the determination of the antineutrino by measuring the energy of the prompt event. The estimation assumes that the neutron has no kinetic energy, which is a good but not exact approximation.

The nucleus on which the neutron is captured determines the energy of the detected delayed event. For the case that the neutron captures on Gd, a total of ∼8 MeV is produced (7.95 or 8.54 MeV depending on the Gd isotope), whereas the capture on ^{1}H releases 2.2 MeV of energy. For simplicity "nGd" will be used to describe both the neutron capture on Gd and the analysis studying this sample, as will "nH" be used for the H case. The capture time in the LS and GdLS regions are ∼200 μs and ∼30 μs, respectively. The time is significantly shorter in the GdLS region due to the larger cross section of a neutron capture on Gd (49 kb) than on H (0.322 b) [60].

These properties of the IBD process were utilized in the planning and designing of the detectors. The GdLS region was designed to be the main target of the AD, specifically for the nGd analysis. The introduction of Gd decreased the capture time and increased the emitted delayed energy, both of which significantly reduced backgrounds in the selection. Furthermore, the LS region helped to catch γ-rays escaping from nGd captures. Without the LS region, the energy associated with those γ-rays would be lost and therefore distort the energy spectrum. Because of this, the most precise θ_{13} measurements from Daya Bay are the result of the nGd analyses. As for the nH analysis, both the GdLS and LS regions are active regions: while most neutrons in the GdLS region will capture on Gd, some still capture on H, in addition to all the neutrons in the LS region. This provides a much larger effective

target for the nH analysis compared to the nGd, and therefore a high statistics sample which is completely distinct. Additionally, the systematics between the two analyses are mostly decoupled, especially for measuring θ_{13}, though larger for the nH analysis. Therefore, the ability to detect both the nGd and nH processes allows Daya Bay the ability to release independent results of both and cross-check itself.

2.3.2 AD Design and Construction

To ensure the accuracy of the relative measurement of θ_{13}, all eight ADs were built following the exact same design specifications and in pairs to minimize any differences between them. Fig 2.5 shows the schematic of the AD design. With a height and diameter of 5 m, each AD had 192 8 inch PMTs around the sides of the outermost cylinder, called the stainless steel vessel (SSV), facing the target volume. Inside the SSV were two nested cylinders, called the inner and outer acrylic vessels (IAV and OAV), which divided the AD into three concentric volumes. Both the IAV and OAV were made of $\sim$1.5 cm thick UV-transparent acrylic. On either end of the OAV, reflectors were installed to improve the light collection by the PMTs. Contained by the 3 m tall, 3 m diameter IAV, the central region was filled with 20 t of GdLS. The intermediate zone, contained by the 4 m tall, 4 m diameter OAV, was filled with 20 t of undoped LS. The third and outermost volume, housing the PMTs, was filled with non-scintillating MO. Both the LS and GdLS regions were connected to overflow tanks to account for slight changes in the temperature and pressure of the ADs. Additionally, each AD was equipped with three automated calibration units (ACUs), which are discussed in Ch. 3. The next paragraphs will discuss further details on the instrumentation of the PMTs in the MO region and the two scintillating regions.

Firstly, the outermost region was filled with MO. Since it does not scintillate, the MO acted as a buffer between the PMTs and the target volumes. Arranged in 8 rings of 24 around the

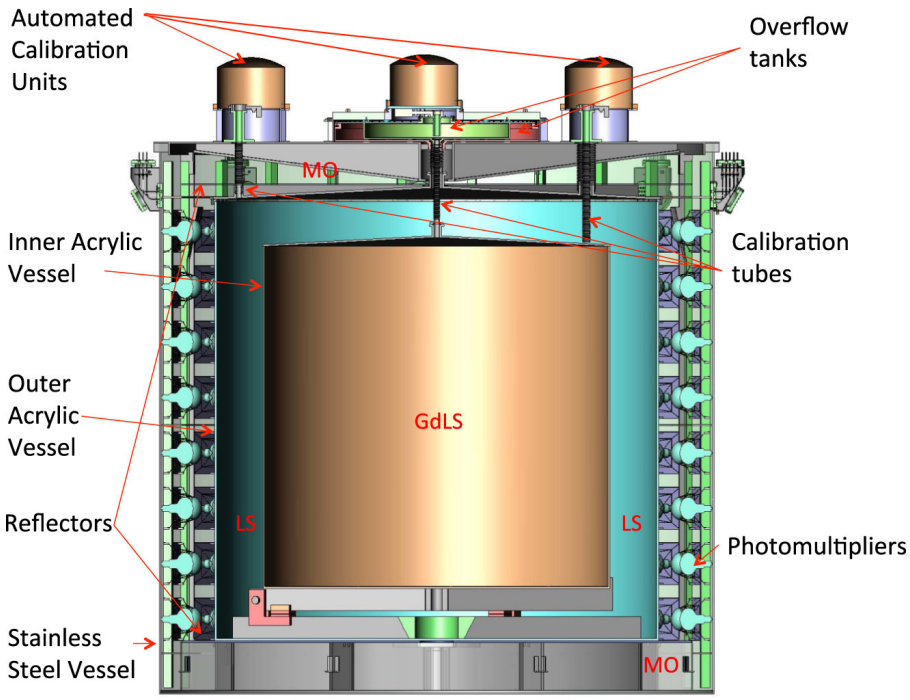

Figure 2.5: Schematic of a Antineutrino Detector (AD). Figure obtained from Ref. [55].

inside of the SSV and submerged in the MO, the 8-inch PMTs were the same Hamamatsu model (R5912) as the newly purchased PMTs in the water pools. Being light-sensitive devices, their purpose in the AD was to detect scintillation light from particle interactions within the detector. They do this by utilizing the photoelectric effect: When an incoming photon hits the sensitive photocathode, it ejects a photoelectron (PE), which then gets accelerated by an electric field in the base of the PMT to a series of charged metal plates, called dynodes. Due to the acceleration, each time an electron hits a dynode, more electrons are ejected, causing an avalanche effect. Finally, these electrons are collected at the end by an anode, producing a signal. These signals were fed into front-end electronics and amplified, then split for measurements of charge and relative arrival time. Each detector (AD, IWS, and OWS) had independent triggers, which were defined through the number of channels over threshold (NHIT) and/or the the analog sum (ESUM) of the signal. Finally, once the detector trigger was enabled, these signals, measured in ADC units, underwent the process of being reconstructed into events, as described Ch. 3.

Secondly, the two scintillating volumes, contained by the acrylic vessels, made up the target volume of the AD. The main ingredient in both the LS and GdLS was linear alkylbenzene (LAB), which is a thoroughly studied medium with desirable properties for large detectors, notably its high light-yield and transparency [60]. The LS was made by dissolving into the LAB was the fluor (2,5-diphenyloxazole (PPO)) and wavelength shifter (p-bis-(o-methylstyryl)-benzene (bis-MSB)) in proportions of 3 g/L and 15 mg/L, respectively. A total of 200 t was produced for the LS regions. As for the GdLS, additional steps were required. To effectively load the gadolinium into LS, the 99.99% pure gadolinium chloride ($GdCl_3xH_2O$) was added to the solution, along with 3,5,5-trimethylhexanoic acid (THMA), which is a stable ligand for bonding gadolinium to the LAB. At the end of this process, the gadolinium made up 0.1% by mass of the GdLS. To ensure the same composition was used across all detectors, the GdLS for all 8 ADs, a total of 185 t, was manufactured at the same time then divided equally between them.

An especially important set of measurements to Daya Bay's oscillation analyses was the number of target protons in each AD, since this has direct relation with the predictions and could bias the measurement of θ_{13}. To calculate the number of target protons, the total mass of each target volume m, listed in Tab. 2.4, is multiplied by the analytically-computed hydrogen mass fraction n_{p} of the materials (LS, GdLS, and acrylic) in said volume which is contributed by protons and the detection efficiency within that volume (Tab. 32 from [61]) [62]. Then the proton number for each volume (GdLS, LS, and other) are summed together:

$$N_{\mathrm{p}} = m_{\mathrm{GdLS}} * n_{\mathrm{p,\ GdLS}} * \varepsilon_{\mathrm{det,\ GdLS}} + m_{\mathrm{LS}} * n_{\mathrm{p,\ LS}} * \varepsilon_{\mathrm{det,\ LS}} + m_{\mathrm{other}} * n_{\mathrm{p,\ other}} * \varepsilon_{\mathrm{det,\ other}}, \quad (2.2)$$

where "other" accounts for the acrylic vessels, reflectors, and other structural pieces within the AD [62]. The uncertainties on the mass measurements were 5 km for GdLS, 28 kg for LS, and 0.5% relative uncertainty for "other".

Table 2.4: Target masses for each detector volume [55, 63, 64] and the total number of target protons per AD [65]. Uncertainties of the mass measurements were 5 kg for GdLS, 28 kg for LS, and a 0.5% relative uncertainty for "other".

Hall	GdLS [kg]	LS [kg]	Other [kg]	N_{p} [$\times 10^{25}$]
EH1-AD1	19941	21573.5	3697	77229.7 ± 81.7691
EH1-AD2	19967	21519.6	3731	77098.1 ± 81.7695
EH2-AD1	19891	21587.2	3664	77234.0 ± 70.1253
EH2-AD2	19944	21449.9	3749	76886.3 ± 70.1564
EH3-AD1	19917	21566.2	3744	77204.8 ± 70.1266
EH3-AD2	19989	21408.8	3864	76811.8 ± 81.7713
EH3-AD3	19892	21652.6	3844	77444.6 ± 81.7703
EH3-AD4	19931	21474.5	3794	76951.8 ± 70.1038

Because it behaves similarly to the detection efficiency (Sec. 4.4), the number of target protons was treated as an effective efficiency:

$$\varepsilon_{\mathrm{p},i} = \frac{N_{\mathrm{p,\ AD}i}}{N_{\mathrm{p,\ EH1\text{-}AD1}}}. \tag{2.3}$$

In this definition, the number of target protons of a given AD is compared to EH1-AD1. This was inputted into the fitter, described in Ch. 7.

Chapter 3

Data Acquisition, Calibrations and Event Reconstruction

Beyond the AD construction, implementation of calibrations and corrections ensured the detectors operated properly, as the accuracy of timing, position, and energy measurements is critical to the relative θ_{13} oscillation analysis.

Data collection occurred in periods known as data runs. Once a large dataset is accumulated, the raw data was prepared for analysis through calibrations and reconstructions. Additionally, the data is monitored and checked during these processes to ensure the detectors are operating normally and that the data is of good quality. The analysis presented in this thesis uses the data from the P17B dataset, which includes data collected from December 24, 2011 through August 30, 2017.

This chapter will discuss the individual steps in the processing of the data. Sec. 3.1 introduces the hardware involved in the data acquisition and and calibration processes, Sec. 3.2 discusses the time calibration and position reconstruction, and Sec. 3.3 explains the many steps of the energy reconstruction process. While the position and energy reconstructions are presented

separately here, in reality, they were done in parallel such that the position reconstruction occurs between the Light Yield Calibration and the Non-Uniformity Correction. Finally, Sec. 3.4 discusses the process of monitoring the data quality which ensured the detectors were operating properly during the data acquisition runs.

3.1 Data Acquisition and Calibration Systems

Quality data for Daya Bay's oscillation analyses first rely on the infrastructure for the data collection and calibration processes. This section discusses the PMT and electronics system which measures and records the detected signals (Sec. 3.1.1) and the instruments implemented for calibrating the detectors reliably (Sec. 3.1.2 and Sec. 3.1.3).

3.1.1 PMT System and Electronics

Supplied with high voltage, the PMTs produce voltage signals according to the amount of light they receive, making them the start of the data stream. If these signals surpassed a threshold of $\sim$0.25 photoelectrons (PE), the channel's time-to-digital converter (TDC) and analog-to-digital converter (ADC) were triggered, therefore recording the time and charge of the signal [57]. These values were measured with resolutions corresponding to 1.6 ns and $\leq$0.1 PE. The signals from the PMTs were then propagated to a master trigger board, which determined if the conditions were satisfied for a trigger of the whole detector. For this analysis, the main trigger criteria were the number of PMT channels triggered (NHIT) or the total analog sum of PMT signal strength (ESUM). Tab. 3.1 summarizes the conditions for the detector trigger. Additionally, the detector could be triggered externally with a trigger associated to a calibration LED within the detector, as described in Sec. 3.2.1.

From here, the TDC and ADC signals was saved into raw data files, which need to then be

processed into physical values for the positions and energies of the reconstructed events.

Table 3.1: Trigger conditions for the whole detector [57]. The trigger conditions for the OWS differ between near and far sites to account for the different amount of overburden.

Detector	Criterion	Trigger Threshold ($\geq$)
AD	NHIT	45 PMTs
AD	ESUM	65 PE $\approx$ 0.4 MeV
IWS	NHIT	6 PMTs
OWS (near/far)	NHIT	7/8 PMTs

3.1.2 Automated Calibration Units

To calibrate according to known sources, automated calibration units (ACUs) were integrated into the detector design. Each ACU was equipped with three sets of sources with different energies which could be deployed individually to specified depths along vertical axes. The supplied sources consisted of an LED, ^{241}Am-^{13}C/^{60}Co, and ^{68}Ge [66]. The LED emitted photons with a maximum wavelength of 435 nm at controllable intensities, and was primarily used in the time calibration (Sec. 3.2.1). The radioactive sources, on the other hand, produced signals of known energies, summarized in Tab. 3.2. These signals were used to calibrate the energy response of the ADs.

For effective calibration throughout the entire detector volume, the ADs were built with three ACUs at various distances from the center of the detector: center (r=0 mm), near the edge of the GdLS region (r=1350 mm), and in the LS region (r=1772.5 mm). During dedicated calibration runs, the sources would be deployed into the detector volume and the collected data would be evaluated to confirm the accuracy of the detector's energy measurements.

Table 3.2: The energies of the radioactive sources deployed by the ACUs.

Source	Radiation	Gamma Energy [MeV]
^{241}Am-^{13}C	neutrons	8
^{60}Co	γ-rays	2.506
^{68}Ge	positrons	1.022

3.1.3 Manual Calibration System

The Manual Calibration System was designed such that the calibration sources could be positioned at any point within the IAV via a central rod and a retractable arm [67]. The depth of the source was controlled by the raising and lowering of the central rod, while the arm could be opened to a perpendicular position relative to the axis of the central rod providing the radial freedom of the MCS. The system deployed the sources with an accuracy of 2.5 cm. A diagram of the source deployment is provided in Fig. 3.1.

While the experiment was shut down, the MCS was installed in EH1-AD1 during the summer

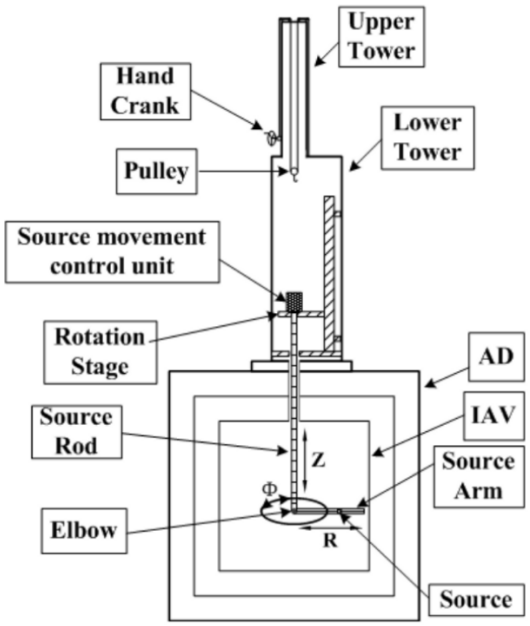

Figure 3.1: Schematic of the manual calibration system (MCS). Figure from Ref. [67].

of 2012. The MCS was equipped with a combined source of ^{60}Co and ^{238}Pu-^{13}C. The ^{60}Co allowed for comparison to the calibrations done with the ACU, while the ^{238}Pu-^{13}C produced neutrons and 6.13 MeV γ-rays.

Data was collected for 1700 unique positions within the detector which provided maps for reconstructing the positions of the signals within the AD, discussed further in Sec. 3.2.2,. Additionally, studies were conducted on neutron capture efficiency [68] and detector uniformity [69].

3.2 Position Reconstruction

The raw data outputted from the PMT system consisted of the timestamp and charge information for each channel in the detector. The next step is for the raw data to be processed to calibrate and reconstruct the individual events within the detector. This section will explain the time calibration (Sec. 3.2.1) and the position reconstruction algorithms (Sec. 3.2.2) at Daya Bay.

3.2.1 Time Calibration

To properly reconstruct the detected events, the timestamps recorded by the TDC for the PMTs must be synchronized, which requires accounting for differences between channels. The first correction addresses differences in recorded hit times between channels, largely due to differences in cable lengths. For this calibration, the LED of ACU-A was utilized: From the center of the detector, the LED was pulsed at the same time as the PMTs were triggered. The signal received at the TDC was converted to a time value utilizing the TDC's time step of 1.5625 ns, then adjusted for the LED-to-PMT distances [70].

The second part of the time calibration targeted the "timewalk" effect, which is the charge-dependent timing difference since larger pulses take less time than smaller pulses to pass the FEE trigger threshold [71]. By varying the LED voltage, a 2D histogram for each channel of the ADC counts vs corrected time was filled and fit to determine the charge-dependent time correction.

3.2.2 Reconstruction Algorithms

Once the timing for each channel was calibrated, the data was ready for position reconstruction. Two independent algorithms, "AdSimple" and "AdScaled", were developed to reconstruct the event positions from the charge distributions across all the PMTs. AdSimple was determined to be more accurate for the nH analysis, and therefore will be the focus of this section [72]. After the introduction of an additional correction related to electronics nonlinearity (see Sec. 3.3.1), AdSimple became AdSimpleNL, which is used in this analysis.

To quickly summarize the AdScaled reconstruction, the center-of-charge position was determined by calculating an average over the PMT positions weighted by the charged measured by each PMT, then applying a parameterized correction determined by simulation [57].

In contrast, AdSimple's algorithm utilized a Monte Carlo simulation to produced a collection of templates of the charge distributions with which to compare each event's charge pattern [73]. Each template correspond to one position within a cylindrical (r, ϕ, z) grid with combinations of 20 r, 24 ϕ, and 20 z positions, totalling 9600 templates for comparison. To determine the best match, a χ^2 was constructed:

$$\chi^2(\mathbf{r}_{\text{rec}}) = \sum_{i=1}^{192} -2 \ln \frac{\text{Poisson}(N_i^{\text{obs}} | N_i^{\text{template}}(\mathbf{r}_{\text{rec}}))}{\text{Poisson}(N_i^{\text{obs}} | N_i^{\text{obs}})}, \tag{3.1}$$

where the sum indexes over the 192 PMTs in the AD. N_i^{obs} is the number of PEs observed

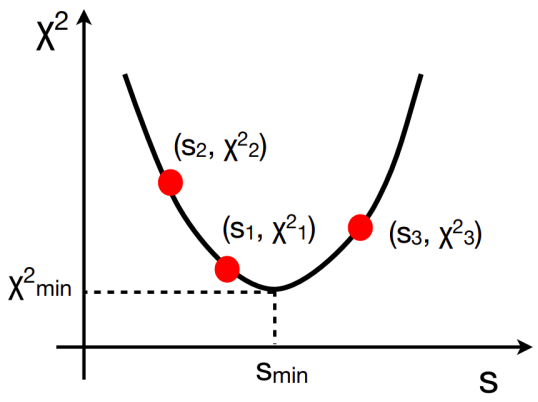

Figure 3.2: Illustration of AdSimple(NL)'s interpolation for determining the $\mathbf{r}_{\text{rec}}$ which minimized χ^2, where s represents the individual coordinates (r, ϕ, z). Plot obtained from Ref. [73].

by PMT i, $N_i^{\text{template}}(\mathbf{r}_{\text{rec}})$ is the template's prediction for PMT i with the reconstructed event located at $\mathbf{r}_{\text{rec}}$, which are fed into the Poisson probability for n observed counts given an expected μ counts, represented as Poisson$(n|\mu)$. After identifying the template with the least χ^2 value, an interpolation was utilized to determine the location with the lowest χ^2 for the entire detector volume, beyond the 9600 points the templates provided. As illustrated in Fig. 3.2, the interpolation was performed for each of the cylindrical dimensions (r, ϕ, z) to find the reconstructed position, $\mathbf{r}_{\text{rec}}$, which minimized the χ^2.

The AdSimple (and AdSimpleNL) reconstruction algorithm was tested against the data collected by the MCS, introduced in Sec. 3.1.3. The data consisted of 1700 different locations around the GdLS region with accuracy of 2.5 cm [67], which was divided into bins in z and r coordinates. To include the γ-ray signal from the ^{60}Co source and the nH capture energy from the ^{238}Pu-^{13}C source, events with energies of (2.3 ± 0.2) MeV were selected for each bin, then the reconstructed positions were compared to the true MCS positions. The resolution and bias were evaluated at $\lesssim 0.4$ m and $\lesssim 0.2$ m, respectively. In order to extend into the LS region, data from the ^{60}Co source deployed by the ACUs returned a resolution of $\lesssim 0.4$ m and a $\lesssim 0.12$ m bias, confirming the reconstruction performance for both the GdLS and LS regions [74]. The results are shown in Fig. 3.3.

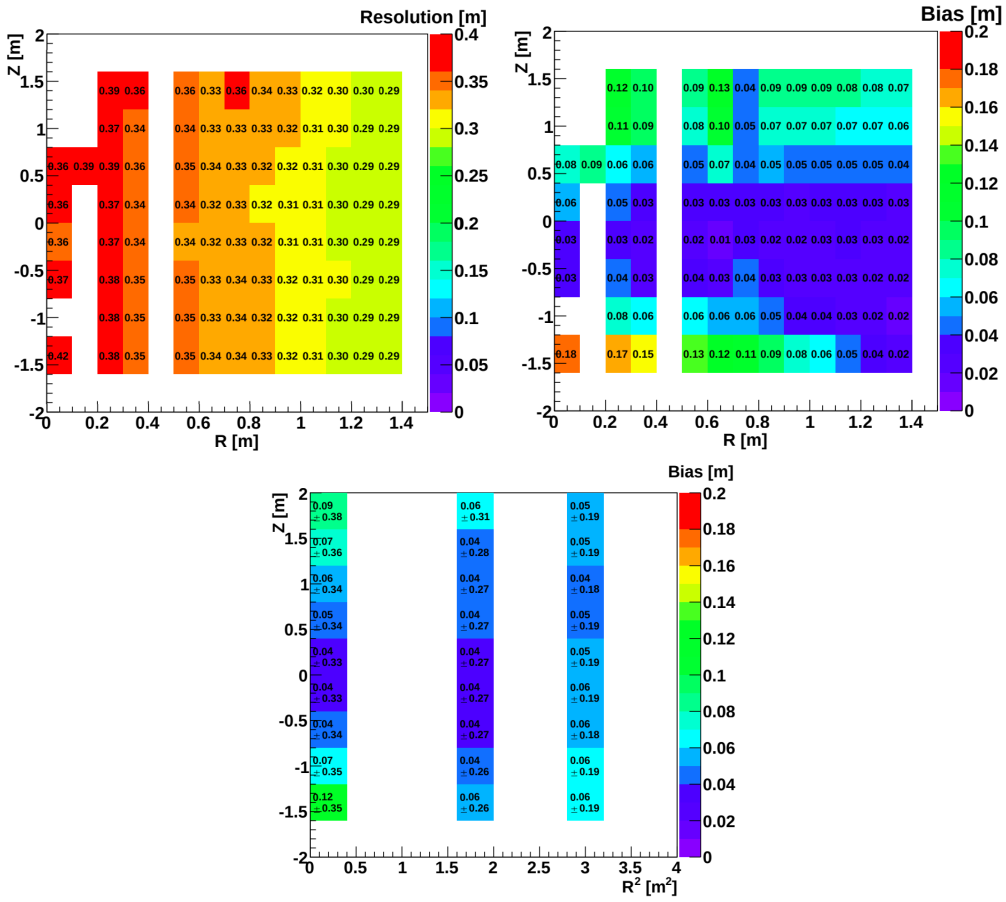

Figure 3.3: Validation of the AdSimple position reconstruction. Top: Resolution (left) and bias (right) observed within the GdLS region through MCS data of nH captures from the ^{238}Pu-^{13}C source and 2.506 MeV γ-rays from the ^{60}Co source. Bottom: Bias and resolution of the ACUs' ^{60}Co γ-rays as observed in EH1-AD2. Each bin is labeled as $\mu \pm \sigma$ where μ and σ represent the bias and sigma, respectively, both measured in m. Plots from [74].

3.3 Energy Reconstruction

Proper energy reconstruction and calibration is essential for the oscillation analyses at Daya Bay. The signals received by the ADCs (measured in ADC counts) must be converted to physical quantities (MeV), which is done by a series of calibrations. Eq. 3.2 summarizes the corrections applied to reconstruct the energy of the physics events observed by the detectors:

$$E_{\mathrm{rec}} = \left(\sum_i \frac{Q_i}{\overline{Q}_i^{\mathrm{SPE}}(t)} f^*_{\mathrm{SCNL}} \right) f_{\mathrm{act}}(t) \frac{1}{N^{\mathrm{PE}}(t)} f_{\mathrm{pos}}(\mathbf{r}_{\mathrm{rec}}, t). \tag{3.2}$$

The first factor, $\overline{Q}_i^{\mathrm{SPE}}(t)$, applied to the charge measured by the i-th PMT, Q_i, adjusts for the performance of each individual channel via PMT gain calibration, specifically to convert the charge to detected light (measured in PE). For one of the reconstruction algorithms (AdSimpleNL), an additional correction (f^*_{SCNL}) was applied to each PMT individually to account for the nonlinearity in the electronics response. Then the contributions of each PMT are summed and a correction factor, $f_{\mathrm{act}}(t)$, is applied to account for any inactive or disabled PMTs, which is determined by the channel quality checks. The gain calibration, channel quality, and electronics nonlinearity correction are described in Sec. 3.3.1, as they are determined on a per-channel basis. The total light observed by the AD then gets converted into energy by a scale factor, $N^{\mathrm{PE}}(t)$, determined by the light yield calibration (Sec. 3.3.2). Finally, a non-uniformity correction, $f_{\mathrm{pos}}(\mathbf{r}_{\mathrm{rec}}, t)$, is applied to account for position dependence of the observed signal (Sec. 3.3.3). The performance of the energy reconstruction is reviewed in the discussion of the energy scale in Sec. 3.3.4.

3.3.1 Individual Channel Calibrations

The first corrections to the raw data are applied to each channel individually. These corrections address the gain of PMT, the quality of the channel's data, and the non-linear response of the electronics. Additional checks to monitor channels carefully were conducted by using the gain and channel quality information, which is also presented in this section.

Gain Calibrations

The gain of a PMT is defined as the amount of amplification that an individual photoelectron experiences in the PMT. Measured in ADC counts per PE, the gain is essential for calculating the physical energies from the measured signals: The gain correction accounts for small differences in gain between the ADs. Because the input voltage, environmental conditions (ex. the temperature), and other effects such as the ageing of photocathodes can influence the PMT response, each channel's gain was measured continuously over the duration of the experiment.

The "rolling gain" was measured using the single PE (SPE) signals arising from PMT dark noise. This dark noise was collected in the few hundred ns of data before each trigger in the AD, during which there were no physics events in the detector. The strength of the ADC signal resulting from SPEs was acquired throughout each day and fit to determine the mean gain for the individual PMT channels. To model the counting of PEs as well as account for the resolution due to the amplification and digitization, a convolution of a

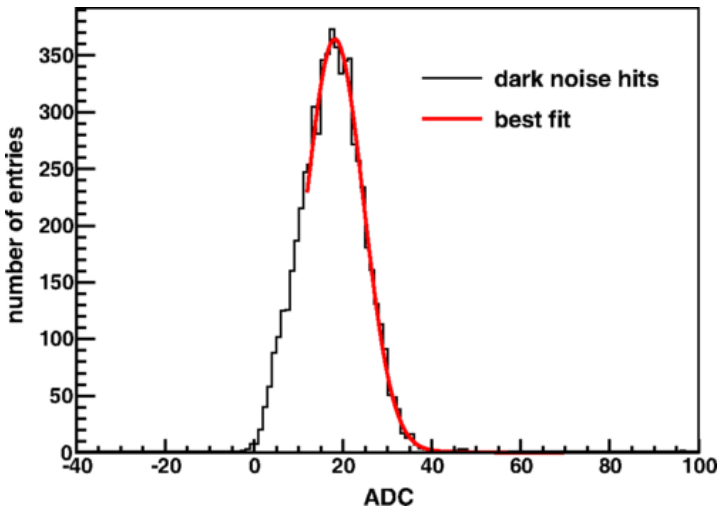

Figure 3.4: Example of a PMT's ADC charge distribution after subtraction of the baseline of uncorrelated signals. Figure from Ref. [57].

Poisson distribution with a Gaussian distribution modeled the ADC charge spectrum [57]:

$$S_i(Q) = \sum_{n=1}^{2} \frac{\mu_i^n e^{-\mu_i}}{n!} \frac{1}{\sigma_{\mathrm{SPE},i}\sqrt{2n\pi}} \exp\left(-\frac{(Q_i - n\overline{Q}_i^{\mathrm{SPE}})^2}{2n\sigma_{\mathrm{SPE},i}^2}\right). \tag{3.3}$$

Here, the distribution for PMT i, $S_i(Q)$, is described in terms of μ, $\overline{Q}_i^{\mathrm{SPE}}$, and $\sigma_{\mathrm{SPE},i}$ corresponding to the mean number of dark noise PEs, the mean ADC counts per PE, and the resolution of the PMT-ADC system. While the index n, the number of PEs, should range from 0 to ∞ in this sum, the dark noise consists almost exclusively of SPEs, and therefore the upper limit of $n = 2$ was implemented without loss of precision. An example of the ADC spectrum and fitted spectrum is shown in Fig. 3.4.

The PMT gain, $\overline{Q}_i^{\mathrm{SPE}}$, was determined by this fit for each channel for each day, which allowed the individual channels, and the entire AD, to be monitored. The average PMT gain for each AD over the duration of the experiment, shown in Fig. 3.5, drifts upwards slightly. The cause of this trend was partially attributed to temperature changes of the front-end electronics, while the remaining drift behavior was potentially due to the aging of the PMTs [57].

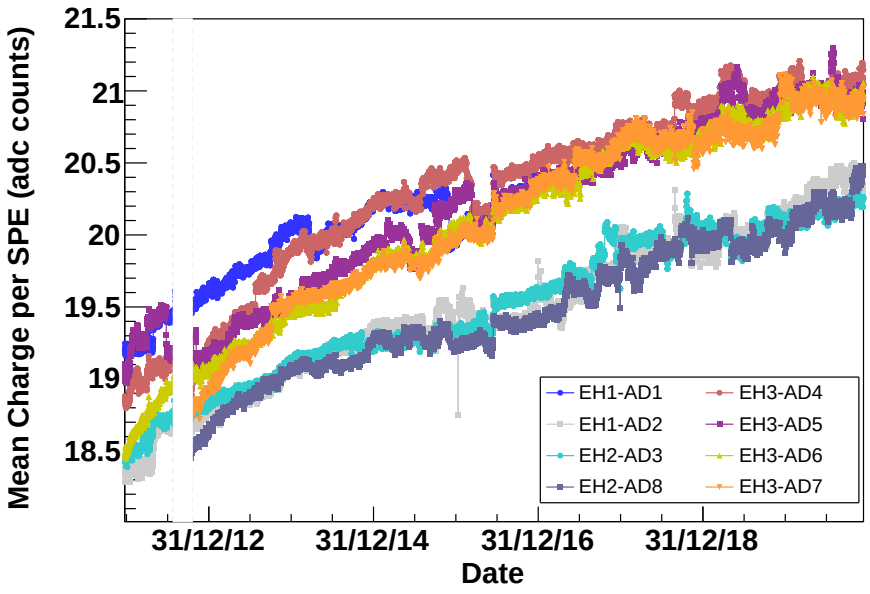

Figure 3.5: Average rolling PMT gain for each AD over time.

Channel Quality

Guaranteeing good quality in each of the channels is a critical step for the data production: A single non-functioning channel affects the measured total charge by up to a factor of $1/192 \approx 0.5\%$.

Channel quality issues fell mainly into two categories: high voltage and electronics issues. The high voltage issues usually appeared as drifting gain and, in the worst cases, dying channels. The electronics issues expressed themselves as noisy channels. For moderate to low noise levels, this was not an issue, though with higher noise, the noise peak prevents clean fits in the gain calibration, as demonstrated in Fig. 3.6.

To identify the bad channels, two main cuts were implemented which monitored the high voltage of the channel and the occupancy of the channel [76]. A stable channel would have a voltage above 1200 V and occupancy of 0.3 or more. Channels with lower voltage (< 1200 V) and/or occupancy less than 0.3, it would be marked as bad. Alternatively, channels with lower voltage and high occupancy were manually checked to determine its behavior. This

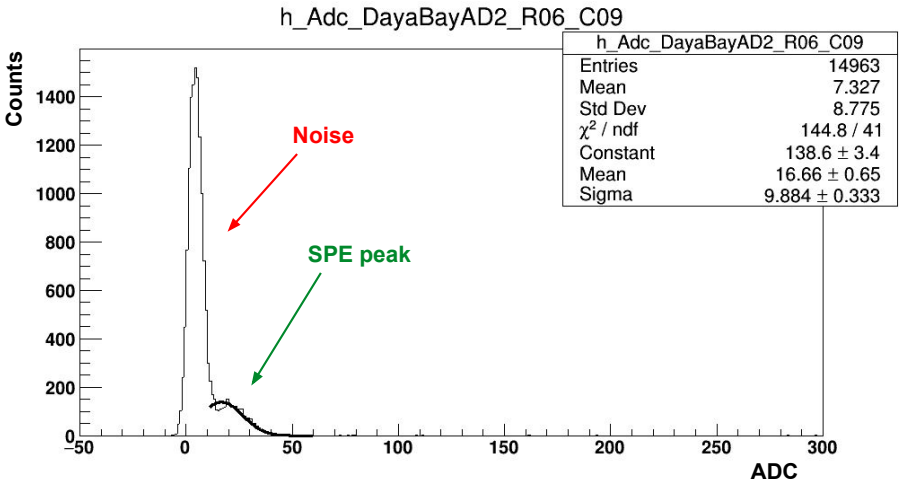

Figure 3.6: Example of a channel with high noise levels. The large noise peak near 5 ADCs clearly biases the fit of the single PE peak near 20 ADCs. If the SPE peak could not be resolved, the channel was flagged for bad quality. Figure taken from Ref. [75].

channel quality information was also used to monitor the health of channels in the detector.

Monitoring Channels Individually

To fully utilize the gain and channel quality calibrations, both sets of information are used to monitor individual channels and identify additional possible issues that were not caught in the channel quality.

Healthy channels have stable gains over time, while less stable gains indicate potentially problematic channels. If the channel is already flagged as bad by the channel quality calibration procedure described in the previous section, the data from the channel, as well as the gain, is already removed. The abnormalities remaining with good channel quality require the further attention.

The two main issues needing intervention were single day poor fits by the gain calibration process and channels with an additional noise peak biasing the fit. For the former, the mean value obtained from the fit does not accurately represent the gain of the channel. The solution for these cases were to replace the inaccurate gain with the average of the gains from the stable period of the same PMT. For the latter, the solution depended on two factors: the severity of the noise peak and the time dependence of the noise. Channels which had clearly separated SPE and noise peaks could still provide the true gain. Channels with short periods of noise could be reliable assigned with the average gain from stable periods. Channels whose gains could not be obtained due to severe noise for long periods of time were instead identified as bad in the channel quality and treated accordingly.

The other causes of unstable gains were largely related to the high voltage modules dying and/or being replaced and therefore altering the gain of the PMT. As these were real effects, the measured gains were true to the system and no action was required.

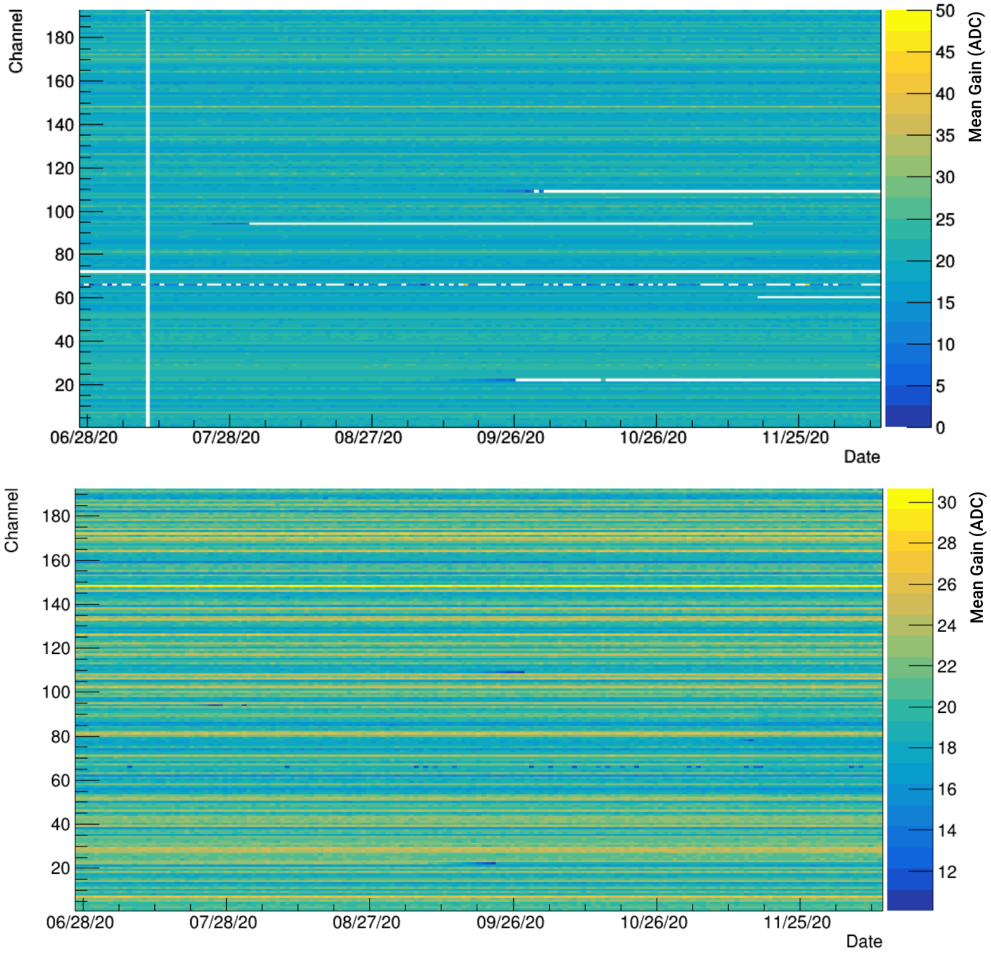

Figure 3.7: The gain of all 192 PMT channels over time for EH1-AD2 for the final six months of data before (top) and after (bottom) additional corrections to individual channels were applied.

Fig. 3.7 exhibits the mean gain of each of the 192 channels over time before and after individual channel behaviors were addressed for the production period spanning from June 27, 2020 to Dec 12, 2020.

Electronics Nonlinearity Correction

Named the "Single Channel Nonlinearity Correction" (SCNL), the final correction applied to each channel separately was the electronics nonlinearity. This correction is the difference

between the AdSimple and AdSimpleNL reconstructions.

The cause of this nonlinearity stems from the PMTs and front-end electronics (FEE) which digitize the PMT signals: Particularly in the case when several pulses are not perfectly aligned, the summing circuit underestimates the total charge collected by the PMT and the magnitude of this effect depends on the total charge measured. To quantify the effect, a flash analog-to-digitize converter (FADC) was installed in EH1-AD1 in 2015 to collect data alongside the standard FEE system. The FADC digitized waveforms at 1 GHz for each of the 192 channels independently and calculated the charge collected to compare to the FEE. The ratio of the two systems is demonstrated in the Fig. 3.8 [77]. The SCNL correction curve, the inverse of this ratio, was implemented for each PMT signal individually in the energy reconstruction process.

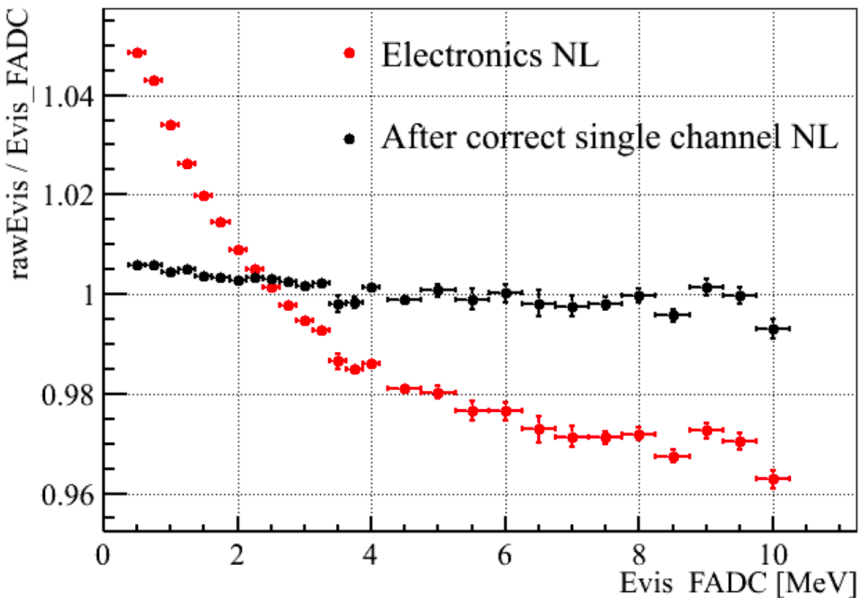

Figure 3.8: Ratio of energy measured by the FEE to that of the FADC as a function of charge measured by the FADC before (red) and after (black) implementing the SCNL correction to account for the electronics nonlinearity. Figure from Ref. [78].

3.3.2 Light Yield Calibration

Two methods of implementing the light yield calibration ensured the accuracy of the conversion from PEs to MeV: weekly calibration runs using the ^{60}Co source as well as continuous calibration during the data collection via spallation neutrons (SPNs).

Both methods utilized the mean of known γ-ray peaks to determine the light yield. For the former, the ^{60}Co source produces a 2.506 MeV signal on which to calibrate. For the latter, the SPNs originate from muons interacting within the environment and materials around the detectors. In the GdLS region of the AD, these neutrons can capture on the two Gd isotopes producing either 7.95 or 8.54 MeV peaks as a reference point. These two overlapping energy peaks were fit with a double Crystal Ball function [79, 80, 81], where a single Crystal Ball function is defined by:

$$f_{\mathrm{CB}}(E;\alpha,n,E_0,\sigma) = N \times \begin{cases} \exp\left(-\frac{(E-E_0)^2}{2\sigma^2}\right), & \frac{E-E_0}{\sigma} > -\alpha \\ \left(\frac{n}{|\alpha|}\right)^2 \exp\left(-\frac{|\alpha|^2}{2}\right)\left(\frac{n}{|\alpha|} - |\alpha| - \frac{E-E_0}{\sigma}\right), & \frac{E-E_0}{\sigma} \leq -\alpha. \end{cases} \tag{3.4}$$

Here E_0 and σ are the peak and resolution of the energy measurement, n is the power law describing the low-energy tail, and α is the transition point between the peak and tail.

For this thesis, the SPNs were used as the primary calibration method, with the lower nGd peak defined as 7.95 MeV in the reconstructed energy. The light yield was studied using other known signals to test the assumed linear relation between measured charge and total energy, and the differences were attributed to the non-linear detector responses, corrected later. The light yield was approximately 170 PEs per MeV, as shown in Fig. 3.9, though this quantity decreased over time, most likely due to the degradation of the scintillator.

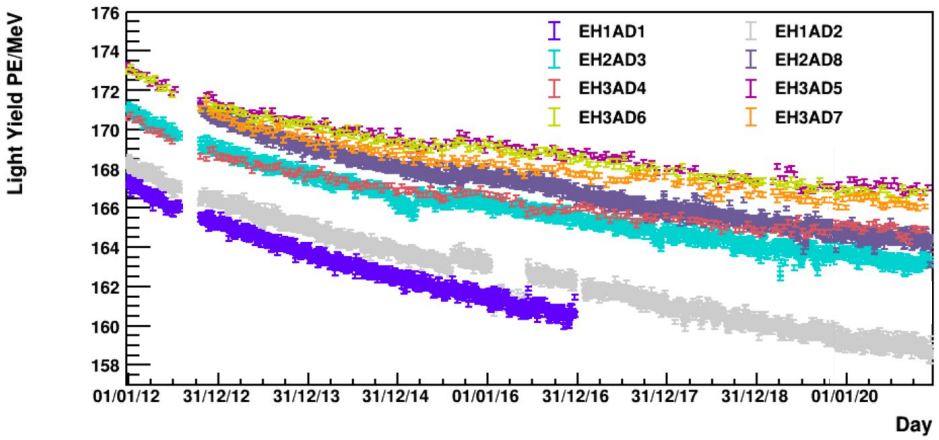

Figure 3.9: Light yield for each AD over time as measured by spallation neutrons. The gradual decline is likely due to scintillator degradation. Figure obtained from Ref. [82].

Post-Muon Energy Scale Correction

While the SPNs provide signals with which to calibrate on, the high energy muons which produced them created a bias in the energy measured by the detector. Therefore, an additional correction needs to be applied. As shown in Fig. 3.10, the nGd peak energy is higher for the SPN sample compared to the IBD sample.

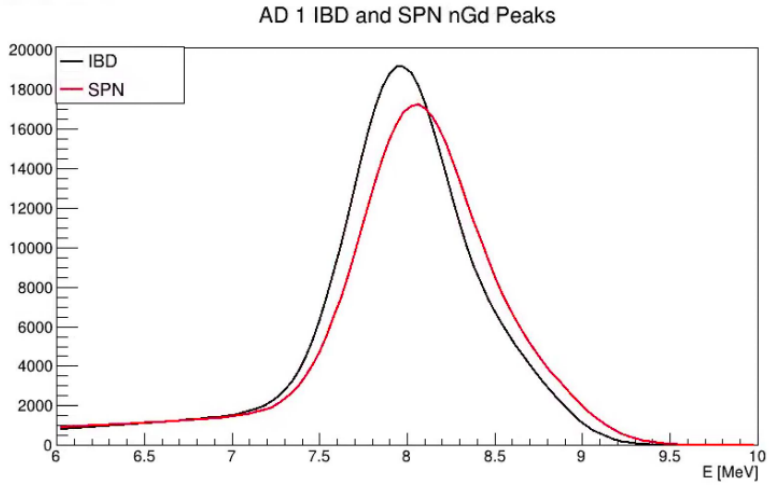

Figure 3.10: Energy spectra of the neutron capture on Gd as measured by IBDs (black) and SPN (red). Figure presented in Ref. [83].

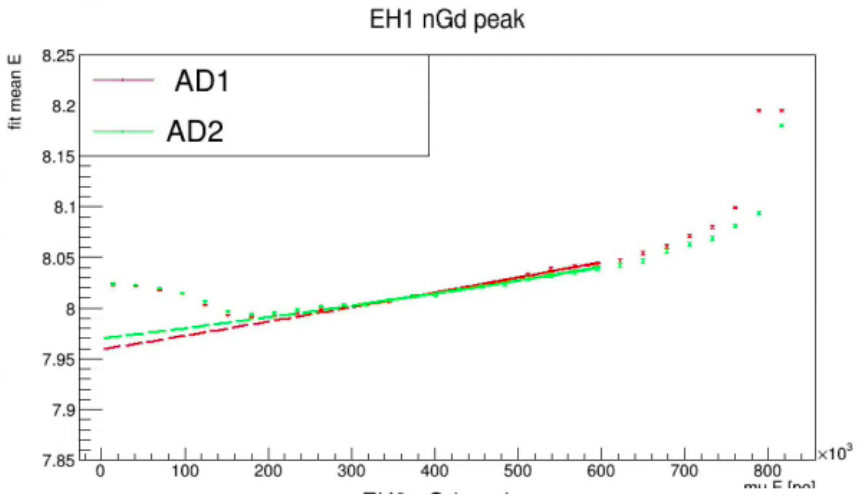

Figure 3.11: SPN nGd peak energy as a function of energy of the preceeding muon. The fit was performed for muons with energy between 3×10^5 and 6×10^5 P.E. to avoid the effects of clipping muons at low energies and saturation on the high energies. Figure taken from Ref. [83].

To properly correct for the muon bias, the reconstructed energy of the SPN, E_{rec}, was studied as a function of preceding muon energy. As shown in Fig. 3.11, the trend was fit with a second order polynomial to extrapolate the value for the case without a preceding muon. The fitted energies and resulting corrections are summarized in Tab. 3.3.

Table 3.3: Summary of nGd peak energies from the IBD sample compared to the SPN sample as determined by extrapolation and the full fit. The ratio of the SPN energies determines the correction factor.

Detector	IBD [MeV]	Extrapolated [MeV] (A)	Full Fit [MeV] (B)	Correction (A/B)
EH1-AD1	7.9585	7.9649	8.0375	0.9910
EH1-AD2	7.9634	7.9688	8.0328	0.9920
EH2-AD1	7.9752	7.9823	8.0493	0.9916
EH2-AD2	7.9741	7.9781	8.0430	0.9919
EH3-AD1	7.9640	7.9714	8.0555	0.9896
EH3-AD2	7.9614	7.9706	8.0510	0.9889
EH3-AD3	7.9589	7.9626	8.0579	0.9882
EH3-AD4	7.9661	7.9725	8.0681	0.9881

3.3.3 Non-Uniformity Correction

The reconstructed energy was dependent on the amount of light detected by the PMTs. Several factors impact this, including the optical properties of the liquid scintillator, acrylic vessels and mineral oil, as well as the geometry of the PMTs with regards to the directional dependence of the incident light and the orientation with respect to the Earth's magnetic field. The task of the non-uniformity correction was to ensure events of a certain energy would be reconstructed with the same energies regardless of the location within the AD.

The entire non-uniformity correction was formed from two separate corrections:

$$f_{\text{pos}}(r, z, \phi, t) = f_{\text{Az}}(r, z, \phi, t) f_{\text{rz}}(r, z) \tag{3.5}$$

where f_{Az} is the azimuthal correction and f_{rz} is the correction in $r - z$ coordinate space. To account for any slight differences between the ADs, non-uniformity maps were created for each detector individually.

The azimuthal correction corrects for the Earth's magnetic field, which is dependent on ϕ and r, as well as dead PMTs and calibration tube effects, which are dependent primarily on ϕ and z, though it also depends on r and t. No significant time dependence was observed except by the sudden onset of several bad PMTs. Two time periods were deemed suitable to account for the temporal instabilities.

Both effects were studied separately, based on correlated $\beta - \alpha$ decays caused by the ^{238}U decay chain, then combined into AD- and time specific correction maps [84]. The final correction took the form of:

$$f_{\text{Az}}(r, z, \phi, t) = 1 - M(\phi, z) \frac{r}{r_0(z)}, \tag{3.6}$$

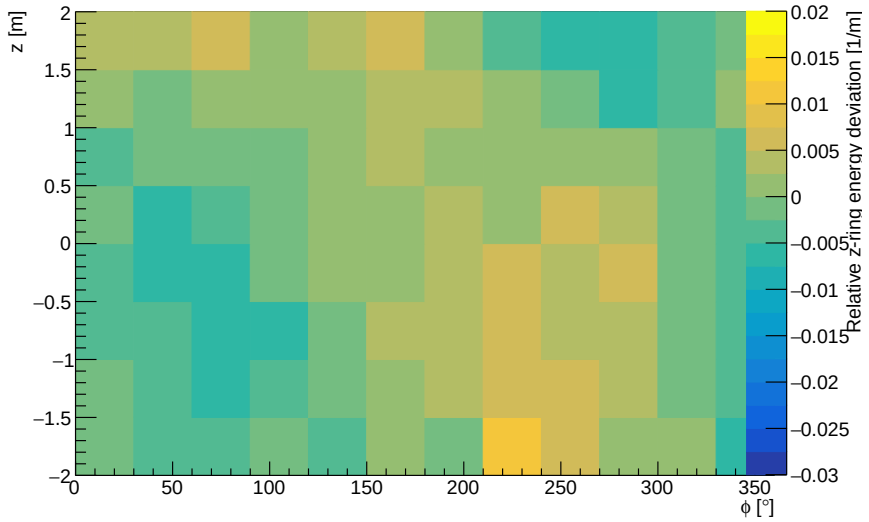

Figure 3.12: Azimuthal non-uniformity Map for EH1-AD1. Figure made from data presented in Ref. [85].

where $M(\phi, z)$ is the correction map for the particular AD in the appropriate time period (example map shown in Fig. 3.12), and $r_0(z)$ is the average radius of events within the AD.

The second half of the non-uniformity correction was created using three separate signals: SPN captured on Gadolinium, SPN captured on Hydrogen, and the α signal from the same correlated $\beta-\alpha$ as for the azimuthal correction. For these maps, the AD was divided into 10 voxels for both the r^2- and z-dimensions, and the ratio of the average energy for the entire AD to the peak energy for the voxel became the correction for that voxel:

$$f_{\mathrm{rz}}(r, z) = \frac{E_{\mathrm{avg}}}{E_{\mathrm{voxel}}(r, z)}. \tag{3.7}$$

All approaches were tried for this analysis and yielded consistent results: both corrections improved the uniformity to within $\pm 3\%$ [86]. The α-only approach was deemed better as these particles' energy deposition is more localized than gammas, and therefore closer to expectations of positrons.

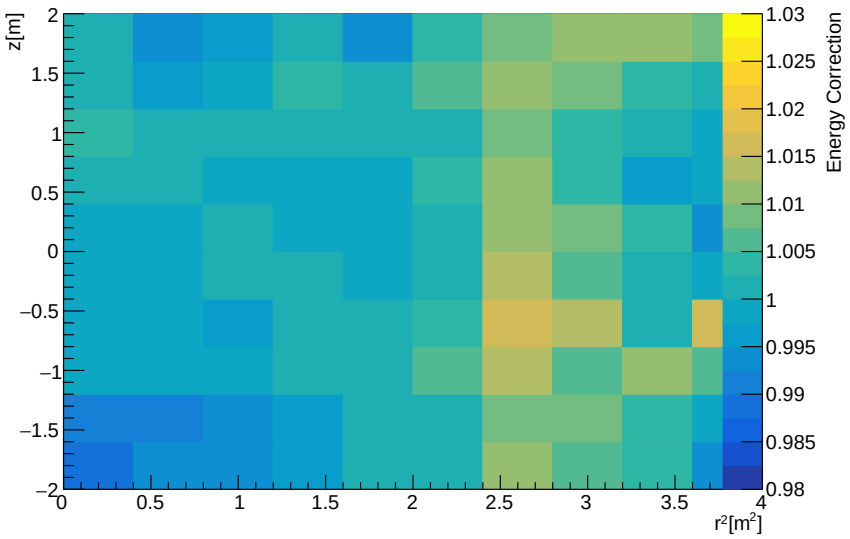

Figure 3.13: $r^2 - z$ non-uniformity correction map for EH1-AD1 using the α signal. Figure made from data presented in Ref. [85].

3.3.4 Energy Scale Validations

After the series of calibrations and reconstructions, the resulting energy resolution of the detectors and the relative energy scale can be used to measure the difference performance of the ADs. Comprehensive understanding of both the absolute and relative energy scales is necessary for Daya Bay's $\overline{\nu}_e$ oscillation analysis.

Energy Resolution

The energy resolution of the ADs was modeled as a function of reconstructed energy, E_{rec}:

$$\frac{\sigma_E}{E_{\text{rec}}} = \sqrt{a^2 + \frac{b^2}{E_{\text{rec}}} + \frac{c^2}{E_{\text{rec}}^2}}, \tag{3.8}$$

where a, b, and c are parameters related to various aspects of the detectors' performance: the non-uniformity of the detector (a), the counting statistics of photons throughout the

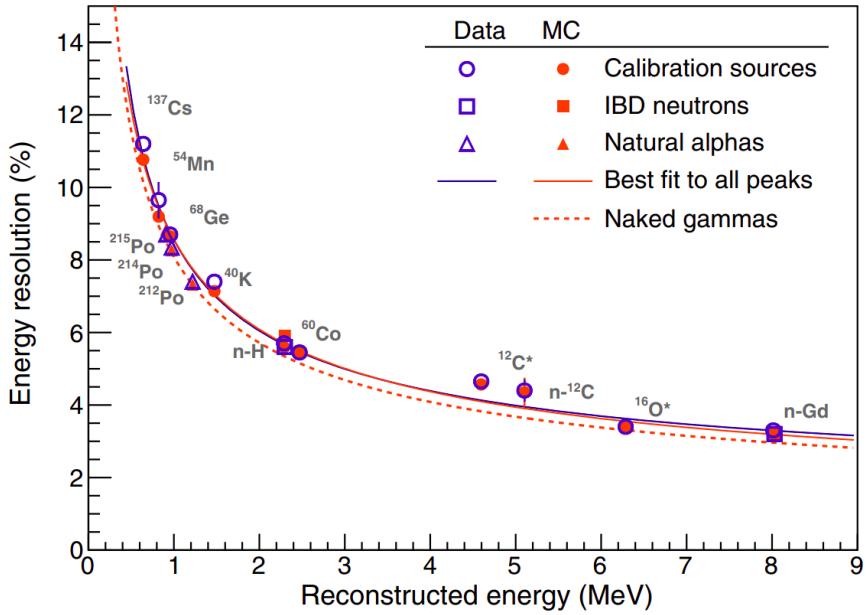

Figure 3.14: Energy resolution for calibration sources, neutron captures and natural α's in the ADs. Figure from Ref. [57].

production, detection, and digitization process (b), and the dark noise of the PMTs (c) [57]. This model was used to fit data collected with various calibration sources to determine the values of the parameters:

$$\begin{aligned} a &= 0.016 \\ b &= 0.081 \text{ MeV}^{1/2} \\ c &= 0.026 \text{ MeV} \end{aligned} \tag{3.9}$$

Shown in Fig. 3.14, the energy resolution is about 8.5% at 1 MeV. This model was incorporated in the detector response model used in the fitter, discussed in Ch. 6.

Relative Energy Scale

With the relative measurement approach taken at Daya Bay, it was essential that all ADs reconstruct the same energies for the same physical processes. Any bias in one AD relative to the others would impact the events passing the IBD selection and therefore bias the

measurement of θ_{13} and Δm^2_{32}. The relative energy scale, defined as the variation in reconstructed energy between ADs, was determined by comparing measurements of the same processes across all detectors. 13 sources were utilized within the GdLS, the results of which are presented in Fig. 3.15, with all variations between the ADs lying within ±0.2% relative to the average of all ADs [57].

For the LS region, the IBD nH capture peaks (Fig. 4.10) were used to calculate the relative energy scale, resulting in a difference of ±0.35% between ADs, which was further verified by the signals from alphas. This value was conservatively used as the relative energy scale uncertainty for the entire detector volume for this analysis, as discussed in Ch. 7.

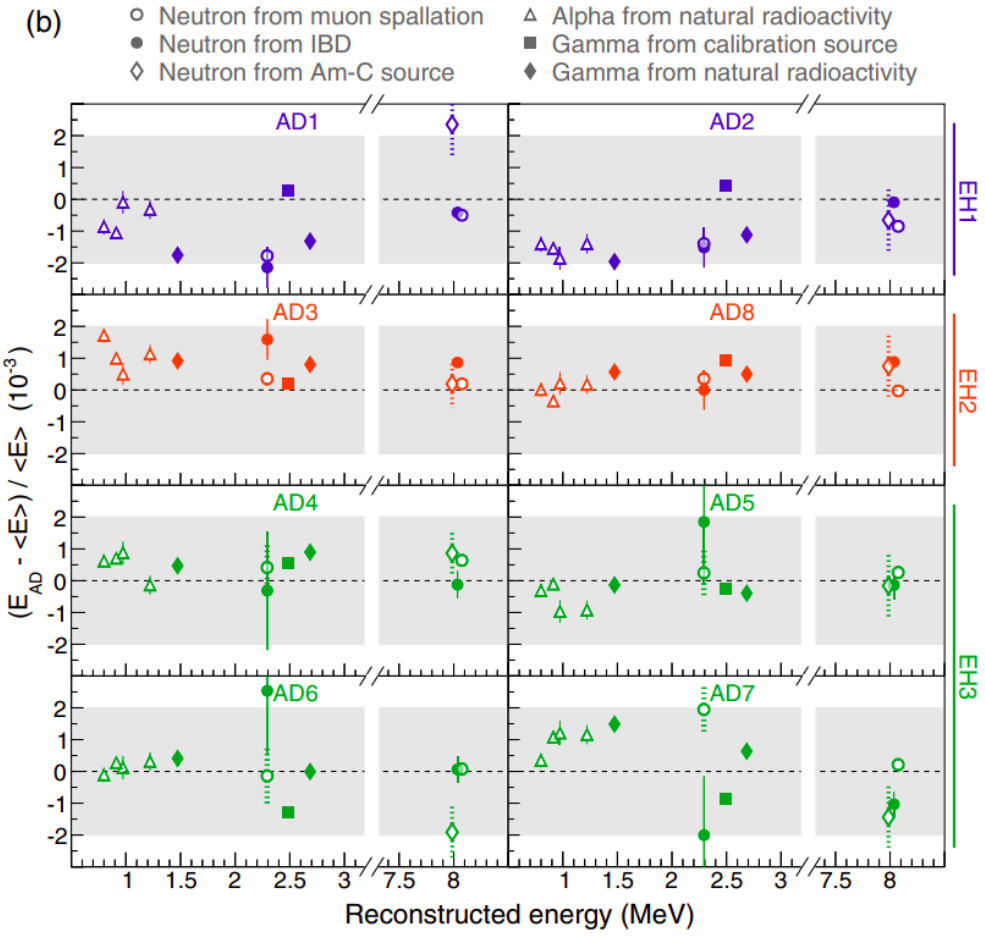

Figure 3.15: Comparison of the 13 sources of in the GdLS region for each AD to measure the relative energy scale. Figure taken from Ref. [57].

Absolute Energy Scale

The energy calibration procedure was designed to uniformize the energy response between all ADs. However, beyond setting the reconstructed nGd capture peak energy to the true 7.95 MeV energy during the Light Yield calibration (Sec. 3.3.2), the reconstructed energy is not required to match the true energy. Knowing the true energy of events, E_{true}, is essential for the oscillation measurement as the survival probability (Eq. 1.32) depends on the antineutrino energy, E_ν, which is determined by the reconstructed energy of the prompt event by Eq. 2.1.

Relating the reconstructed energy to the true energy, the absolute energy scale is affected by nonlinearity effects induced by Cherenkov radiation and quenching in the liquid scintillator [77].

Cherenkov light is produced when a charged particle travels through a medium faster than the speed of light in the medium. For example, an electron traveling through the LS with more than 0.2 MeV of kinetic energy produces Cherenkov light in addition to scintillation light. However, with lower kinetic energy, only the scintillation light is produced and detected.

Quenching effects are also energy dependent: Particles which deposit more energy per distance traveled dE/dx create higher densities of excited molecules in the LS. A portion of the energy deposited therefore goes to the interactions with the LS, rather than into scintillation light, which causes the reconstructed energy to be significantly less than the true deposited energy. Since the light yield calibration is done using SPN events captured on Gadolinium, signals from electrons, positrons, and gammas were generally reconstructed closer to their true energies.

Given that both the Cherenkov radiation and quenching processes of the LS depend on energy and particle type, the nonlinearity effects from both can be addressed simultaneously. These

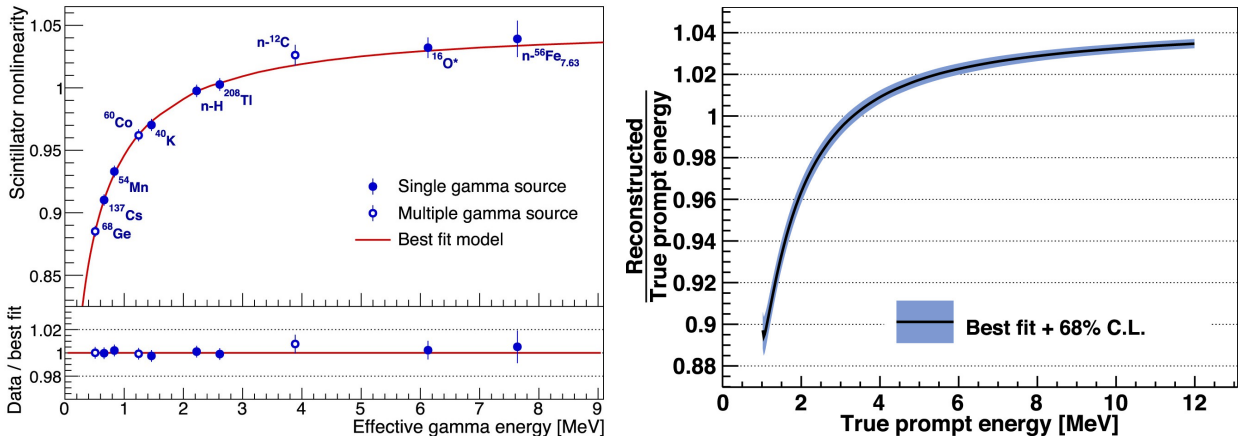

Figure 3.16: Liquid scintillator nonlinearity curves for γ-rays (left) and positrons (right). Figures from Ref. [77]

nonlinearity effects were quantified using multiple sources, to measure the dependence on both the energy and particle type. Fig. 3.16 shows the liquid scintillator nonlinearity for γ-rays and positrons. Unlike the other corrections, the liquid scintillator nonlinearity was not corrected for in the energy reconstruction process, but instead accounted for in the analysis during the fitting stage. For this analysis, it is incorporated in the fitter, see Ch. 6.

3.4 Data Quality

Finally, to further guarantee the data's integrity for the use in physics analyses, the data runs were comprehensively monitored in both real-time by collaborators on shift ("shifters") and retrospectively by the Data Quality Working Group (DQWG). The data quality was thoroughly monitored and reviewed to remove data runs for which the detectors were not operating properly, therefore potentially introducing biases to the analyses. Possible issues included hardware malfunctions, misconfigured runs, and incorrect calibrations.

Firstly, a minimum of one shifter actively checked the detector systems and the data during the data run. The shifters monitored rates and sizes of PMT hits, trigger rates and types,

and watched for alarms from the Detector Control System with regards to PMT high voltage readings, liquid levels, environmental conditions (including humidity and temperature), and the status of mechanical and electrical systems. Any anomalies or issues identified during this process were reported to the DQWG for further evaluation.

As the data files were written, the data automatically underwent the production processing including the calibration and reconstruction algorithms described in this chapter. These calibrations were done using "old" constants from the end of the previous data productions, which are sufficient for preliminary data quality checks, such as detector stability. The proper calibration constants were properly applied later.

From here, physics-driven metrics were obtained and reviewed by data quality shifters. The main metrics included prompt-like event rates, the peak energy of ^{40}K, and the AD and WS blocked trigger rates. The shifters could manually tag a file as "bad" based on these metrics. The data quality information, as well as the metrics, was stored in a Data Quality Database, which was then reviewed by the DQWG, thus finalizing the initial data quality review process.

From here, the data was properly processed through the calibrations (with the true calibration constants) and reconstructions. The data not tagged as "bad" was then compiled in a preliminary "good run list" for a final round of data quality checks during which a number of analysis groups ran a series of independent checks where outliers indicated potential DQ issues. After the investigation of these cases, a final good run list was produced for the analyses to use.

Chapter 4

IBD Candidate Selection and Efficiencies

As described in Sec. 2.3.1, antineutrino interactions within the ADs are identified through the double coincidence signature of the inverse beta decay (IBD). This provides a handle on which to detect antineutrino interactions from the myriad of other types of events detected by the PMTs, namely muons, products of muon interactions, and radioactivity from the materials of the AD and surrounding environment. Additionally, the electronics in the base of the PMTs were known to spark on occasion, thus introduced light into the detector which was detected and reconstructed as events, called "flashers".

To select the IBD candidates, the two event signals (prompt and delayed) must be coincident in time and space and, in this analysis, must form an unambiguous pair in the coincident time window. Outlined in Tab. 4.1, the selection process begins by tagging muon events and applying vetoes to remove their signals and the backgrounds they cause (Sec. 4.1). Secondly, the unphysical flasher events must be removed from the data (Sec. 4.2). Finally, with the data clean of muons and flashers, the search for the IBD candidates can ensue through a

Table 4.1: Table of the cuts applied during the IBD selection. These cuts remain the same for the singles selection with the exception of the multiplicity cut.

Muon Vetoes		Sec. 4.1
Name	Identification	Veto
Water pool muon	NHIT $>$ 12/15 (IWS/OWS)	400 μs
AD muon	$E > 20$ MeV	800 μs
Shower muon	$E > 2.5$ GeV	1 s
Flasher Removal		Sec. 4.2
Name	Criterion	
Nominal	$f_{\text{ellipse}} > 0$	
2-Inch PMT flasher	MaxQ $>$ 100 P.E.	
Top Ring	$z > 2.4$ m and $r^2 > 0.5$ m^2	
Large-R	$R > 2.2$ m	
Cluster	$Q_1/Q_2 > 0.6$ and $f_{\text{ellipse}} > 0.5 \times Q_1/Q_2 - 0.8$ and $f_{\text{ellipse}} > -0.3$	
IBD Candidate Selection		Sec. 4.3
Quantity	Criterion	
Low Energy	$>$ 1.5 MeV	
t_c	1-1500 μs	
Multiplicity	1 prompt-like event within t_c before the delayed-like event AND no additional prompt-like event within $t_c + 400$ μs before or 400 μs after the delayed like-event	
E_p	1.5-12 MeV	
E_d	within floating $\mu \pm$ floating 3σ	
DT $\equiv \Delta D + \frac{1\text{ m}}{600\ \mu\text{s}}\Delta t$	$<$ 1 m	

series of energy, time, and distance related cuts (Sec. 4.3). These cuts introduce inefficiencies that are evaluated in Sec. 4.4.

4.1 Muon Vetoes

Signals caused by muons and their products create backgrounds for the IBD search. Since an abundance of muons are produced in interactions between cosmic rays and the upper atmosphere, the underground experimental halls utilized the mountains as shielding to reduce

the number of muons arriving at the ADs.

Depositing $\sim$ 2 MeV for every centimeter traveled in the scintillator regions, muon signals are much more energetic than the antineutrino events. While this contaminates the data, it also allows for easy selection and removal. Secondarily, muons are also the cause of other backgrounds to this analysis, i.e. "fast" neutrons and unstable isotopes. The former originates from muon interactions in the rock around the ADs. These energetic neutrons could enter the AD, collide with a nucleus in the LS or GdLS, then capture on H or Gd. The recoil of the initial collision produces a prompt-like signal, while the capture creates the delayed-like signal. Alternatively, in the case of the latter, the muon could enter the AD and create many unstable isotopes, most of which quickly decay. Two isotopes, ^{9}Li and ^{8}He, are long lived and produce their own double coincidence signature in their decays. Therefore, vetoes were implemented to remove data for a period of time post-muon to remove the short lived isotopes and reduce the impact of the ^{9}Li and ^{8}He backgrounds. The remaining ^{9}Li and ^{8}He events were later estimated and subtracted, as discussed in Sec. 5.2.2. The duration of the muon veto depends on the location and energy deposition of the muon, thus leading to the muon classifications: water pool, AD, and shower muons.

As mentioned in Sec. 2.2, the water pools surrounding the ADs were designed and implemented to be able to tag muons: any event which triggered $>$ 12 PMTs in the inner water shield and/or $>$ 15 PMTs in the outer water shield were classified as water pool muons. These cuts successfully selected nearly all the muons and majority of the fast neutron events following the water pool muons were finished within 400 μs [58], therefore defining the water pool muon veto.

While all muons near the ADs can cause signals detected by the ADs, muons within the target volumes are guaranteed to do so. A 20 MeV cut on the reconstructed energy was applied to select these AD muons, and any event within the AD surpassing this threshold was assigned an 800 μs veto.

The most problematic muons are those which deposit very large amounts of energy. These energy deposits arise from showers of particles produced by high energy muons. Among the particles produced are the unstable isotopes ^{9}Li and ^{8}He, in much larger quantities compared to the lower energy muons. For the muon veto to include the decay and double coincidence signals of these particles, whose lifetimes are 257.23 ms and 171.60 ms, respectively, the veto must be considerably longer than the previous muon vetoes. Therefore the shower muon veto of 1 s was implemented for events with energies larger than 2.5 GeV in the AD. Being ~ 4 times the ^{9}Li lifetime, this cut successfully removed majority of these background events from the IBD candidate pool.

Any remaining fast neutron, ^{9}Li, and ^{8}He background events are quantified from data using the methods described in Ch. 5.

4.2 Flasher Cuts

Electronics at high voltages are prone to electrostatic breakdown, commonly known as sparking. The electronics in the base of Daya Bay's PMTs were no exception, as demonstrated by Fig. 4.1 [87]. While the PMT electronics were shielded from the AD detection volume, the light from these sparks could enter through the PMTs themselves or any tiny gap in the shielding. The photons could then be detected and reconstructed as events. As they are unphysical, these "flasher" events need to be removed from the data in order to not affect the IBD selection. In the event that the flasher events also qualified as muons according to the muon vetoes, they were treated as muons to be conservative.

Five categories of flashers were observed, identified, and removed:

- "Nominal flashers": The spark triggers the flashing PMT, resulting in a large signal, in addition to PMTs directly across the AD receiving large signals, while adjacent PMTs

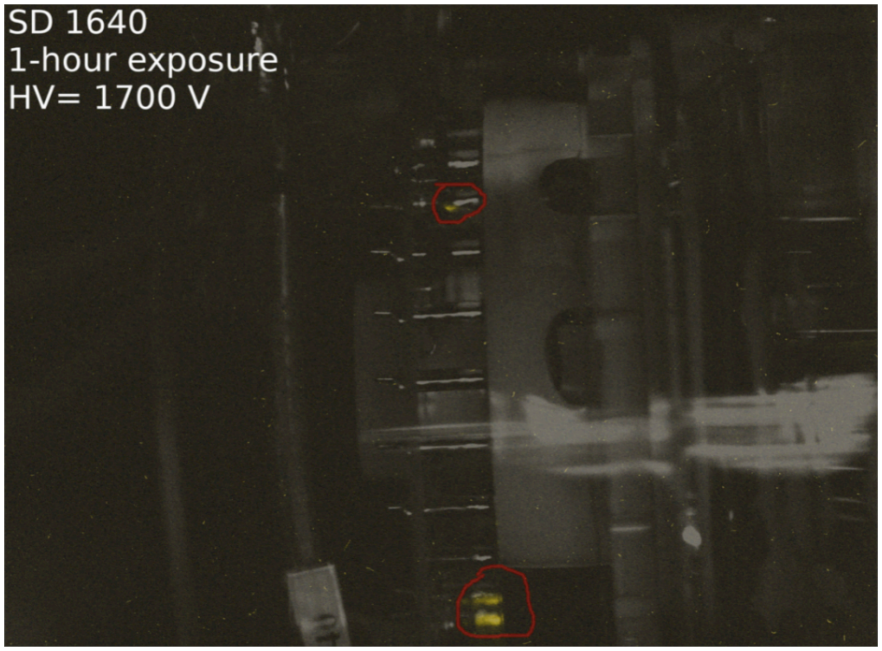

Figure 4.1: Image of spark within the base of a PMT [87].

only detect smaller signals.

- "2-inch flashers": Flasher events originating from the three 2-inch PMTs at the top of each AD, whose purpose was to monitor the quality of the scintillator and mineral oil. While these PMTs were positioned at both the top and bottom of each AD, the top were more prone to flash. As a result, several were turned off, in addition to the removal of their flasher events. A large signal in one of these PMTs indicated a 2-inch flasher event.

- "Top-ring flashers": These events had reconstructed locations outside of the scintillating region of the AD, above the top ring of the PMTs. Regarding the source of these events, the leading theory is the light from the spark emanated out of the PMT base and passed through a small gap in the radial shield and reflector at the top of the AD.

- "Large-R flashers": The reconstructed positions of these flashers were well beyond the scintillating region of the detector. While their origin is not well understood, these events clearly could not be physical events in the AD.

- "Cluster flashers": Clusters of reconstructed events at various locations without physical explanations were observed during flasher studies and suspected to be flashers. The origin is also not well understood.

Until this analysis, only the first two categories (Sec. 4.2.1) were identified and removed: The last three which had yet to be discovered, now collectively classified as "residual flashers," were treated as part of the uncorrelated background. Further investigations identified these events and determined that timing of multiple flashers from any one PMT could not occur in fast enough succession to form correlated pairs. Ultimately, the residual flasher cuts were implemented in this analysis to properly remove these events (Sec. 4.2.2).

4.2.1 Nominal and 2-Inch Flashers

The directionality of the nominal flashers enabled a simple selection cut to efficiently remove them from the data on an event-by-event basis. The cut was based on two properties of these flashers: the flashing PMT registers the largest charge signal compared to the other PMTs, and the light was emitted directly across to the other side of the AD. The first step was to identify the suspected flasher, which was the PMT with the largest charge signal, and determine its contribution to the total charge of the event: $f_{\text{max}} = Q_{\text{max}}/Q_{\text{total}}$. Compared to physical events, flashers have much larger values of f_{max}. Then to confirm the event as a flasher, the distribution around the AD of the light detected was studied. The columns of the AD were assigned to quadrants according to their locations, with Quadrant 1 centered around the suspected flasher and Quadrant 3 directly across from it. Defining the charge observed by Quadrant i as Q_i, the calculation $f_{\text{quad}} = Q_3/(Q_2 + Q_4)$ quantified the distribution of light among the PMTs. For nominal flashers, the light was mainly focused at Quadrant 3, leading to large values of f_{quad} relative to physics events. Finally, these two values were

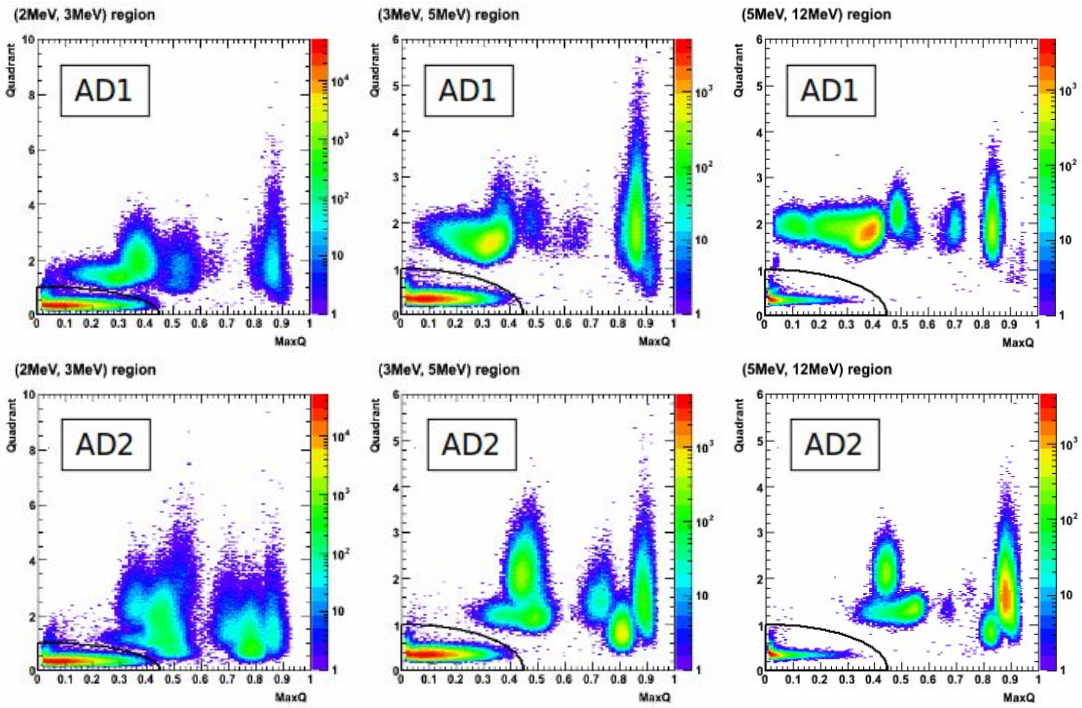

Figure 4.2: Demonstration of the ellipse cut (black line) for removing nominal flashers in EH1-AD1 (top row) and EH1-AD2 (bottom row) for three energy ranges spanning 2 MeV to 12 MeV. The x-axes represent f_{max}, while the y-axes represent f_{Quad} [88].

combined into what is known as the "ellipse cut":

$$f_{\text{ellipse}} = \log_{10}\left[f_{\text{Quad}}^2 + \left(\frac{f_{\text{max}}}{0.45}\right)^2\right], \tag{4.1}$$

where $f_{\text{ellipse}} > 0$ for nominal flasher events and < 0 for physics events [88]. The ellipse cut is demonstrated for a few energy ranges of both ADs in EH1 in Fig. 4.2. All events with $f_{\text{ellipse}} > 0$ were removed from the data as they were deemed to be nominal flashers.

The 2-inch PMT category simply classified flashers originating from the 2-inch PMTs at the top of the AD. As with the nominal case, the flashing PMT registers a large charge signal with the spark. Additionally, the 2-inch PMTs never measured $>$ 100 P.E. from physics events, only flasher events registered signals of this size. Therefore, any signals in these PMTs over 100 P.E. were tagged as 2-inch flashers and removed.

4.2.2 Residual Flashers

The term "residual flashers" was used to refer to the remaining three flasher types: top-ring, large-R, and cluster. After a thorough study of the suspect events, the time between signals indicated periods of charging and flashing, in contrast to uncorrelated singles which would not have such a relation [89]. With the observed timing being on the order of seconds, this behavior forbids correlated pairs of flashers in the IBD selection. However, the signals would still introduce uncorrelated single events, so to minimize their influence, cuts were designed to remove them.

The first two were named for their reconstructed positions primarily residing well outside the bounds of the ADs. Their removal was similarly designed. The top-ring flasher events were located above the top of the PMTs, therefore rejecting events with $z > 2.4$ m and $r^2 > 0.5$ m^2 were applied. As for the large-R flashers, the events located beyond the scintillating volume, $r > 2.2$ m, were removed. Fig. 4.3 shows the reconstructed positions of the top-ring and large-R residual flashers. Through several toy Monte Carlo studies, both sets of cuts successfully removed the un-physical flasher events while only negligibly affecting the true events.

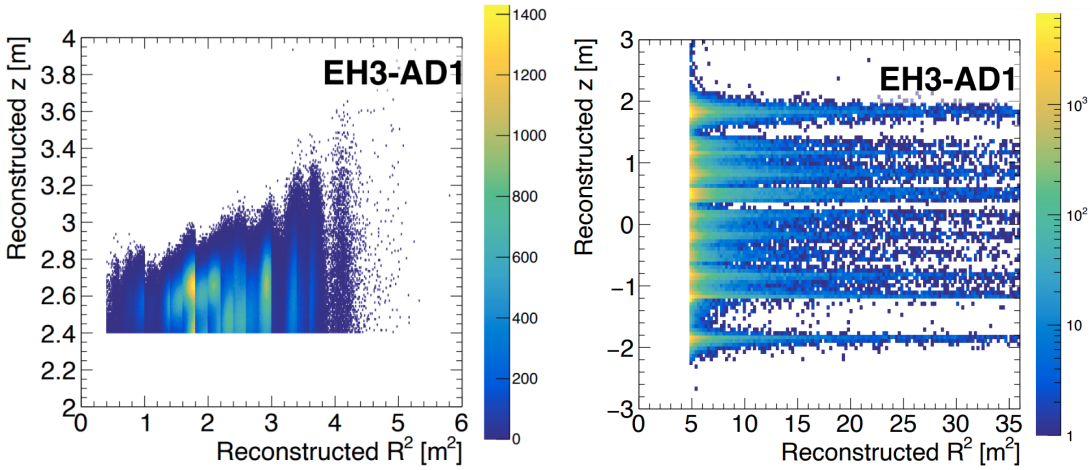

Figure 4.3: Positions of events in EH3-AD1 passing the muon vetoes and nominal flasher cuts, but were removed by one of the top-ring (right) and large-R (left) residual flasher cuts. [70].

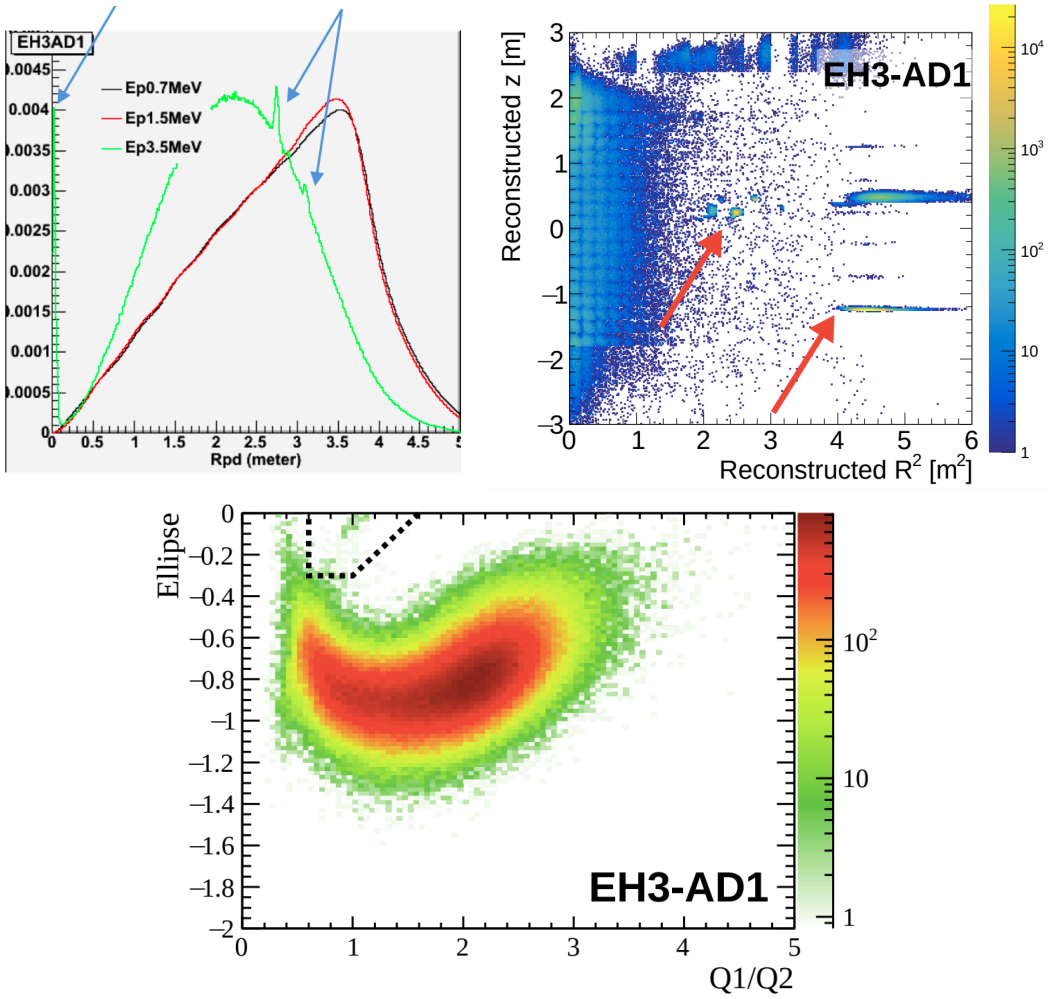

Figure 4.4: Top left: Prompt-delayed coincidence distance with additional spikes coming from the cluster flashers. Top right: Reconstructed positions of cluster flashers. Bottom: Trapezoidal cut in f_{ellipse} and Q_1/Q_2 parameter-space used to remove cluster flasher events. Demonstrated with EH3-AD1 [90, 89, 91].

The final category, cluster flashers, first appeared as spikes in the distribution of distances between consecutive events of the far hall. EH3-AD3, and EH3-AD4 had an excess of events at 0 m, and EH3-AD1 had additional peaks at 2.75, 2.9, and 3.1 m. Under further examination, these peaks were associated with "hot spots" in the position reconstructions, confirming them as flasher events. Conveniently, they form a group in the parameter-space defined by f_{ellipse} and Q_1/Q_2. The spikes in the prompt-delayed coincidence distance and the reconstructed positions of the cluster flashers are shown in Fig. 4.4, along with the

trapezoidal cut defined by $Q_1/Q_2 > 0.6$, $f_{\text{ellipse}} > 0.5 \times Q_1/Q_2 - 0.8$, and $f_{\text{ellipse}} > -0.3$. Events qualifying for all three conditions were considered as flashers, which proved effective in removing $> 80\%$ of flashers while only rejecting $\sim 0.02\%$ of true IBDs, as determined through toy Monte Carlo studies [61]. As mentioned, the remaining flasher events enter the IBD candidate selection exclusively as uncorrelated single events and are accounted for in the singles selection (Sec. 5.1).

4.3 IBD Candidate Selection

With the muons vetoed and the flasher events removed, the data was officially prepared for the IBD candidate selection, which begins with searching for pairs of events passing the coincidence requirements. There are four conditions that must be satisfied for a pair of events to be counted as potential IBD candidates:

1. the candidate must have an eligible delayed energy E_d,
2. the candidate must have an eligible prompt energy E_p,
3. the prompt and delayed events must be within the coincidence time window, and
4. there must only be the one prompt-like and one delayed-like event in the coincidence time plus isolation windows.

These conditions are illustrated in Fig. 4.5. For the initial search, the delayed energy cut is applied as a fixed 1.5-3 MeV range, spanning the nH capture peak at ~ 2.2 MeV. The floating $\mu \pm 3\sigma$ delayed energy cut listed in Tab. 4.1, which is robust against differences in the relative energy scale, is not applied until after the initial selection when the delayed energy peaks can be fit for each AD separately (Sec. 4.3.3). Sec. 4.3.1 discusses the prompt

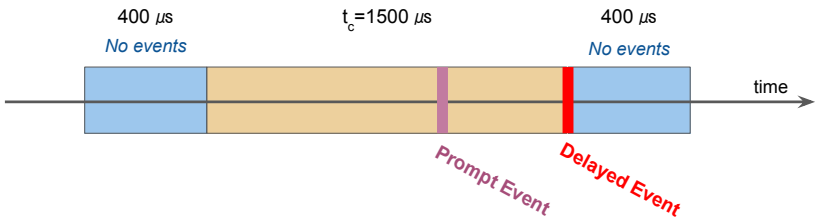

Figure 4.5: Schematic of multiplicity cut requirement enforced for the IBD selection: the 1500 μs coincidence window (yellow), defined with respect to the delayed-like event which contains only one prompt-like event, is book-ended by 400 μs isolation windows (blue), neither of which may contain a prompt-like event. The combination of these time windows must be entirely outside muon vetoes.

energy criterion; conditions 3 and 4 form the "multiplicity" cut, whose efficiency is discussed in Sec. 4.4.2.

The implementation of the multiplicity cut in this analysis follows the form of a fixed coincidence and isolation window in Analysis B of [57]. Requiring that the two events are isolated from muon vetoes and other prompt-like events ensures no ambiguity in the proper pairing of events. Without this requirement, for example, two or more prompt-like events could be present in the coincidence window, which eliminates confidence of which one is the true prompt event. This approach does result in a slightly smaller multiplicity efficiency compared to the approach without fixed window, however, in addition to the unambiguous sample, it provides a simple calculation of the multiplicity efficiency (Sec. 4.4.2), while decoupling the muon veto and multiplicity efficiencies.

While scanning the chronological events of the data-taking runs individually, these criteria were checked through the following procedure:

1. Identify a delayed-like event, at least $t_c + 400\ \mu\text{s} = 1900\ \mu\text{s}$ after the start of the data-taking window or the end of the previous muon veto. The delayed-like event must have a reconstructed energy between 1.5 and 3 MeV.

2. Scan backwards in time from 1 μs to $t_c + 400$ μs $= 1900$ μs before the delayed-like event looking for prompt-like events, whose energy falls between 1.5 and 12 MeV. The 1 μs lower bound ensures distinct prompt and delayed events due to the 1 μs data recording window.

    - If no prompt-like event exists in the $t_c + 400$ μs $= 1900$ μs before the delayed-like event, this event can not qualify as a candidate, and the search for the next IBD candidate begins.
    - If more than one prompt-like event exists in either t_c or $t_c + 400$ μs $= 1900$ μs prior to the delayed-like event, it is unclear which is the true prompt event. Therefore, to remove the ambiguity, it is not considered to be an IBD candidate in this selection. The process restarts for the next IBD candidate.
    - If only one prompt-like event exists within t_c and is the only prompt-like event in the $t_c + 400$ μs $= 1900$ μs window before the delayed-like event, the pair proceeds to the next step.

3. Scan forwards in time for 400 μs after the delayed-like event looking for prompt-like events and muons.

    - If a muon or prompt-like event occurs within the post-delayed isolation buffer, this pair is not considered as an IBD candidate.
    - If this time period is void of muons and prompt-like events, this pair has successfully passed the initial IBD candidate selection process.

Discussed in Sec. 5.1, a similar process was applied to address the so-called "accidental" background, caused by uncorrelated events passing the IBD candidate selection criteria. After the initial selection of both the IBD candidates and the accidental backgrounds, the final coincidence distance and time (DT) and delayed energy cuts were applied to both samples. Secs. 4.3.1-4.3.3 present the details of the prompt energy, DT cut, and delayed

energy cuts. Fig. 4.6 shows the delayed vs prompt energy spectra for the candidates after subtracting accidentals and applying the DT, proper delayed energy cuts have yet to be applied.

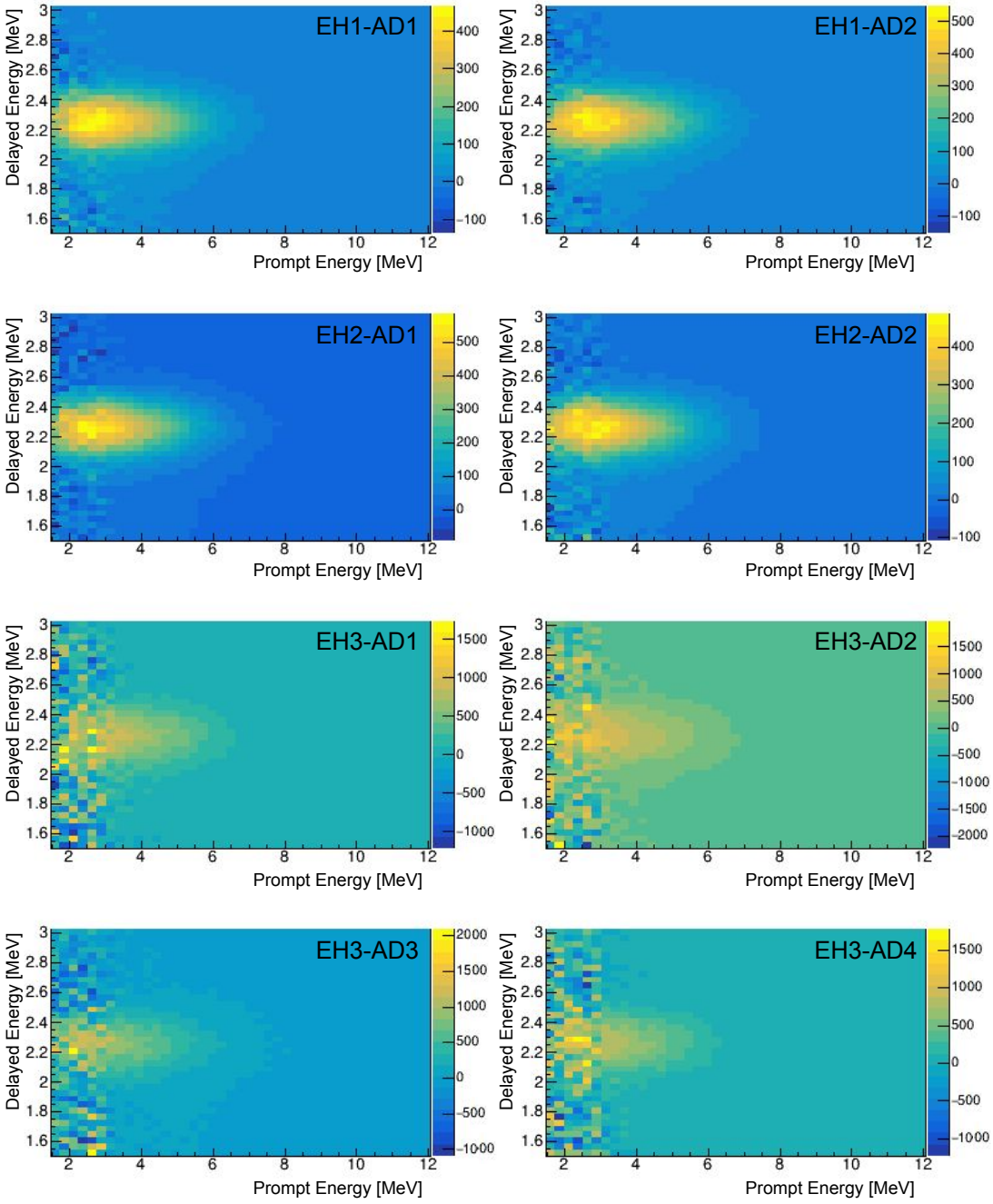

Figure 4.6: Delayed vs prompt energy of the IBD candidate selection after accidental subtraction. The proper delayed energy E_d cuts have yet to be applied.

4.3.1 Prompt Energy Cut

The prompt energy bounds of this analysis follow those set for past nH oscillation analyses at Daya Bay [61, 92]: 1.5-12 MeV. Since the reactor $\overline{\nu}_e$ spectrum is very low beyond 8 MeV, as shown in Fig. 4.7, the 12 MeV upper bound on the prompt energy introduced essentially no loss of events. On the other hand, the low energy cut was designed specifically to remove a substantial number of radioactive decay background events: primarily the ^{238}U and ^{232}Th decay chains: ^{214}Bi-^{214}Po-^{210}Pb and ^{212}Bi-^{212}Po-^{208}Pb, respectively [92]. The energies of the associated α's were reconstructed with peaks at 1.26 and 1.00 MeV. Though the tail extends past the 1.5 MeV cut, the cut was designed to optimize the removal of background events while minimizing the loss of IBD events.

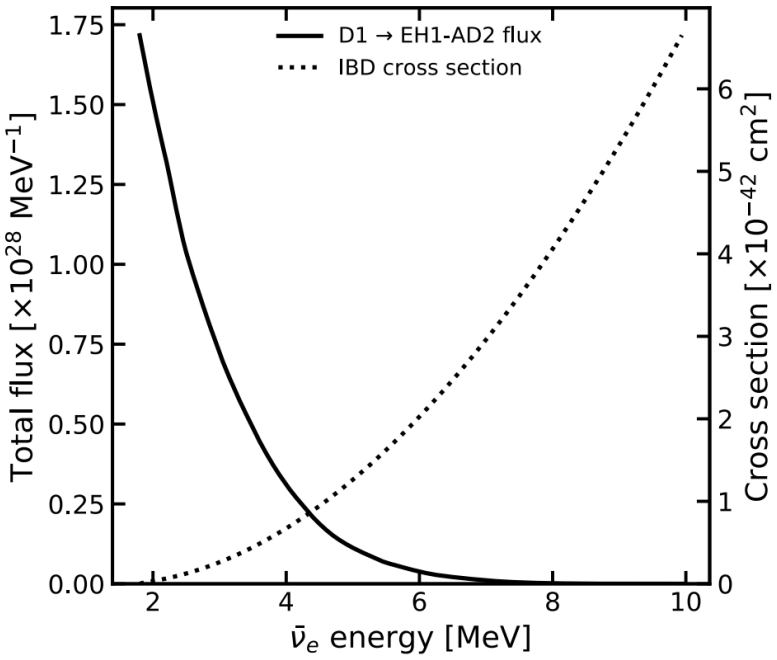

Figure 4.7: Total $\overline{\nu}_e$ flux produced by reactor core D1 over the livetime of EH1-AD2. The IBD cross section is provided for reference. At energies above ∼8 MeV, the $\overline{\nu}_e$ flux is negligible, and thus, the upper limit of the prompt energy cut removes essentially no IBD events [70].

4.3.2 Coincidence Distance-Time Cuts

The selection cuts are designed specifically around the double coincidence signature of IBDs. In the initial selection, the prompt and delayed events must be separated by < 1500 μs, which is nearly 7 times longer than the mean nH capture time. This coincidence time, t_c, is large enough to accept many cases of two uncorrelated single events as IBD candidates, which constitutes the "accidental" background (see Sec. 5.1). Unlike IBDs, the prompt- and delayed-like events of the accidental pairs are not correlated in time. Another difference between IBDs and accidentals is the coincidence distance: the neutron travels ~ 25 cm on average before capturing on a hydrogen nucleus, whereas accidental pairs tend to be made of events around the sides of the detector and therefore, the mean coincidence distance is ~ 4 m. Both the distance and time differences motivated the introduction of coincidence cuts.

Fig. 4.8 presents the distance vs time spectrum for EH1-AD1 after subtraction of the accidental background. In earlier nH analyses, these variables were assigned separate cuts, demonstrated by the green box: $\Delta D < 0.5$ m and $\Delta t < 400$ μs. In the analysis presented here, these variables are combined into a single "DT" variable defined as:

$$\mathrm{DT} \equiv \Delta D + \frac{1\ \mathrm{m}}{600\ \mu\mathrm{s}}\Delta t, \tag{4.2}$$

where the fraction $\frac{1\ \mathrm{m}}{600\ \mu\mathrm{s}}$ is close to the speed of thermalized neutrons. This DT cut was designed to efficiently select IBDs while removing accidentals. Represented by the white line, this analysis selects only events with DT < 1 m. As detailed in Appendix A.1, this DT cut improved the signal-to-background ratio and reduced the relative detection efficiency uncertainty. Sec. 7.2.1 presents the impact of the DT cut value on the final result.

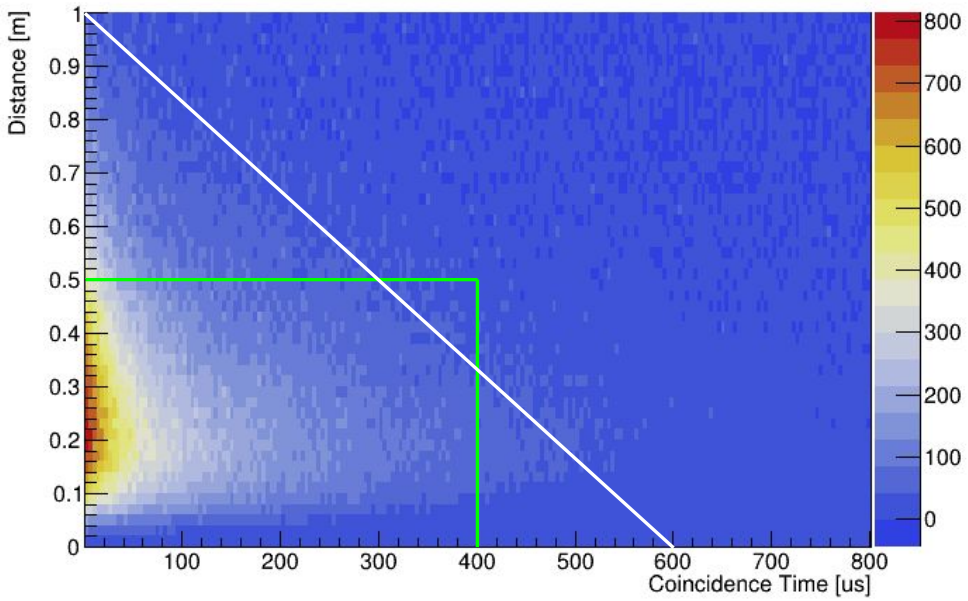

Figure 4.8: Distance vs time spectrum for IBD candidates, after accidentals subtraction (see Sec. 5.1). Early nH analyses implemented separate distance and time cuts, identified by the green box. This selection utilizes a cut on the combined coincidence distance-time DT variable, shown here as the white line.

4.3.3 Delayed Energy Cuts

The neutron capture on hydrogen provides a characteristic delayed energy at 2.22 MeV. A narrow $\pm 3\sigma$ cut around the peak is able to select neutrons captured on hydrogen almost exclusively, as the signals from captures on carbon and gadolinium are at significantly higher energies. The delayed energy cut bounds were determined after applying the DT cut and subtracting the accidental background (Sec. 5.1). While the correlated backgrounds still exist in the IBD sample, their delayed signals are all produced by neutron captures on hydrogen and therefore do not affect the determination of the delayed energy cuts.

The floating 3σ cut was designed to be consistent for all ADs even accounting for variations due to energy reconstruction and minor differences between them. The delayed energy spectrum is a nearly Gaussian peak near 2.22 MeV, with a low energy tail associated with events where some of the energy escaped the LS region, referred to as "energy leakage".

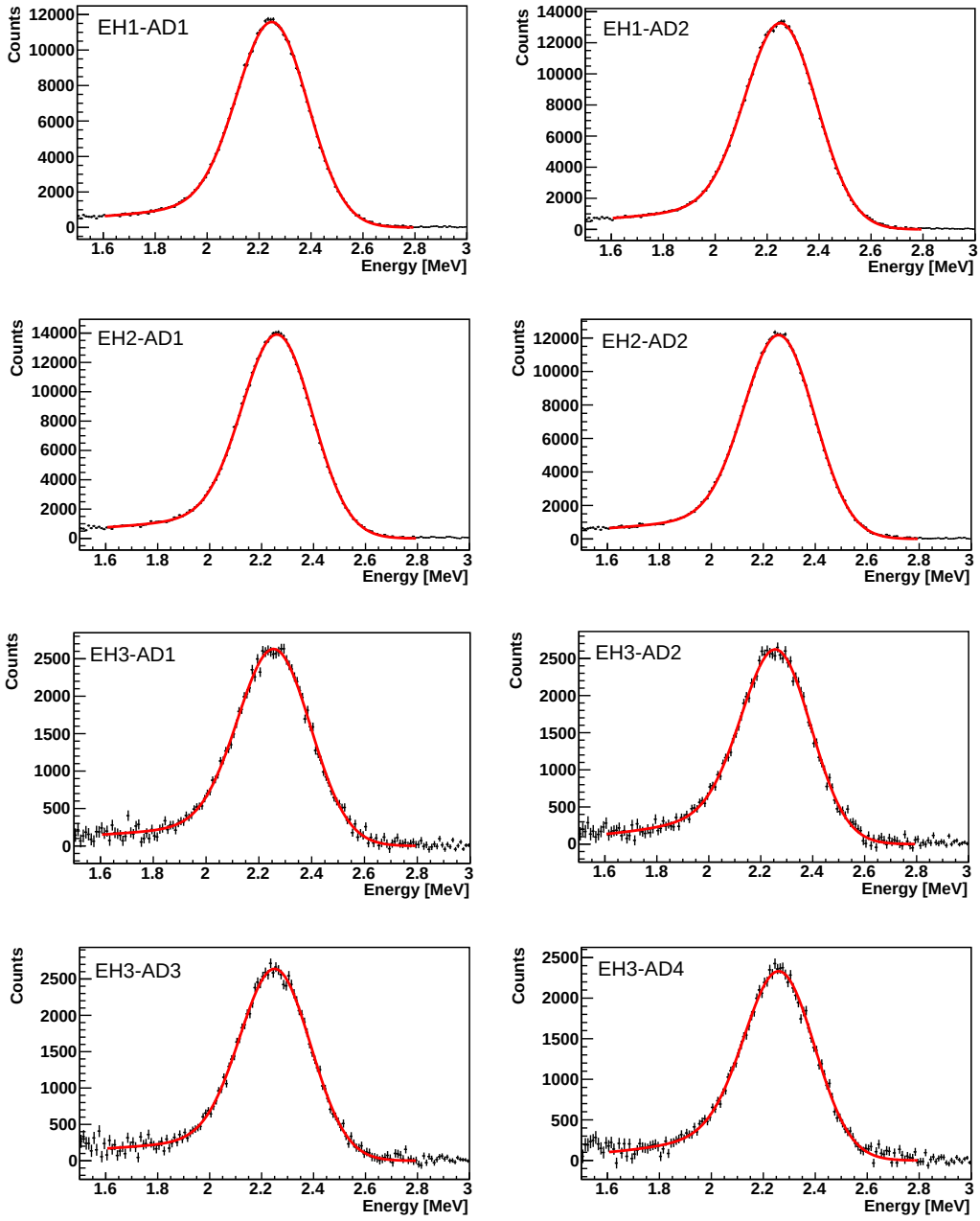

Figure 4.9: Delayed energy spectra of IBD candidates after subtraction of accidentals (Ch. 5.1) for each AD, which were fit with a calorimeter function to determine the delayed energy cut bounds.

As shown in Fig. 4.9, the spectra were fit with a calorimeter function which models the response to a monoenergetic process with a tail due to only partial absorption of energy in the sensitive volume [93]. This fit relied on four parameters:

1. μ, the true energy,

2. σ, the peak width which represents the detector's energy resolution,

3. α, the fraction of the events entirely contained in the AD, and

4. λ, the tail slope which corresponds to the energy leakage.

Before considering the smearing contribution of the σ parameter, the function takes the form:

$$f_{\text{unsmeared}}\left(E;\mu,\lambda,\alpha\right)=\begin{cases}\alpha\delta(E-\mu)+(1-\alpha)\lambda e^{\lambda E} & 0<E\leq\mu\\ 0 & E>\mu\end{cases}. \tag{4.3}$$

To represent the energy response, Eq. 4.3 was convolved with a Gaussian function with peak width of σ:

$$f_{\text{cal}}\ =f_{\text{unsmeared}}\ \otimes\ \text{Gaussian}\ , \tag{4.4}$$

which returns the final calorimeter fit function:

$$\begin{aligned}f_{\text{cal}}\left(E;\mu,\sigma,\lambda,\alpha\right)&=\int_0^{\mu}dE'f_{\text{unsmeared}}\ \left(E';\mu,\lambda,\alpha\right)\cdot\text{Gaussian}\left(E'-E;\sigma\right)\\&=\alpha\frac{1}{\sigma\sqrt{2\pi}}e^{-\frac{(E-\mu)^2}{2\sigma^2}}+\frac{(1-\alpha)}{2}\frac{\lambda e^{\frac{\sigma^2\lambda^2+2\lambda E}{2}}}{e^{\lambda\mu}-1}\left[\text{erf}\left(\frac{\mu-E-\sigma^2\lambda}{\sqrt{2}\sigma}\right)\right.\\&\quad\left.-\text{erf}\left(\frac{-E-\sigma^2\lambda}{\sqrt{2}\sigma}\right)\right].\end{aligned} \tag{4.5}$$

The best fit parameters for each AD are provided in Tab. 4.2 and shown in Fig. 4.10. The delayed energy peaks are consistent to within $\pm0.35\%$ which corresponds to the uncertainty in the relative energy scale.

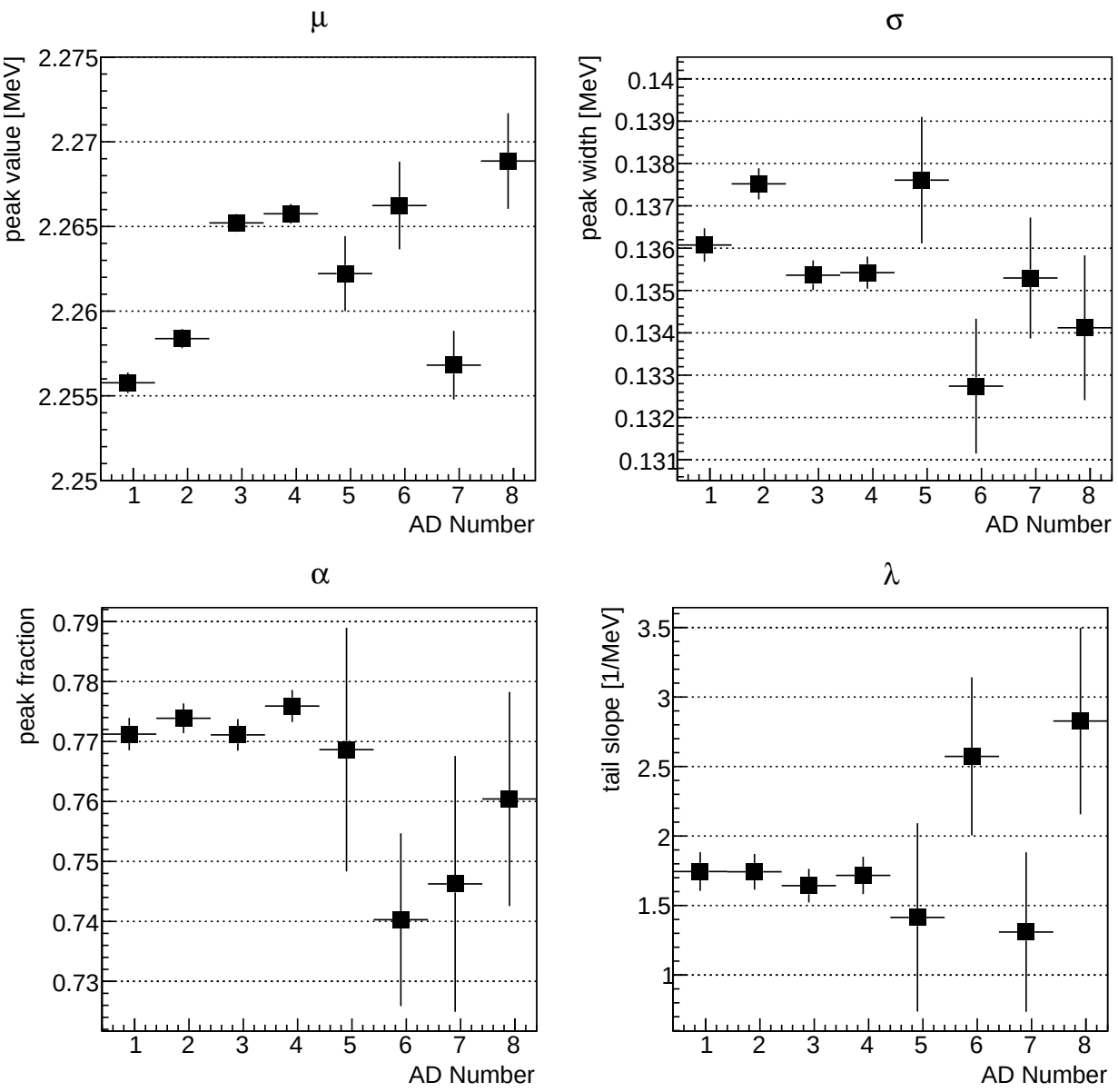

Figure 4.10: Best fit parameters of the delayed energy spectra for each AD. Top left: peak energy (μ), top right: peak width (λ), bottom left: peak fraction (α), bottom right: tail slope (λ). The peak energies are consistent to within $\pm 0.35\%$ which is used as the uncertainty in the relative energy scale across all ADs. The delayed energy cuts are determined for each AD as $\mu \pm 3\sigma$.

Table 4.2: Summary of best fit values of each AD's delayed energy spectrum.

	Peak Energy [MeV] μ	Peak Width [MeV] σ	Peak Fraction α	Tail Slope [1/MeV] λ
EH1-AD1	2.2558	0.1361	0.7712	1.7445
EH1-AD2	2.2584	0.1375	0.7739	1.7428
EH2-AD1	2.2652	0.1354	0.7711	1.6428
EH2-AD2	2.2658	0.1354	0.7759	1.7166
EH3-AD1	2.2622	0.1376	0.7686	1.4144
EH3-AD2	2.2662	0.1327	0.7403	2.5727
EH3-AD3	2.2568	0.1353	0.7463	1.3092
EH3-AD4	2.2689	0.1341	0.7604	2.8273

Table 4.3: Delayed energy cut bounds for each AD as determined by $\mu \pm 3\sigma$ from the best fit values (Tab. 4.2).

	Lower Bound [MeV]	Upper Bound [MeV]
EH1-AD1	1.8476	2.6640
EH1-AD2	1.8458	2.6709
EH2-AD1	1.8591	2.6713
EH2-AD2	1.8595	2.6720
EH3-AD1	1.8494	2.6750
EH3-AD2	1.8680	2.6645
EH3-AD3	1.8509	2.6627
EH3-AD4	1.8665	2.6712

4.4 Selection Efficiencies

Each of the selection cuts is aimed at improving the signal to background ratio. In doing so, these cuts must be evaluated for the percentage of IBD events which pass the criterion, known as the efficiency. The efficiencies and corresponding efficiency uncertainties are then propagated to the final fit so the data can be corrected for the loss of events. With the relative near-far approach, the AD-correlated efficiencies cancel, and therefore the main impact of the efficiencies on the final fit is caused by the differences between the ADs. Sec. 4.4.1 and 4.4.2 discuss the muon veto and multiplicity cut efficiencies, respectively; Sec. 4.4.3 and

4.4.5 address the calculations of the prompt and delayed energy cut efficiencies; Sec. 4.4.4 describes the DT cut efficiency evaluations.

4.4.1 Muon Veto Efficiency

The muon veto efficiency is used to quantify and correct for the amount of data removed due to the muon vetoes. The muon veto efficiency also needs to account for the strict isolation timing window requirements of the IBD candidates, since the IBD candidates must be void of all muon vetoes (detailed in Sec. 4.3).

The efficiency definition is therefore adjusted to be the fraction of time which a delayed-like event can occur out of the total data-taking window. Three methods of accounting for the isolation windows were tested:

1. simply extending each muon veto by $(t_c + 2 \times 400\ \mu\text{s})$,
2. counting all intervals shorter than $(t_c + 2 \times 400\ \mu\text{s})$ as well as $(t_c + 2 \times 400\ \mu\text{s})$ of each longer interval as vetoed time, or
3. effectively attaching the 400 μs post-delayed-event buffers and the $(t_c + 400\ \mu\text{s})$ pre-delayed-event buffers to the start and end of the muon vetoes, respectively. The pre- and post-delayed-event buffers must also be assigned to the start and ends of the data-taking window. (Illustrated in Fig. 4.11).

It is important to note that overlapping muon vetoes are treated as one continuous muon veto, therefore no time is double counted. All three methods were consistent with one another. Since the third method follows the implementation of the IBD selection, this was the calculation used for this analysis.

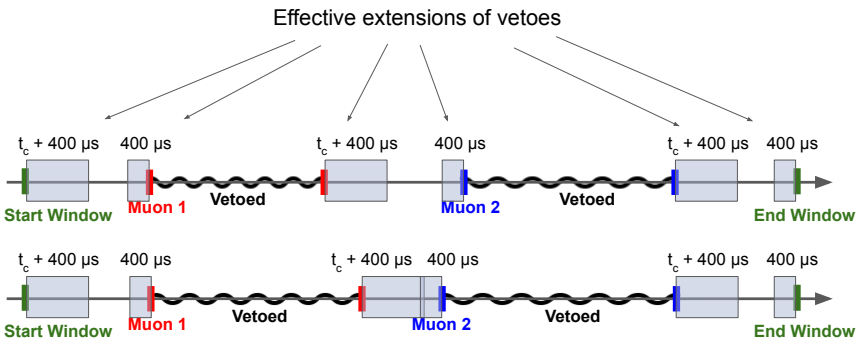

Figure 4.11: Schematic of muon vetoes. Due to the isolation requirements of the IBD candidate selection, the delayed events must be at least $t_c + 400$ μs$= 1900$ μs after and 400 μs before any muon veto, as represented by the shaded boxes. These isolation buffers also forbid the delayed events from occurring too close to the start and end of the data taking window, identified by the green markers. The muon veto efficiency is defined as the percent of time between the start and ends of the window which is not within the muon vetoes or the isolation buffers.

Mathematically, the muon veto efficiency was calculated for each run as:

$$\epsilon_\mu = \frac{\sum_i \Delta t_i}{t_{\mathrm{DAQ}}}, \tag{4.6}$$

where Δt_i is the live time (un-vetoed and separate from the effective extensions) in the i-th interval between muons, and t_{DAQ} is the total time for which the detector is acquiring data (DAQ time). This quantity is calculated for each AD individually. Fig. 4.12 shows the resulting muon veto efficiency vs run index for each of the detectors, and Tab. 4.4 summarizes the muon veto efficiencies of each AD for the whole P17B data set. The error for these efficiencies is negligible ($< 0.1\%$) and was therefore not considered in this analysis.

Table 4.4: Muon veto efficiencies for each AD for the entire P17B data set.

	EH1		EH2		EH3			
	AD1	AD2	AD1	AD2	AD1	AD2	AD3	AD4
ϵ_μ	0.5444	0.5418	0.6264	0.6258	0.9544	0.9543	0.9542	0.9546

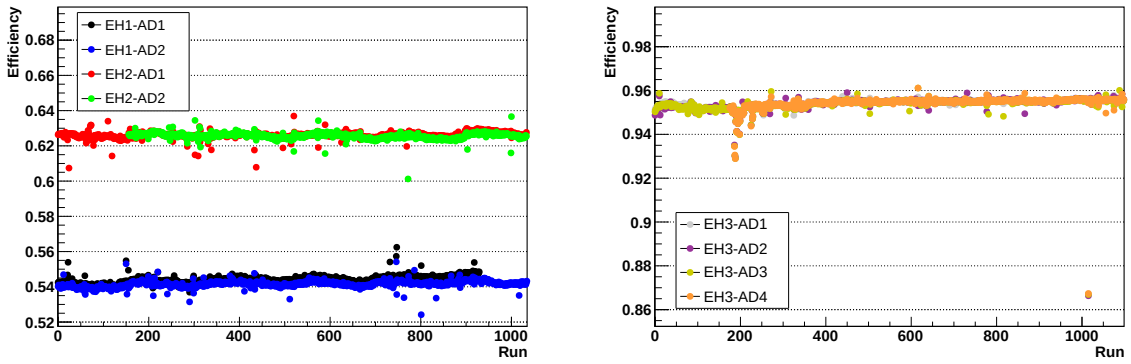

Figure 4.12: Muon veto efficiency vs run index for near (left) and far (right) ADs. The muon veto efficiencies are clustered by hall due to the amount of overburden shielding the ADs from atmospheric muons. Extreme points are caused by short runs with limited statistics.

4.4.2 Multiplicity Cut Efficiency

The multiplicity cut efficiency accounts for the events rejected by the requirement that the IBD candidate pair is isolated from other prompt-like events. This requirement also ensures isolation from other delayed-like events as they are a subset of the prompt-like events.

The calculation of the multiplicity cut efficiency relies on the basis that the extra prompt-like events are uncorrelated single events. This implies that they are equally likely to occur for all parts of the isolation window. Using the prompt-like singles rate calculated in Eq. 5.1, the multiplicity cut efficiency is

$$\epsilon_m = e^{-(t_c + 2\times 400\ \mu\text{s})\times R_{\text{prompt}}} \tag{4.7}$$

where R_{prompt} is the prompt-like singles rate, after correcting for the isolation buffers of the singles selection (see Sec. 5.1.1 for the calculation). Fig. 4.13 presents the multiplicity cut efficiency vs run for each of the ADs, while Tab. 4.5 summarizes each AD's multiplicity cut efficiency for the entire P17B period. As with the muon veto efficiencies, the error on the multiplicity cut efficiencies is negiligible ($< 0.1\%$) and therefore was not included in this

analysis. The increase of efficiency at the start of the data-taking period was due to some contamination in the ADs which decayed with time, leading to the stable efficiencies.

Table 4.5: Multiplicity cut efficiencies for each AD for the entire P17B data set.

	EH1		EH2		EH3			
	AD1	AD2	AD1	AD2	AD1	AD2	AD3	AD4
ϵ_m	0.9593	0.9595	0.9604	0.9607	0.9613	0.9605	0.9605	0.9608

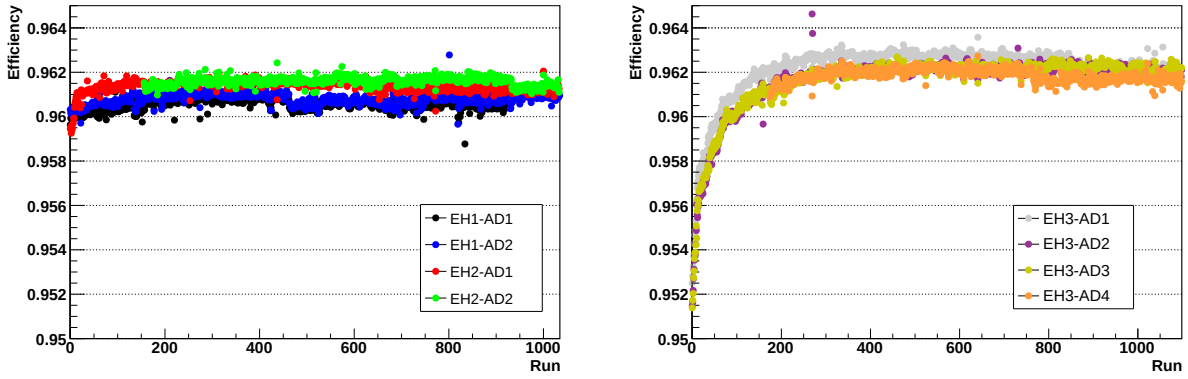

Figure 4.13: Multiplicity cut efficiency vs run index for near (left) and far (right) ADs. Extreme points are caused by short runs with limited statistics.

4.4.3 Prompt Energy Cut Efficiency

As mentioned in Sec. 4.3.1, the 12 MeV upper bound of the prompt energy cut removed essentially no IBDs. Rather, the inefficiency was caused by the 1.5 MeV lower bound. Furthermore, the true $\overline{\nu}_e$ energy spectra were different for the various ADs due to oscillations effects, and consequently the same prompt energy cut removed different fractions of the IBDs [92]. To elaborate, the near halls observe majority of the oscillation effects at low energies, hence few events were removed, giving a higher efficiency at the near halls. Alternatively, the far hall ADs observe neutrinos with prompt energy between 2 and 3 MeV oscillating the most. Therefore, the 1.5 MeV cut affected more events than at the near halls

while also reducing the total number of observed events, leading to lower prompt energy cut efficiencies at the far hall.

Because this thesis presents a relative measurement, the absolute prompt energy cut efficiency is not necessary to obtain the best fit. For reference, however, an estimate on the absolute efficiency was made via Monte Carlo by Ref. [70] to be $\sim 88\%$.

As with all the efficiencies, the AD-uncorrelated uncertainty was important to quantify. In this case, the uncorrelated uncertainty was dominated by the energy scale differences between ADs. As noted in Sec. 4.3.3, the energy scales of the ADs were consistent to within 0.35%. Propagating it to the prompt energy cut efficiency, the Monte Carlo reconstructed prompt energy spectrum was varied by $\pm 0.35\%$, which led to a relative uncertainty of 0.13%. However, this uncertainty was accounted for in the relative energy scale uncertainty and its careful treatment in the fitter via pull curves (see Sec. 6.3).

4.4.4 DT Cut Efficiency

As mentioned in Sec. 4.3.2, the DT cut was designed to efficiently select IBDs while reducing the number of accidental background events in the sample. Appendix A.1 presents a comparison of the efficiencies between the separate distance and time cuts to the singular DT cut. Fig. 4.14 shows the DT spectra of IBD candidates (black) and accidentals (red) for EH1-AD1 and EH3-AD1, representing the spectra of the near and far ADs, respectively. The bottom panels show the accidentals-subtracted spectra, used in the evaluation of the DT cut efficiency. At values of DT larger than 3 m, all the IBD candidates are accidentals, therefore 3 m was used as the definition of 100% efficiency, while mitigating the noise from accidentals:

$$\epsilon_{\mathrm{DT}}(\mathrm{DT}_{\mathrm{cut}}) = \frac{\int_{0\ \mathrm{m}}^{\mathrm{DT}_{\mathrm{cut}}} \Delta\mathrm{DT}_{\mathrm{sub}}\, d(\Delta\mathrm{DT})}{\int_{0\ \mathrm{m}}^{3\ \mathrm{m}} \Delta\mathrm{DT}_{\mathrm{sub}}\, d(\Delta\mathrm{DT})}. \tag{4.8}$$

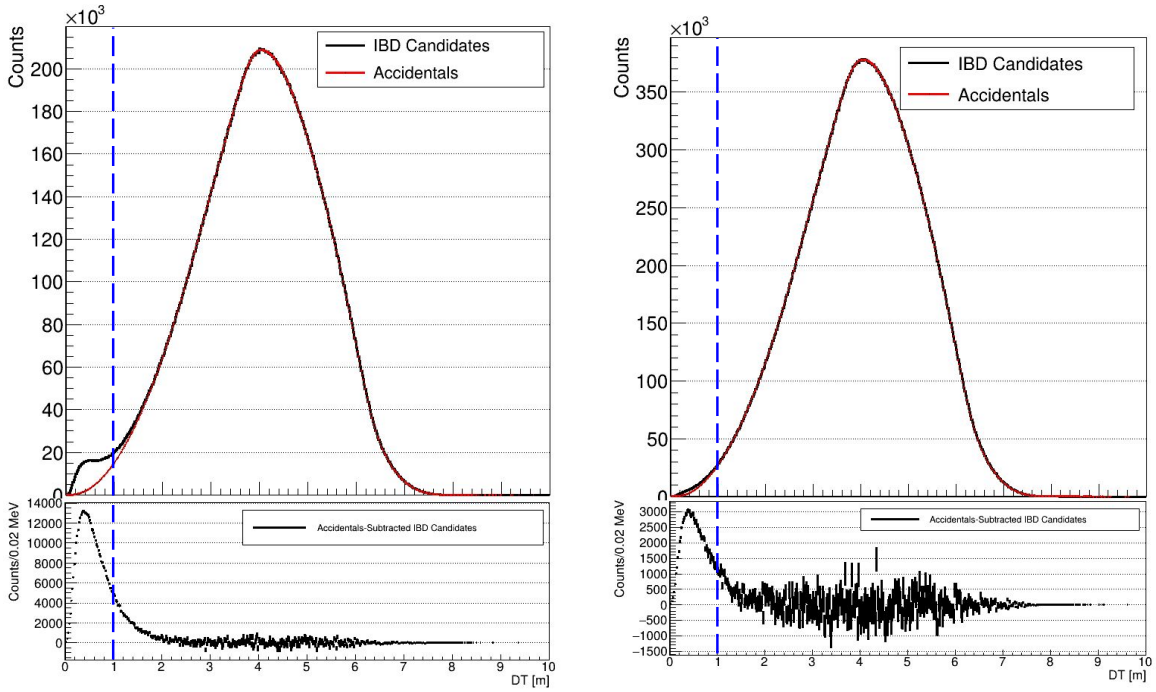

Figure 4.14: DT spectra for IBD candidates (black) and accidentals (red) for EH1-AD1 (left) and EH3-AD1 (right). Bottom pannels show the DT spectra of the accidentals-subtracted IBD candidates. The DT < 1 m cut is drawn in as the blue dashed line.

From here, the DT cut efficiency was calculated as a function of DT cut, presented in Fig. 4.15, along with the efficiencies for each AD as determined by the DT < 1 m cut implemented in this selection. A study on dependence of the final fitted result on the DT cut value is presented in Sec. 7.2.1.

A number of methods, illustrated in Fig. 4.16, of calculating the DT efficiency and uncertainty were tested to understand the impact on the fitted results (see Sec. 7.2.2):

1. Full Envelope: The DT cut efficiency was treated as a single value for all ADs and was evaluated as the average of all ADs. The uncertainty was calculated as the spread of the near AD efficiencies to reduce statistical fluctuations experience by the far ADs. This spread was defined as half the difference between the highest and lowest DT efficiencies.

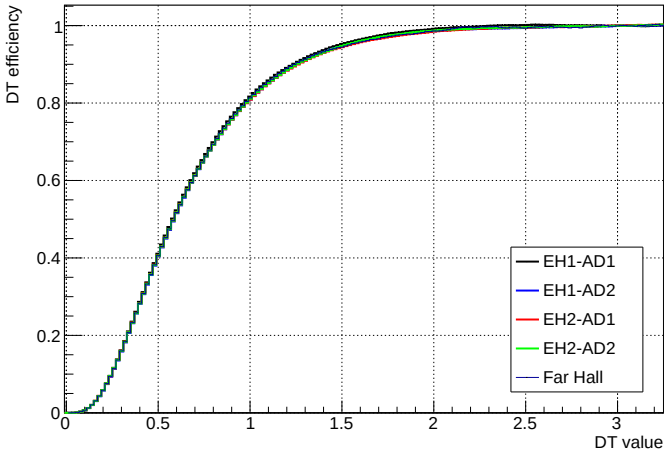

Figure 4.15: DT cut efficiency as a function of DT cut value. Far ADs are combined to reduce statistical fluctuations. Efficiencies for the DT < 1 m cut are shown in Fig. 4.16.

2. Half Envelope: Again, the DT cut efficiency was calculated as the average of all ADs. The uncertainty was half of the spread of the near ADs.

3. Gaussian Fit: Demonstrated in Fig. 4.16(b), the efficiencies of the individual ADs were plotted in a 1-dimensional histogram and fit with a Gaussian function to obtain the mean and sigma of the distribution. These values were then used as the efficiency and uncertainty, respectively.

4. Weighted Average: The efficiencies and uncertainties were calculated by an average of all eight individual DT efficiencies weighted by the inverse of their error bars. To clarify, AD i with efficiency $\epsilon_{\mathrm{DT},i} \pm \sigma_{\mathrm{DT},i}$ is weighted by $1/\sigma^2_{\mathrm{DT},i}$. This leads to a weighted average defined by [94]:

$$\epsilon_{\mathrm{DT,\ w.avg.}} = \frac{\sum_i w_i \epsilon_{\mathrm{DT},i}}{\sum_i w_i}, \tag{4.9}$$

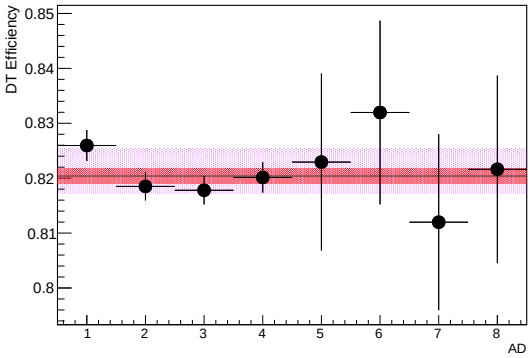

(a) Full Envelope, Weighted Average

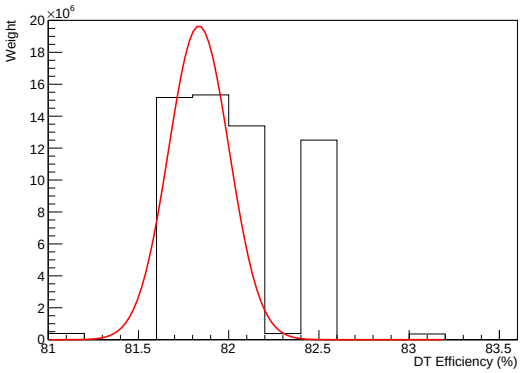

(b) Gaussian Fit

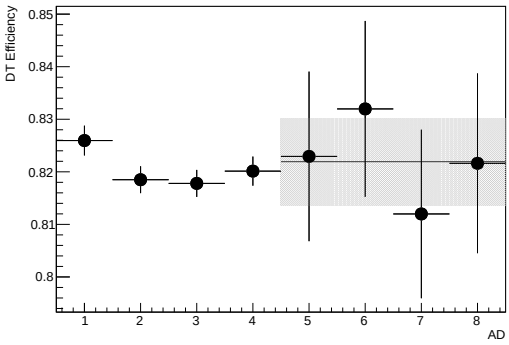

(c) Individual Efficiencies

Figure 4.16: Methods for calculating the DT cut efficiency uncertainty. (a) DT cut efficiencies for the 8 ADs with the full envelope method indicated with the violet band and the weighted average drawn in red. The half envelope method is simply half the full envelope shown here. (b) After weighting the DT efficiency of AD i by $1/\sigma_i^2$, the DT efficiency distribution was fit with a Gaussian fit, whose mean and sigma were used as the average efficiency and uncertainty, respectively. (c) Individual DT cut efficiencies method where the DT efficiencies were applied on a per-AD basis, with the far ADs combined in a weighted average (grey band) to increase statistics.

with a weighted uncertainty of

$$\begin{aligned}\sigma_{\text{DT, w.avg.}} &= \frac{1}{\sqrt{\sum_i w_i}} \\ &= \frac{1}{\sqrt{\sum_i \frac{1}{\sigma_i^2}}}.\end{aligned} \tag{4.10}$$

5. Individual DT Efficiencies: Each of the near ADs were assigned their own efficiencies

and uncertainties. The far ADs were combined in a weighted average calculation (Eq. 4.9 and Eq. 4.10) to increase the statistics of these ADs.

Table 4.6: DT cut efficiency uncertainty for the various calculation methods. The values for the individual DT efficiencies method are not included in this table as five sets of numbers were provided to the fitter (four for the near ADs, one for the far ADs).

Method	Efficiency (%)	Uncertainty (%)
Full Envelope	82.14	±0.41
Half Envelope	82.14	±0.20
Gaussian Fit	81.20	±0.17
Weighted Average	82.04	±0.13

4.4.5 Delayed Energy Cut Efficiency

Much like the prompt energy cut efficiency, the absolute efficiency of the delayed energy cut does not affect the final oscillation fit. The only impact is caused by the relative difference between the ADs and the AD-uncorrelated uncertainty. In this analysis, both of these quantities are evaluated using the pseudo-efficiency of the delayed energy cut: 1.5 MeV is treated as the lower bound of all possible IBD events to remove a huge portion of low energy background events. Since it plays the same role as the absolute efficiency would, the pseudo-efficiency will be referred to simply as the efficiency.

Taking the proper delayed energy cut bounds from Tab. 4.3 as the nominal range for each AD, the delayed energy cut efficiency was calculated using a fixed extended range of 1.5-2.8 MeV as 100% efficiency:

$$\epsilon_{\text{delayed}} = \frac{N_{\text{nominal}}}{N_{\text{extended}}}, \tag{4.11}$$

where N_x is the number of events in the prescribed x energy range of the accidentals-subtracted IBD candidates (Sec. 5.1). The lower limit of the extended range was chosen due

to the low energy β-α correlated backgrounds, while at the upper limit, the delayed energy spectrum was consistent with 0.

Two additional variations on the delayed energy cut efficiency calculation were implemented to reduce any biases introduced by the correlated backgrounds which remained in the accidentals-subtracted IBD sample. Both calculations used a sample of spallation neutrons (SPNs) captured on hydrogen, which was free of correlated backgrounds. The first calculation used fixed bounds of (1.85, 2.75) MeV for the nominal and (1.5, 2.8) MeV for the extended ranges, consistent for all ADs. The other used fitted bounds $(\mu - 3\sigma, \mu + 3\sigma)$ and $(\mu - 5\sigma, \mu + 4\sigma)$ for nominal and extended ranges, respectively, which was largely independent of the shifts of the energy scales relative to the other ADs.

The delayed energy cut efficiencies for the three methods are presented in Fig. 4.18. All three methods observed a difference between the near and far ADs. The average over all ADs was used as the delayed energy cut efficiency, while the uncertainty was calculated as half the dif-

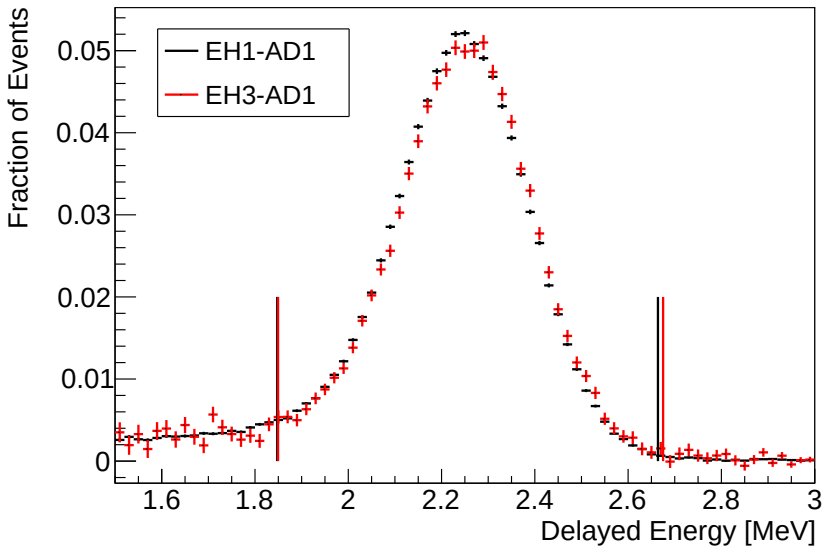

Figure 4.17: Delayed energy spectra for EH1-AD1 (black) and EH3-AD1 (red), both normalized to one for shape comparison. The floating delayed energy cut bounds are drawn as the vertical lines.

ference between the largest and smallest efficiencies. All three methods provided comparable efficiencies, though the cleaner SPN samples exhibited significantly smaller uncertainties, as summarized in Tab. 4.7. With the additional advantage that the relative energy scale shifts were removed, the efficiency and uncertainty calculated from the SPNs with the fitted range was used in the final fit. Additional checks on the delayed energy cut efficiency calculation, primarily focused on the near-far differences, are presented in Appendix A.2. These checks did not identify anything wrong with the selection, though the efficiencies obtained with the SPN selection was chosen for the analysis since it was free of correlated backgrounds.

Table 4.7: Delayed energy cut efficiencies and uncertainties according to the three calculation methods. The uncertainty is calculated as half the difference between the largest and smallest efficiencies of the near ADs. Comparable efficiencies are obtained with all three methods, the SPN sample presents less uncertainty due to the cleaner sample.

Method	Efficiency (%)	Near Uncertainty (%)
IBD Selection	93.4	$\pm$0.11
SPNs: Fixed Ranges	92.1	$\pm$0.06
SPNs: Fitted Ranges	93.4	$\pm$0.04

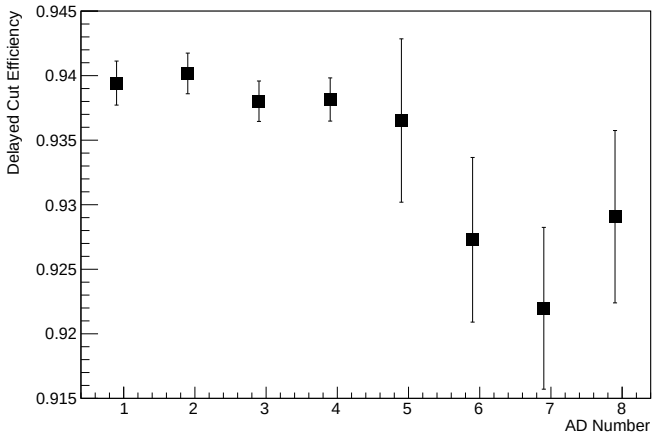

(a) IBD Selection

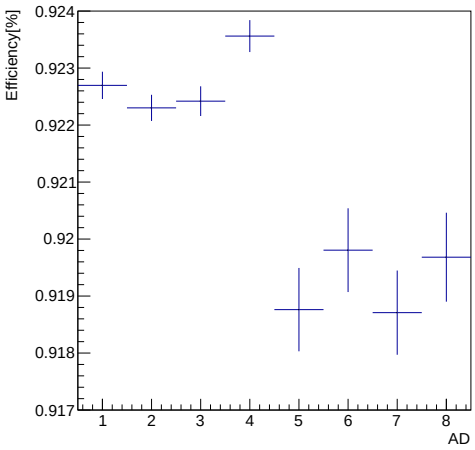

(b) SPNs: Fixed Ranges

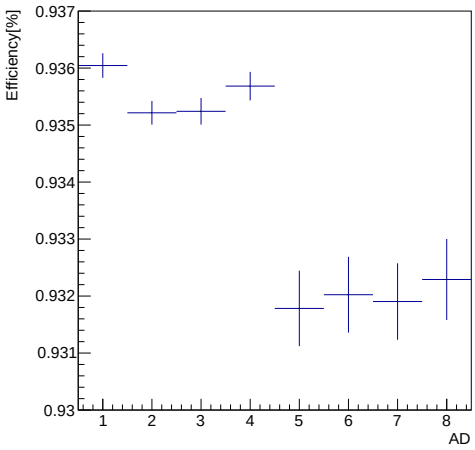

(c) SPNs: Fitted Ranges

Figure 4.18: Delayed energy cut efficiencies determined by the IBD selection (top) and the SPN sample, the latter being evaluated with both fixed (bottom left) and fitted (bottom right) ranges.

Chapter 5

Backgrounds

The selection process also admits other pairs of events besides IBDs, namely backgrounds producing correlated events in double-coincidence, as well as otherwise uncorrelated events occuring within the criteria of the nH selection, which mimic the IBD signature. Known as "accidentals," these uncorrelated pairs of events make up the overwhelming majority of the background events in the nH analysis (Sec. 5.1). The correlated backgrounds, discussed in Sec. 5.2, consist of muon-induced events (fast neutrons and ^{9}Li/^{8}He) and radioactive decays (^{241}Am-^{13}C and radiogenic neutrons). As an illustration, Fig. 5.1 presents the prompt energy spectrum of the IBD candidates and the backgrounds in EH1-AD1 observed by this analysis.

5.1 Accidental Background

The signals which create the accidental background, referred to as "singles," primarily originate from radioactivity in the PMTs and the surrounding environment. These uncorrelated events can occur within the spacial and temporal requirements of the IBD selection and therefore be considered as an IBD candidate.

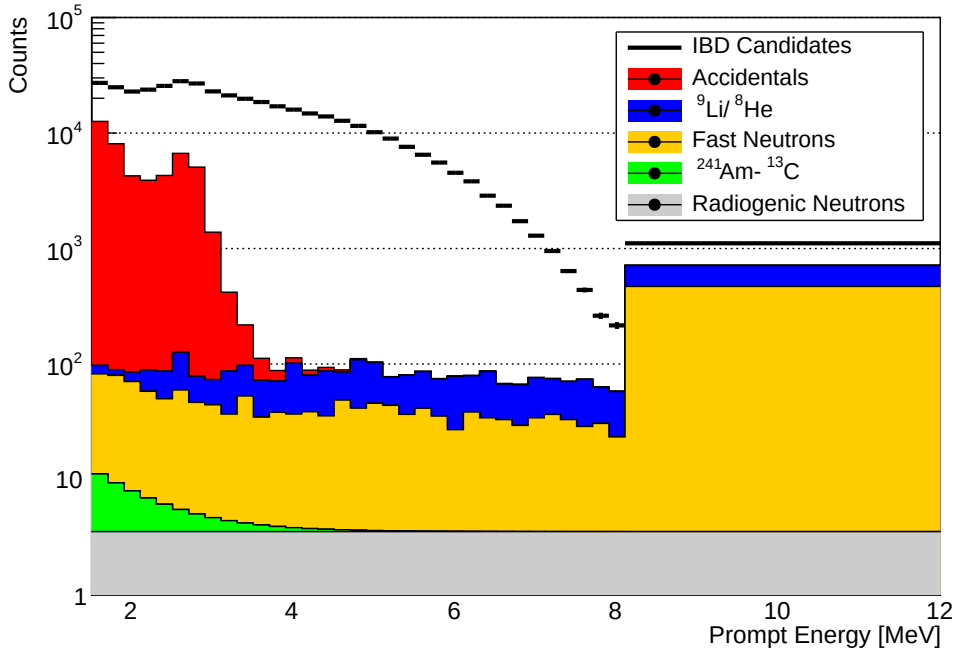

Figure 5.1: Prompt energy spectrum of IBD candidates (black) and the various backgrounds contaminating the sample.

An important advantage of this background is that it can be precisely determined through measuring the singles rate and mimicking the accidentals in the IBD candidate pool to form a data-driven synthetic accidental background. The process is simply: find single events, pair them randomly, then scale the spectra to match the number passing the timing requirements of the IBD selection. Sec. 5.1.1 describes the selection of the uncorrelated single events, while the pairing and scaling is addressed in Sec. 5.1.2.

5.1.1 Singles Selections

To accurately model the accidentals in the IBD candidate sample, the selection criteria for the singles was nearly identical to that of the IBD candidates by construction, except the multiplicity cut: instead of two events in the coincidence time window, the singles selection required exactly one event. Additionally, to match the details of the prompt-like and delayed-

like events of the IBD selection, two corresponding samples of singles were obtained.

Fig. 5.2 illustrates the altered multiplicity cuts for both samples. For the delayed-like sample, the loose delayed energy cut bounds (1.5-3 MeV) were used in the initial selection. When a delayed-like event was identified, the data in the $t_c + 400$ μs$= 1900$ μs time window was scanned for any prompt-like events, as well as the 400 μs after, matching the timing of the delayed-like events of the IBD selection. If both of these periods were void of prompt-like singles and muon vetoes, this event was regarded as a delayed-like single. In contrast to the delayed-like events, the time windows of the IBD selection was not defined with regards to the prompt-like events, however, the mean time between the prompt-like and delayed-like events was $\sim$100 μs. Therefore, the timing requirements of the prompt-like singles sample was adapted to best match the timing of the accidentals in the IBD sample: $t_c + 400$ μs-100 μs$= 1800$ μs before and 400 μs$+100$ μs$= 500$ μs after the prompt-like event must be void of muon vetoes and other prompt-like events. The choice of the 100 μs isolation

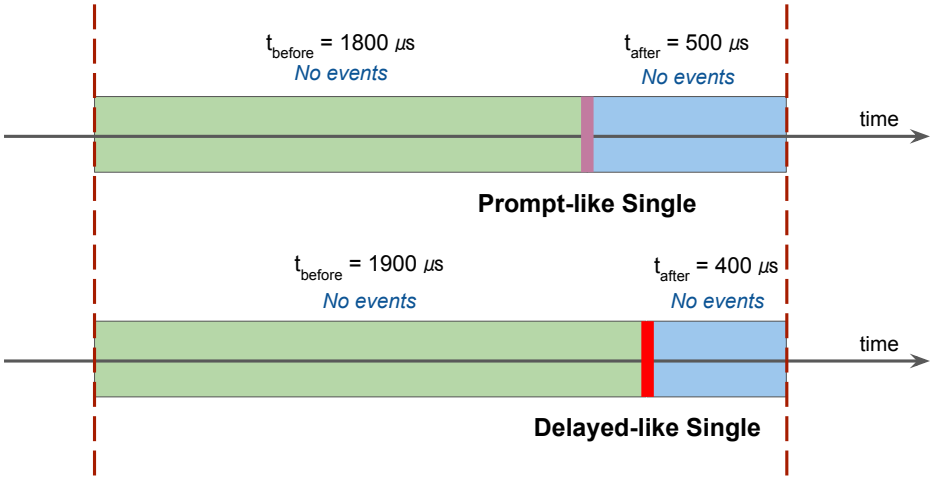

Figure 5.2: Multiplicity cuts of the prompt- and delayed-like singles' selections, designed to best match the IBD candidate selection. As before, the entire window must not contain any muon vetoes or other prompt-like events. The prompt-like singles window is offset by 100 μs with respect to the delayed-like singles window corresponding to the mean time between prompt- and delayed-like events observed in the IBD candidates.

time shift was decided after a few variations showed negligible effect on the rates and spectra.

From the number of events in each sample and the total un-vetoed time, the measured rates of each sample were calculated. However, these rates do not represent the true uncorrelated singles rates since the selection required isolation from prompt-like events. Therefore, the true rates were obtained by correcting the measured rates:

$$R_{\text{single}} = \frac{R^{\text{m}}_{\text{single}}}{e^{-(t_c+2\times 400\,\mu\text{s})*R_{\text{prompt}}}}. \tag{5.1}$$

Here, the true prompt- or delayed-like singles rate, R_{single}, is calculated by adjusting the measured rate, $R^{\text{m}}_{\text{single}}$, in order to account for the probability of interruption to the isolation time window by one or more prompt-like singles. Hence, the denominator depends on the true prompt-like singles rate, R_{prompt}, for both the prompt- and delayed-like singles. The measured (top) and corrected (bottom) singles rates are summarized in Tab. 5.1, with the corrected singles rates vs run order presented in Fig. 5.3.

Table 5.1: Measured (left) and true (right) prompt- and delayed-like singles rates. To obtain the true singles rates, the measured rates were corrected according to Eq. 5.1.

	Measured		True	
	$R^{\text{m}}_{\text{prompt}}$ [Hz]	$R^{\text{m}}_{\text{delayed}}$ [Hz]	R_{prompt} [Hz]	R_{delayed} [Hz]
EH1-AD1	17.42 ± 0.05	17.05 ± 0.05	18.16 ± 0.05	17.78 ± 0.05
EH1-AD2	17.33 ± 0.05	16.97 ± 0.05	18.07 ± 0.05	17.69 ± 0.05
EH2-AD1	17.07 ± 0.04	16.70 ± 0.04	17.78 ± 0.04	17.40 ± 0.04
EH2-AD2	17.00 ± 0.04	16.63 ± 0.04	17.71 ± 0.05	17.32 ± 0.05
EH3-AD1	16.67 ± 0.03	16.31 ± 0.03	17.35 ± 0.04	16.97 ± 0.03
EH3-AD2	16.87 ± 0.03	16.52 ± 0.03	17.57 ± 0.04	17.20 ± 0.03
EH3-AD3	16.87 ± 0.03	16.52 ± 0.03	17.57 ± 0.04	17.20 ± 0.03
EH3-AD4	16.82 ± 0.04	16.46 ± 0.04	17.51 ± 0.04	17.14 ± 0.04

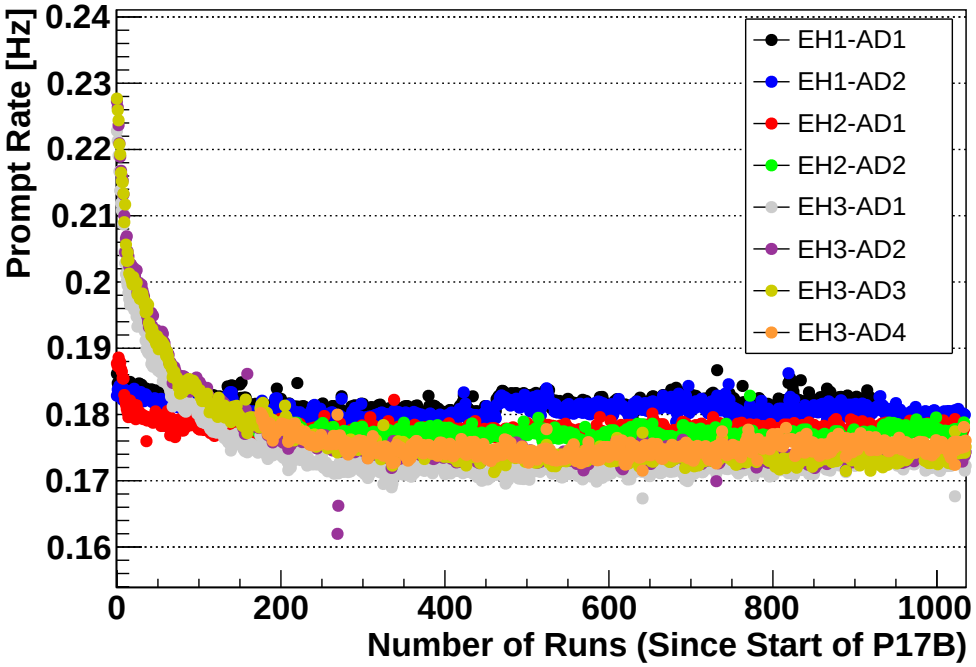

Figure 5.3: Prompt singles rates vs number of runs since the start of P17B for each AD. Due to radioactivity of the materials in the ADs, the singles rates were higher at the start of the data taking, then quickly reduce to a stable rate.

5.1.2 Synthetic Accidentals Pairing and Scaling

After obtaining the prompt- and delayed-like singles samples, a synthetic accidental sample was constructed by randomly pairing events from each. Since the delayed-like sample was smaller due to the smaller range of allowed energies, each delayed-like single was used exactly once and assigned a prompt-event at random. Additionally, to replicate the equal probability for all coincidence times, each pair was assigned a random value between 1 and 1500 μs.

At this stage, the synthetic accidental background has many more pairs compared to the accidentals in the IBD candidate sample. Therefore, as a final step, it was scaled to the proper number of events. This was done on a run-by-run basis to account for changes in the singles rates. Three methods were utilized to cross-check one another:

1. Rate-corrected: From the measured singles rates (Tab. 5.1), calculate the expected rate of accidentals passing the IBD selection criteria:

$$R_{\text{acc}} = R_{\text{prompt}} * R_{\text{delayed}} * (t_c - 1\ \mu\text{s}) * e^{-(t_c + 2\times 400\ \mu\text{s})R_{\text{prompt}}}. \tag{5.2}$$

   Here, the combination of the first three terms represents the rate at which the prompt- and delayed-like singles occur within the required coincidence time, t_c, but separated by at least 1 μs. The exponential term, on the other hand, represents the requirement that the two events be isolated from other prompt-like events.

2. Distance-normalized: Utilizing the fact that nearly all IBDs have a coincidence distance (ΔD) of less than 1 m between prompt and delayed events, this method normalizes the synthetic accidental distribution with $\Delta D > 2$ m to that of the IBD candidates with the same condition.

3. DT-normalized: Following the same logic as the distance-normalized method, but by normalizing according to the number of events with coincidence distance-time (DT) larger than 3 m.

Tab. 5.2 summarizes the consistency between the three methods of $< 0.06\%$ for all ADs

Table 5.2: Percent difference in total number of accidentals between the normalization methods to the rate-corrected method. Largest difference of 0.055%, without significant bias.

Detector	$(1 - \frac{N_{\text{norm}}}{N_{\text{rate}}})[\%]$	$(1 - \frac{N_{\text{DTnorm}}}{N_{\text{rate}}})[\%]$
EH1-AD1	-0.004	0.010
EH1-AD2	-0.016	-0.007
EH2-AD1	-0.013	-0.002
EH2-AD2	-0.055	-0.041
EH3-AD1	0.018	0.012
EH3-AD2	-0.002	0.007
EH3-AD3	-0.008	-0.004
EH3-AD4	-0.029	-0.028

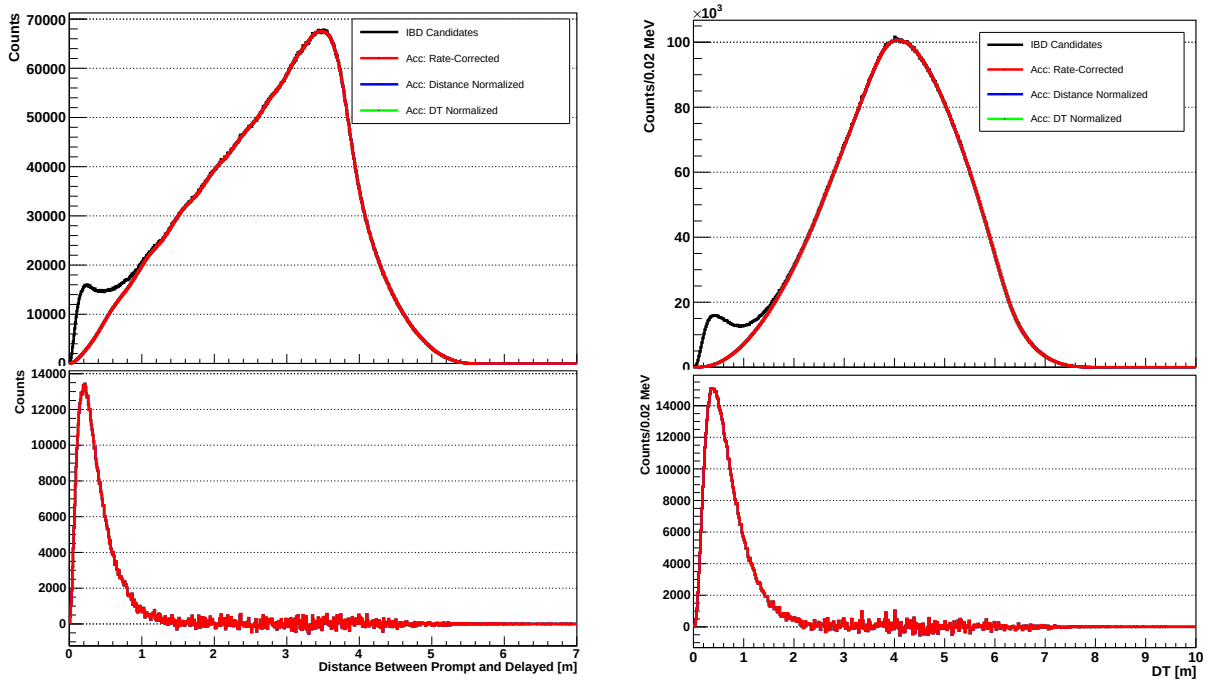

Figure 5.4: Coincidence distance (left) and DT (right) spectra of the IBD candidates (black) and scaled accidentals: rate-corrected (red), distance-normalized (blue), and DT-normalized (green). The bottom panels are the spectra obtained by subtracting the scaled accidentals from the IBD candidates. The consistency between the scaling methods is represented by the apparent absence of the normalized scaling methods.

without consistent bias between them. The coincidence distance and DT spectra for the IBD candidates and the scaled accidentals (all methods), as well as the spectra after subtracting the accidentals, are shown in Fig. 5.4 for EH1-AD1 representing all ADs. While all three scaling methods are included, the distance- and DT-normalized methods are not visible by eye due to consistency between all three. Further indicating the scaling was done properly, the spectra are flat beyond 2 m and 3 m for the coincidence distance and DT spectra, respectively.

Being derived directly from the singles rates, the rate-corrected method was adopted as the standard scaling method for the synthetic accidental background for this analysis. The remaining accidentals after subtraction at the large distances and DT values are summarized in Tab. 5.3. No bias of over- or under-subtracting accidentals is observed, with the percent-

Table 5.3: Comparison of the number of the events with distance values between 2 m and 5 m (left) and DT values larger than 3 m (right). N_{IBD} pertains to the IBD candidates before subtraction, while N_{sub} is the number of events remaining after subtraction of the rate-corrected method. The residual accidental events are between -0.04% and 0.06% for all ADs.

	2 m $< D <$ 5 m			$DT >$ 3 m		
	N_{IBD}	N_{sub}	$\frac{N_{sub}}{N_{IBD}}$[%]	N_{IBD}	N_{sub}	$\frac{N_{sub}}{N_{IBD}}$[%]
EH1-AD1	1.08726×10^7	-1464.1	-0.0135	1.12938×10^7	-3102.3	-0.0275
EH1-AD2	1.23395×10^7	6840.3	0.0554	1.28190×10^7	6636.6	0.0518
EH2-AD1	1.33178×10^7	5083.1	0.0382	1.38318×10^7	4464.2	0.0323
EH2-AD2	1.16993×10^7	5652.5	0.0483	1.21498×10^7	4471.5	0.0368
EH3-AD1	1.95546×10^7	-3614.6	-0.0185	2.03083×10^7	-3261.8	-0.0161
EH3-AD2	1.93096×10^7	-6948.7	-0.0360	2.00601×10^7	-6147.9	-0.0306
EH3-AD3	1.99914×10^7	-1181.4	-0.0059	2.07640×10^7	-1968.0	-0.0095
EH3-AD4	1.72721×10^7	974.7	0.0056	1.79393×10^7	1927.7	0.0107

ages of residual accidentals landing between -0.04% and 0.06% for all ADs. Fig. 5.5 shows the rate of accidentals for each AD over time, and the averaged rates of accidentals in the IBD candidate sample for each AD are presented in Tab. 5.4.

Table 5.4: Daily rate of accidentals as calculated by Eq. 5.2 with the values in Tab. 5.1.

	Accidentals (day^{-1})
EH1-AD1	120.05 ± 0.06
EH1-AD2	119.04 ± 0.06
EH2-AD1	111.02 ± 0.05
EH2-AD2	108.12 ± 0.06
EH3-AD1	107.64 ± 0.04
EH3-AD2	106.05 ± 0.04
EH3-AD3	109.74 ± 0.04
EH3-AD4	104.87 ± 0.04

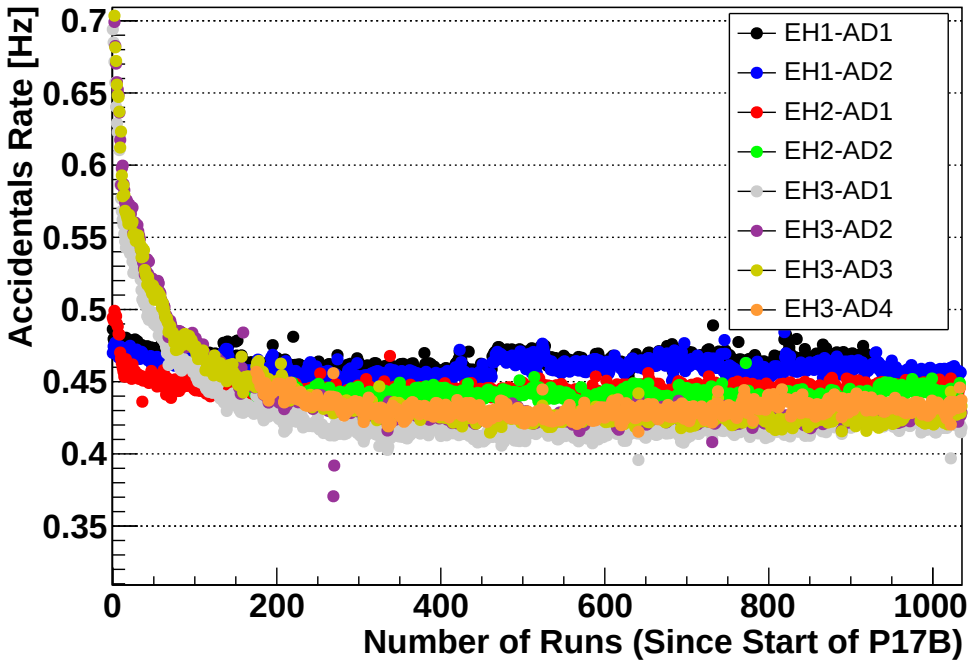

Figure 5.5: Rate of accidentals vs the number of runs since the start of P17B. The higher rate at the start of data-taking was due to the radioactivity in the materials of the ADs, which quickly reduced to a stable rate.

5.2 Correlated Backgrounds

In addition to the accidental background, correlated events can produce the same signature as IBDs. The correlated backgrounds in this analysis originate primarily from energetic muon interactions and radioactivity events entering the ADs. Muons can transfer energy to neutrons in the rock surrounding the experimental halls which can cause proton recoils before eventually capturing on nuclei in the ADs, producing prompt- and delayed-like events. Muons can also produce unstable isotopes within the LS, whose decays create a double coincidence signature. While muon vetoes were designed to target these backgrounds, some events escape the vetoes. These backgrounds are discussed in Sec. 5.2.1 and Sec. 5.2.2, respectively. Alternatively, radioactive decays from the ^{241}Am-^{13}C calibration sources and the AD materials can introduce correlated backgrounds, as discussed in Sec. 5.2.3 and Sec. 5.2.4.

The estimations presented here were performed by Daya Bay Collaborators.

5.2.1 Fast Neutron Background

As mentioned in Sec. 4.1, energetic muons can produce energetic "fast" neutrons in the rock surrounding the detectors. The fast neutrons slow down as they collide with protons, then eventually capture on a nucleus. The light emitted from the initial collisions can form a prompt signal and the neutron capture becomes the delayed signal. The muon vetoes are specifically designed to remove this background, however, the muon veto system does not have perfect efficiency. Furthermore, they are not removed by the vetoes if the muons do not enter the waterpool, and instead the fast neutrons enter the detectors without a detected preceding muon.

To identify and remove the fast neutron background, two samples were used [84]. The first was obtained by a modification to the IBD selection such that the threshold energy of the AD muon was raised to 300 MeV, as was the upper limit of the prompt energy cut. The second was a sample of IBD candidates whose events were coincident with muons only tagged by the outer water pool (OWP), illustrated by Fig. 5.6. In order to obtain the OWP-tagged sample, a trigger in the OWS was required within $t_{p-ows} \in (-300, 600)$ ns. Additionally, no IWS triggers or AD muons were allowed within the 600 μs prior to the prompt event or 2 μs

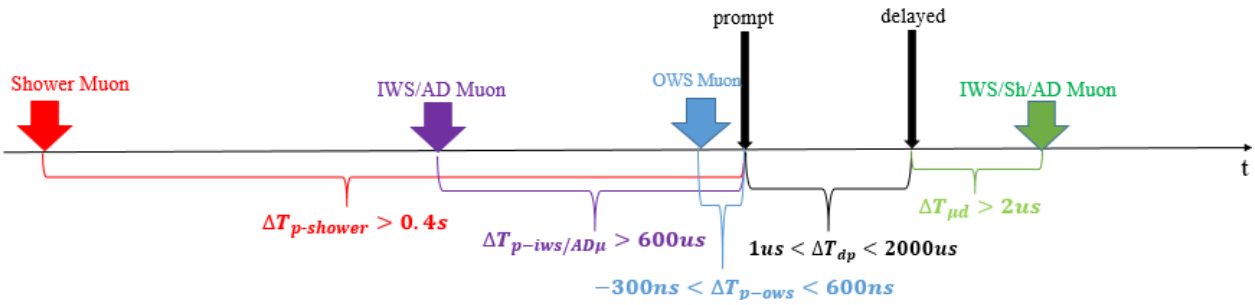

Figure 5.6: Schematic of the selection for the OWP-tagged sample for the fast neutron background evaluation [84].

after the delayed event. Shower muons were required to be at least 0.4 s before the prompt signal.

Pairs in the first sample with prompt energy higher than 20 MeV were expected to be purely fast neutrons, as well as the entire second sample. Therefore, the two allow for proper evaluation of the true rate and spectra of the fast neutron background in the IBD sample via

$$\begin{aligned} N_{\text{FastN}} =& N_{\text{OWP\_LE}} \times k \\ =& N_{\text{OWP\_LE}} \times \frac{N_{\text{IBD\_HE}}}{N_{\text{OWP\_HE}}}. \end{aligned} \tag{5.3}$$

Here, the low energy OWP events $N_{\text{OWP\_LE}}$ are scaled according to the ratio of the events from the IBD selection $N_{\text{IBD\_HE}}$ to the OWP sample $N_{\text{OWP\_HE}}$ in the high energy range ($E_p \in (20, 300)$ MeV).

Slight differences in the vertex distributions of the IBD and OWP fast neutron samples introduces a difference in the prompt energy spectrum shape. This was accounted for through a systematic uncertainty which was calculated through varying the maximum energy for calculating the normalization factor k: the median value was chosen for the normalization and the difference between the maximum and median value was counted as the systematic uncertainty [84]. Additionally, the statistical uncertainty was calculated through:

$$\frac{\sigma_{\text{stat}}}{k} = \sqrt{\frac{1}{N_{\text{IBD\_HE}}} + \frac{1}{N_{\text{OWP\_HE}}}} \tag{5.4}$$

Table 5.5: Summary of values used in determining the fast neutron background rates for each hall [95].

	$N_{\text{OWP\_LE}}$	Factor k	N_{FastN}	ϵ_m	Live Time [d]	R_{FastN} [$\text{d}^{-1}\text{AD}^{-1}$]
EH1	2867	1.33 ± 0.026	3814.8 ± 246.6	0.9363	1884.9	2.16 ± 0.14
EH2	2132	1.48 ± 0.026	3162.7 ± 159.4	0.9322	2148.8	1.58 ± 0.08
EH3	379	2.24 ± 0.101	850.3 ± 126.9	0.9306	6458.0	0.14 ± 0.02

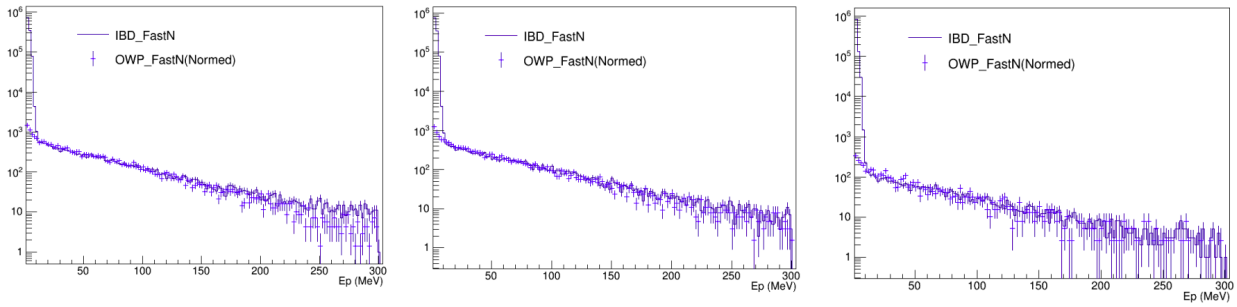

Figure 5.7: Fast neutron prompt energy spectra for the three halls (left to right: EH1, EH2, EH3) [95].

The inputs to Eq. 5.3 and the resulting background rates for each hall are presented in Tab. 5.5, while the prompt energy spectra for each hall are shown in Fig. 5.7.

5.2.2 ^{9}Li/^{8}He Background

The other muon-induced correlated background is the ^{9}Li/^{8}He background: incoming muons can produce unstable isotopes. While majority of these isotopes decay quickly and are removed with the muon vetoes, two longer-lived isotopes can exist past the vetos, namely ^{9}Li and ^{8}He. These β-decay into unstable excited isotopes, ^{8}Be and ^{8}Li, respectively, then undergo $\beta-$n cascades, which can have the same double coincidence signature as IBDs.

The ^{9}Li and ^{8}He mean lifetimes ($\tau_{\text{Li9}} = 257$ ms and $\tau_{\text{He8}} = 172$ ms, respectively) extend beyond the muon vetoes, therefore leaving many of these events in the IBD sample. Even the 1 s shower muon veto allows for $\sim e^{-4}$ of the events to remain. However, the known mean lifetimes of these decays allows for fitting the ^{9}Li and ^{8}He components of the time-to-last-muon distributions of IBD candidates. Since these events are indistinguishable in this analysis, ^{9}Li will be used to denote both ^{9}Li and ^{8}He for this section, unless otherwise noted.

In order to quantify this background, the selection compared the different time-to-last-muon distribution of ^{9}Li to other double coincidences [84]. First, the water pool and AD muon

vetoes were removed and the shower muon veto was reduced from 1 s to 0.8 ms so that the ^{9}Li contribution was increased. Additionally, the lower bound of the prompt energy cut was raised to 3.5 MeV to reduce the number of accidentals.

These altered cuts are accounted for through additional efficiencies. The efficiency for the muon veto change, $\eta_{\mu_{veto}}$, is calculated as [84]:

$$\eta_{\mu_{veto}} = \frac{\int_{1\ s}^{\infty} \frac{1}{\tau_{\mathrm{Li}}} e^{-t/\tau_{\mathrm{Li}}} dt}{\int_{800\ \mu s}^{\infty} \frac{1}{\tau_{\mathrm{Li}}} e^{-t/\tau_{\mathrm{Li}}} dt} \approx 0.0205. \tag{5.5}$$

This efficiency was assigned a 2% uncertainty. As for the efficiency of the change to the prompt energy cut, the ^{9}Li sample still includes IBD and other backgrounds. Another sample was made with only non-^{9}Li events by requiring that no muon with energy > 1200 MeV occurs within 1.5 s before the events [84]. This non-^{9}Li sample was then subtracted from the nominal ^{9}Li sample and through integration, the efficiency was calculated to be $\epsilon_{Ep} = 0.785 \pm 0.048$.

Continuing, muons were classified as "neutron-tagged" if an AD event with energy between 1.8 and 12 MeV occurred within (20, 200) μs of the muon. These neutron-tagged muons were more likely to produce ^{9}Li. The data was divided into 3 subsets depending on the deposited energy of the preceding muon: (0.02, 1) GeV, (1, 2.5) GeV, and > 2.5 GeV. Then the samples were fit with the following fit function:

$$f(t) = N_{\mathrm{Li+He}}(r \cdot \lambda_{\mathrm{Li}} \cdot e^{-\lambda_{\mathrm{Li}} t} + (1-r) \cdot \lambda_{\mathrm{He}} \cdot e^{-\lambda_{\mathrm{He}} t}) + N_{\mathrm{IBD\_cand}} \cdot R_\mu \cdot e^{-R_\mu t}, \tag{5.6}$$

where $\lambda_{\mathrm{Li}} \equiv R_\mu + 1/\tau_{\mathrm{Li}}$, r is the fraction of ^{9}Li vs ^{8}He in the total N_{Li+He} sample, and $N_{\mathrm{IBD\_cand}}$ is the number of IBD candidates. The fits are shown in Fig. 5.8 for each EH, as ^{9}Li rates were the same for all ADs in the same hall.

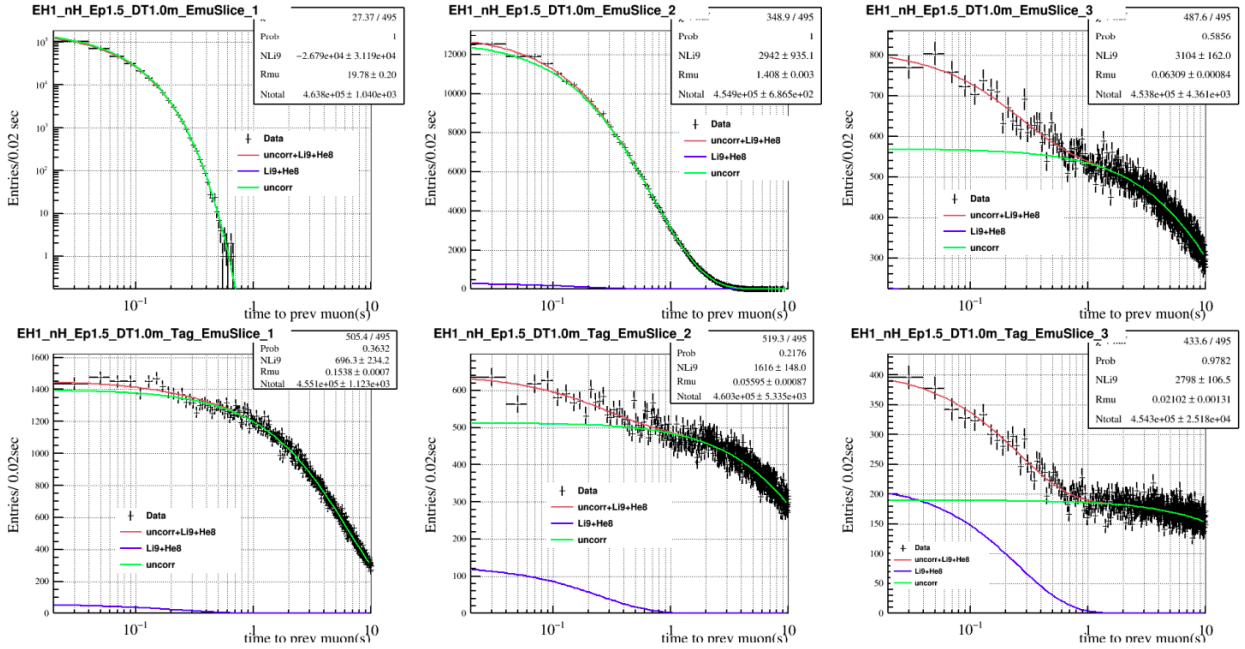

Figure 5.8: ^{9}Li/^{8}He spectra and fits for EH1 for no-tag (top row) and neutron-tagged (bottom row) for all three muon energy subsets (left to right: (0.02, 1) GeV, (1, 2.5) GeV, and $>$ 2.5 GeV). Other halls have similar fits [96].

The fit results were then used to calculate the final rate of ^{9}Li in the IBD selection:

$$\begin{aligned} R_{\mathrm{Li}} &= \frac{N_1^{\text{tagged}}/\epsilon_{\text{tag}} + N_2^{\text{no-tag}} + N_3^{\text{no-tag}} \cdot \eta_{\mu_{\text{veto}}}}{\epsilon_{Ep} \cdot T_{\text{live}}} \\ &= \frac{N_1^{\text{tagged}} \cdot \frac{N_2^{\text{no-tag}}}{N_2^{\text{tagged}}} + N_2^{\text{no-tag}} + N_3^{\text{no-tag}} \cdot \eta_{\mu_{\text{veto}}}}{\epsilon_{Ep} \cdot T_{\text{live}}}, \end{aligned} \tag{5.7}$$

where N_i^{tagged} and $N_i^{\text{no-tag}}$ indicate the fit results of the i-th muon region with and without neutrons tagged, respectively. ϵ_{tag} represents the neutron tag efficiency. ϵ_{Ep} and $\eta_{\mu_{\text{veto}}}$ indicate the pseudo-efficiency of the modified 3.5 MeV prompt cut and shower muon veto. The systematic uncertainties feeding into this estimation were the 2% relative uncertainty on $\eta_{\mu_{\text{veto}}}$, 6% from ϵ_{Ep}, and 100% from ϵ_{tag} [84]. Tab. 5.6 summarizes the final ^{9}Li rates for all halls.

Table 5.6: ^{9}Li/^{8}He background rates for each hall for the P17B data set [96].

	EH1	EH2	EH3
R_{Li9} [day^{-1}]	2.28 ± 1.02	2.22 ± 0.86	0.14 ± 0.05

5.2.3 ^{241}Am-^{13}C Background

As described in Ch. 3, the ADs were instrumented with ^{241}Am-^{13}C sources which released neutrons at a rate of ~ 0.7 Hz for additional calibrations [57]. Except during the calibration runs, the sources were contained in the ACUs to largely prevent their emissions from entering the scintillating volume. The ^{241}Am-^{13}C background was caused by correlated signals caused by inelastic collisions of the neutrons with nuclei in the stainless steel (Fe, Cr, Mn, or Ni) forming a prompt signal, then capturing on either nuclei in the LS or the steel as the delayed event.

The background was estimated by deploying a stronger ^{241}Am-^{13}C source which produced nearly 80 times more neutrons than the calibration sources [64]. The special source was positioned on the top of EH3-AD2, shown in Fig. 5.9, for a special 10-day data run in 2012. In addition to the stronger source, the ^{241}Am-^{13}C background assessment utilized the fact that the ^{241}Am-^{13}C sources were positioned on the top of the AD, therefore, the background events were also located near the top.

The first step was to determine the number of extra correlated events (IBD candidates) using the stronger source compared to the calibration sources. The distribution of z-position after subtracting the accidentals from the IBD candidates, shown in Fig. 5.10, demonstrating the z-dependence of the ^{241}Am-^{13}C background events. From here, the number of correlated events of the standard calibration source, $N_{\mathrm{calib}}^{\mathrm{corr}}$, was subtracted from that of the strong

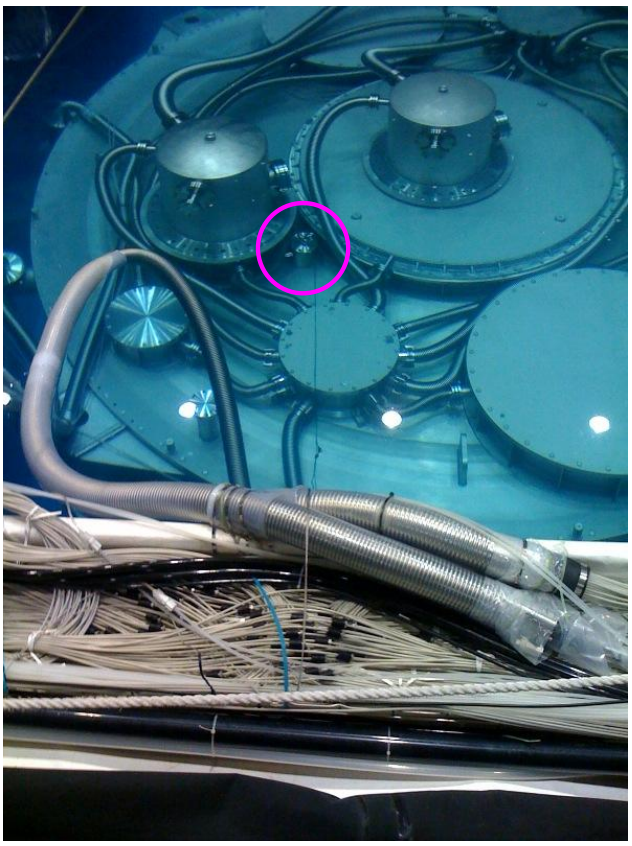

Figure 5.9: Location of the special ^{241}Am-^{13}C source on top of EH3-AD2 to characterize the ^{241}Am-^{13}C background [97].

source, $N^{\text{corr}}_{\text{strong}}$, to calculate the number of additional correlated events:

$$N_{\text{strong}} = N^{\text{corr}}_{\text{strong}} - N^{\text{corr}}_{\text{calib}}. \tag{5.8}$$

The difference between the strong and calibration events also provides the prompt energy distribution of the ^{241}Am-^{13}C background, presented in Fig. 5.11, which was fit with an exponential:

$$f(E; N, E_0) = Ne^{-E/E_0}. \tag{5.9}$$

The next step was to determine the number of singles caused by the calibration and strong sources. This was done by looking at the asymmetry in the z-position of the reconstructed

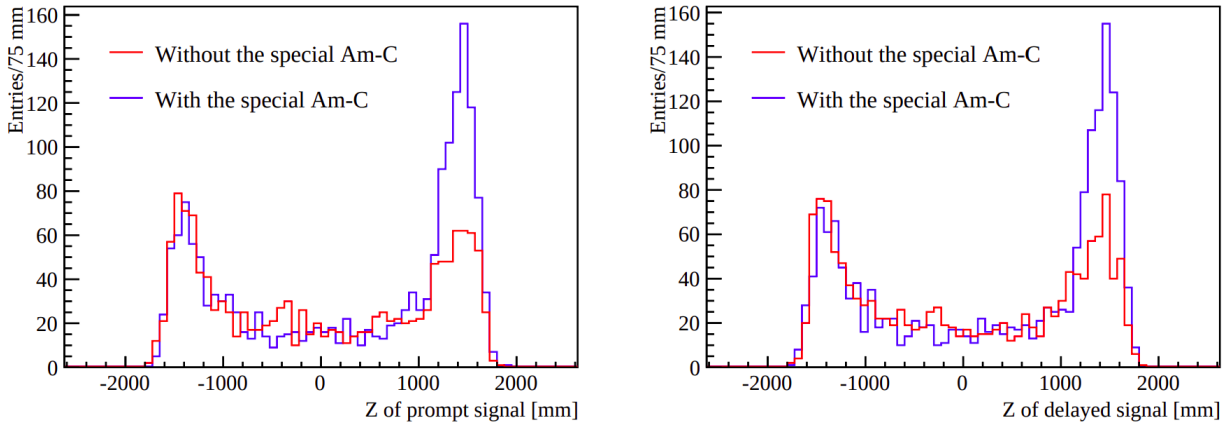

Figure 5.10: Z position distributions with and without the special ^{241}Am-^{13}C background source for prompt and delayed events of IBD candidates, where the asymmetry is due to the proximity to the ^{241}Am-^{13}C source [64].

events, as the ^{241}Am-^{13}C background was concentrated at the top of the ADs, closest to the sources:

$$N^{\text{s, asym}} = N^{\text{s}}_{z>0} - N^{\text{s}}_{z<0}, \tag{5.10}$$

where the subscripts indicate the z-position of the singles, and $N^{s,asym}$ refers to the difference in the number of singles at the top compared to the bottom of the detector. This was done for the calibration and strong sources, $N^{\text{s, asym}}_{\text{calib}}$ and $N^{\text{s, asym}}_{\text{strong}}$, respectively.

Finally, the number of correlated ^{241}Am-^{13}C background events was estimated by scaling the number of additional correlated events from the strong source, N_{strong} by the ratio of the ^{241}Am-^{13}C singles caused by the standard calibration source to that of the strong source:

$$N_{\text{calib}} = N_{\text{strong}} \times \left(\frac{N^{\text{s, asym}}_{\text{calib}}}{N^{\text{s, asym}}_{\text{strong}}} \right). \tag{5.11}$$

The rates were calculated by accounting for the live time and the muon and multiplicity efficiencies. A conservative 50% uncertainty was assigned to this background. The final rates are summarized in Tab. 5.7.

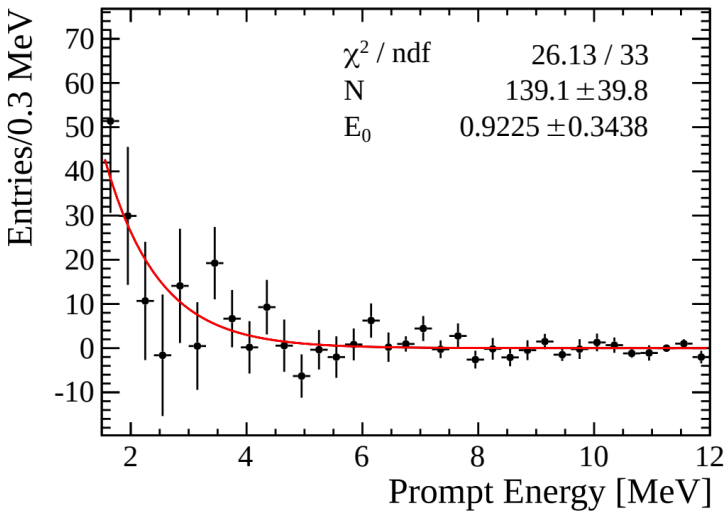

Figure 5.11: Prompt energy spectrum of the correlated ^{241}Am-^{13}C background, with the best fit Eq. 5.9 [64]. This was obtained by subtracting the prompt spectrum of the calibration source from that of the strong source.

Table 5.7: Estimated daily rates of the ^{241}Am-^{13}C background for each AD [98]

	$R_{\text{Am-C}}$ [day^{-1}]
EH1-AD1	0.05 ± 0.03
EH1-AD2	0.05 ± 0.03
EH2-AD1	0.04 ± 0.02
EH2-AD2	0.04 ± 0.02
EH3-AD1	0.02 ± 0.01
EH3-AD2	0.02 ± 0.01
EH3-AD3	0.02 ± 0.01
EH3-AD4	0.01 ± 0.01

5.2.4 Radiogenic Neutron Background

While extensive efforts were made to minimize radioactivity in the ADs [99], some radioactivity remained, particularly in the borosilicate glass of the PMTs. Two decay processes contributed to the radiogenic neutron background [100, 101]: Spontaneous fissions and X(α, n)Y reactions can result in the production of neutrons and/or γ-rays. The γ-rays or neutron recoils on protons create prompt-like signals, while the neutron captures form the delayed-like

signals. With the shielding provided by the LS region to the GdLS region, this background only affects the nH analysis, not the nGd.

Directly measuring the radiogenic neutron background was not an option since the rate was significantly lower than the other backgrounds. Instead, the radiogenic neutron background rates were estimated via a full Monte Carlo simulation supplied with data of the PMT glass composition and flurocarbon paint [102], with an uncertainty which accounts for the uncertainty of all the inputs used in the simulation. The final rate was $R_{\text{rad-n}}$ [day^{-1}] = 0.20 ± 0.04 [98].

Chapter 6

Fitter Prediction

The Daya Bay experiment was designed to precisely measure the θ_{13} neutrino oscillation parameter by measuring the $\overline{\nu}_e$ flux at the far ADs relative to the near ADs. Compared to an absolute measurement which fits the measured rate at a single location to a model, the relative measurement significantly reduces the systematic uncertainties due to absolute detection efficiency and the reactor $\overline{\nu}_e$ model. Two styles of fitter have been developed and utilized by the Daya Bay Collaboration: The first predicts the $\overline{\nu}_e$ flux at near and far ADs from a reactor $\overline{\nu}_e$ emission model and oscillation effects, and simultaneously fits all the near and far data while allowing the absolute normalization and the shape of the spectrum to float [57, 92]. The second method, known as the "near-far projection," predicts the $\overline{\nu}_e$ flux at the far ADs by applying oscillation and baseline effects to the measured near AD flux [103, 104, 70]. Sec. 6.1 introduces the reactor neutrino model used in the fitter, while Sec. 6.2 presents the implementation of the near-far projection fitter used in this analysis.

6.1 Reactor Antineutrino Model

Regardless of the fitter style, a model of the reactor $\overline{\nu}_e$'s is necessary to either make the prediction at all halls or to separate the observed $\overline{\nu}_e$ spectrum into the contributions of the six individual cores. For modeling the fission-produced $\overline{\nu}_e$ spectra, the Daya Bay Collaboration utilizes Huber's conversions of the total β^- spectra of ^{235}U, ^{239}Pu, and ^{241}Pu at Institut Laue-Langevin [105] and Mueller's *ab initio* calculations for ^{238}U [106]. The prediction incorporates time-dependent corrections for non-equilibrium effects in the reactor and the $\overline{\nu}_e$ emission from the spent nuclear fuel (SNF) pools.

Provided by the power company, the weekly average power W_{th} and fission fractions f_q for each core k were combined with the energy emitted per fission for each isotope e_q [107] to calculate the total number of $\overline{\nu}_e$'s with energy E produced:

$$\frac{d\phi_k^d}{dt}(E) = \sum_{\substack{\text{weeks} \\ w \in d}} \left\{ \frac{T_{\text{DAQ},w} W_{\text{th},w}}{\sum_q f_{q,w} e_q} \sum_{\substack{\text{isotopes} \\ q}} f_{q,w} S_q(E) \left[1 + c_q^{\text{ne}}(E)\right] \right\} + S^{\text{snf}}(E), \tag{6.1}$$

where $S_q(E)$ is the Huber-Mueller spectrum for isotope q, $c_q^{\text{ne}}(E)$ are the non-equilibrium corrections, and $S^{\text{snf}}(E)$ represents the $\overline{\nu}_e$'s originating from the SNF. T_{DAQ} denotes the DAQ time for a given data-taking period (6-, 8-, or 7-AD period), during which the $\overline{\nu}_e$ rate and spectrum was assumed to be identical for all ADs in operation.

To determine the number of $\overline{\nu}_e$'s produced during the operation of AD i, the spectral rates must be multiplied by the DAQ time for each of the data-taking periods and summed:

$$\phi_{ik}(E) = T_{\text{DAQ},i}^{\text{6-AD}} \frac{d\phi_k^{\text{6-AD}}}{dt}(E) + T_{\text{DAQ},i}^{\text{8-AD}} \frac{d\phi_k^{\text{8-AD}}}{dt}(E) + T_{\text{DAQ},i}^{\text{7-AD}} \frac{d\phi_k^{\text{7-AD}}}{dt}(E). \tag{6.2}$$

With these $\overline{\nu}_e$ spectral predictions, it is possible to build our fitter. Sec. 6.2.3 will described how the fitter utilizes this information.

6.2 Near-Far Projection Method

Building to the full Daya Bay configuration, it is instructive to first consider the simplest arrangement with a singular isotropic $\overline{\nu}_e$ source, one near detector and one far detector. The ratio of the number of observed events at the far hall (N_{f}) to that at the near hall (N_{n}) is determined by [57]:

$$\frac{N_{\mathrm{f}}}{N_{\mathrm{n}}} = \left(\frac{T_{\mathrm{p,f}}}{T_{\mathrm{p,n}}}\right)\left(\frac{L_{\mathrm{f}}}{L_{\mathrm{n}}}\right)^2\left(\frac{\epsilon_{\mathrm{f}}}{\epsilon_{\mathrm{n}}}\right)\left[\frac{P_{\mathrm{sur}}(E_\nu, L_{\mathrm{f}})}{P_{\mathrm{sur}}(E_\nu, L_{\mathrm{n}})}\right]. \tag{6.3}$$

With careful evaluation of the number of target protons ($T_{\mathrm{p,n/f}}$), the baselines of the detectors from the source ($L_{\mathrm{n/f}}$), the detection efficiencies ($\epsilon_{\mathrm{n/f}}$), this ratio reveals the survival probability at the near and far distances ($P_{\mathrm{sur}}(E_\nu, L_{\mathrm{n/f}})$). Furthermore, this ratio illustrates the cancellation in the correlated uncertainties of both the reactor prediction and the detection efficiencies.

In extending to Daya Bay's real configuration, Eq. 6.3 must be adapted to account for four near ADs, four far ADs, and six nuclear reactor cores with individually varying power, all of which impact the $\overline{\nu}_e$ spectrum over time. As used in this analysis, the near-far projection method entails a crucial step: disentangling the contributions from each reactor core. This process involves decomposing the measured spectra at each AD into their individual reactor core components, which is essential for the accurate application of oscillation effects corresponding to the different baselines.

Summarized in both cartoon form (Fig. 6.1) and with actual data (Fig. 6.2) and described in detail in the following sections, the six steps the fitter takes to correctly predict the observed spectra at the far ADs are as follows:

1. Subtraction of the background events in the near AD measurements and correcting for the detection efficiencies (Sec. 6.2.1)

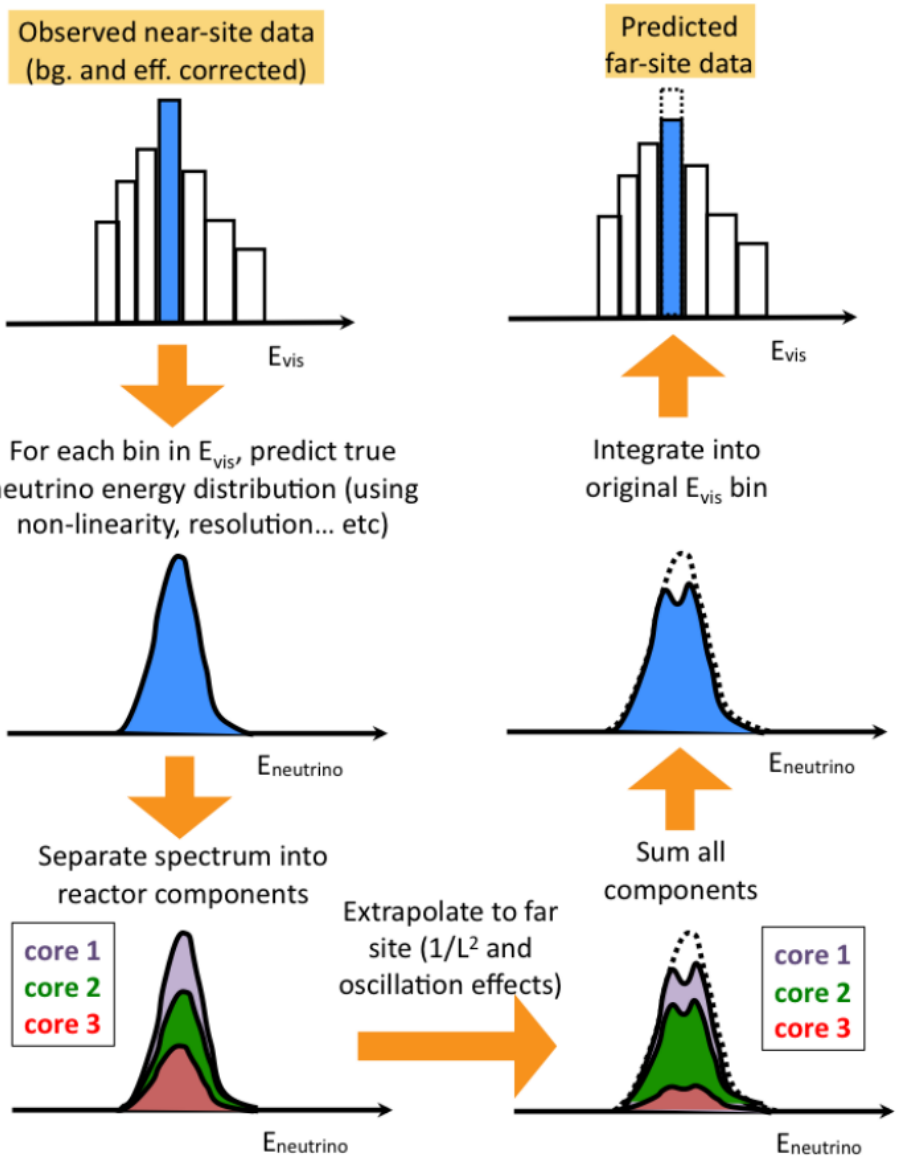

Figure 6.1: Cartoon of the prediction method. The left column pertains to the near AD's observations, while the right column pertains to the far AD's prediction. The no-oscillation prediction is included for comparison to the oscillated prediction. Graphic obtained from [103].

2. Conversion from the reconstructed prompt energy spectrum to the true $\overline{\nu}_e$ spectrum (Sec. 6.2.2) via detector response matrix

3. Decomposition of the observed $\overline{\nu}_e$ spectra into the contributions of each reactor core (Sec. 6.2.3), utilizing the Huber-Mueller reactor neutrino model and adjusting for oscillation effects

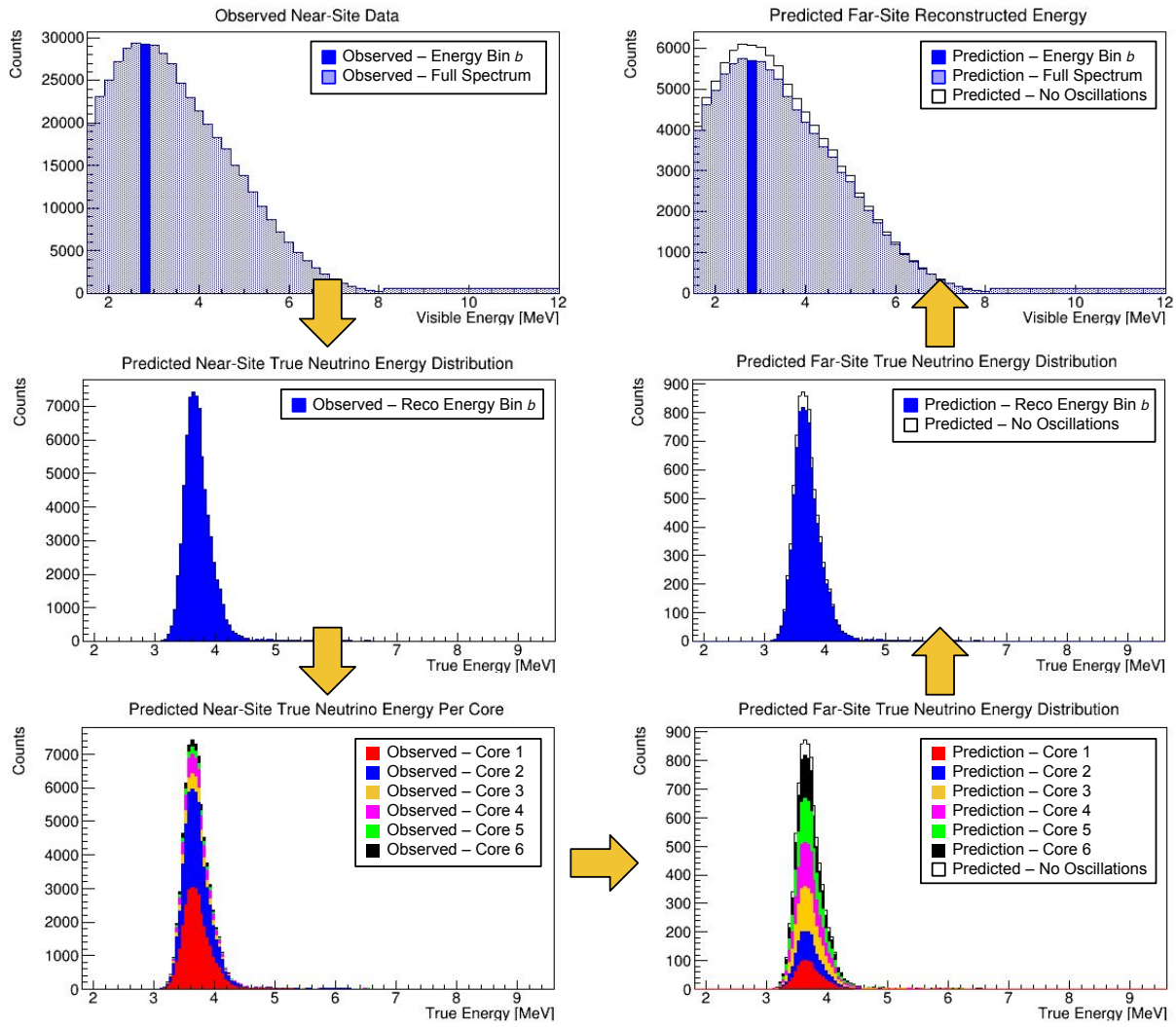

Figure 6.2: Stages of the fitting process. Following the same order as Fig. 6.1, the figures show the progression from the observations at EH1-AD2 (left plots) to the prediction at EH3-AD1 (right plots) with $\sin^2(2\theta_{13}) = 0.077$ and $\Delta m^2_{ee} = 0.00278$ eV^2 as inputs. The no-oscillation prediction is included for comparison to the oscillated prediction.

4. Extrapolation of the $\overline{\nu}_e$ spectrum from each core to each far AD accounting for baseline and oscillation effects, followed by the summation to determine the total $\overline{\nu}_e$ spectrum at each far AD (Sec. 6.2.4)

5. Conversion of the far true $\overline{\nu}_e$ spectra to the reconstructed prompt energy spectrum (Sec. 6.2.5)

6. Correction for the detection efficiencies and backgrounds for each far AD for comparison to observation (Sec. 6.2.6)

This process is done for each reconstructed energy bin, hereafter identified by the superscript (b). In the following sections, the indices i and j correspond to individual near and far ADs, respectively, while k and l refer to reactor cores.

6.2.1 Near AD Backgrounds and Efficiencies

The first step of the near-far prediction is to determine the observed IBD spectra, free of backgrounds. This requires the subtraction of accidentals, ^{9}Li/^{8}He, fast neutrons, ^{241}Am-^{13}C, and radiogenic neutrons. The processes of obtaining the background rates and spectra is described in Ch. 5.

Then the observed near AD IBD spectrum must be corrected for the detection efficiencies. The muon-veto livetime efficiency (ϵ_μ) and multiplicity cut efficiency (ϵ_m) are well understood and precisely measured for each AD without any corresponding uncertainty. The remaining efficiencies are evaluated for the average over all ADs and assigned a relative uncertainty. Utilizing the benefit of the relative measurement, only relative differences in efficiency between ADs impact the final prediction. The relative detection efficiency (ϵ_i) and uncertainty encompass the prompt and delayed energy cut efficiencies, distance-time (DT) cut efficiencies, and total target proton number. In principle, the prompt energy cut efficiency should also be included here, however, the effects of the prompt energy cut are already accounted for: To adjust the shape due to the relative energy scale, for example, the content of each bin is updated accordingly, which changes the prompt energy cut. Therefore, the prompt energy cut efficiency becomes equivalent across all ADs and cancels in the final ratio.

For reconstructed energy bin b of near AD i with $N^{(b)}_{\mathrm{cand},i}$ IBD candidates and $N^{(b)}_{\mathrm{bg},i,u}$ estimated

counts for background u, the predicted number of IBDs is determined by:

$$N^{(b)}_{\mathrm{IBD},i}(\theta_{13},\Delta m^2_{32}) = \frac{N^{(b)}_{\mathrm{cand},i}\left(1+\eta^{(b)}_{N,i}\right) - \sum_u N^{(b)}_{\mathrm{bg},i,u}\left(1+\eta^{(b)}_{B,i,u}\right)}{\epsilon_{\mu,i}\epsilon_{m,i}\epsilon_{p,i}(1+\epsilon_i)\left(1+\eta_{\mathrm{relE},i}\cdot a^{(b)}_{\mathrm{relE},i}(\theta_{13},\Delta m^2_{32})\right)} \times \frac{1}{\left(1+\eta_{\mathrm{IAV},i}\cdot a^{(b)}_{\mathrm{IAV},i}\right)\sum_{d=1}^{4}\left(1+\eta_{\mathrm{NL},d}\cdot a^{(b)}_{\mathrm{NL},i,d}\right)}, \tag{6.4}$$

where $\eta^{(b)}_{N,i}$ and $\eta^{(b)}_{B,i,u}$ are the nuisance parameters for $N^{(b)}_{\mathrm{cand},i}$ and $N^{(b)}_{\mathrm{bg},i,u}$. These represent the fractional variations of their assigned quantities. The relative energy scale is included in the denominator, where the nuisance parameter ($\eta_{\mathrm{relE},i}$) adjusts for the fractional deviation in energy scale compared to the average of all ADs by multiplying by adjusting the spectral distortion resulting from a $1\sigma \sim 0.35\%$ shift in relative energy scale ($a^{(b)}_{\mathrm{relE},i}$). Similarly, the effects of uncertainties in the thicknesses of the IAV and detector nonuniformity are incorporated in the nuisance parameters, $\eta_{\mathrm{IAV},i}$ and $\eta_{\mathrm{NL},d}$, and the 1σ spectral distortions, $a^{(b)}_{\mathrm{IAV},i}$ and $a^{(b)}_{\mathrm{NL},i,d}$, respectively. Four nonlinearity pull curves, identified here by d, were applied for each AD separately, though since the LS and GdLS for of all ADs were the same, only one nuisance parameter was used for each curve for all detectors. The process of applying the effects of these nuisance parameters are detailed in Sec. 6.3. These, as well as the nuisance parameters introduced later, were allowed to vary during the fitting process, with the variations limited by penalty terms, as shown in Eq. 7.5.

$N^{(b)}_{\mathrm{IBD},i}(\theta_{13},\Delta m^2_{32})$ represents the number of IBD interactions in reconstructed prompt energy bin b of AD i, which pass all selection requirements and corrected for the loss of livetime incurred by the muon and multiplicity vetoes. It is corrected for AD-to-AD differences in target proton number, energy scale, and all detection efficiencies.

6.2.2 Converting to True $\overline{\nu}_e$ Energy via Detector Response Matrix

While the reconstructed prompt energy spectra of the near ADs have been corrected for backgrounds and efficiencies, the oscillation probabilities depend on the true $\overline{\nu}_e$ energy spectrum. Therefore, a conversion from reconstructed prompt energy to the true $\overline{\nu}_e$ energy was implemented in the form of a detector response matrix.

Accounting for the energy resolution, calibrations, and the nonlinearities introduced and discussed in Ch. 3, the detector response was built from full Monte Carlo simulation, inputted with an incident $\overline{\nu}_e$ energy spectrum, which was created by weighting the expected reactor $\overline{\nu}_e$ flux spectrum [105, 106] with the differential IBD cross section [108, 109]. This simulation, based on GEANT4 and tuned to correspond to the observed detector response and followed by extensive validations [55], determined the relation between antineutrino and positron energy, accounting for the response of the real detectors. The simulation was tuned to align with measurements of 59 different source and location combinations. This encompassed the effects of the absolute energy scale, liquid scintillator nonlinearity, energy leakage, and energy resolution of the AD [110]. Each simulated event was binned according to the true incoming $\overline{\nu}_e$ energy and the reconstructed prompt energy, shown in Fig. 6.3.

From the detector response matrix (DRM), each slice of the reconstructed energy corresponds to a probability function of the true $\overline{\nu}_e$ energy, which is finely binned in 0.05 MeV wide bins. For reconstructed bin b, the probability of the true $\overline{\nu}_e$ energy, E_{true}, is represented by $f_{\text{DRM}}^{(b)}(E_{\text{true}})$. Examples of the nominal probability distribution functions (PDFs) are provided in Fig. 6.4. These PDFs were then adjusted to incorporate the oscillation effects, therefore making them AD-specific and dependent on both θ_{13} and Δm^2_{32}. These oscillation effects are updated in the fitting process to use the best fit values.

Using the corresponding PDF, $f_{\text{DRM},i}^{(b)}(E_{\text{true}}; \theta_{13}, \Delta m^2_{32})$, a true $\overline{\nu}_e$ energy spectrum was com-

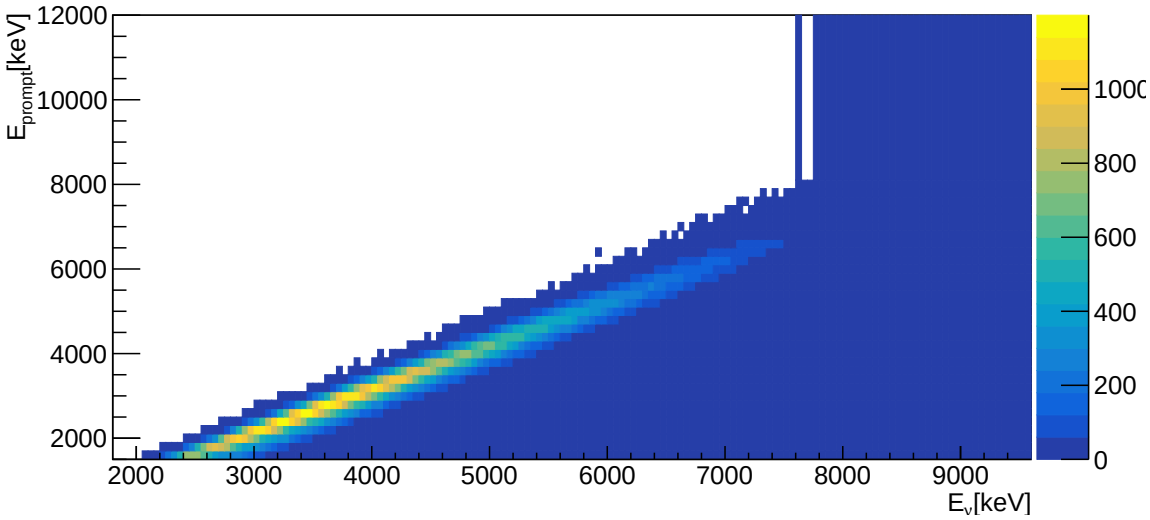

Figure 6.3: Detector response matrix for fitter obtained from simulation. The color represents the number of IBD events in the particular bin.

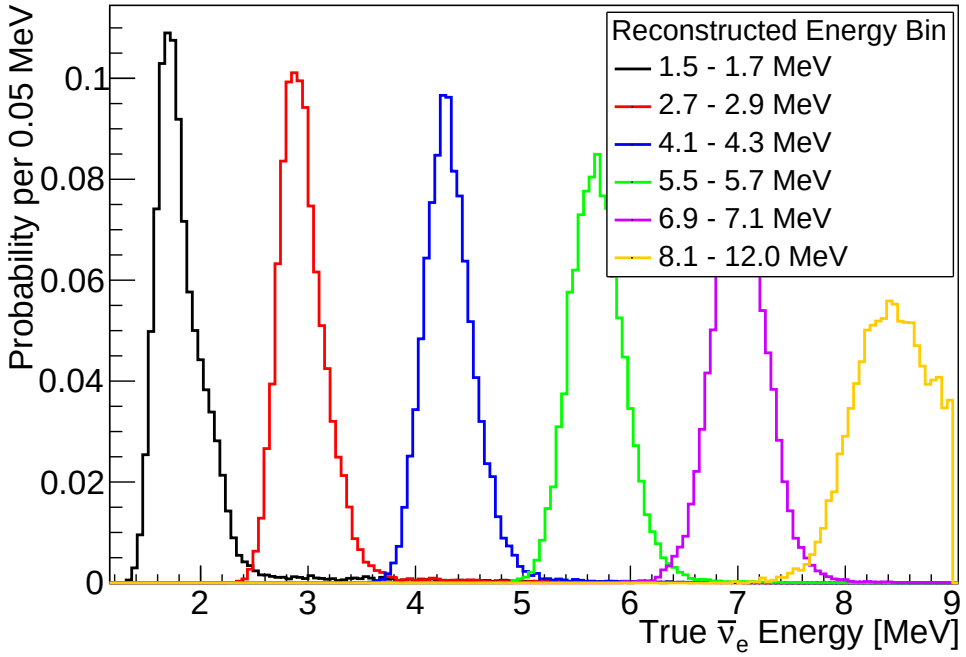

Figure 6.4: Example probability functions $f_{\mathrm{DRM}}^{(b)}(E_{\mathrm{true}})$ for EH1-AD1 produced by the detector response matrix, each function corresponding to a reconstructed energy bin and normalized to one.

puted for the IBD events observed in reconstructed energy bin b of near AD i:

$$N_i^{(b)}(E_{\text{true}}) = N_{\text{IBD},i}^{(b)} \cdot f_{\text{DRM},i}^{(b)}(E_{\text{true}}; \theta_{13}, \Delta m^2_{32}), \tag{6.5}$$

where $N_{\text{IBD},i}^{(b)}$ is the number of IBDs observed in near AD i after subtracting backgrounds and accounting for efficiencies (Sec. 6.2.1).

6.2.3 Distinguishing Individual Core Contributions to Near ADs

With six separate reactor cores producing $\overline{\nu}_e$ detected by the ADs, it is crucial to account for the differences in the contributions of each core and the distances to the ADs so to properly extrapolate to the far hall and determine the oscillation effects. Therefore, for each near AD i, the number of true $\overline{\nu}_e$ in reconstructed energy bin b, $N_i^{(b)}(E)$, needs to be decomposed into the contributions of each reactor core k, $N_{ik}^{(b)}(E)$, such that $\sum_k N_{ik}^{(b)}(E) = N_i^{(b)}(E)$. In order to do this, power and fission fraction information for each core is used alongside the Huber Mueller model to create a ratio, $N_{ik}^{(b)}(E)$ to $N_i^{(b)}(E)$, which is known as the flux fraction. By doing so, the uncertainty in the flux is largely cancelled out. This ratio is computed by comparing the expected $\overline{\nu}_e$ flux from each core, ϕ_{ik} (Eq. 6.2), to the sum of all the reactors, including the $1/L^2$ distance effects of the isotropic $\overline{\nu}_e$ emission and oscillation effects:

$$f_{ik}(E; \theta_{13}, \Delta m^2_{32}) = \frac{\phi_{ik}(E)(1+\alpha_k) P_{\text{sur}}(L_{ik}, E; \theta_{13}, \Delta m^2_{32})/L^2_{ik}}{\sum_l \phi_{il}(E)(1+\alpha_l) P_{\text{sur}}(L_{il}, E; \theta_{13}, \Delta m^2_{32})/L^2_{il}}. \tag{6.6}$$

The sum over l in the denominator represents the total of all six reactor cores. The α parameters represent the fractional uncertainty due to the uncertainty of the reactor power and are included in the fitter as pull parameters. For completeness, the IBD cross section $\sigma_{\text{IBD}}(E)$ should be included in the flux calculation as $\phi \to \sigma_{\text{IBD}}\phi$, however this factor is constant across all cores and ADs and therefore cancels out in the calculation of f_{ik}. It is important to note that the flux fraction is not dependent on the reconstructed energy bin

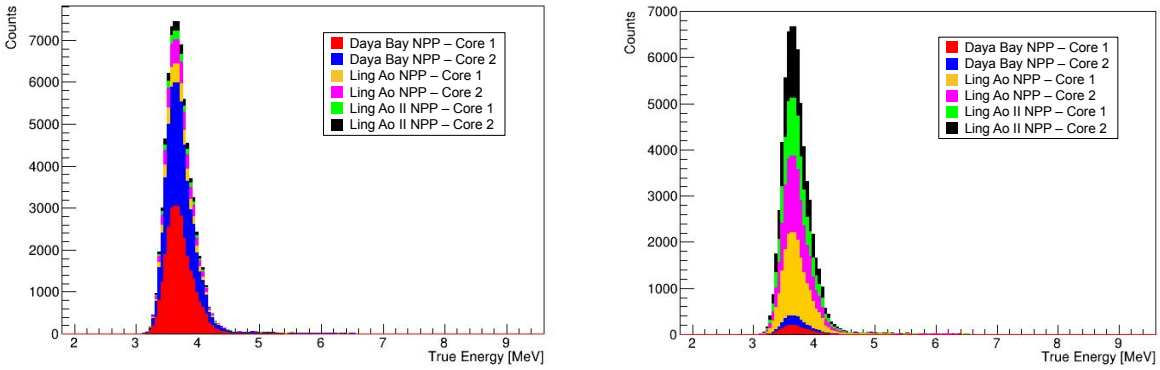

(a) EH1-AD2 (b) EH2-AD1

Figure 6.5: Examples of true $\overline{\nu}_e$ energy spectra decomposed into contributions by each core as measured by EH1-AD2 and EH2-AD1 for the reconstructed energy bin ranging from 2.7 to 2.9 MeV. Determined by the proximity to the separate cores, the majority of the neutrino flux at EH1 is dominated by the Daya Bay reactor cores while at EH2, it is predominately the Ling Ao reactor cores.

b; it only depends on the true $\overline{\nu}_e$ energy. As with the efficiencies of the selection, only the uncorrelated uncertainties between the cores due to the reactor $\overline{\nu}_e$ model affect the relative measurement of θ_{13} and therefore must be accounted for in the fit.

From the flux fraction, the total number of IBDs observed at AD i by $\overline{\nu}_e$ originating from reactor core k is

$$N_{ik}^{(b)}(E) = f_{ik}(E) \times N_i^{(b)}(E). \tag{6.7}$$

Fig. 6.5 presents the true $\overline{\nu}_e$ energy spectra for the same reconstructed energy bin (2.7 to 2.9 MeV) for EH1-AD2 and EH2-AD1, illustrating the difference in contributions by each reactor core as seen by the different near halls. These spectra now enable the ability to predict the far AD spectra.

6.2.4 Extrapolating to Far ADs

The next step for the near-far projection is predicting the number of IBDs at far AD j in reconstructed energy bin b from reactor core k based on the number of events observed in near AD i. The 96 combinations of the six reactor cores, four near ADs and four far ADs each produce ratios comparable to the simple "near-far ratio" presented in Eq. 6.3. These ratios, also known as extrapolation factors, are computed as:

$$e_{j,ik}(E;\theta_{13},\Delta m^2_{32}) = \frac{\phi_{jk}(E)P_{\text{sur}}(L_{jk},E;\theta_{13},\Delta m^2_{32})/L^2_{jk}}{\phi_{ik}(E)P_{\text{sur}}(L_{ik},E;\theta_{13},\Delta m^2_{32})/L^2_{ik}}. \tag{6.8}$$

In contrast to Eq. 6.3, the extrapolation factors account for differences in $\overline{\nu}_e$ exposure and livetime between the ADs (in the ϕ terms as defined in Eq. 6.2), but not for differences in target proton numbers or the detection efficiency differences as these are accounted for in the other steps. Additionally, the uncertainty of reactor flux α introduced in Eq. 6.6 are not included here since the extrapolation factor is calculated for a single reactor core and this uncertainty therefore cancels out.

The number of IBDs at near AD i from reactor core k combined with the extrapolation factor, the predicted count of IBDs at far AD j for the same reconstructed energy bin b is given by:

$$F^{(b)}_{j,ik}(E;\theta_{13},\Delta m^2_{32}) = e_{j,ik}(E;\theta_{13},\Delta m^2_{32}) \times N^{(b)}_{ik}(E;\theta_{13},\Delta m^2_{32}). \tag{6.9}$$

A simple summation of the prediction for each reactor core produces the prediction of total number of IBDs at far AD j based on observations at near AD i:

$$F^{(b)}_{j,i}(E;\theta_{13},\Delta m^2_{32}) = \sum_k F^{(b)}_{j,ik}(E;\theta_{13},\Delta m^2_{32}). \tag{6.10}$$

6.2.5 Translating Back to Prompt Energy Spectrum

At this point of the near-far projection, the true $\overline{\nu}_e$ energy spectra for far AD j based on observations at near AD i were independently predicted for each bin of reconstructed prompt energy b: $F_{j,i}^{(b)}(E)$. Prior to comparing the predictions to the observed spectra at the far ADs, the predictions must be converted back to the reconstructed energy. Because each predicted true $\overline{\nu}_e$ spectrum originated from a single reconstructed prompt energy bin b, these predictions still correspond to the same reconstructed bin in the far ADs. This relies on the assumption that the ADs are identical, with only minor differences between them, which is reasonable for this experiment as determined through all the calibrations and validations.

Therefore, the PDF method removed the need to invert the detector response matrix, and the predicted spectrum $F_{j,i}^{(b)}(E)$ corresponds to predicted IBDs in the reconstructed energy bin b:

$$F_{j,i}^{(b)}(\theta_{13}, \Delta m^2_{32}) = \sum_E F_{j,i}^{(b)}(E; \theta_{13}, \Delta m^2_{32}). \tag{6.11}$$

6.2.6 Far AD Backgrounds and Efficiencies

The final step before comparing to the observed counts at far AD j is to incorporate the efficiencies and backgrounds into the prediction. Therefore, the predicted number of counts for far AD j from the observed counts at near AD i for reconstructed energy bin b, $F_{j,i}^{(b)}(\theta_{13}, \Delta m^2_{32})$, needs to be corrected as such:

$$\begin{aligned} F_{\text{pred},j,i}^{(b)}(\theta_{13}, \Delta m^2_{32}) =& F_{j,i}^{(b)}(\theta_{13}, \Delta m^2_{32}) \epsilon_{\mu,j} \epsilon_{m,j} \epsilon_{p,j} (1+\epsilon_j) \left[1 + \eta_{\text{relE},j} \cdot a_{\text{relE},j}^{(b)}(\theta_{13}, \Delta m^2_{32})\right] \\ & \times \left(1 + \eta_{\text{IAV},j} \cdot a_{\text{IAV},j}^{(b)}\right) \sum_{d=1}^{4} \left(1 + \eta_{\text{NL},d} \cdot a_{\text{NL},j,d}^{(b)}\right) \\ & + \sum_{u \in \text{backgrounds}} N_{\text{bg},j,u}^{(b)} (1 + \eta_{B,j,u}). \end{aligned} \tag{6.12}$$

As in Eq. 6.4, the effects of the differences in energy scales, IAV thicknesses, and nonlinearity uncertainties are included as the 1σ spectrum shifts $a^{(b)}_{\text{relE},}j$, $a^{(b)}_{\text{IAV},j}$, and $a^{(b)}_{\text{NL},j,d}$, and the corresponding pull terms $\eta_{\text{relE},}j$, $\eta_{\text{IAV},j}$, and $\eta_{\text{NL},d}$, respectively.

While this is comparable to the observations at the far ADs, these predictions are produced from each near AD i. Therefore, to make a single prediction for comparison to observation, the four predictions from the near ADs are averaged into a single prediction for each far AD.

6.2.7 Prediction Summary

Combining Eqs. 6.4-6.12, the predicted number of events for reconstructed energy bin b of far AD j based on the observations of near AD i can be written in a singular formula:

$$
\begin{aligned}
F^{(b)}_{\text{pred },j,i}\left(\theta_{13},\Delta m^2_{32}\right) = \Bigg\{ & \left[N^{(b)}_{\text{cand },i}\left(1+\eta^{(b)}_{N,i}\right) - \sum_{u\in\text{backgrounds}} N^{(b)}_{\text{bg},i,u}\left(1+\eta_{B,i,u}\right)\right] \\
& \times \frac{\varepsilon_{\mu,j}\varepsilon_{m,j}\varepsilon_{p,j}\left(1+\epsilon_j\right)\left[1+\eta_{\text{relE},j}\cdot a^{(b)}_{\text{relE},j}\left(\theta_{13},\Delta m^2_{32}\right)\right]}{\varepsilon_{\mu,i}\varepsilon_{m,i}\varepsilon_{p,i}\left(1+\epsilon_i\right)\left[1+\eta_{\text{relE},i}\cdot a^{(b)}_{\text{relE},i}\left(\theta_{13},\Delta m^2_{32}\right)\right]} \\
& \times \frac{\left(1+\eta_{\text{IAV},j}\cdot a^{(b)}_{\text{IAV},j}\right)\sum_{d=1}^{4}\left(1+\eta_{\text{NL},d}\cdot a^{(b)}_{\text{NL},j,d}\right)}{\left(1+\eta_{\text{IAV},i}\cdot a^{(b)}_{\text{IAV},i}\right)\sum_{d=1}^{4}\left(1+\eta_{\text{NL},d}\cdot a^{(b)}_{\text{NL},i,d}\right)} \\
& \times \sum_{E,k}\Bigg[\frac{\phi_{ik}(E)\left(1+\alpha_k\right)P_{\text{sur}}\left(L_{ik},E;\theta_{13},\Delta m^2_{32}\right)/L^2_{ik}}{\sum_l \phi_{il}(E)\left(1+\alpha_l\right)P_{\text{sur}}\left(L_{il},E;\theta_{13},\Delta m^2_{32}\right)/L^2_{il}} \\
& \qquad \times \frac{\phi_{jk}(E)P_{\text{sur}}\left(L_{jk},E;\theta_{13},\Delta m^2_{32}\right)/L^2_{jk}}{\phi_{ik}(E)P_{\text{sur}}\left(L_{ik},E;\theta_{13},\Delta m^2_{32}\right)/L^2_{ik}} \times f^{(b)}_{\text{DRM},i}(E)\Bigg]\Bigg\} \\
& \qquad\qquad + \sum_{u\in\text{backgrounds}} N^{(b)}_{\text{bg},j,u}\left(1+\eta_{B,j,u}\right),
\end{aligned}
\tag{6.13}
$$

where η, ϵ, and α represent pull parameters for model input uncertainties including statistical uncertainty of near AD observations, background estimates, and efficiencies. The oscillation effects exist primarily within the survival probability P_{sur} factors in the the flux fraction and extrapolation factor terms, with smaller effects arising from the relative energy scale

uncertainty a_{relE}. As mentioned in Sec. 6.2.1, the effects of the prompt energy cut are incorporated in the implementation of the other corrections, and therefore, the corresponding absolute efficiencies are equal across all ADs and cancel in this ratio.

Notably, the denominator of the extrapolation factor is equivalent to the numerator of the flux fraction term, excluding the reactor power uncertainty, and therefore does not influence the final prediction. This results in a reduced dependence on the reactor prediction ϕ model compared to the approaches where the prediction is directly compared to the observation in all sites, further exploiting the relative near-far experimental design.

6.3 Pull Curves and Nuisance Parameters

Several nuisance parameters are included in the fitter as pull terms to account for the uncertainties of the inputs. These pulls affect the number of events in each bin allowing them to tweak the number of counts and, for several of them, the spectra.

The reactor power, detection efficiency, and background rate pulls are applied as scale factors in the fitting process, as they do not affect the spectral shape. Specifically with regards to the reactors, the power plants provide the reactor information, including uncertainties in both the total power and the fission fractions. The fission fraction affects the spectra directly, while the power determines the total rate. With the near-far projection method, the spectra obtained by the near ADs is extrapolated to the far predictions, and therefore the reactor spectrum uncertainty is essentially negligible in the fit. This leaves the reactor power uncertainty, which is applied as a simple scale factor to the energy spectrum.

Additionally, the relative energy scale, nonlinearity (due to the absolute energy scale), and IAV thickness uncertainty pulls affect rate and shape of the spectra. For these, Monte Carlo simulations were used to determine the spectra for $\pm 1\sigma$ of each uncertainty individually, as

demonstrated in Fig. 6.6. These spectra were then compared to the nominal to quantify the effect of each bin i:

$$V_i = \frac{N_{\text{pull},i}}{N_{\text{nom},i}} - 1, \tag{6.14}$$

where $N_{\text{pull},i}$ and $N_{\text{nom},i}$ represent the bin content in the pulled and nominal spectra, respectively, to determine the pull value for the i-th bin V_i. These are referred to as the "pull curves". Fig. 6.7 shows the pull curves for all three cases.

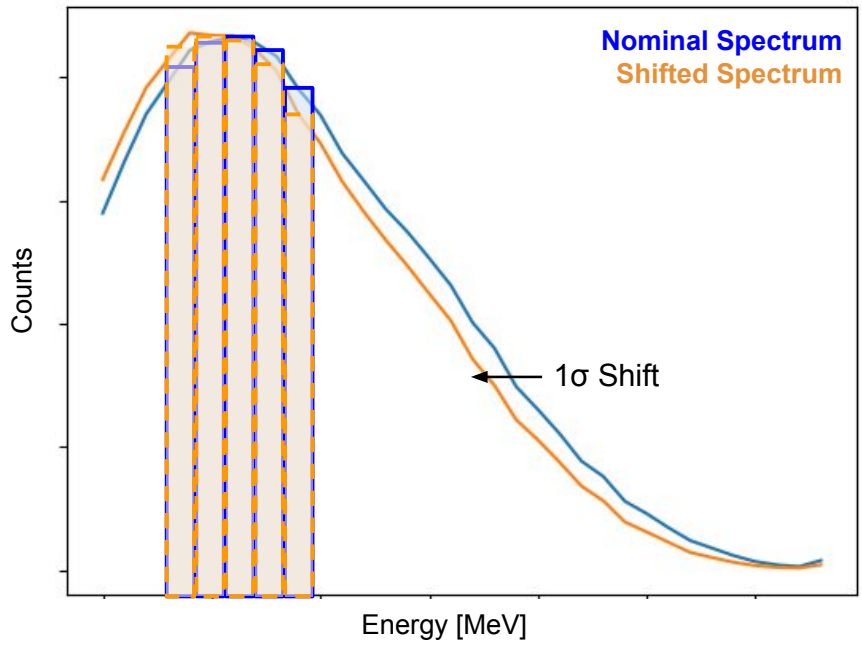

Figure 6.6: Cartoon of the nominal spectrum (blue) and the shifted spectrum by the 1σ uncertainty of a systematic (orange), highlighting the change in counts of each bin due to this shift.

In the fit, the nuisance parameter is a singular value which determines the size of the change, then scales the pull curves and adjusts the spectrum via:

$$N_{\text{pull},i} = N_{\text{meas},i}\,(1 + \eta V_i)\,, \tag{6.15}$$

where η is the nuisance parameter used in the fit (discussed in detail in Ch. 7) which adjusts

the measured counts, $N_{\mathrm{meas},i}$, to obtain the pulled counts, $N_{\mathrm{pull},i}$. Not only does this method adjust the shape, but it also accounts for net changes in the number of events resulting from the prompt energy cut: each bin is independently adjusted according to the difference in events it contains as determined with the simulation without the prompt energy cut. Therefore, no additional correction needs to be applied for the prompt energy cut efficiency uncertainty.

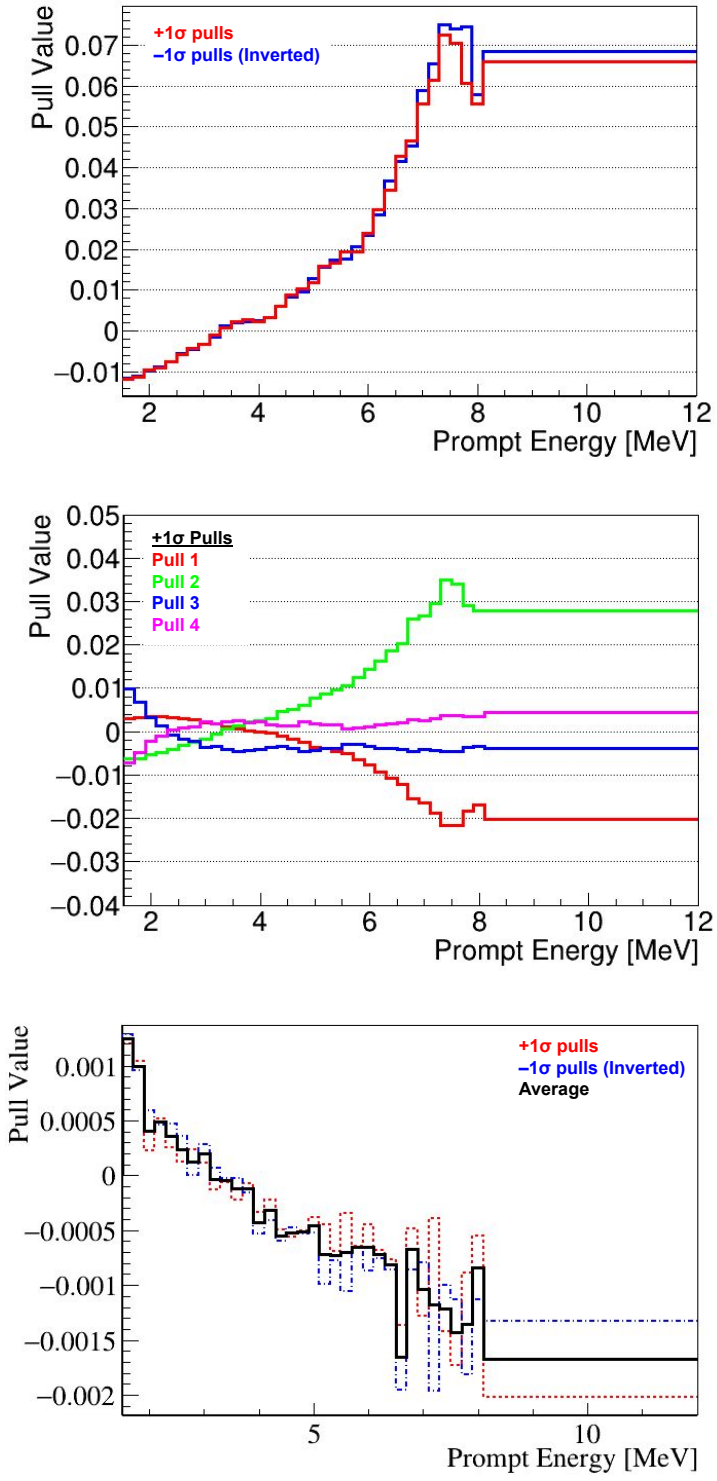

Figure 6.7: Pull curves associated to 1σ shift in relative energy scale (top), nonlinearity (middle), and IAV thickness (bottom).

Chapter 7

Fitter Measurement

Provided with the data at both the near and far ADs, the fitter compares the observations at the far ADs to the prediction based on the near ADs, as described in Ch. 6. The fit can be performed either as "rate-only" or "rate+shape". The rate-only method compares the total number of counts for both the observed and predicted values. Alternatively, the rate+shape fit incorporates the spectral information by comparing observation and prediction for each energy bin separately. While the rate-only method requires a prior on Δm^2_{32}, the rate+shape approach measures this parameter from the energy dependence of the disappearance.

In addition to fitting Δm^2_{32} for both the normal and inverted mass ordering cases, the data is fit with an expression for the disappearance probability that depends on a single model-independent frequency, Δm^2_{ee}, which is defined by [111]:

$$P_{ee} = 1 - \sin^2(2\theta_{13}) \sin^2\left(\Delta m^2_{ee} \frac{L}{4E}\right) - \cos^4\theta_{13} \sin^2(2\theta_{12}) \sin^2\left(\Delta m^2_{21} \frac{L}{4E}\right). \tag{7.1}$$

This form allows for interpretation under either mass ordering as well as in frameworks with more than three neutrinos. The results are presented in all three forms, however many of the checks presented in this chapter focused on the Δm^2_{ee} parameter.

Sec. 7.1 introduces the statistical methods for determining the best-fit results for this analysis. Sec. 7.3 presents the results obtained by this analysis. Discussion, along with a couple of studies on the effects of varying the DT cut value and its uncertainty, are presented in Sec. 7.2.

7.1 Statistical Method

To compare the data and the 3-flavor neutrino oscillation model, Daya Bay's analyses implement standard frequentist techniques to evaluate the best fit and goodness-of-fit. This analysis utilizes a χ^2 expression with pull parameters, as has been done in previous Daya Bay oscillation analyses (both nH and nGd) and absolute reactor $\overline{\nu}_e$ flux and spectral measurements [57, 92, 110, 112].

For particular values of the oscillation and pull parameters, the fitter compares the observed $\overline{\nu}_e$ candidates in the four far ADs to the prediction based on the observations at the near ADs. The χ^2 used in determining the goodness-of-fit is made up of statistical and systematic components:

$$\chi^2(\boldsymbol{\theta};\boldsymbol{\eta}) = \chi^2_{\text{stat}}(\boldsymbol{\theta};\boldsymbol{\eta}) + \chi^2_{\text{sys}}(\boldsymbol{\eta}). \tag{7.2}$$

Here, the model parameters of interest are represented by $\boldsymbol{\theta}$, while $\boldsymbol{\eta}$ is the set of remaining pull parameters. In the fitting process, the values for both $\boldsymbol{\theta}$ and $\boldsymbol{\eta}$ are varied in order to minimize Eq. 7.2 and obtain the best-fit values for the parameters of interest. The full χ^2 expressions for both the rate-only and rate+shape fitting modes are detailed in Sec. 7.1.1 and 7.1.2.

The statistical term, χ^2_{stat}, uses the maximum likelihood for Poisson-distributed data since it more accurately reflects the variations in the number of events, particularly bins with smaller

number of events. Hence, it takes the form of

$$\chi^2_{\text{stat}}(\boldsymbol{\theta};\boldsymbol{\eta}) = 2\sum_{i=1}^{n}\left(F_{\text{pred},i}(\boldsymbol{\theta};\boldsymbol{\eta}) - F_{\text{obs},i} + F_{\text{obs},i}\ln\frac{F_{\text{obs},i}}{F_{\text{pred},i}(\boldsymbol{\theta};\boldsymbol{\eta})}\right), \tag{7.3}$$

as expressed by Eq. 40.16 of [34], where $F_{\text{obs},i}$ and $F_{\text{pred},i}$ are the observed and predicted counts, respectively, for the i-th data point.

On the other hand, the systematic term only depends on the pull parameters, which are dimensionless quantities representing the relative deviation from an associated physical quantity A_j, such as background rates or detection efficiency. The values of A_j remain constant during the fitting procedure, though the pull parameters tune the contribution to the fit by:

$$A_j \to (1+\eta_j)A_j. \tag{7.4}$$

These values are constrained by the relative uncertainty, $\tilde{\sigma}^2_{\eta,j}$, which limits the allowable values of η_j:

$$\chi^2_{\text{sys}}(\boldsymbol{\eta}) = \sum_j \frac{\eta_j^2}{\tilde{\sigma}^2_{\eta,j}}. \tag{7.5}$$

These pull parameters are therefore required to be small compared to the associated uncertainties, since larger values increase the χ^2_{sys} term. A non-zero η_j best-fit result indicates a preference for a deviated value over the estimated value of the physical quantity A_j. The pull parameters implemented in the fitter are summarized in Tab. 7.1. All pull parameters are applied consistently between the rate-only and rate+shape fitting methods, except for the pull term associated with Δm^2_{32}. For rate+shape, Δm^2_{32} is one of the free parameters and therefore does not get a pull parameter.

The reactor power and fission fraction information was provided by the power plant on a weekly basis. The detection efficiency is the combination of the individual uncertainties from Ch. 4, less the prompt energy cut efficiency as explained in Ch. 6.2. The relative energy

Table 7.1: Summary of systematic uncertainties and corresponding pull terms. All pull terms are implemented consistently between rate-only and rate+shape fitting methods, with the exception of the Δm^2_{32} pull parameter, since Δm^2_{32} is fit in the rate+shape method and therefore does not use a pull term.

Systematic	Symbol	Relative Uncertainty	# of Pull Terms
Reactor power	$\boldsymbol{\alpha}$	0.8%	6 (1 per core)
Reactor spectrum[1]	–	negligible	–
Detection efficiency[2]	$\boldsymbol{\epsilon}$	0.35%	8 (1 per AD)
Relative energy scale[3]	$\boldsymbol{\eta}_{\mathrm{relE}}$	0.35%	8 (1 per AD)
All other detector response[1]	–	negligible	–
Absolute energy scale [NL]	$\boldsymbol{\eta}_{\mathrm{NL}}$	$< 1\%$	4
IAV thickness	$\boldsymbol{\eta}_{\mathrm{IAV}}$	1%	8 (1 per AD)
Accidental background rate	$\boldsymbol{\eta}_{\mathrm{B}}^{(\mathrm{acc})}$	0.038% to 0.053%	8 (1 per AD)
^{9}Li/^{8}He background rate	$\boldsymbol{\eta}_{\mathrm{B}}^{(\mathrm{Li9})}$	36.8% to 38.7%	3 (1 per EH)
Fast neutron background rate	$\boldsymbol{\eta}_{\mathrm{B}}^{(\text{fast n})}$	5.08% to 11.76%	3 (1 per EH)
^{241}Am-^{13}C background rate	$\boldsymbol{\eta}_{\mathrm{B}}^{(\text{Am-C})}$	50%	1
Radiogenic neutron background rate	$\boldsymbol{\eta}_{\mathrm{B}}^{(\text{rad-n})}$	20%	8 (1 per AD)
Near AD statistical uncertainty	$\boldsymbol{\eta}_{\mathrm{N}}$	$1/\sqrt{N^{(b)}_{\mathrm{cand},i}}$	136 (1 per bin per near AD)
Input mixing parameters	$\boldsymbol{\eta}_{\mathrm{osc}}$	2.4% for Δm^2_{21} 2.6% for θ_{12} 2.8% for Δm^2_{32}	1 1 1 for rate-only

[1]Through to the bin-by-bin near-far projection method, the uncertainties in the reactor spectrum are negligible in this analysis.
[2]Includes ΔT_p, excludes prompt-energy cut efficiency.
[3]Accounts for the prompt-energy cut efficiency.

scale uncertainty was calculated as half the spread of the delayed energy peaks (Fig. 4.10), while the absolute energy scale/nonlinearity and IAV thickness uncertainties were taken from Ref. [61]. Finally, the uncertainties of the background rates are detailed in Sec. 5.1-5.2.

The best fit (minimum) χ^2 distribution of repeated hypothetical experiments is expected to follow a χ^2 distribution with the corresponding number of degrees of freedom:

$$\mathrm{NDF} = n - \mathrm{len}(\boldsymbol{\theta}), \tag{7.6}$$

where n is the number of data points and len($\boldsymbol{\theta}$) is the number of free parameters of $\boldsymbol{\theta}$.

To minimize Eq. 7.2, the `optimize.least_squares` function from the SciPy Python package was implemented, which utilizes the Trust Region Reflective algorithm [113, 114]. The following sections detail the specifics of χ^2 for both the rate-only and rate+shape fits.

7.1.1 Rate-Only

For the rate-only fitting method, the fitter tunes the pull parameters to best fit the total number of observed events in each of the four far ADs. This means there are only four data points for the rate-only analysis:

$$\mathbf{F}_{\text{obs}} = (F^{\text{obs}}_{\text{EH3-AD1}}, F^{\text{obs}}_{\text{EH3-AD2}}, F^{\text{obs}}_{\text{EH3-AD3}}, F^{\text{obs}}_{\text{EH3-AD4}}). \tag{7.7}$$

Correspondingly, the prediction also must have four components:

$$\mathbf{F}_{\text{pred}}(\boldsymbol{\theta};\boldsymbol{\eta}) = (F^{\text{pred}}_{\text{EH3-AD1}}(\boldsymbol{\theta};\boldsymbol{\eta}), F^{\text{pred}}_{\text{EH3-AD2}}(\boldsymbol{\theta};\boldsymbol{\eta}), F^{\text{pred}}_{\text{EH3-AD3}}(\boldsymbol{\theta};\boldsymbol{\eta}), F^{\text{pred}}_{\text{EH3-AD4}}(\boldsymbol{\theta};\boldsymbol{\eta})). \tag{7.8}$$

The predicted values are determined by the process described in Sec. 6.2. For the rate-only analysis, the individual reconstructed energy bins of each far AD j are summed to obtain the total number of predicted events based on a single near AD i:

$$F_{\text{pred},j,i}(\boldsymbol{\theta};\boldsymbol{\eta}) = \sum_b F^{(b)}_{\text{pred},j,i}(\boldsymbol{\theta};\boldsymbol{\eta}). \tag{7.9}$$

The four near AD predictions are then averaged together for a single prediction for each far AD j:

$$F_{\text{pred},j}(\boldsymbol{\theta};\boldsymbol{\eta}) = \frac{1}{4}\sum_i F_{\text{pred},j,i}(\boldsymbol{\theta};\boldsymbol{\eta}). \tag{7.10}$$

A simple unweighted average was sufficient for combining the predictions of the near ADs as they were highly consistent with one another and implementing weights based on the livetimes of the near ADs would not significantly impact the final result.

The prediction, $\mathbf{F}_{\text{pred}}(\boldsymbol{\theta};\boldsymbol{\eta})$, is based on the oscillation parameters and the quantities measured by the experiment. These measurements include the observed number of events in the near ADs, and reactor power and fission fractions, as well as background rates, detection efficiencies, the conversion between reconstructed prompt energy and the true $\overline{\nu}_e$ energy. For the rate-only analysis, the parameter of interest and the pull parameters associated with the fit are:

$$\begin{aligned}\boldsymbol{\theta} &= (\theta_{13}) \\ \boldsymbol{\eta} &= (\boldsymbol{\alpha}, \boldsymbol{\epsilon}, \boldsymbol{\eta}_{\text{relE}}, \boldsymbol{\eta}_{\text{B}}, \boldsymbol{\eta}_{\text{N}}, \boldsymbol{\eta}_{\text{NL}}, \boldsymbol{\eta}_{\text{osc}}).\end{aligned} \tag{7.11}$$

The pull parameters are grouped according to the uncertainties to which they correspond: $\boldsymbol{\alpha}$ for reactor $\overline{\nu}_e$ flux, $\boldsymbol{\epsilon}$ for detection efficiency (minus the relative energy scale), $\boldsymbol{\eta}_{\text{relE}}$ for the relative energy scale, $\boldsymbol{\eta}_{\text{NL}}$ for the scintillator nonlinearity, $\boldsymbol{\eta}_{\text{B}}$ for the background rates, $\boldsymbol{\eta}_{\text{N}}$ for the near AD statistics, and $\boldsymbol{\eta}_{\text{osc}}$ for the other oscillation parameters of the 3-neutrino oscillation model (θ_{12}, Δm^2_{21}, and Δm^2_{32}). Sec. 6.3 describes how these pulls affect the spectra and the fit.

For the rate-only measurement, the statistical contribution to the χ^2 calculation follows Eq. 7.3, where each AD enters the sum once:

$$\chi^2_{\text{stat}}(\theta_{13};\boldsymbol{\eta}) = 2 \sum_{\substack{j\in \\ \text{far ADs}}} \left(F_{\text{pred},j}(\theta_{13};\boldsymbol{\eta}) - F_{\text{obs},j} + F_{\text{obs},j} \ln \frac{F_{\text{obs},j}}{F_{\text{pred},j}(\theta_{13};\boldsymbol{\eta})} \right), \tag{7.12}$$

while the systematic term is expressed by:

$$\chi^2_{\text{sys}}(\theta_{13};\boldsymbol{\eta}) = \sum_{\substack{r\in\\ \text{reactors}}} \frac{\alpha_r^2}{\tilde{\sigma}_R^2} + \sum_{\substack{d\in\\ \text{all ADs}}} \left(\frac{\epsilon_d^2}{\tilde{\sigma}_D^2} + \frac{\eta^2_{\text{relE},d}}{\tilde{\sigma}^2_{\text{relE}}} + \frac{\eta^2_{\text{IAV},d}}{\tilde{\sigma}^2_{\text{IAV}}} + \sum_{\substack{u\in\text{bg.}\\ \text{sources}}} \frac{\eta^2_{\text{B},d,u}}{\tilde{\sigma}^2_{\text{B},d,u}} \right) + \sum_{\substack{i\in\\ \text{near ADs}}} \sum_{b\in\text{bins}} \left(\frac{\eta^{(b)}_{\text{N},i}}{\tilde{\sigma}^{(b)}_{\text{obs},i}} \right)^2 + \sum_{\substack{w\in\\ \text{NL pulls}}} \frac{\eta^2_{\text{NL},w}}{\tilde{\sigma}^2_{\text{NL},w}} + \frac{\eta^2_{\theta_{12}}}{\tilde{\sigma}^2_{12}} + \frac{\eta^2_{\Delta m^2_{21}}}{\tilde{\sigma}^2_{21}} + \frac{\eta^2_{\Delta m^2_{32}}}{\tilde{\sigma}^2_{32}}. \tag{7.13}$$

Rate-Only Validations

The rate-only performance of the fitter was initially evaluated using simulated data sets with known values of θ_{13}, presented in Sec. 6.3.1 of Ref. [70]. To summarize, the fitter's performance was assessed on simulated data sets both with and without statistical and systematic fluctuations. These test data sets were generated using a code entirely independent of the fitter using the same procedure which has been tested and used for the nGd analysis: using the Huber [105] and Mueller [106] spectra, the IBD cross-section and detector response effects were applied, then the backgrounds were included. 36 data sets with unique pairs of (θ_{13}, Δm^2_{ee}) were used for the study without fluctuations (the inputted Δm^2_{ee} gets converted to Δm^2_{32} internally). Additionally, fluctuations were included in a simulated data sample of 190 data sets for 9 of these parameter combinations (1710 total data sets). 66% of the fits of the fluctuated data sets returned a mean $\sin^2(2\theta_{13})$ value within ± 1 standard error of the truth value of the simulation, illustrating the statistical consistency of the fitter and the simulation. Fig. 7.1 shows the results obtained from the 1710 simulated data sets with statistical and systematic fluctuations.

Another validation of the rate-only fitter was to compare the distribution of χ^2_{min} of the 1710 simulated data sets to the expected χ^2_{min} distribution with three degrees of freedom since

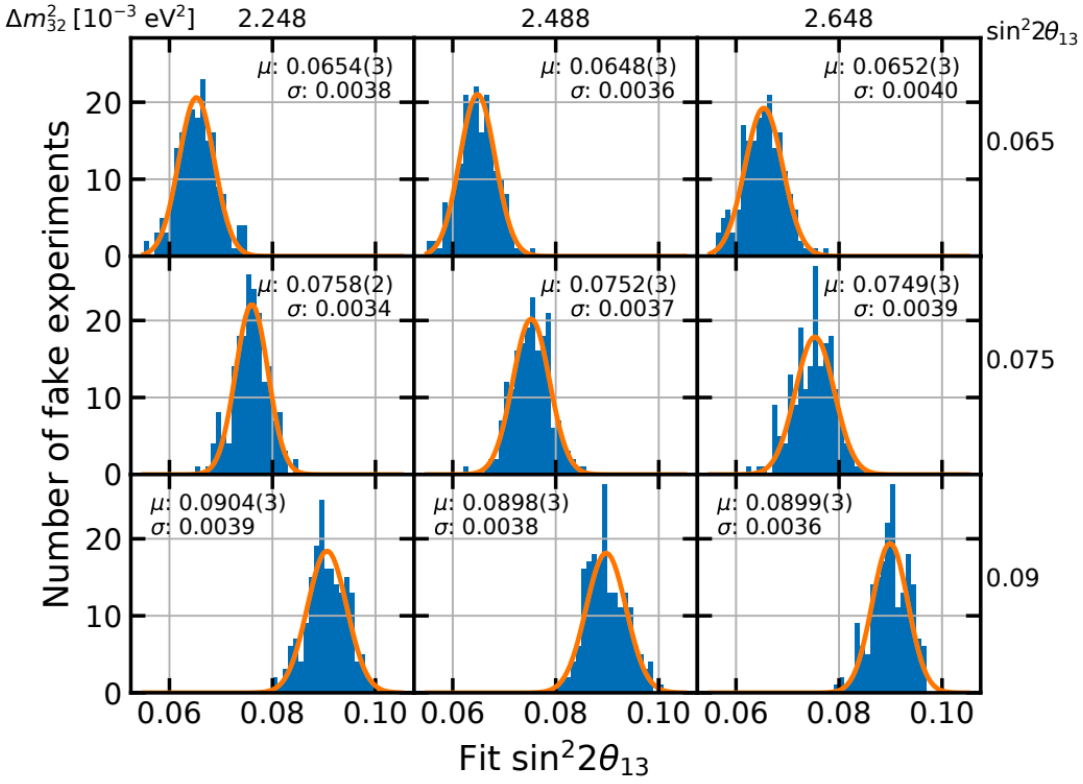

Figure 7.1: Initial results of rate-only fits of 1710 simulated data sets (190 data sets for each of the 9 combinations of $\sin^2(2\theta_{13})$ and Δm^2_{32}) with statistical and systematic fluctuations (Fig. 6.6 in [70]). Each row shares a true $\sin^2(2\theta_{13})$, while each column shares a true Δm^2_{32}. The best-fit Gaussian distribution for each sample is shown in orange. The mean μ and standard deviation σ for each sample is provided for each, with the standard error of the mean indicated in parentheses as the uncertainty in the final digit.

the fit was done on one bin for each far AD with one parameter being fit, θ_{13}. With all pull parameters fixed at 0, the extracted spectrum matched the distribution predicted from theory [70]. With the pull terms, the χ^2_{min} spectrum shifted to lower values, which was due to pull parameters related to the AD-to-AD variation: The near AD observations, with pulls applied, predict the far AD spectra to be compared to the far observations. This means that adjusting the near AD pull parameters affects both the near and far spectra, in addition to the far AD pulls' effect on the spectra. The shift in the χ^2_{min} spectra shown in Fig. 7.2 was attributed to this explanation [70].

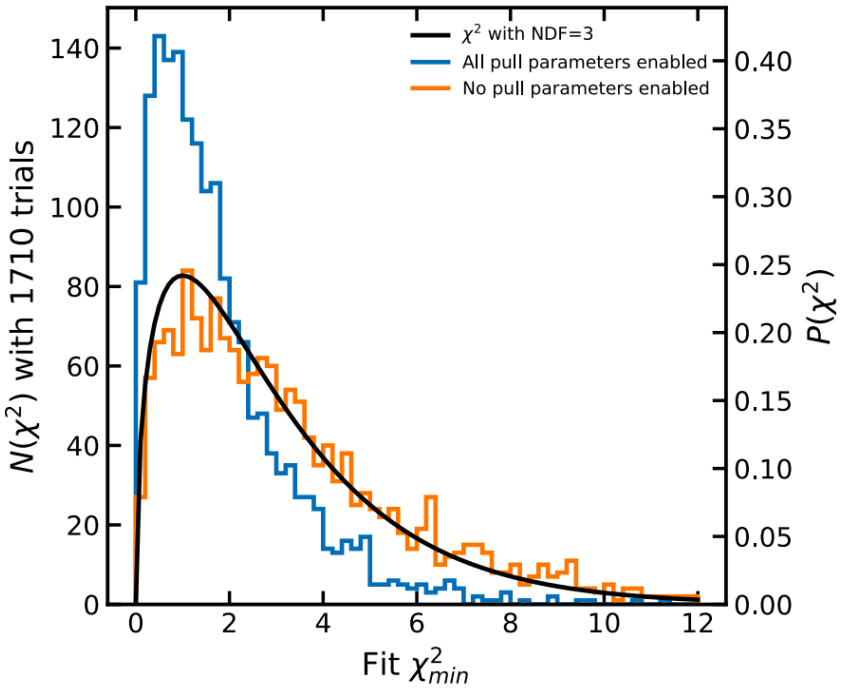

Figure 7.2: χ^2_{min} distributions for the rate-only fits of 1710 simulated data sets (Fig. 6.7 in [70]). The orange histogram shows the spectrum with all pull parameters disabled (fixed at 0), which matches the theoretical prediction for 3 degrees of freedom (black curve). The blue spectrum corresponds to the results with all pull parameters enabled, which has a lower mean than is expected with 3 degrees of freedom.

Following some minor modifications to the fitter, an additional round of validations were done, which was comprised of two sets of toy Monte Carlo simulations without statistical or systematic fluctuations. The first set consisted of 20 points with $\sin^2(2\theta_{13})$ values spanning from 0.005 to 0.1, which were produced with an independent code originally designed for the nGd analysis which was modified to simulate nH events. In addition to changing the binning, the detector response and backgrounds were updated to correspond to the nH selection. The fitted values were within 0.05% of the inputted value with χ^2_{min} values consistently around 3.5×10^{-8}, as presented in Fig. 7.3. The second test was conducted on 9 simulated toy Monte Carlo data sets by the parallel analysis. Compared to the $\sin^2(2\theta_{13})$ uncertainty of 0.007 of both this and the parallel analysis [61], all fitted results were within $\pm 0.1\sigma_{\text{rate}}$ from the truth value of the simulation, as shown in Fig. 7.4 [115]. Furthermore, these fits did not

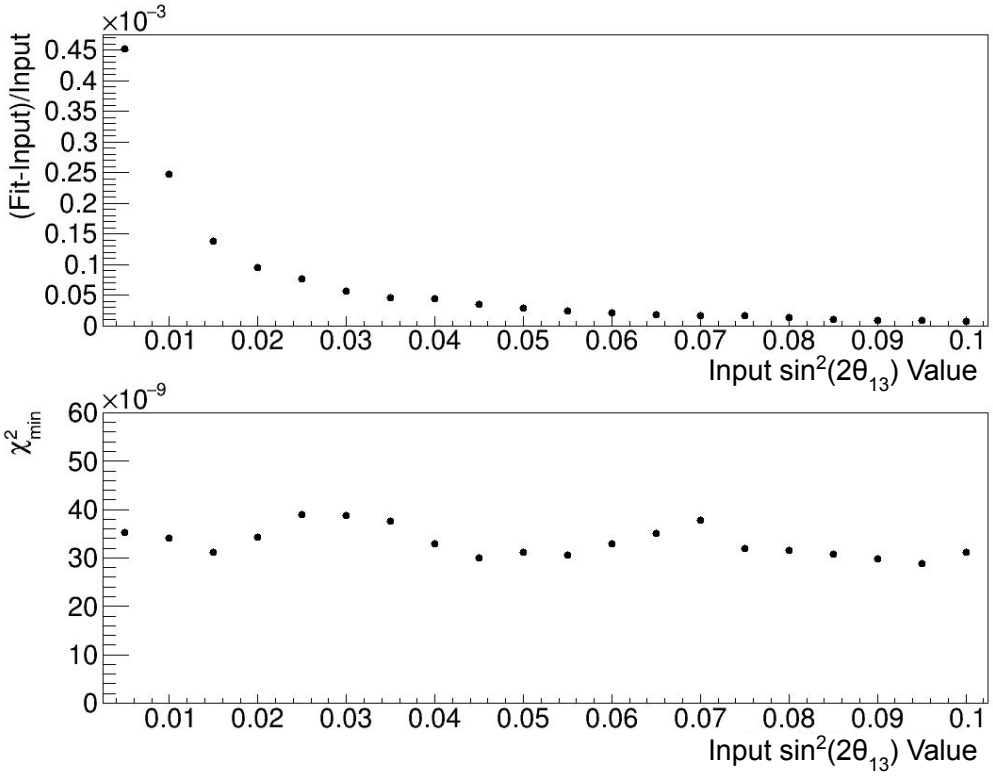

Figure 7.3: Rate-only fit results of 20 toy Monte Carlo data sets produced in house. The difference between the fit result and the inputted value (top) for all points is less than 0.05%, with values around 0.002% closer to the value of $\sin^2(2\theta_{13})$ as measured by other analyses. The χ^2_{min} values are consistently around 3.5×10^{-8}.

experience a bias compared to the truth. Additionally, the χ^2_{min} for all fits were less than 0.002.

7.1.2 Rate+Shape

The rate+shape analysis follows the same idea as the rate-only analysis, except the energy spectral shape is also accounted for. In contrast to Eq. 7.11, the rate+shape analysis includes Δm^2_{32} in the parameters of interest, instead of in the oscillation pull parameters $\boldsymbol{\eta}_{\text{osc}}$:

$$\begin{aligned} \boldsymbol{\theta} &= (\theta_{13}, \Delta m^2_{32}) \\ \boldsymbol{\eta} &= (\boldsymbol{\alpha}, \boldsymbol{\epsilon}, \boldsymbol{\eta}_{\text{relE}}, \boldsymbol{\eta}_{\text{B}}, \boldsymbol{\eta}_{\text{N}}, \boldsymbol{\eta}_{\text{NL}}, \boldsymbol{\eta}_{\text{osc}}). \end{aligned} \tag{7.14}$$

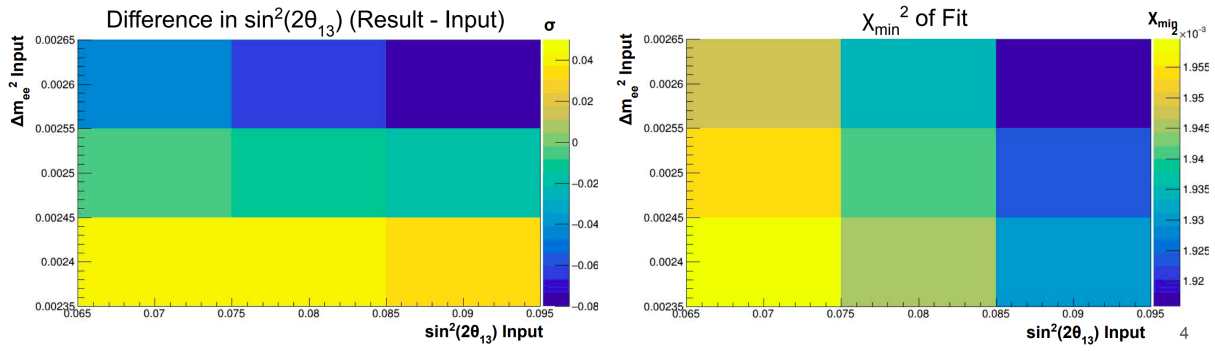

Figure 7.4: Left: Difference between the rate-only $\sin^2(2\theta_{13})$ fit results and the true input values of 9 non-fluctuated simulated data sets produced by the parallel analysis. All results were within $\pm 0.1\sigma_{\text{rate}}$, where $\sigma_{\text{rate}} = 0.007$ is the total uncertainty of [61]. Right: χ^2_{min} from each of the rate-only fits, all had values less than 0.002. Figures from [115].

As mentioned in Sec. 7.1, the fit compares the observation at the far ADs with the prediction from the near ADs for every reconstructed prompt energy bin. The reconstructed prompt energy spectrum is made of 0.2 MeV wide bins from 1.5 to 8.1 MeV with one additional bin extending from 8.1 to 12 MeV. Therefore, each of the four rate-only data points in Eq. 7.7 is replaced with a vector with 34 data points, each corresponding to an individual bin:

$$\mathbf{F}_{\text{obs}} = (\boldsymbol{F}^{\text{obs}}_{\text{EH3-AD1}}, \boldsymbol{F}^{\text{obs}}_{\text{EH3-AD2}}, \boldsymbol{F}^{\text{obs}}_{\text{EH3-AD3}}, \boldsymbol{F}^{\text{obs}}_{\text{EH3-AD4}}). \tag{7.15}$$

Similarly, Eq. 7.9 becomes

$$\mathbf{F}_{\text{pred}}(\boldsymbol{\theta};\boldsymbol{\eta}) = (\boldsymbol{F}^{\text{pred}}_{\text{EH3-AD1}}(\boldsymbol{\theta};\boldsymbol{\eta}), \boldsymbol{F}^{\text{pred}}_{\text{EH3-AD2}}(\boldsymbol{\theta};\boldsymbol{\eta}), \boldsymbol{F}^{\text{pred}}_{\text{EH3-AD3}}(\boldsymbol{\theta};\boldsymbol{\eta}), \boldsymbol{F}^{\text{pred}}_{\text{EH3-AD4}}(\boldsymbol{\theta};\boldsymbol{\eta})). \tag{7.16}$$

Constructing the prediction vector, the prediction from each near AD i for far AD j for bin b is averaged the same way as the rate-only fit:

$$F^{(b)}_{\text{pred},j}(\boldsymbol{\theta};\boldsymbol{\eta}) = \frac{1}{4}\sum_i F^{(b)}_{\text{pred},j,i}(\boldsymbol{\theta};\boldsymbol{\eta}). \tag{7.17}$$

Finally, the rate+shape statistical and systematic components of χ^2 are given by

$$\chi^2_{\text{stat}}(\boldsymbol{\theta};\boldsymbol{\eta}) = 2 \sum_{\substack{j\in \\ \text{far ADs}}} \sum_{\substack{b\in \\ \text{bins}}} \left(F^{(b)}_{\text{pred},j}(\boldsymbol{\theta};\boldsymbol{\eta}) - F^{(b)}_{\text{obs},j} + F^{(b)}_{\text{obs},j} \ln \frac{F^{(b)}_{\text{obs},j}}{F^{(b)}_{\text{pred},j}(\boldsymbol{\theta};\boldsymbol{\eta})} \right), \tag{7.18}$$

$$\begin{aligned}\chi^2_{\text{sys}}(\boldsymbol{\theta};\boldsymbol{\eta}) = & \sum_{\substack{r\in \\ \text{reactors}}} \frac{\alpha_r^2}{\tilde{\sigma}_R^2} + \sum_{\substack{d\in \\ \text{all ADs}}} \left(\frac{\epsilon_d^2}{\tilde{\sigma}_D^2} + \frac{\eta^2_{\text{relE},d}}{\tilde{\sigma}^2_{\text{relE}}} + \frac{\eta^2_{\text{IAV},d}}{\tilde{\sigma}^2_{\text{IAV}}} + \sum_{\substack{u\in\text{bg.} \\ \text{sources}}} \frac{\eta^2_{\text{B},d,u}}{\tilde{\sigma}^2_{\text{B},d,u}} \right) \\ & + \sum_{\substack{i\in \\ \text{near ADs}}} \sum_{b\in\text{bins}} \left(\frac{\eta^{(b)}_{\text{N},i}}{\tilde{\sigma}^{(b)}_{\text{obs},i}} \right)^2 + \sum_{\substack{w\in \\ \text{NL pulls}}} \frac{\eta^2_{\text{NL},w}}{\tilde{\sigma}^2_{\text{NL},w}} \\ & + \frac{\eta^2_{\theta_{12}}}{\tilde{\sigma}^2_{12}} + \frac{\eta^2_{\Delta m^2_{21}}}{\tilde{\sigma}^2_{21}}.\end{aligned} \tag{7.19}$$

Rate+Shape Validations

As with the rate-only validations, the rate+shape fitting performance was assessed using simulated data. The initial validations were done using 1000 simulated nGd data sets for each of 36 pairs of (θ_{13}, Δm^2_{ee}) [116]. Since the fitter was designed to work on both nGd and nH, these results also evaluate the performance of both. For this study, fluctuations were included in the far AD statistics, but not for backgrounds or systematics. For each of the 36 pairs, the mean of the 1000 fit results was compared to the true value via a relative difference, shown in Fig. 7.5. Both the $\sin^2(2\theta_{13})$ and Δm^2_{ee} distributions are located around 0, indicating the fitter's accuracy.

Also in Fig. 7.5, the best-fit χ^2_{min} for each of these 36,000 simulated data sets is compared to the expected distribution [116]. Since the data sets were simulated as nGd events, the nGd binning was used which has 37 bins, instead of the 34 for nH. Therefore the total number of degrees of freedom is 146 (37 bins $*$ 4 ADs $-$ 2 parameters of interest). At 145.86, the mean of the fits corresponds almost exactly to the expected value.

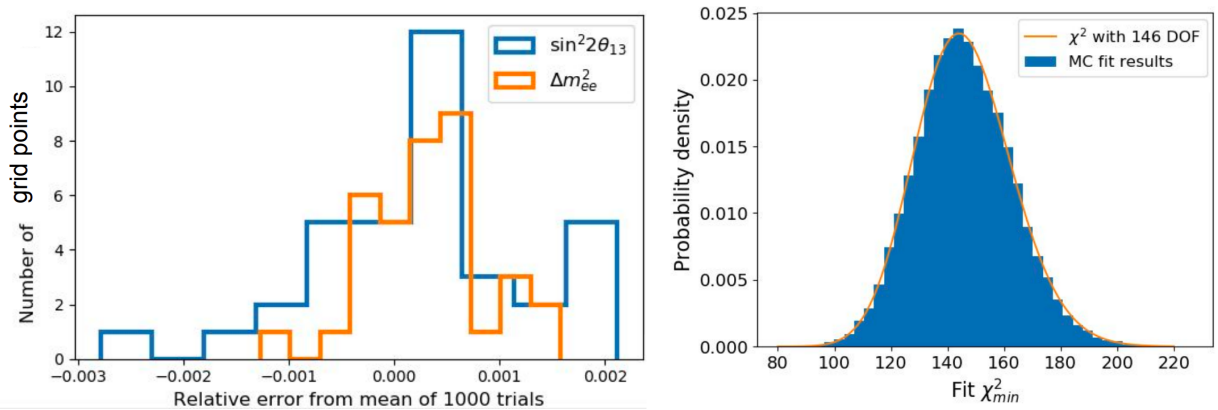

Figure 7.5: Left: Comparison of the mean value of the 1000 fits for each of the sets of simulation to the true values for $\sin^2(2\theta_{13})$ (blue) and Δm^2_{ee} (orange). Both spectra are located close to 0, indicating proper rate+shape fitting. Right: χ^2_{min} distribution for the 36,000 fits compared to the distribution expected with 146 degrees of freedom. Figures from [116].

Finally, after a few minor adjustments to the fitter, another round of validation tests were done using unfluctuated toy Monte Carlo data sets. As with the rate-only validations (Sec. 7.1.1), the fitter was tested using data sets produced both in house and by the parallel analysis. For the former studied 28 combinations of $\sin^2(2\theta_{13})$ and Δm^2_{ee}, for which the results are presented in Fig. 7.6. The fitted values were consistently within 0.007% of the inputted value, with χ^2_{min} values less than 2.5×10^{-4}. The latter studied the same 9 toy Monte Carlo simulated nH data sets as the rate-only test. The uncertainties for $\sin^2(2\theta_{13})$ and Δm^2_{ee} from Ref. [61] of $\sigma_{\sin^2 2\theta_{13}} = 0.0057$ and $\sigma_{\Delta m^2_{ee}} = 0.14 \times 10^{-3}$ eV^2, respectively, were used to quantify the performance [115]. All results were within $\pm 0.11\ \sigma_{\sin^2 2\theta_{13}}$ and $\pm 0.08\ \sigma_{\Delta m^2_{ee}}$, without bias in the results. The χ^2_{min} values were less than 0.159 for all fits.

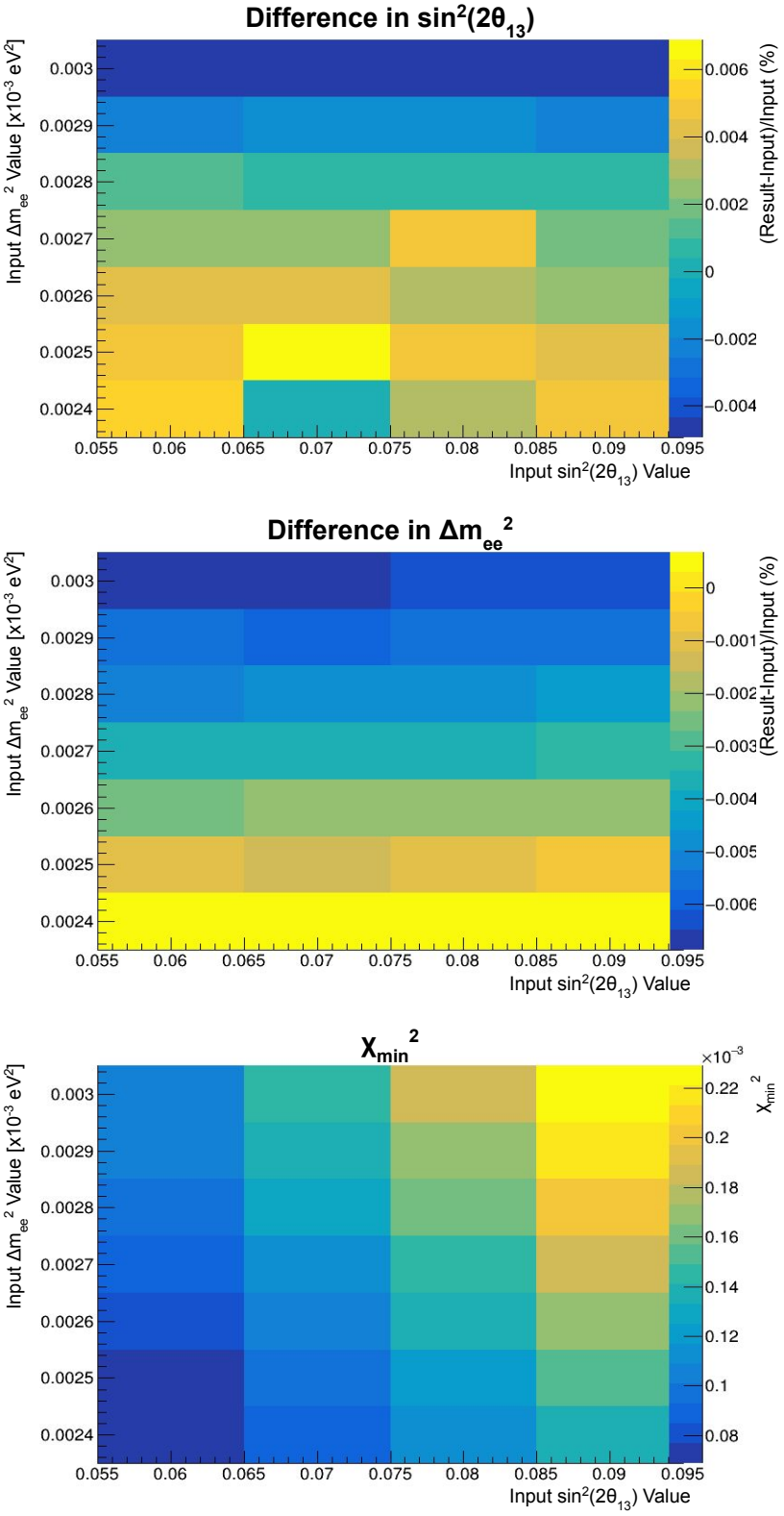

Figure 7.6: Rate+shape fit results of 28 toy Monte Carlo data sets produced in house. The best fit was consistently within 0.007% of the inputted value for both $\sin^2(2\theta_{13})$ (top) and Δm^2_{ee} (middle). The χ^2_{min} (bottom) for each fit was less than 2.5×10^{-4}.

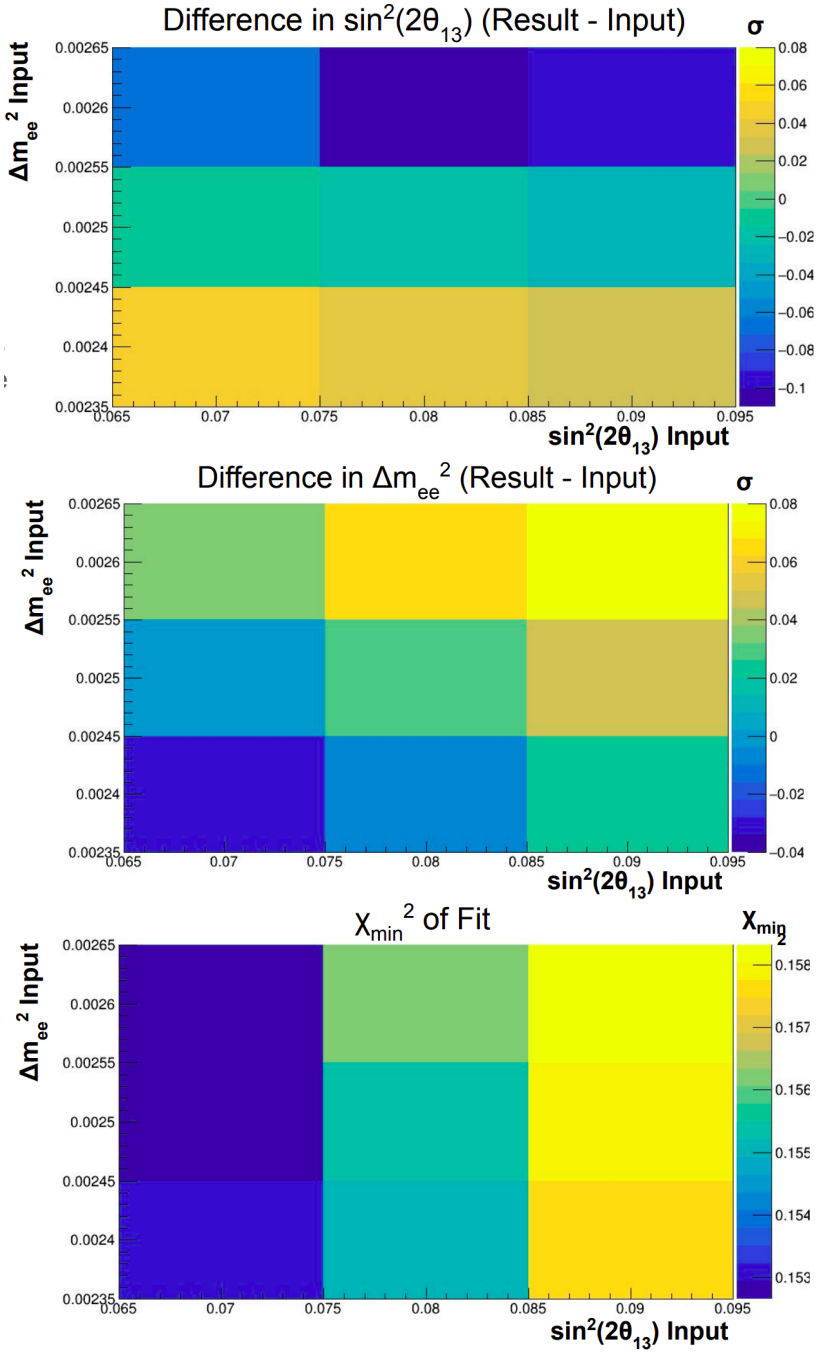

Figure 7.7: Rate+shape results from an additional 9 simulated nH data sets. Difference between rate+shape $\sin^2(2\theta_{13})$ (top) and Δm^2_{ee} (middle) fit results and the true input value in terms of the uncertainty from [61]: $\sigma_{\mathrm{s22t13}} = 0.0057$ and $\sigma_{\mathrm{dm2ee}} = 0.14 \times 10^{-3}$ eV^2. All fits resulted in values within ± 0.11 σ_{s22t13} and ± 0.08 σ_{dm2ee} without bias. Bottom: χ^2_{min} from each of the rate+shape fits, all fits resulting in values less than 0.159. Figures from Ref. [115].

7.2 DT Cut Studies

With the fitter and the analysis set, two studies investigated the DT cut's influence on the final results. The first study, presented in Sec. 7.2.1, was conducted by gradually increasing the DT cut value to optimize the cut to use for the final result, in addition to checking the stability of the result with different signal to background ratios. The second studied the impact of the various methods of calculating the DT cut efficiency and uncertainty on the final results, which is shown in Sec. 7.2.2.

7.2.1 DT Cut Scan

Prior to the final selection, the dependence of the fitted result on the DT cut was investigated. Selecting different DT cut values changes the signal to background ratio of the spectrum (Fig. 4.14). Therefore, checking the stability of the results for various DT cut values is a powerful test of the fitter's robustness and the background subtraction. Since the result is stable, the optimum DT cut value could be determined: That which gives the most precise measurement.

This study was done with a previous version of the selection which used non-uniformity corrections based on the peaks of both nGd and alpha events, in contrast to the final analysis which only used the alpha signals. The differences between the two non-uniformity corrections had minor effects on the data and lead to consistent results. Additionally, at the time of this study, the nominal DT cut value was 800 mm, and therefore was taken as the baseline on which to compare the other DT cut values.

The goal of this study was to assess the cost versus benefit of applying a tighter DT cut, which would provide a purer albeit smaller sample of IBDs, in contrast to a looser DT cut, which would select all the IBDs at the expense of having more backgrounds in the sample. For this

study, various DT cut values ranged from 300 mm as the most stringent to 2000 mm, which removes very few events from the selection. For the selections of both the IBD candidates and accidentals, the DT cuts were fully applied. For the correlated backgrounds, the rates were estimated by comparing the DT cut efficiencies of the new cut to the 800 mm cut using the accidentals-subtracted IBD candidates:

$$R(DT_{\text{new}}) = R(DT = 800 \text{ mm}) \times \frac{\epsilon_{DT_{\text{new}}}}{\epsilon_{800 \text{ mm}}}. \tag{7.20}$$

For each of these cuts, the delayed energy spectra were fit following the same procedure as described in Sec. 4.3.3. The delayed energy cut efficiencies were estimated following the procedure described in Sec. 4.4.5 for each AD as a function of DT cut value are shown in Fig. 7.8. The 'x' markers indicate the efficiencies calculated using the delayed energy cuts by the DT≤800 mm selection while the boxes represent the proper bounds to the delayed energy. Both methods were consistent with one another. For this reason, the study proceeded with the delayed energy bounds defined by the nominal 800 mm DT cut value.

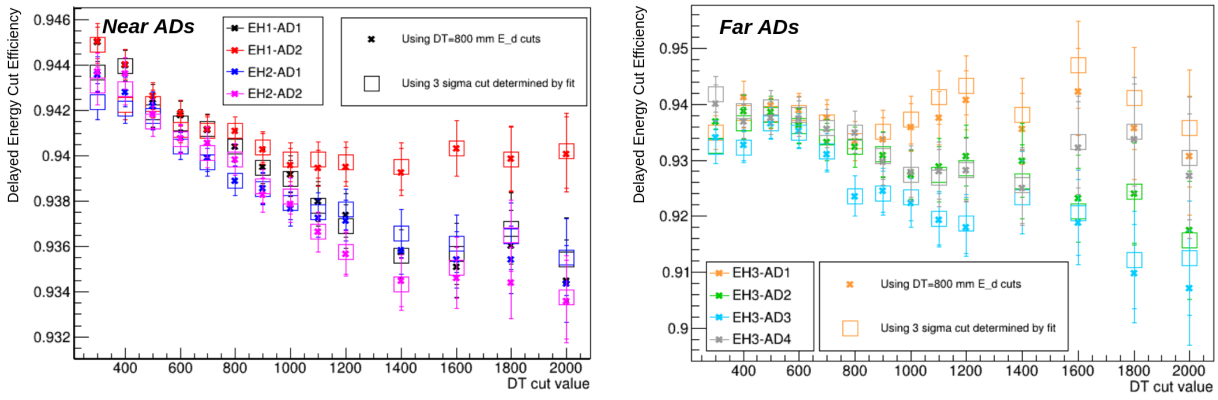

Figure 7.8: Comparison of the delayed energy cut efficiencies for each near (left) and far (right) hall ADs as a function of the DT cut. The points marked with the 'x' use the delayed energy cut bounds as determined by the selection using DT≤800 mm cut, whereas the boxes represent the efficiency using the proper delayed energy cut bounds for that DT cut value. These points are consistent, indicating that using the same delayed energy cuts for all points would be sufficient for this study.

The final best fit values as a function of DT cut value are shown in Fig. 7.9, where the final results are presented in the left plots while the final uncertainties are shown in the right plots. The yellow boxes in the best fit plots and the pink dashed line in the uncertainty plots highlight the results of the DT$\leq$800 mm cut. Two sets of points are plotted in the best fit value plots: The empty circles represent the case where the DT$\leq$800 mm cut detector response matrix was used for all DT cut values, while the solid points indicate the case where the detector response matrix was regenerated using each of the DT cut values. As seen in the figure, these cases produce nearly identical results. The $\sin^2(2\theta_{13})$ fit results are stable as a function of DT cut value for both the rate-only and rate+shape analyses. The Δm^2_{ee} best fits, however, exhibit some dependence on the DT cut value. Between the moderate size of the fluctuations and the highly correlated nature of the events included for each point, this dependence was determined to not be a showstopper for this analysis.

Optimization of the cut came through minimizing the uncertainty of the final fits as a function of DT cut value. The DT cut values between 700 and 1000 mm minimized the uncertainty on Δm^2_{ee}, while for $\sin^2(2\theta_{13}$, the uncertainty was reduced at larger DT cut values, near 1300 mm, for both rate-only and rate+shape. The DT$\leq$1000 mm cut was chosen to optimize the final fit uncertainty.

7.2.2 DT Cut Uncertainty Variations

In addition to studying the dependence of the final result on the DT cut value, a comparison was done between results using various calculations of the DT cut uncertainty, as alluded to in Sec. 4.4.4. The uncertainty associated with the DT cut efficiency is the largest of the systematics. In order to understand the impact, several studies were conducted with regards to changing the way it was quantified.

The methods in the first comparison utilized the spread in DT cut efficiency directly, while

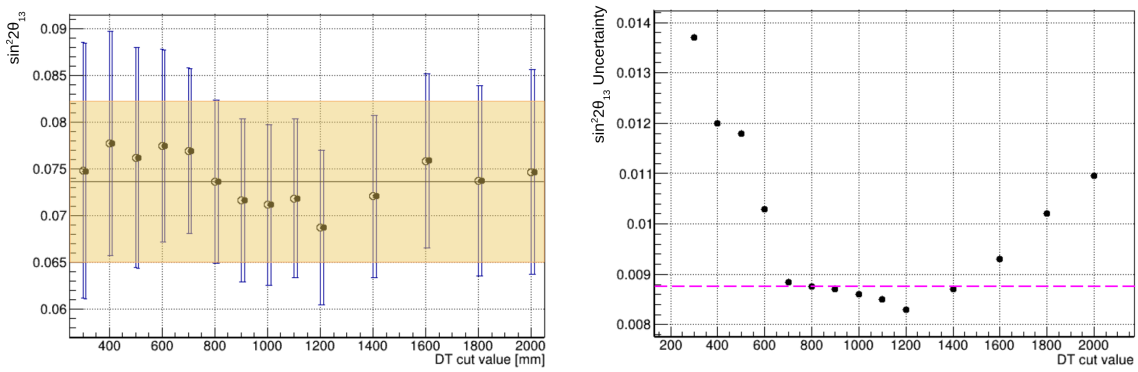

(a) Rate-Only

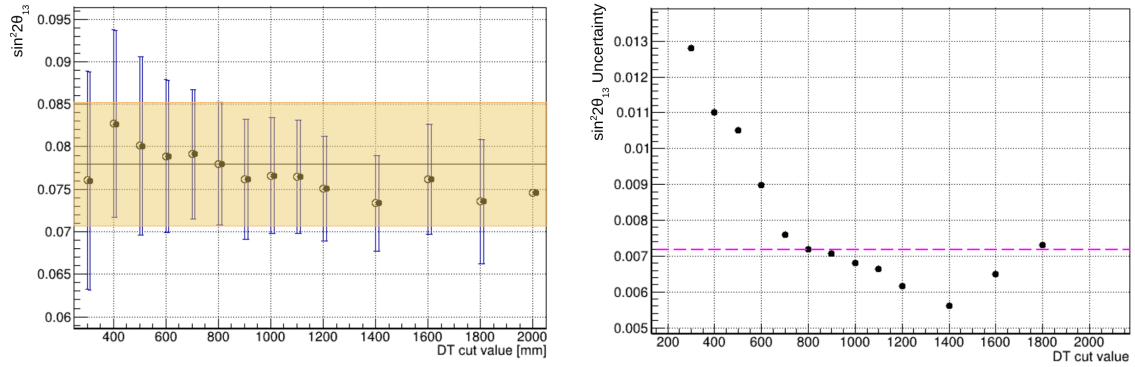

(b) Rate+Shape $\sin^2(2\theta_{13})$

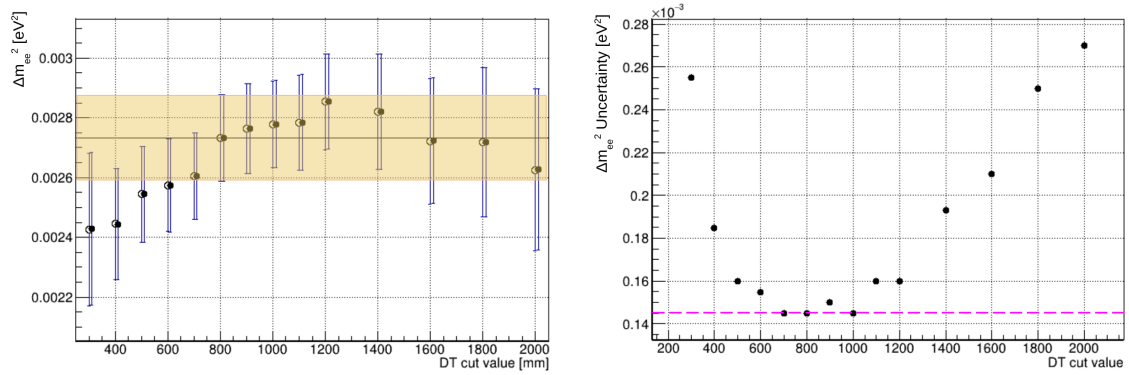

(c) Rate+Shape Δm^2_{ee}

Figure 7.9: Best fit results (left) and uncertainty (right) as a function of DT cut value for rate-only $\sin^2(2\theta_{13})$, and both $\sin^2(2\theta_{13})$ and Δm^2_{ee} from rate+shape. The hollow points in the best fit scans using one detector response matrix for all DT cut values, while the solid points detector response matrices with the associated DT cut applied. The yellow boxes of the best fit scans and the magenta dashed lines indicate the results from the DT$\leq$800 mm selection, which was the standard at the time of this study. The DT cut was optimized at DT$\leq$1000 mm by minimizing the best fit uncertainties for all three parameters.

Table 7.2: Summary of DT cut efficiencies and total detection efficiencies for each near AD and the weighted average of the far ADs. Only the statistical uncertainty is included here.

Detector(s)	DT Efficiency	Total Detection Efficiency
EH1-AD1	0.8259 ± 0.0028	0.7714 ± 0.0044
EH1-AD2	0.8185 ± 0.0026	0.7645 ± 0.0042
EH2-AD1	0.8178 ± 0.0026	0.7638 ± 0.0042
EH2-AD2	0.8201 ± 0.0028	0.7660 ± 0.0044
Weighted Average of Far ADs	0.8219 ± 0.0082	0.7677 ± 0.0104

the second comparison included slightly more complex calculations. Unless otherwise noted, the far hall ADs were averaged together to reduce the uncertainty due to the lower statistics compared to the near ADs. As shown in Fig. 4.16(c), the weighted average of the far ADs is consistent with the near ADs. The AD specific DT cut efficiencies and uncertainties are summarized in the Tab. 7.2.

For the first comparison, the various calculations followed the same approach: using a single efficiency and uncertainty for all ADs, with the uncertainty being determined from the spread of the individual AD efficiencies. The goal of this study was to see the impact of changing the method of calculating the uncertainty.

The first calculation, the "full envelope" method, was defined as half of the difference between the highest and lowest DT cut efficiencies, which amounted to ± 0.0041. The two other methods in the first comparison were the "half envelope" and the "double envelope" where the uncertainty from the full envelope method was simply halved and doubled, respectively. Assuming the AD efficiencies are distributed normally, the half envelope method yields roughly the 1-σ uncertainty of the efficiency. On the other hand, the double envelope calculation is overly conservative and was considered specifically to see its impact.

The results are shown in Fig. 7.10. As expected, the rate-only best fit values did not change, only the uncertainty on the result was affected. For the rate+shape results, the best fit

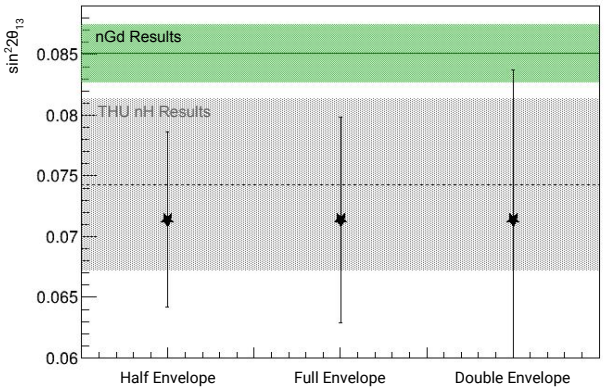

(a) Rate-Only

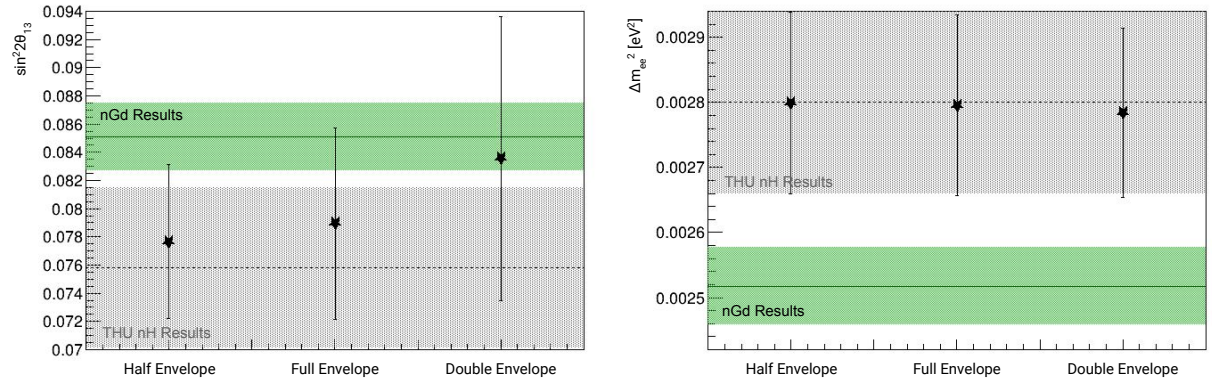

(b) Rate+Shape

Figure 7.10: Results of the best fits using the full envelope calculation of the DT cut efficiency uncertainty compared to half and double the uncertainty. The green and grey bands represent the results from the nGd analysis [49] and the results measured by the parallel analysis by another Daya Bay group [61].

values trended towards higher values of $\sin^2(2\theta_{13})$ and lower values of Δm^2_{ee} with larger DT cut uncertainties, in addition to the effects on the size of the error bars.

The methods in the second comparison included a Gaussian fit and a weighted average of the DT cut efficiencies, defined in Sec. 4.4.4. These uncertainties are summarized in Tab. 7.3. For these calculations, the ADs were weighted based on the statistical uncertainty of each AD, and therefore the far ADs were not averaged together as was done for the envelope methods. Compared to the envelope calculations, the Gaussian fit method resulted in an

Table 7.3: DT cut efficiencies and total detection efficiencies for the full envelope, weighted average, and Gaussian fit calculations.

Method	DT Efficiency	Total Detection Efficiency
Full Envelope	0.8214 ± 0.0041	0.7671 ± 0.0058
Weighted Average	0.8204 ± 0.0013	0.7662 ± 0.0032
Gaussian Fit	0.8120 ± 0.0017	0.7584 ± 0.0035

uncertainty which was a little less than the half envelope method which had an uncertainty of 0.0041.

Also presented in the second comparison, the case for which the DT cut efficiency and uncertainty was applied for each AD individually (as summarized in Tab. 7.2) was also evaluated. In this case, the Far ADs were combined via a weighted average, whereas the near ADs were assigned their individual values, as shown in Fig. 4.16. To disentangle the effects of the individual efficiencies and the individual uncertainties, an intermediate step was designed such that the independent efficiencies were applied with a common uncertainty: For this test point, the full envelope uncertainty was used.

The results are presented in Fig. 7.11. Between the weighted average, Gaussian fit, and full envelope methods (ordered by increasing DT cut uncertainty), the trend was consistent with the results of the first comparison. The difference was dominated by the change in the DT cut uncertainty; the minor changes in the mean efficiency between the methods had little effect on the results. The fourth point, which used the efficiencies for each AD individually with a common uncertainty, exhibits an increased value in the best fit for $\sin^2(2\theta_{13})$ for both rate-only and rate+shape, and a slight decrease in Δm^2_{ee}. Between the fourth and fifth points, where only the uncertainty changes, the same trend is observed as the first study. The changes in the best fit values were attributed the independent adjustments to both near and far spectra, therefore allowing for more adjustments to the near-far ratio.

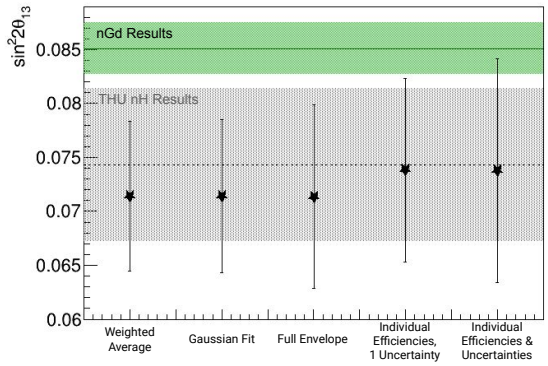

(a) Rate-Only

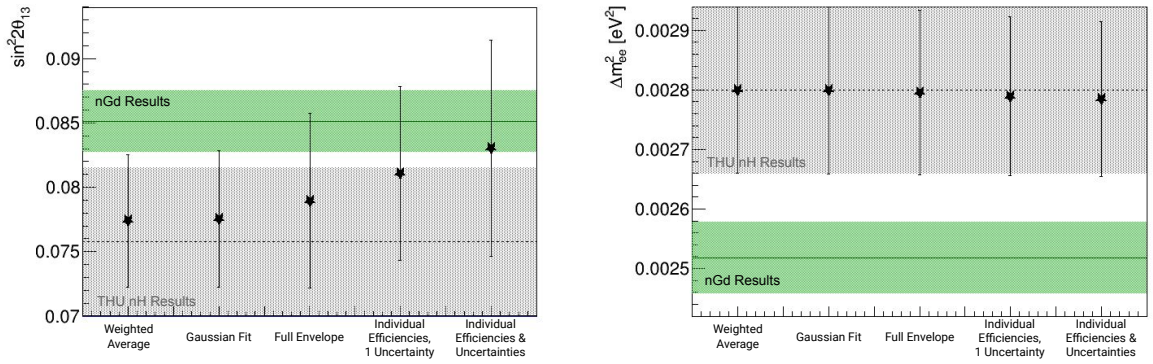

(b) Rate+Shape

Figure 7.11: Best fit results using the weighted average, Gaussian fit, and full envelope calculations of the DT cut efficiency uncertainty, in addition to the results obtained with the individual DT cut efficiencies and uncertainties applied for each AD. To decouple the impact from applying the efficiencies and uncertainties for each AD individually compared to one value for all eight, an intermediate step was included using individual efficiencies but a common uncertainty: the full envelope uncertainty. The green and grey bands represent the results from the nGd analysis [49] and the results measured by the parallel analysis by another Daya Bay group [61].

These studies on the effects of changing the DT cut efficiency uncertainty exhibit only sizeable variation for $\sin^2(2\theta_{13})$ when the uncertainty is increased significantly beyond what is reasonable. The results presented in this thesis use the Gaussian fit approach to be consistent with the parallel Daya Bay analysis by Tsinghua University (Ref. [61]).

7.3 Results

As detailed in the preceding chapters, the event selection of this analysis was carefully designed to identify the rates and spectra of IBD events from $\overline{\nu}_e$ interactions (Ch. 4). The irreducible backgrounds were estimated as described in Ch. 5. A summary of the rates obtained through this analysis is provided in Tab. 7.4.

Both rate-only and rate+shape fits described in Sec. 7.1 were performed on the rates and spectra observed by this selection to obtain values for $\sin^2(2\theta_{13})$ and Δm^2_{ee} that best described the experimental observations. To account for all the oscillation effects, the values for $\theta_{12} = 0.587$ and $\Delta m^2_{21} = 7.53 \times 10^{-5}$ eV^2 in this analysis were taken from Ref. [117]. Additionally, since the rate-only measurement only measures the value of $\sin^2(2\theta_{13})$, the $\Delta m^2_{32} = 2.45 \times 10^{-3}$ eV^2 value was also used [117].

The best fits obtained from both the rate-only and rate+shape methods resulted in the

Table 7.4: Summary of the $\overline{\nu}_e$ event selection.

	EH1-AD1	EH1-AD2	EH2-AD1	EH2-AD2	EH3-AD1	EH3-AD2	EH3-AD3	EH3-AD4
DAQ live time (days)	1536.624	1737.620	1741.214	1554.046	1739.010	1739.010	1739.010	1551.381
IBD candidates	518082	595250	619406	540947	268557	264137	270823	234572
$\varepsilon_\mu \times \varepsilon_m$	0.5228	0.5206	0.6028	0.6013	0.9183	0.9178	0.9177	0.9180
Accidentals (day^{-1})	120.05 ± 0.06	119.04 ± 0.06	111.02 ± 0.05	108.12 ± 0.06	107.64 ± 0.04	106.05 ± 0.04	109.74 ± 0.04	104.87 ± 0.04
Fast neutron (AD^{-1} day^{-1})	2.75 ± 0.17		1.97 ± 0.10			0.17 ± 0.02		
^{9}Li/^{8}He (AD^{-1} day^{-1})	3.18 ± 1.28		2.92 ± 1.09			0.19 ± 0.07		
Am-C correlated (day^{-1})	0.05 ± 0.03	0.05 ± 0.03	0.04 ± 0.02	0.04 ± 0.02	0.02 ± 0.01	0.02 ± 0.01	0.02 ± 0.01	0.01 ± 0.01
Radiogenic neutron (day^{-1})	0.20 ± 0.04	0.20 ± 0.04	0.20 ± 0.04	0.20 ± 0.04	0.20 ± 0.04	0.20 ± 0.04	0.20 ± 0.04	0.20 ± 0.04
IBD rate (day^{-1})	518.69 ± 1.53	532.81 ± 1.51	473.96 ± 1.33	465.61 ± 1.35	59.89 ± 0.34	58.80 ± 0.34	59.33 ± 0.34	59.21 ± 0.35

Table 7.5: Best fit results of the nH analysis using both rate-only and rate+shape.

Method	Results
Rate-only	$\sin^2(2\theta_{13}) = 0.0714 \pm 0.0071$ $\chi^2/\text{NDF} = 1.55/3$
Rate+Shape	$\sin^2(2\theta_{13}) = 0.0776 \pm 0.0053$ $\Delta m^2_{ee} = (2.80 \pm 0.14) \times 10^{-3}$ eV^2 $\Delta m^2_{32} = (2.75 \pm 0.14) \times 10^{-3}$ eV^2 (NO) $\Delta m^2_{32} = (-2.85 \pm 0.14) \times 10^{-3}$ eV^2 (IO) $\chi^2/\text{NDF} = 149.7/134$

measured values presented in Tab 7.5. This nH rate+shape result is the first of its kind at Daya Bay. Compared to the expectation with no oscillation effects, Figure 7.12 shows the prompt energy spectrum observed at the far hall along with the spectrum obtained from the best fit. The bottom panel presents the ratio to the un-oscillated spectrum.

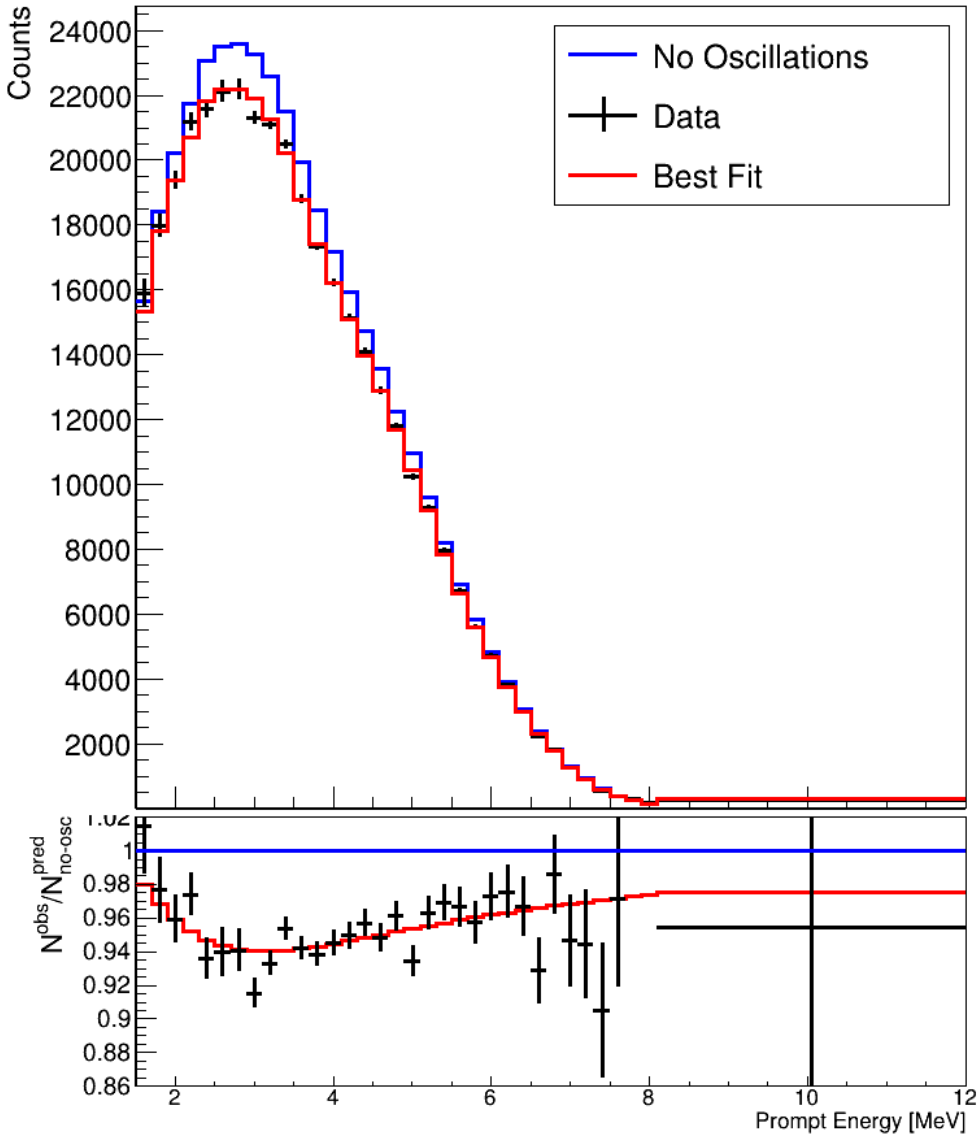

Figure 7.12: Prompt energy spectrum observed at the far hall (black) compared to the prediction with no oscillations (blue) with the rate+shape best fit results (red). Bottom panel shows the ratio of these spectra with respect to the no oscillations prediction.

In the rate-only case, the probability of getting a χ^2 of 1.55 or lower for 3 degrees of freedom is roughly 33%. Additionally, the distribution does not exactly match the distribution with 3 degrees of freedom. In contrast, the reduced χ^2 of the rate+shape method is quite near to 1, as expected. The 134 degrees of freedom was calculated as the total number of bins in the fit (34 bins for each of the 4 far ADs) minus the number of parameters in the fit (2: θ_{13} and Δm^2_{ee}).

For both methods, χ^2 scans over the fitted parameters were performed to determine the uncertainty of the measurements. The rate-only $\Delta\chi^2 \equiv \chi^2 - \chi^2_{\text{min}}$ values as a function of $\sin^2 2\theta_{13}$ is presented in Fig. 7.13; in this scan, the given value of $\sin^2 2\theta_{13}$ was held constant and the χ^2 was minimized by adjusting only the nuisance parameters. Fig 7.14 shows the corresponding minimized χ^2 scans for the rate+shape analysis. In the central plot, the scan was done holding both $\sin^2 2\theta_{13}$ and Δm^2_{ee} fixed and minimizing the nuisance parameters. The 1-, 2-, and 3-σ confidence levels for the 2-D fit, marked with the black ellipses, indicate the space for which the $\Delta\chi^2$ is less than or equal to 2.296, 6.180, and 11.836, respectively.

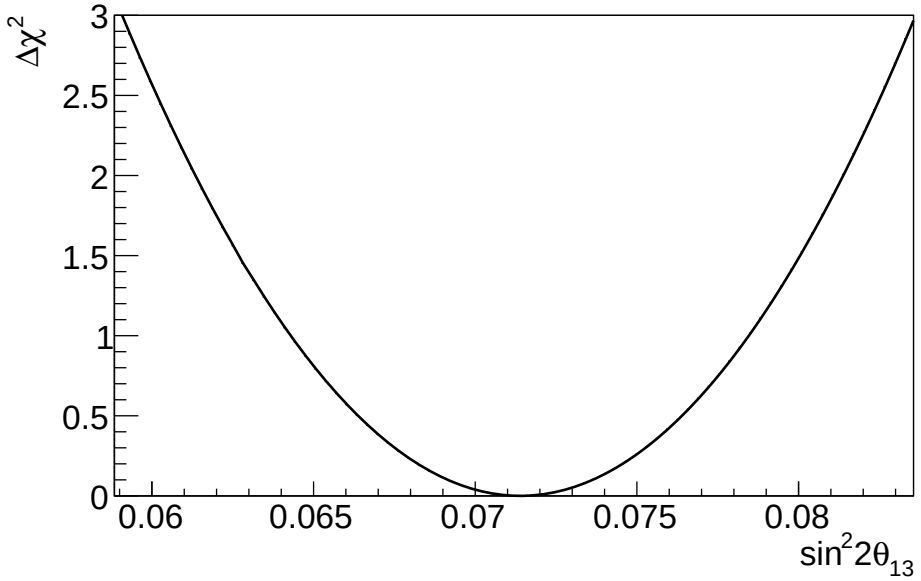

Figure 7.13: χ^2 profile for the rate-only analysis. The 1-σ uncertainty was determined by the intercepts of the intercepts at $\Delta\chi^2 = 1$.

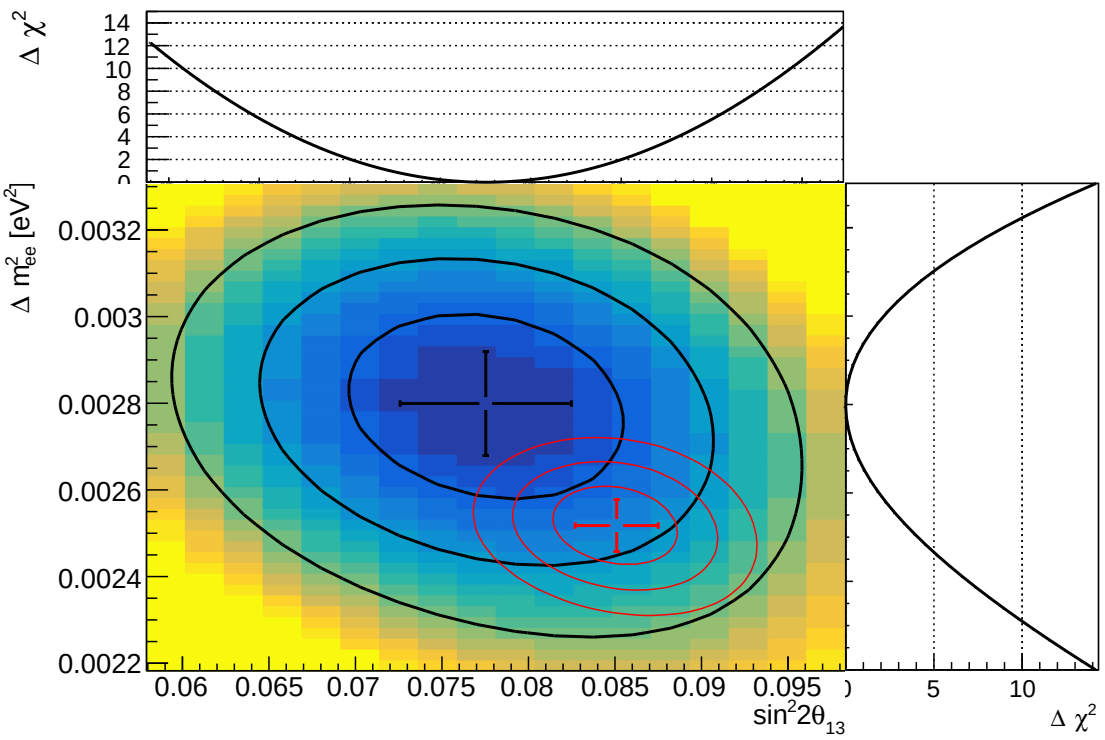

Figure 7.14: χ^2 contours for the rate+shape analysis and the 1-D $\Delta\chi^2$ profiles of both $\sin^2 2\theta_{13}$ and Δm^2_{ee} parameters. The red ellipses present the Daya Bay's most recent nGd results from Ref. [49] for comparison.

The similar contours from the nGd analysis drawn in red [49]. For the 1-D χ^2 scans of the $\sin^2 2\theta_{13}$ and Δm^2_{ee} parameters, the parameter of interest was held constant while the other parameter was free to float in the minimization process. The 1-σ uncertainty is determined by the intercepts at $\Delta\chi^2 = 1$.

The error budget was calculated through methodically enabling and disabling nuisance parameters to determine the size of each systematic's contribution to the total uncertainty. The disabled nuisance parameters were held at the best fit values. Two methods were implemented: the subtraction and addition methods [64].

The subtraction method is done by evaluating the 1-σ uncertainty of the fit with all nuisance parameters enabled except for one, u. Subtracting in quadrature this uncertainty, $\sigma_{\mathrm{all}-u}$, from

the best fit uncertainty, σ_{all}, results in the "effective uncertainty" of the u systematic:

$$\sigma_u^2 = \sigma_{\text{all}}^2 - \sigma_{\text{all}-u}^2. \tag{7.21}$$

Alternatively, the addition method compares the 1-σ uncertainty of the case with only statistics nuisance parameters enabled, σ_{stat}, to that with the statistics and one nuisance parameter, $\sigma_{\text{stat}+u}$, to determine the effective uncertainty of u:

$$\sigma_u^2 = \sigma_{\text{stat}+u}^2 - \sigma_{\text{stat}}^2. \tag{7.22}$$

In either case, the percentage each uncertainty source contributed to the final error was then calculated from the fraction of the contributed uncertainty to the total uncertainty.

$$f_u = \frac{\sigma_u^2}{\sigma_{\text{all}}^2}. \tag{7.23}$$

Both methods were done and provided consistent results, shown in Tab. 7.6 and Tab. 7.7. The sum of the individual factions are listed in the final rows of the tables. The individual contributions sum to values marginally different than 100%: the difference caused by correlations between the uncertainties. Fig. 7.15 expresses these error budget graphically for the subtraction method. Only the sources with contributions larger than 3% are labeled.

Table 7.6: Percentage breakdown of the contributions to the overall uncertainty by the various sources for the rate-only and rate+shape results via the subtraction method. The total percentage for each is slightly larger than 100% due to correlations between the uncertainty sources.

	Contribution f_u [%]		
	Rate-Only	Rate+Shape	
Uncertainty Source	$\sin^2 2\theta_{13}$	$\sin^2 2\theta_{13}$	Δm^2_{ee}
Accidentals	0.41	0.10	0.95
AmC	0.04	0.01	0.06
Relative Efficiency	49.47	62.45	1.58
Fast neutrons	0.47	0.05	0.10
IAV	3.19	3.96	0.15
Input mixing parameters	0.15	0.01	0.01
Li9/He8	12.72	0.18	1.25
Nonlinearity	0.02	0.01	0.23
Radiogenic neutrons	0.36	0.17	0.60
Reactor	5.39	6.59	0.13
Relative energy scale	2.94	1.88	30.67
Near Stats	1.45	3.36	5.43
Far Stats	23.40	21.93	61.47
Total Percentage	100.01	100.71	102.63

Table 7.7: Percentage breakdown of the contributions to the overall uncertainty by the various sources for the rate-only and rate+shape results via the addition method. The total percentage is not identically 100% due to correlations between the uncertainty sources.

	Contribution f_u [%]		
	Rate-Only	Rate+Shape	
Uncertainty Source	$\sin^2 2\theta_{13}$	$\sin^2 2\theta_{13}$	Δm^2_{ee}
Accidentals	0.40	0.17	0.76
AmC	0.03	0.02	0.06
Efficiency	49.48	62.38	0.31
Fast neutrons	0.46	0.08	0.07
IAV	3.20	4.77	0.98
Input mixing parameters	0.15	0.01	0.01
Li9/He8	12.74	0.40	0.75
Nonlinearity	0.02	0.01	0.21
Radiogenic neutrons	0.35	0.25	0.47
Reactor	5.41	7.42	0.04
Relative energy scale	2.96	0.61	27.49
Near Stats	1.45	2.61	4.04
Far Stats	23.40	21.93	61.47
Total Percentage	100.07	100.66	96.67

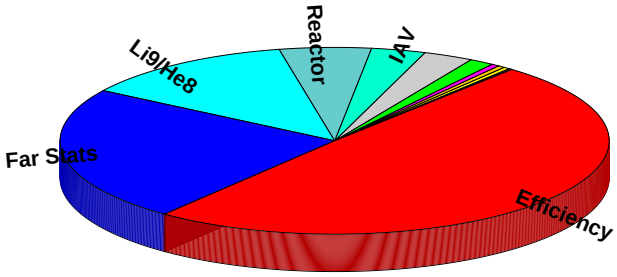

(a) Rate-Only

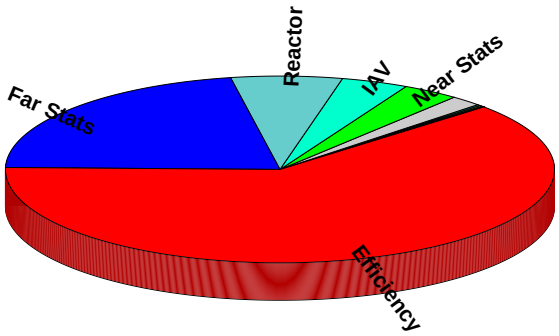

(b) Rate+Shape $\sin^2 2\theta_{13}$

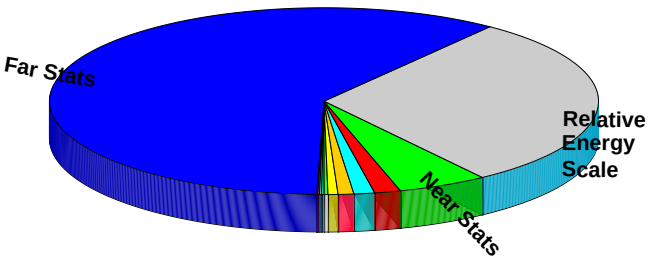

(c) Rate+Shape Δm^2_{ee}

Figure 7.15: The error budgets for the rate-only and rate+shape fit results. Sources contributing more than 3% to the overall uncertainty are labeled here.

Chapter 8

Conclusions

This thesis presented a measurement of the θ_{13} and Δm^2_{32} neutrino mixing parameters through the observation of reactor $\overline{\nu}_e$ disappearance at the Daya Bay Reactor Neutrino Experiment via the IBD reaction with neutrons captured on hydrogen (nH). First, neutrino oscillation was introduced in a comprehensive summary of its history and theory. Secondly, the experimental design of Daya Bay was presented, along with the processes used to reconstruct detected events and calibrate the eight identically-designed antineutrino detectors (ADs). The event selection of the nH IBDs and the irreducible backgrounds was detailed and used to measure the neutrino oscillation parameters. This measurement was obtained through a near-to-far projection approach, where the near hall observations were extrapolated to the far hall ADs to determine the predicted event count and spectra based on the assumed values of the θ_{13} and Δm^2_{ee} oscillation parameters. A fit was performed utilizing a χ^2 expression based on the Poisson maximum likelihood estimator with nuisance parameters to account for the statistical and systematic uncertainties of the inputs, respectively. By minimizing the χ^2 expression, the best fit values of the oscillation parameters were determined through both rate-only and rate+shape methods.

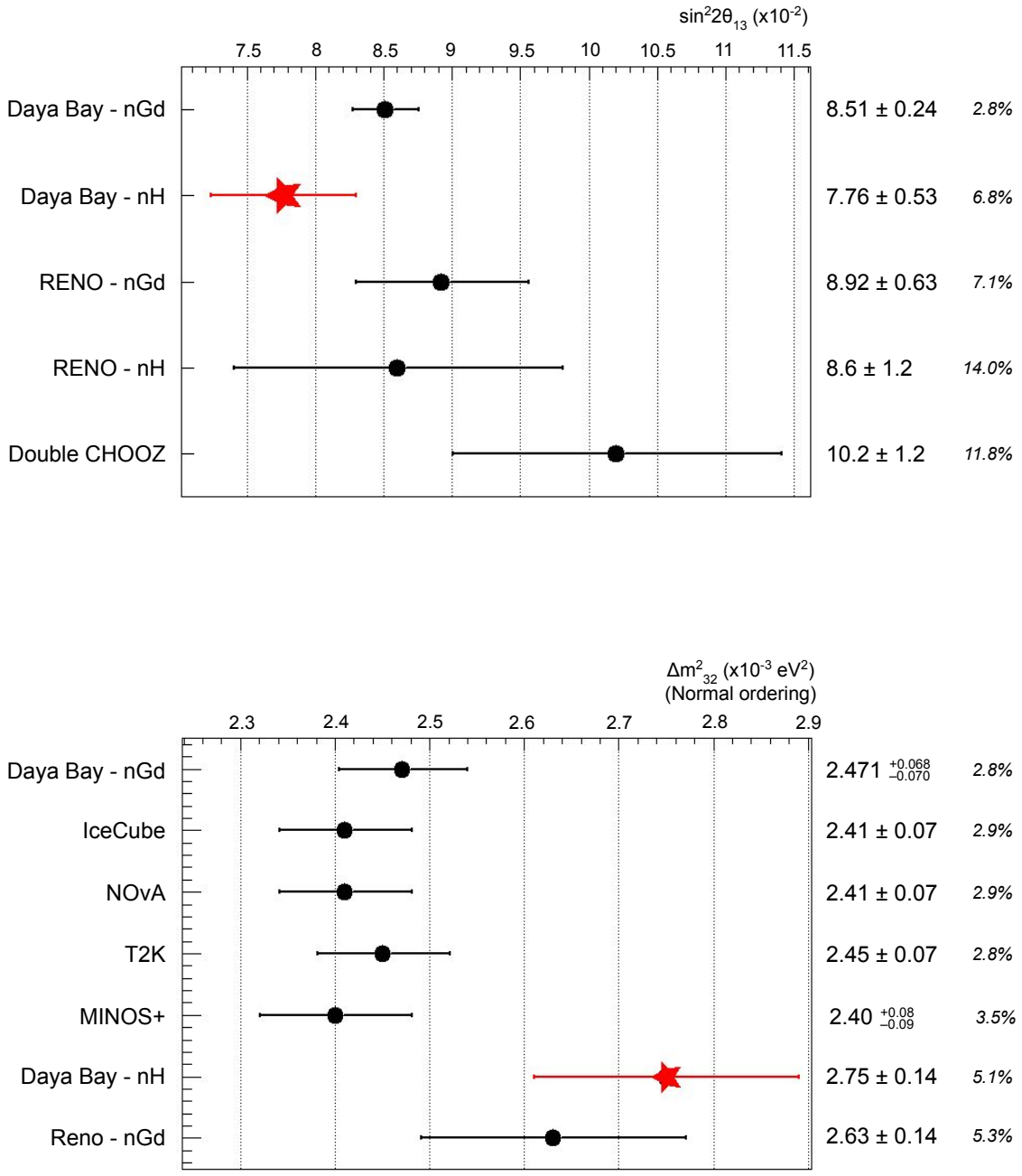

Figure 8.1: Comparison of the five most precise results of $\sin^2 2\theta_{13}$ (top) and seven most precise results of Δm^2_{32} (NO) globally, with the analysis presented in this thesis (red). This measurement of $\sin^2 2\theta_{13}$ is the second most precise behind the Daya Bay nGd result.

Table 8.1: Comparison of best fit results to the parallel analysis (Ref. [118]).

Method	Quantity	This Analysis	Parallel Analysis
Rate-only	$\sin^2(2\theta_{13})$	0.0714 ± 0.0071	0.0743 ± 0.0071
	χ^2/NDF	1.55/3	4.5/6
Rate+Shape	$\sin^2(2\theta_{13})$	0.0776 ± 0.0053	0.0758 ± 0.0057
	Δm^2_{ee} $[\times 10^{-3}\text{eV}^2]$	2.80 ± 0.14	$2.80^{+0.14}_{-0.15}$
	Δm^2_{32} $[\times 10^{-3}\text{eV}^2]$ (NO)	2.75 ± 0.14	$2.74^{+0.14}_{-0.15}$
	Δm^2_{32} $[\times 10^{-3}\text{eV}^2]$ (IO)	-2.85 ± 0.14	$-2.84^{+0.15}_{-0.14}$
	χ^2/NDF	149.7/134	255.0/234

Fig. 8.1 presents the best fit results obtained through this analysis compared to the current measured values of $\sin^2 2\theta_{13}$ and Δm^2_{ee} globally. This analysis of the nH selection of the 1958 days data set at Daya Bay is among the most precise measurements to date. These results are consistent with that of the parallel analysis of Ref. [61] (updated values in Ref. [118]), summarized in Tab. 8.1. A Daya Bay publication of both results is in preparation.

This nH analysis measured a value of $\sin^2(2\theta_{13})$ which is independent from the nGd result, the two of which are consistent to within 1σ. The Δm^2_{ee} result is within 2σ's of the nGd result, though unlike the $\sin^2(2\theta_{13})$ results, the two are not independent.

It is unclear what caused the slight tension between the nH and nGd results, particularly for $\sin^2(2\theta_{13})$. The nH analysis was done by two independent groups, utilizing different selections, background assessments, and fitting approaches, both of which yielded consistent results. Many checks were done, as detailed in this thesis, and no issues were identified.

Finally, this analysis used 1958 days of data at Daya Bay, though the full data set includes an additional 1200 days. The results with the full 3158 days of data may be able to shed some light on the tensions in θ_{13} and Δm^2_{32} observed by this analysis in comparison to the nGd analysis.

Bibliography

[1] J. Chadwick, The intensity distribution in the magnetic spectrum of beta particles from radium (B + C), Verh. Phys. Gesell. **16**, 383 (1914).

[2] W. Pauli, Pauli letter collection: letter to Lise Meitner, Handwritten copy.

[3] F. Reines and C. L. Cowan jun., The neutrino, Nature **178**, 446 (1956).

[4] R. Davis, Attempt to Detect the Antineutrinos from a Nuclear Reactor by the $Cl^{37}(\overline{\nu}, e^{-})Ar^{37}$ Reaction, Phys. Rev. **97**, 766 (1955).

[5] M. Goldhaber, L. Grodzins, and A. W. Sunyar, Helicity of neutrinos, Phys. Rev. **109**, 1015 (1958).

[6] L. Grodzins, The tabletop measurement of the helicity of the neutrino, Nuclear Physics B - Proceedings Supplements **229-232**, 5 (2012), Neutrino 2010.

[7] G. Danby *et al.*, Observation of high-energy neutrino reactions and the existence of two kinds of neutrinos, Phys. Rev. Lett. **9**, 36 (1962).

[8] M. L. Perl *et al.*, Evidence for Anomalous Lepton Production in e+ - e- Annihilation, Phys. Rev. Lett. **35**, 1489 (1975).

[9] G. Feldman, 15th Rencontres du Vietnam, Conference presentation, 2019.

[10] A. M. Cnops *et al.*, Experimental limits on heavy lepton production by neutrinos, Phys. Rev. Lett. **40**, 144 (1978).

[11] P. Fritze *et al.*, Further study of the prompt neutrino flux from 400 gev proton-nucleus collisions using bebc, Physics Letters B **96**, 427 (1980).

[12] M. Roos *et al.*, Review of particle properties: Particle data group, Physics Letters B **111**, i (1982).

[13] K. Kodama *et al.*, Observation of tau neutrino interactions, Physics Letters B **504**, 218 (2001).

[14] DONuT Collaboration, K. Kodama *et al.*, Final tau-neutrino results from the donut experiment, Phys. Rev. D **78**, 052002 (2008).

[15] S. L. Glashow, Partial-symmetries of weak interactions, Nuclear Physics **22**, 579 (1961).

[16] A. Salam and J. Ward, Electromagnetic and weak interactions, Physics Letters **13**, 168 (1964).

[17] S. Weinberg, A model of leptons, Phys. Rev. Lett. **19**, 1264 (1967).

[18] F. Hasert *et al.*, Observation of neutrino-like interactions without muon or electron in the gargamelle neutrino experiment, Physics Letters B **46**, 138 (1973).

[19] F. Hasert *et al.*, Observation of neutrino-like interactions without muon or electron in the gargamelle neutrino experiment, Nuclear Physics B **73**, 1 (1974).

[20] F. Hasert *et al.*, Search for elastic muon-neutrino electron scattering, Physics Letters B **46**, 121 (1973).

[21] J. N. Bahcall, B. T. Cleveland, J. Davis, R., and J. K. Rowley, Chlorine and gallium solar neutrino experiments, The Astrophysical Journal **292** (1985).

[22] R. L. Hahn, Radiochemical solar neutrino experiments, 'successful and otherwise', Journal of Physics: Conference Series **136**, 022003 (2008).

[23] R. Davis, D. S. Harmer, and K. C. Hoffman, Search for Neutrinos from the Sun, Phys. Rev. Lett. **20**, 1205 (1968).

[24] C. Giunti and C. W. Kim, *Fundamentals of Neutrino Physics and Astrophysics* (Oxford University Press, 2007).

[25] F. Reines, Iv. high energy neutrinos underground: Status of the case-wits-irvine experiment and future prospect, Proceedings of the Royal Society of London. Series A, Mathematical and Physical Sciences **301**, 125 (1967).

[26] T. J. Haines *et al.*, Calculation of Atmospheric Neutrino Induced Backgrounds in a Nucleon Decay Search, Phys. Rev. Lett. **57**, 1986 (1986).

[27] K. Hirata *et al.*, Experimental study of the atmospheric neutrino flux, Physics Letters B **205**, 416 (1988).

[28] Super-Kamiokande Collaboration, Y. Fukuda *et al.*, Evidence for oscillation of atmospheric neutrinos, Phys. Rev. Lett. **81**, 1562 (1998).

[29] Super-Kamiokande, Y. Fukuda *et al.*, Measurements of the solar neutrino flux from Super-Kamiokande's first 300 days, Phys. Rev. Lett. **81**, 1158 (1998), hep-ex/9805021, [Erratum: Phys.Rev.Lett. 81, 4279 (1998)].

[30] SNO Collaboration, Q. R. Ahmad *et al.*, Measurement of the rate of $\nu_e + d \rightarrow p + p + e^-$ interactions produced by ^8b solar neutrinos at the sudbury neutrino observatory, Phys. Rev. Lett. **87**, 071301 (2001).

[31] KamLAND, K. Eguchi *et al.*, First results from KamLAND: Evidence for reactor anti-neutrino disappearance, Phys. Rev. Lett. **90**, 021802 (2003), hep-ex/0212021.

[32] E. C. Huang, *Precise Measurement of Mixing Parameters and Sterile Neutrino Search at Daya Bay*, PhD thesis, University of Illinois at Urbana-Champaign, 2016.

[33] J. N. Bahcall and C. Peña-Garay, A road map to solar neutrino fluxes, neutrino oscillation parameters, and tests for new physics, Journal of High Energy Physics **2003**, 004 (2003).

[34] Particle Data Group, R. L. Workman *et al.*, Review of Particle Physics, Progress of Theoretical and Experimental Physics **2022**, 083C01 (2022), https://academic.oup.com/ptep/article-pdf/2022/8/083C01/49175539/ptac097.pdf.

[35] P. F. de Salas *et al.*, 2020 global reassessment of the neutrino oscillation picture, Journal of High Energy Physics **2021**, 71 (2021).

[36] Z. D. Greenwood *et al.*, Results of a two position reactor neutrino oscillation experiment, Phys. Rev. D **53**, 6054 (1996).

[37] M. Apollonio *et al.*, Limits on neutrino oscillations from the chooz experiment, Physics Letters B **466**, 415 (1999).

[38] F. Boehm *et al.*, Final results from the palo verde neutrino oscillation experiment, Phys. Rev. D **64**, 112001 (2001).

[39] T2K Collaboration, K. Abe *et al.*, Indication of electron neutrino appearance from an accelerator-produced off-axis muon neutrino beam, Phys. Rev. Lett. **107**, 041801 (2011).

[40] MINOS Collaboration, P. Adamson *et al.*, Improved search for muon-neutrino to electron-neutrino oscillations in minos, Phys. Rev. Lett. **107**, 181802 (2011).

[41] L. A. Mikaélyan and V. V. Sinev, Neutrino oscillations at reactors: What is next?, Physics of Atomic Nuclei **63**, 1002 (2000).

[42] Double Chooz Collaboration, Y. Abe *et al.*, Indication of reactor $\overline{\nu}_e$ disappearance in the double chooz experiment, Phys. Rev. Lett. **108**, 131801 (2012).

[43] F. P. An *et al.*, Observation of Electron-Antineutrino Disappearance at Daya Bay, Phys. Rev. Lett. **108**, 171803 (2012).

[44] RENO, S.-H. Seo, New Results from RENO using 1500 Days of Data, J. Phys. Conf. Ser. **1342**, 012045 (2020), 1710.08204.

[45] Double Chooz, H. de Kerret *et al.*, Double Chooz θ_{13} measurement via total neutron capture detection, Nature Phys. **16**, 558 (2020), 1901.09445.

[46] T2K Collaboration, K. Abe *et al.*, Search for *cp* violation in neutrino and antineutrino oscillations by the t2k experiment with 2.2×10^{21} protons on target, Phys. Rev. Lett. **121**, 171802 (2018).

[47] NOvA, P. Adamson *et al.*, First measurement of electron neutrino appearance in NOvA, Phys. Rev. Lett. **116**, 151806 (2016), 1601.05022.

[48] M. Gonchar, Global oscillation parameters comparison for neutrino 2022, Daya Bay DocDB-12715-v14, 2022.

[49] Daya Bay Collaboration, F. P. An *et al.*, Precision measurement of reactor antineutrino oscillation at kilometer-scale baselines by daya bay, Phys. Rev. Lett. **130**, 161802 (2023).

[50] K. Abe, others, and The T2K Collaboration, Constraint on the matter–antimatter symmetry-violating phase in neutrino oscillations, Nature **580**, 339 (2020).

[51] DUNE, B. Abi *et al.*, Long-baseline neutrino oscillation physics potential of the DUNE experiment, The European Physical Journal C **80** (2020).

[52] H.-K. Proto-Collaboration *et al.*, Physics potential of a long-baseline neutrino oscillation experiment using a J-PARC neutrino beam and Hyper-Kamiokande, Progress of Theoretical and Experimental Physics **2015**, 053C02 (2015), https://academic.oup.com/ptep/article-pdf/2015/5/053C02/7697513/ptv061.pdf.

[53] DUNE, A. Abed Abud *et al.*, Snowmass Neutrino Frontier: DUNE Physics Summary, (2022), 2203.06100.

[54] Daya Bay Collaboration, Brookhaven National Laboratory Report No. BNL-77369-2006-IR; Lawrence Berkeley National Laboratory Report No. 62137; Tsinghua University Report No. TUHEP-EX-06-003 (unpublished), 2007.

[55] F. An *et al.*, The detector system of the daya bay reactor neutrino experiment, Nuclear Instruments and Methods in Physics Research Section A: Accelerators, Spectrometers, Detectors and Associated Equipment **811**, 133 (2016).

[56] J. Cao and K.-B. Luk, An overview of the Daya Bay Reactor Neutrino Experiment, Nucl. Phys. B **908**, 62 (2016), 1605.01502.

[57] Daya Bay Collaboration, F. P. An *et al.*, Measurement of electron antineutrino oscillation based on 1230 days of operation of the daya bay experiment, Phys. Rev. D **95**, 072006 (2017).

[58] F. An *et al.*, The muon system of the daya bay reactor antineutrino experiment, Nuclear Instruments and Methods in Physics Research Section A: Accelerators, Spectrometers, Detectors and Associated Equipment **773**, 8 (2015).

[59] JUNO, Daya Bay, A. Abusleme *et al.*, Optimization of the JUNO liquid scintillator composition using a Daya Bay antineutrino detector, Nucl. Instrum. Meth. A **988**, 164823 (2021), 2007.00314.

[60] W. Beriguete *et al.*, Production of a gadolinium-loaded liquid scintillator for the Daya Bay reactor neutrino experiment, Nucl. Instrum. Meth. A **763**, 82 (2014), 1402.6694.

[61] S. Chen, X. Ji, J. Li, and Z. Wang, Precise Measurement of Theta13 with P17B Hydrogen Neutron Capture Data (Note), Daya Bay DocDB-12359, 2023.

[62] C. Lewis, T. Langford, and W. Wang, Summary of all organic target masses in ads, Daya Bay DocDB-9586, 2014.

[63] K. Heeger, T. Langford, C. Lewis, and W. Wang, Unblinded target masses for AD7 and AD8, Daya Bay DocDB-9803, 2014.

[64] S. Chen *et al.*, Spectral measurement of electron antineutrino oscillation via neutron capture on hydrogen, Daya Bay DocDB-11457, 2017.

[65] O. Dalager and B. Roskovec, UCI nH Update, Daya Bay DocDB-12752, 2022.

[66] J. Liu *et al.*, Automated calibration system for a high-precision measurement of neutrino mixing angle θ_{13} with the Daya Bay antineutrino detectors, Nucl. Instrum. Meth. A **750**, 19 (2014), 1305.2248.

[67] H. X. Huang *et al.*, Manual Calibration System for Daya Bay Reactor Neutrino Experiment, JINST **8**, P09013 (2013), 1305.2343.

[68] J. Xu, Spill-out assessment using MCS data and MC, Daya Bay DocDB-9665, 2014.

[69] J. Ling, Position-dependence of energy resolution study with spallation and MCS data, Daya Bay DocDB-8674, 2012.

[70] S. Kohn, *Measurement of the Neutrino Mixing Angle θ_{13} Using Neutron Capture on Hydrogen at the Daya Bay Reactor Neutrino Experiment*, Ph.d. thesis, 2021.

[71] M. Kramer, *Robust Measurement of Mixing Parameters* $\sin^2 2\theta_{13}$ *and* Δm^2_{ee} *with Reactor Antineutrinos at Daya Bay*, Ph.d. thesis, 2022.

[72] T. Dohnal, ADs energy response cross-check for nH analysis, Daya Bay DocDB-11990, 2019.

[73] Y. Nakajima, Vertex reconstruction using charge template, Daya Bay DocDB-7423, 2012.

[74] H. Wong, P. Ochoa, and H. Steiner, AdTime performance report, Daya Bay DocDB-9367, 2013.

[75] O. Dalager, P20B Gain Calibration, DocDB-12265, 2020.

[76] M. Kramer and W. Gu, Channel Quality DB Status, DocDB-11488, 2017.

[77] Daya Bay, D. Adey *et al.*, A high precision calibration of the nonlinear energy response at Daya Bay, Nucl. Instrum. Meth. A **940**, 230 (2019), 1902.08241.

[78] Y. Huang, Z. Yu, and J. Hu, FEE electronics non-linearity measurement, Daya Bay DocDB-11460, 2017.

[79] T. Skwarnicki, *A study of the radiative CASCADE transitions between the Upsilon-Prime and Upsilon resonances*, PhD thesis, Cracow, INP, 1986, Appendix E.

[80] M. Oreglia, *A Study of the Reactions* $\psi' \to \gamma\gamma\psi$, PhD thesis, 1980, Appendix D.

[81] J. E. Gaiser, *Charmonium Spectroscopy From Radiative Decays of the* J/ψ *and* ψ', Other thesis, 1982, Appendix F.

[82] C. "Marshall, P21A SPN Energy Scale, Daya Bay DocDB-12347, 2021.

[83] K. "Dugas, Correcting the Spallation Neutron Energy Scale for After-Muon Effects, Daya Bay DocDB-12798, 2022.

[84] O. Dalager *et al.*, Berkeley-Czech-Irvine-Shandong nH Analysis Note, Daya Bay DocDB-12593, 2022.

[85] T. Dohnal and B. Roskovec, Some Plots for the nGd Analysis, Daya Bay DocDB-12718, 2022.

[86] T. Dohnal, Precision Measurement of Neutrino Oscillations Parameters, Daya Bay DocDB-12836, 2022.

[87] P. Tsang, H. Steiner, A. Wong, Y. Nakajima, and J. Ochoa, Lab study of flasher PMTs SD-0150, SD-0191, SD-1639, SD-1640, Daya Bay DocDB-8142, 2012.

[88] L. Wen, J. Cao, S. Jetter, and L. Zhan, Full control of the flashers, Daya Bay DocDB-7143, 2011.

[89] B. Roskovec, Residual Flashers, Daya Bay DocDB-12169, 2020.

[90] Q. Wu, SDU P17B oscillation Study-Part 5–Update, DocDB-12130, 2020.

[91] J. Li, Impact of residual flashers on nH oscillation result, Daya Bay DocDB-12229, 2020.

[92] Daya Bay, F. P. An *et al.*, New measurement of θ_{13} via neutron capture on hydrogen at Daya Bay, Phys. Rev. D **93**, 072011 (2016), 1603.03549.

[93] J.-H. Cheng, Z. Wang, L. Lebanowski, G.-L. Lin, and S. Chen, Determination of the total absorption peak in an electromagnetic calorimeter, Nuclear Instruments and Methods in Physics Research Section A: Accelerators, Spectrometers, Detectors and Associated Equipment **827**, 165 (2016).

[94] J. R. Taylor, *An Introduction to Error Analysis: The Study of Uncertainties in Physical Measurements* (University Science Books, 1982).

[95] W. Wei, B. Ma, and Q. Wu, Fast N Rate update with nH DT<1m, Daya Bay DocDB-12914, 2023.

[96] W. Wei and Q. Wu, Li9/He8 Rate update with nH DT<1m, Daya Bay DocDB-12918, 2023.

[97] X. Ma, Location of Strong AmC Source on the AD Lid, Daya Bay DocDB-8503, 2012.

[98] J. Li and Z. Wang, Release of nH analysis result with the DT cut value of 1 m, Daya Bay DocDB-12915, 2023.

[99] Daya Bay, F. P. An *et al.*, A side-by-side comparison of Daya Bay antineutrino detectors, Nucl. Instrum. Meth. A **685**, 78 (2012), 1202.6181.

[100] Z. Chen, Z. Yu, and X. Zhang, Radiogenic Neutron Background in Daya Bay, Daya Bay DocDB-12306, 2021.

[101] Z. Chen, X. Zhang, Z. Yu, J. Cao, and C. Yang, Radiogenic neutron background in reactor neutrino experiments, Phys. Rev. D **104**, 092006 (2021), 2109.06506.

[102] Z. Chen and Z. Yu, Updated Radiogenic Neutron Background in nH Analysis, Daya Bay DocDB-12326, 2021.

[103] Y. Nakajima, P. Ochoa, and P. Tsang, A Measurement of $\sin^2 2\theta_{13}$ and Δm^2_{ee} at Daya Bay Using Rate and Shape Information, Daya Bay DocDB-87740-v10, 2013.

[104] Y. Nakajima, P. Ochoa, P. Tsang, and H. Wong, LBNL Oscillation Analysis on P14A TechNote, Daya Bay DocDB-9999-v2, 2014.

[105] P. Huber, Determination of antineutrino spectra from nuclear reactors, Phys. Rev. C **84**, 024617 (2011).

[106] T. A. Mueller *et al.*, Improved Predictions of Reactor Antineutrino Spectra, Phys. Rev. C **83**, 054615 (2011), 1101.2663.

[107] V. Kopeikin, L. Mikaelyan, and V. Sinev, Reactor as a source of antineutrinos: Thermal fission energy, Phys. Atom. Nucl. **67**, 1892 (2004), hep-ph/0410100.

[108] P. Vogel and J. F. Beacom, Angular distribution of neutron inverse beta decay, anti-neutrino(e) + p —> e+ + n, Phys. Rev. D **60**, 053003 (1999), hep-ph/9903554.

[109] C. Lewis, W. Wang, and L. Zhan, Cross check the IBD cross sections used by different groups, Daya Bay DocDB-7654, 2012.

[110] Daya Bay, F. P. An *et al.*, Improved Measurement of the Reactor Antineutrino Flux and Spectrum at Daya Bay, Chin. Phys. C **41**, 013002 (2017), 1607.05378.

[111] T. D. B. Collaboration, Response to comment on daya bay's definition and use of delta(m^2_{ee}), 2019, 1905.03840.

[112] Daya Bay, D. Adey *et al.*, Extraction of the ^{235}U and ^{239}Pu Antineutrino Spectra at Daya Bay, Phys. Rev. Lett. **123**, 111801 (2019), 1904.07812.

[113] P. Virtanen *et al.*, SciPy 1.0–Fundamental Algorithms for Scientific Computing in Python, Nature Meth. **17**, 261 (2020), 1907.10121.

[114] M. A. Branch, T. F. Coleman, and Y. Li, A subspace, interior, and conjugate gradient method for large-scale bound-constrained minimization problems, SIAM Journal on Scientific Computing **21**, 1 (1999).

[115] O. "Dalager and B. Roskovec, UCI nH Update, Daya Bay DocDB-12777, 2022.

[116] S. Kohn", Rate-only nH analysis results and next steps, Daya Bay DocDB-12407, 2021.

[117] Particle Data Group, P. A. Zyla *et al.*, Review of Particle Physics, PTEP **2020**, 083C01 (2020).

[118] J. Li and Z. Wang, Release of nH analysis result with the DT cut value of 1 m, DocDB-12915, 2023.

Appendix A

Detection Efficiency Calculation Checks

Several checks were done for evaluating the correctness of the efficiency calculations, especially the DT and delayed energy cuts. This appendix will discuss the extra checks not included in Sec. 4.4. Appendix A.1 discusses the separate distance and time cuts, which was the method prior to the combined DT cut. Finally, a number of checks were done for the delayed energy cut efficiency, which are covered in Appendix A.2.

These studies were done with earlier selections, with slight differences in non-uniformity corrections, energy corrections, and/or coincidence time cuts. However, these differences would not affect the conclusions of the checks, and therefore, they were not redone with the final selection.

A.1 Distance and Time Cut Efficiencies

Prior to the DT cut, the selection used two separate cuts for the distance and time variables: $\Delta D < 0.5$ m and $\Delta t < 400$ μs, shown again in Fig. A.1. These cuts were varied to study the dependence the efficiencies and uncertainties had on the cut values, before the DT cut was ultimately implemented. This section will discuss the efficiencies of both the distance and time cuts, the methods of combining them, and the comparison to the DT cut (with the prior value of 0.8 m).

These studies were done before the non-uniformity correction was applied, as well as the previous set of corrections for the post-muon energy scale. The coincidence time was also set at 2000 μs, in contrast to the final selection which uses 1500 μs. The difference caused by these modifications do not affect the conclusions made by these studies.

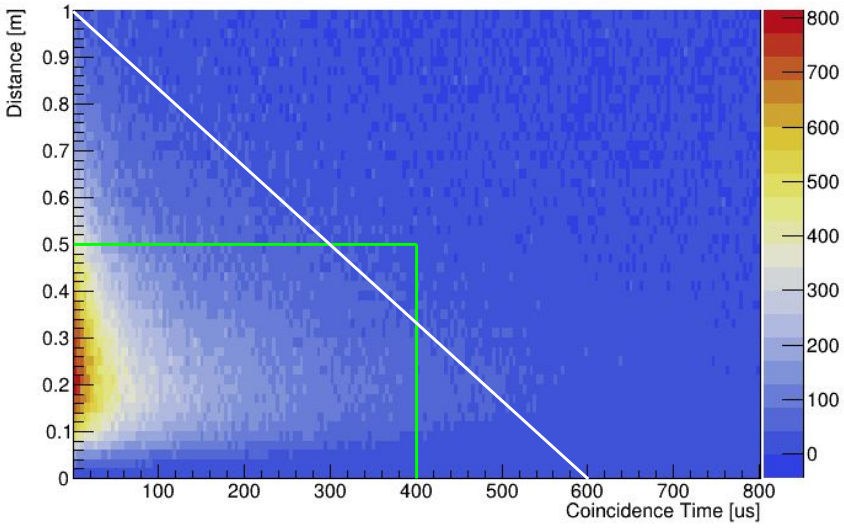

Figure A.1: Distance vs time spectrum for IBD candidates, after accidentals subtraction (see Sec. 5.1). Early nH analyses implemented separate distance and time cuts, identified by the green box. This selection utilizes a cut on the combined coincidence distance-time DT variable, shown here as the white line.

A.1.1 Time Cut Efficiency

First step to evaluating the time cut efficiency, the distribution of time between the prompt and delayed signals was fit with a double exponential function. This was also used to verify the selection by checking the capture times of the neutron on hydrogen:

$$f(\Delta t) = \text{const} + p_1 \times e^{-\Delta t/\tau_{LS}} + p_3 \times e^{-\Delta t/\tau_{GdLS}}. \tag{A.1}$$

The constant accounts for the flat time spectrum of the uncorrelated accidental background. τ_{LS} and τ_{GdLS} are the mean capture times of the neutron on hydrogen in the LS and GdLS regions, with p_1 and p_3 as the respective coefficients. The time fits were evaluated with various distance cuts and as seen in Fig. A.2, applying a distance cut improved the agreement between the fit values and the expected capture times.

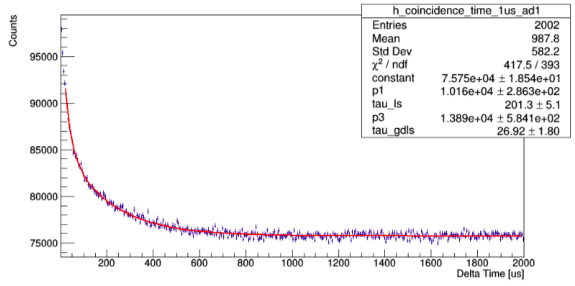

(a) No Distance Cut

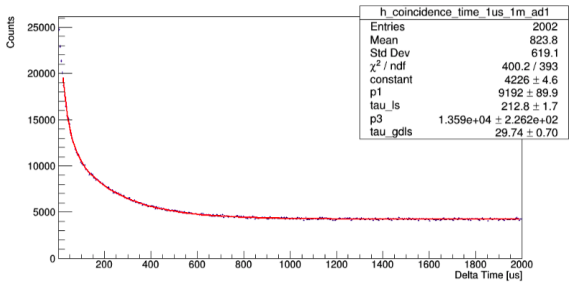

(b) 1 m Distance Cut

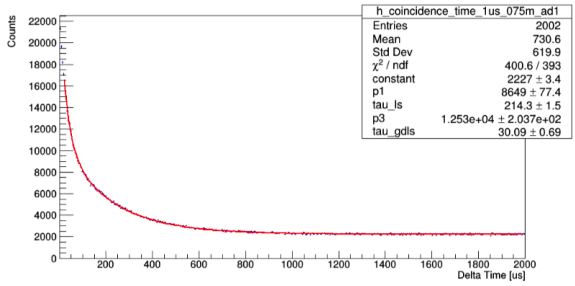

(c) 0.75 m Distance Cut

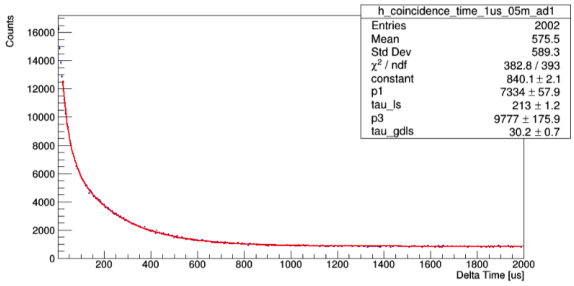

(d) 0.5 m Distance Cut

Figure A.2: Fits of the time between prompt and delayed using Eq. A.1 for EH1-AD1 for various distance cuts. These fits returned appropriate capture times for the neutron in both the LS and GdLS regions, and were used to calculate the time cut efficiency curves (Fig. A.3).

From here, the time cut efficiency was calculated using both the data and the fit functions:

$$\epsilon_{\mathrm{t}}(t_{\mathrm{cut}}) = \frac{\int_{0\ \mu s}^{t_{\mathrm{cut}}} (f(\Delta t) - \mathrm{const})\, d\Delta t}{\int_{0\ \mu s}^{2000\ \mu s} (f(\Delta t) - \mathrm{const})\, d\Delta t}. \tag{A.2}$$

The subtraction of the constant removes the accidental backgrounds. For proper determination of the time cut efficiency, 100% efficiency would be defined at infinity, however this is not realistically possible. Instead, a larger coincidence time window of 2000 μs marked 100% efficiency for this study, a reasonable choice being nearly 10 times the average capture time for the LS region.

Time cut efficiency curves, Fig. A.3, were created for both the data and the fit functions for the various values of the distance cut. In both Fig. A.2 and Fig. A.3, EH1-AD1 is used

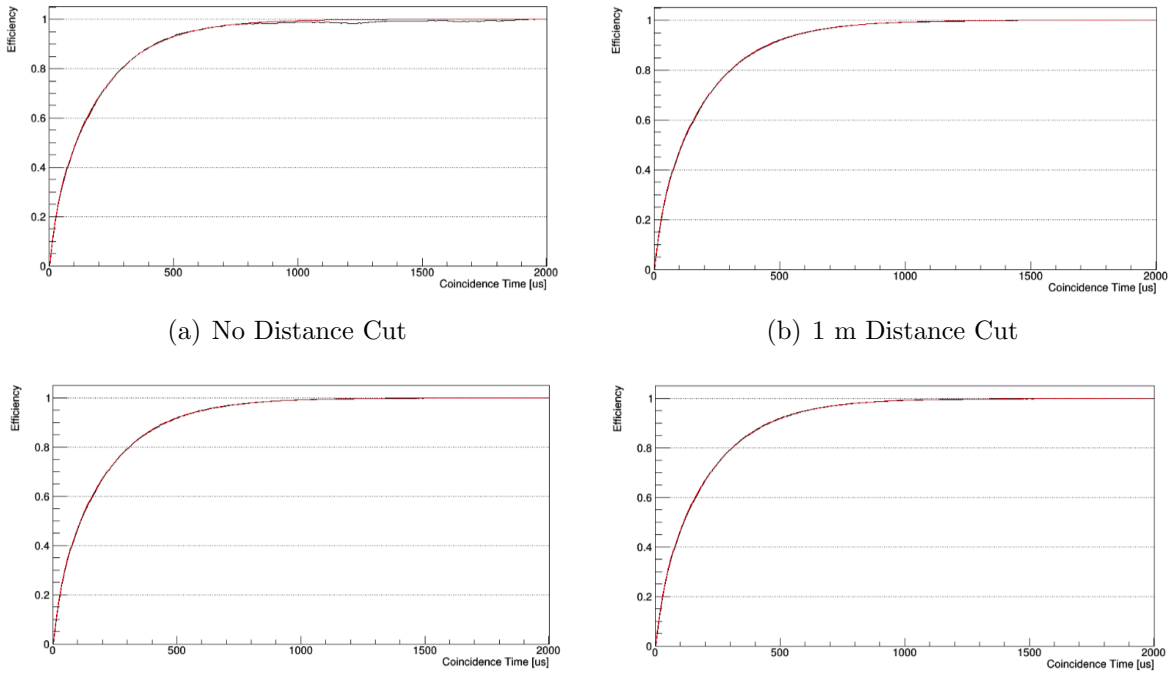

(a) No Distance Cut

(b) 1 m Distance Cut

(c) 0.75 m Distance Cut

(d) 0.5 m Distance Cut

Figure A.3: Time cut efficiency curves for EH1 AD1 for various distance cuts calculated using Eq. A.2. Black curves are calculated from the data, while the red curves are calculated using the fits, demonstrated in Fig. A.2.

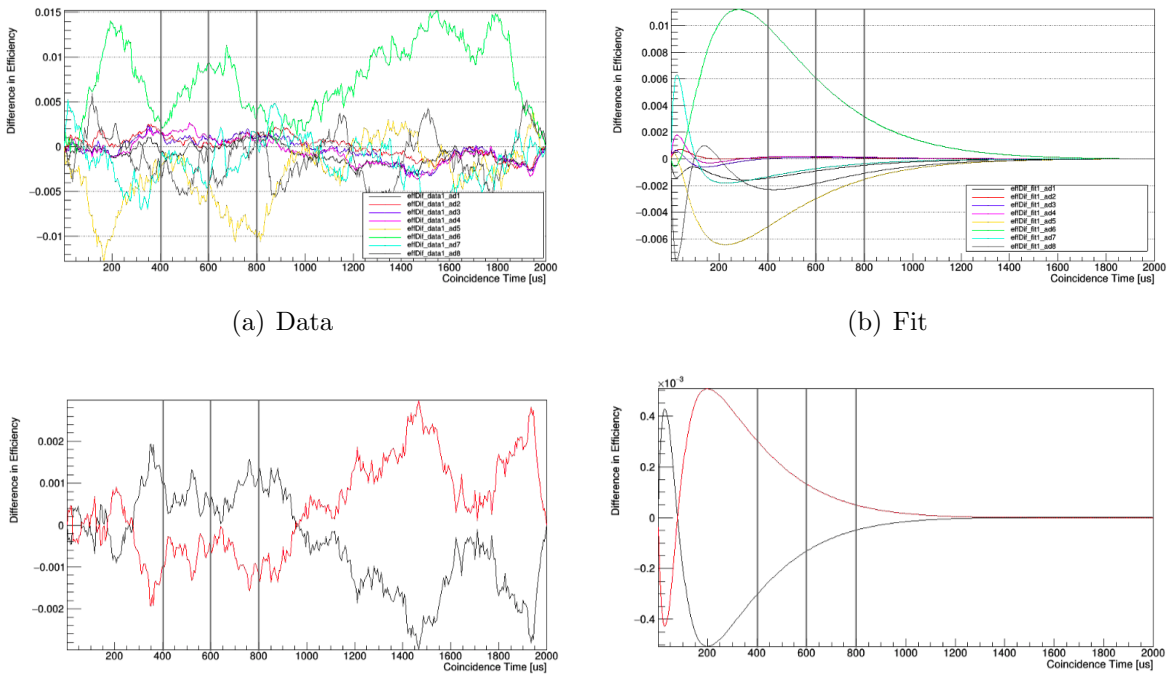

(a) Data

(b) Fit

(c) Data - Near vs Far

(d) Fit - Near vs Far

Figure A.4: Difference of time cut efficiencies for the 1 m distance cut, where the difference in efficiency for AD i is defined as $\epsilon_i - \bar{\epsilon}$. Lines indicate the various time cuts used in the distance cut efficiency study. (a) and (b) are the results of the 8 ADs treated separately, while (c) and (d) average the near (black) and far (red) ADs to investigate any potential near-far difference. The mirror-like symmetry of (c) and (d) results from the construction of the difference in efficiency.

to represent the results for all ADs as their results were characteristically similar. The ADs were then compared to the average between them (Fig. A.4) to determine the uncorrelated uncertainty of the time cut, which was estimated as half the largest difference between the ADs at the particular time cut.

In the cases where no distance cut or a loose 1.5 m distance cut was applied, a hint at a slight near-far difference was observed. This was not unreasonable as the signal to background ratios and correlated backgrounds, which have not been subtracted yet, are different between the halls. However, investigation into the source of the difference was crucial in the event that this was not the case.

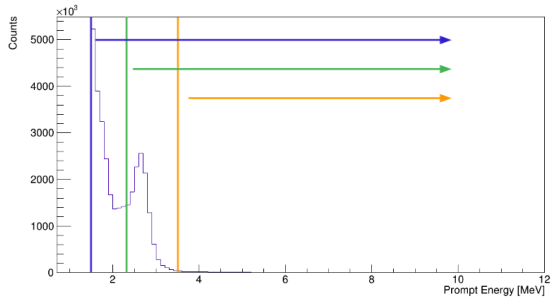

(a) Prompt energy lower bound cuts

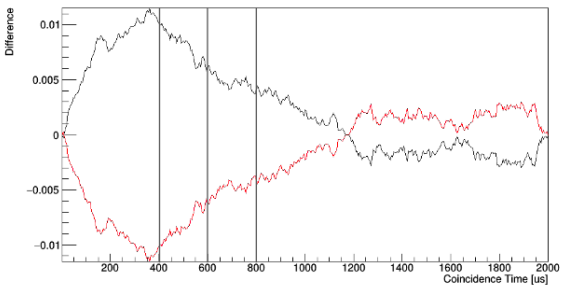

(b) Near-Far Difference: 1.5 MeV $\leq E_p \leq$ 12 MeV

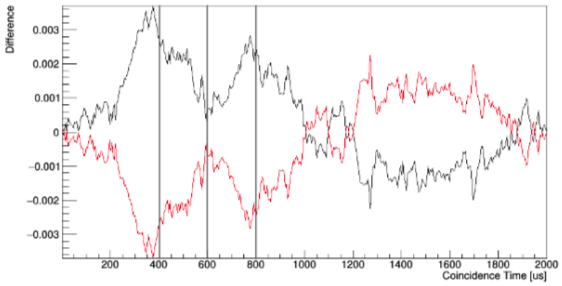

(c) Near-Far Difference: 2.3 MeV $\leq E_p \leq$ 12 MeV

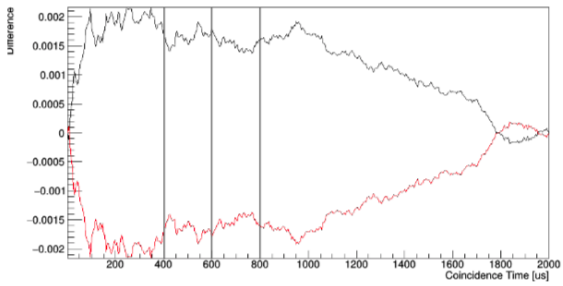

(d) Near-Far Difference: 3.5 MeV $\leq E_p \leq$ 12 MeV

Figure A.5: Near-far difference check for coincidence time cut efficiencies: (a) Diagram of the various prompt energy cuts: 1.5 MeV, 2.3 MeV, 3.5 MeV lower bounds are in blue, green, and orange, respectively; (b)-(d) near-far difference from average time cut efficiency for the various energy cuts, all with 1.5 m distance cut applied. The difference in efficiency for AD i is defined as $\epsilon_i - \bar{\epsilon}$. The mirror-like symmetry of (b)-(d) results from the construction of the difference in efficiency.

To check if it could be related to a correlated background, a few lower bound prompt energy E_p cuts were applied: the standard 1.5 MeV cut, as well as cuts at 2.3 and 3.5 MeV. The cuts and the resulting near-far differences are presented in Fig. A.5. With the same efficiency calculation process as before, the near-far difference decreased with increasing low-energy prompt energy cut, suggesting that the difference was caused by events with lower prompt energy.

A.1.2 Distance Cut Efficiency

The distance cut efficiency was evaluated after accidental background subtraction as

$$\epsilon_{\mathrm{D}}(D_{\mathrm{cut}}) = \frac{\int_{0\ \mathrm{m}}^{D_{\mathrm{cut}}} \Delta D_{\mathrm{sub}}\, d\Delta D}{\int_{0\ \mathrm{m}}^{2\ \mathrm{m}} \Delta D_{\mathrm{sub}}\, d\Delta D}. \tag{A.3}$$

It is important to remember that the coincidence distance spectrum is made entirely of accidental pairs at large distances (> 2 m), while all correlated events have shorter distances. Therefore, 100% efficiency was defined at 2 m to mitigate the noise from additional accidental statistics.

Following the procedure of the time cut efficiency, the distance cut efficiency was evaluated for several time cuts: 400 μs, 600 μs, 800 μs, and 2000 μs. To reduce data processing time , the 2000 μs selection was used with sub-selections of 400 μs, 600 μs, and 800 μs. This means the isolation criteria is the same as the 2000 μs selection, but the events were required to be within the smaller coincidence time. To validate this choice, both the sub-selections and the full selection with these coincidence times were run for EH1 and compared: the difference was less than 0.2% between the corresponding selections and sub-selections, consistent with statistical fluctuations. Shown in Fig. A.6, no noticeable bias was observed deeming this choice as reasonable.

For each of these sub-selections, the distance cut efficiency curves were produced by way of Eq. A.3, presented in Fig. A.7. Similar to the time cut efficiency, the uncorrelated uncertainty of the distance cut efficiency was calculated as half the largest difference between the ADs for a particular distance cut value.

To check the agreement between the detectors, the difference from the average efficiency curves was studied (Fig. A.8), where the far ADs are averaged together to compensate for the significantly lower statistics compared to the near ADs.

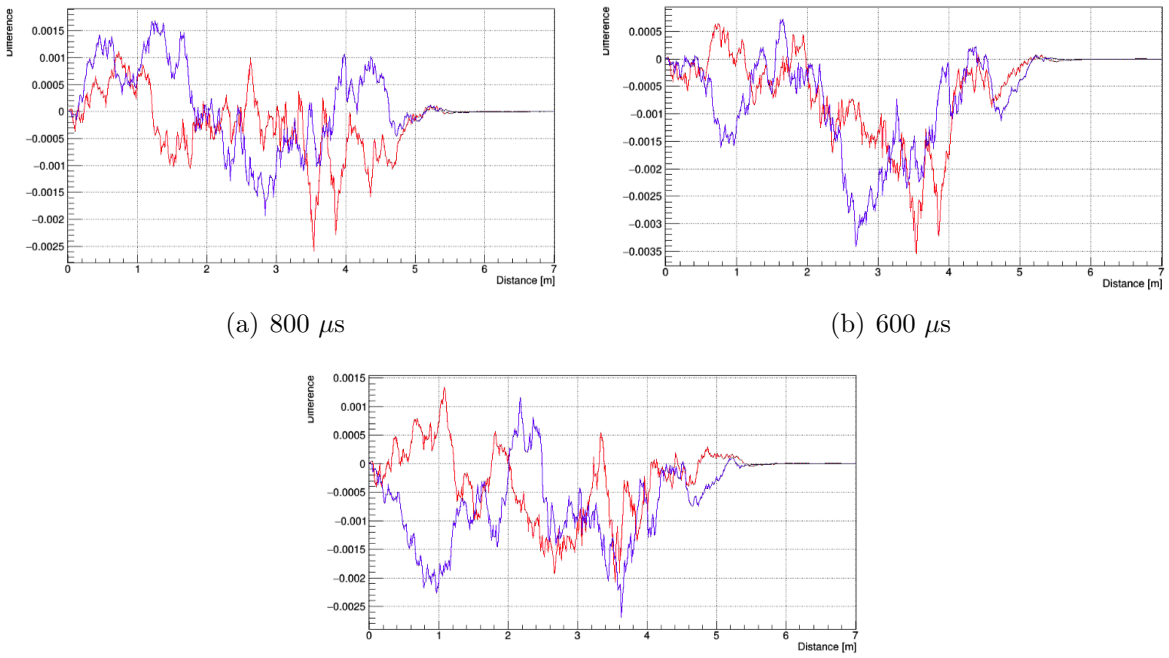

(a) 800 μs

(b) 600 μs

(c) 400 μs

Figure A.6: Selection vs Sub-Selection Check: Difference between selection and sub-selection of EH1 (AD1 in red, AD2 in purple) for 800 μs, 600 μs, and 400 μs. No significant bias between the selections and sub-selections for the various times, suggesting the sub-selections are representative of the selections. This check was done with the original definition of 100% efficiency at 7 m, however, this check was to confirm no bias in the sub-selection method and therefore does not change the efficacy of the check.

Furthermore, the average of the near ADs and the average of the far ADs were compared against the average of all 8, to investigate the possibility of a near-far bias. Presented in Fig. A.9, no near-far bias was identified in any of the sub-selections.

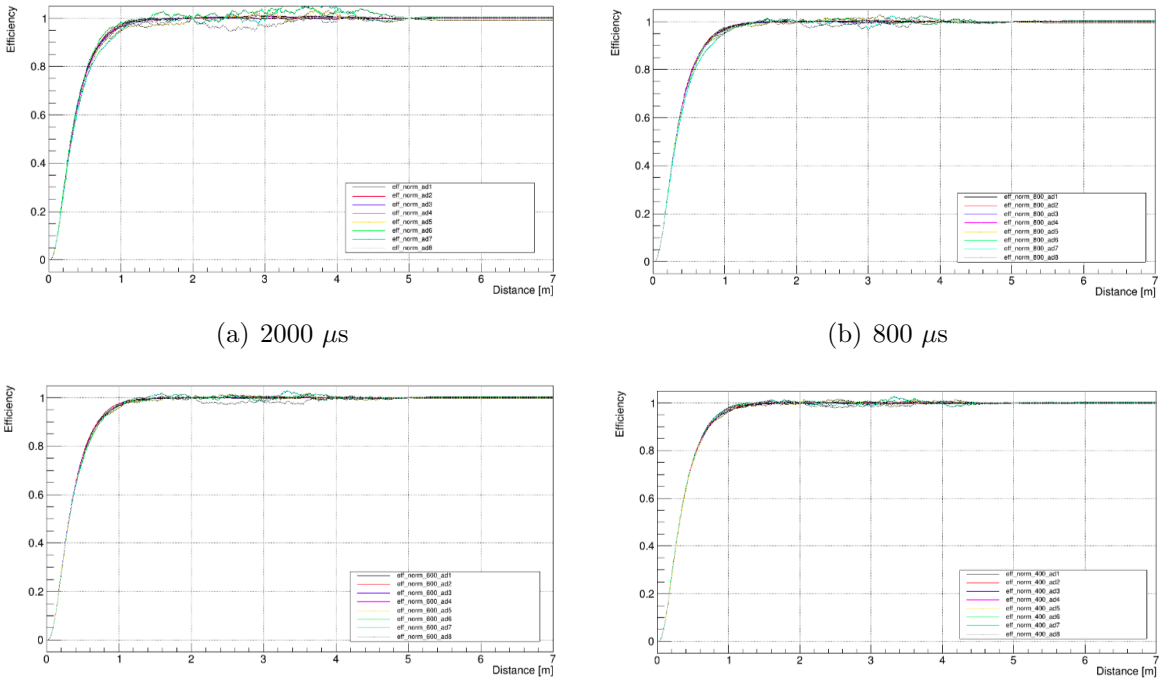

(a) 2000 μs

(b) 800 μs

(c) 600 μs

(d) 400 μs

Figure A.7: Efficiency Curves for all 8 ADs for the various sub-selections. 100% efficiency is defined at 2 m to mitigate statistical fluctuations in the accidental subtraction. This definition paired with statistical fluctuations allows for efficiencies greater than 1.

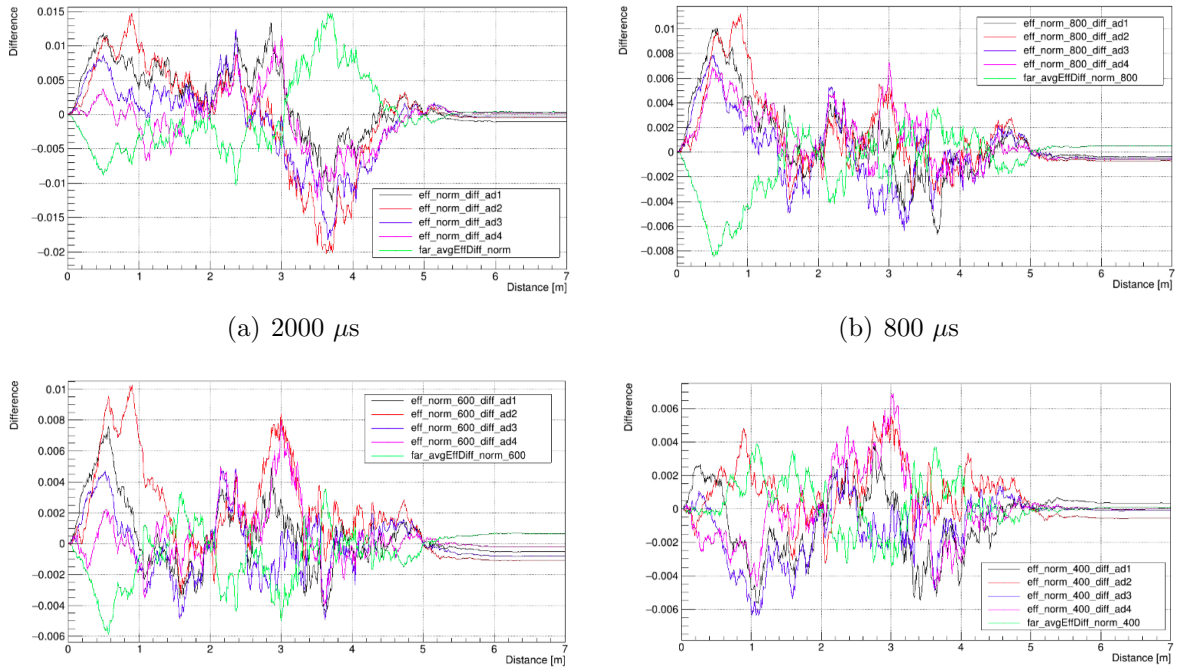

(a) 2000 μs

(b) 800 μs

(c) 600 μs

(d) 400 μs

Figure A.8: Distance Cut Efficiency Difference from Average: Sub-selections, far ADs averaged. The difference in efficiency for AD i is defined as $\epsilon_i - \bar{\epsilon}$. Check of the near-far consistency investigated in Fig. A.9.

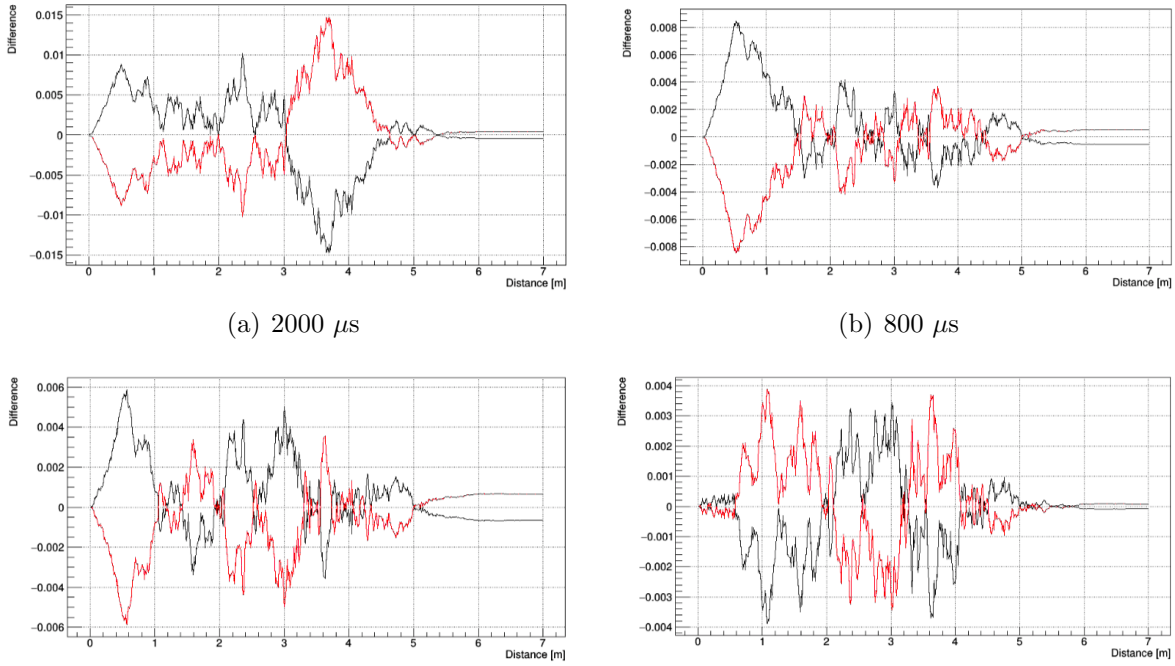

(a) 2000 μs

(b) 800 μs

(c) 600 μs

(d) 400 μs

Figure A.9: Near-Far Difference in Distance Cut Efficiency: Sub-selections, average of near ADs in black, average of far ADs in red. The mirror-like symmetry is by construction. No obvious near-far bias.

A.1.3 Combining Distance and Time Cuts

To calculate the total efficiency, three methods were designed: 1) distance cut was first applied, then the time cut, 2) time cut applied first, distance cut second, or 3) applying both at the same time.

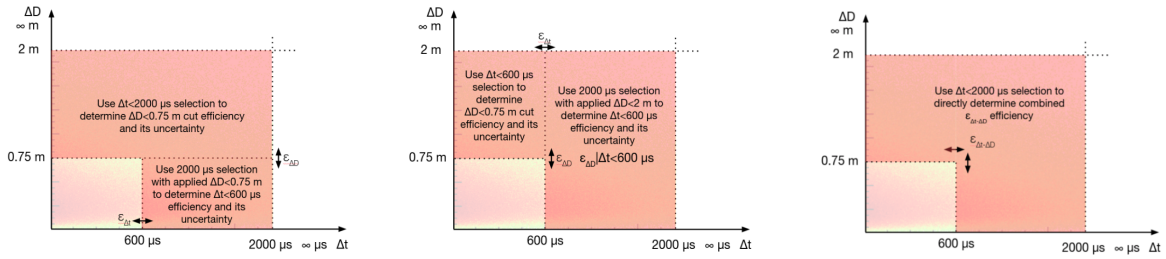

(a) Method 1 (b) Method 2 (c) Method 3

Figure A.10: Cartoon illustrating the three separate methods of combining the distance and time cuts

All three methods were implemented and applied to the selection for consistency checks. The results for a few combinations of distance and time cuts are presented in Fig. A.11. As expected, the three methods were consistent values with negligible differences.

Following the process described in Sec. 4.3.2, the DT cut efficiency was also computed with this preliminary selection with a DT cut value of 0.8 m and compared to the results of the separate distance and time cuts. The cut values used for the results in Tab. A.2 were the standard values at the time: $\Delta D < 0.5$ m and $\Delta t < 400$ μs or $DT < 0.8$ m. The uncertainty was calculated as half the difference between the largest and smallest efficiencies, a conservative calculation as it takes the full envelope of the efficiencies. The first four rows in Tab. A.2 were calculated using the extended delayed energy E_d range, while the final row is the DT method with the final 3σ E_d range. Compared to the separate distance and time cuts, the DT cut provided a larger efficiency while keeping the uncertainty about the same. This motivated the use of the DT cut over the previous cuts.

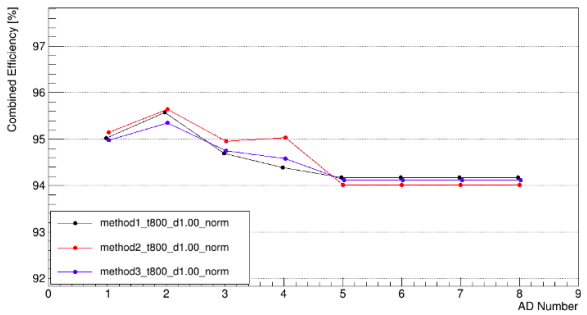

(a) $\Delta D = 1$ m, $\Delta t_c = 800$ μs

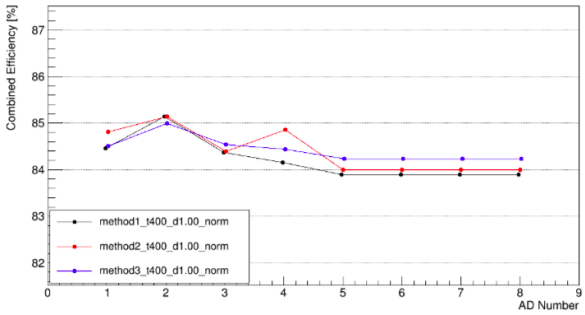

(b) $\Delta D = 1$ m, $\Delta t_c = 400$ μs

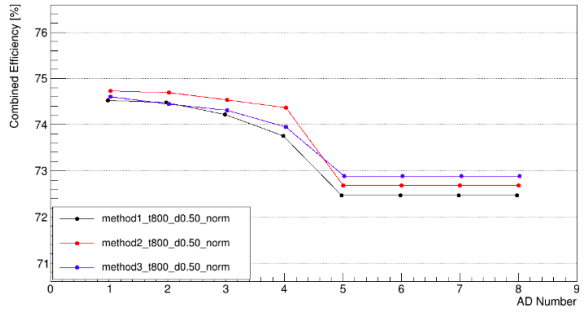

(c) $\Delta D = 0.5$ m, $\Delta t_c = 800$ μs

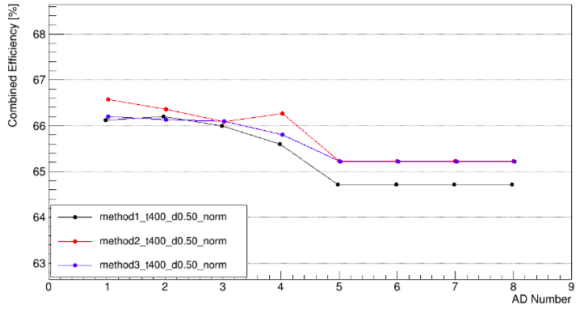

(d) $\Delta D = 0.5$ m, $\Delta t_c = 400$ μs

Figure A.11: Results of the three methods of combining the distance and time cuts for various values of distance and time. Methods 1, 2, and 3 are indicated by black, red, and purple, respectively. Far ADs averaged to decrease statistical fluctuations, hence all far AD points are the same. The three methods follow the same behavior for each AD an all combinations of distance and time cuts.

Table A.1: Comparison of efficiency results from the distance and time cuts and the DT cut. Methods 1-3 refer to the combining methods of the distance and time cuts outlined in Fig. A.10 using values of $D_{\text{cut}} = 0.5$ m and $t_{\text{cut}} = 400$ μs. The DT cuts used were the standard 800 mm cut, where the E_p threshold applies the 3.5 MeV prompt energy threshold. The uncertainties are the calculated as half the difference between the largest and smallest efficiencies. The DT cut has an improved efficiency over the combined distance and time cuts, with an uncertainty of similar to the other methods. The prompt energy threshold further increases the efficiency while reducing the uncertainties.

Method	Efficiency (%)	Uncertainty (%)	Near-Only Uncertainty (%)
Method 1	65.1	$\pm$2.1	$\pm$0.5
Method 2	65.7	$\pm$1.5	$\pm$0.2
Method 3	65.4	$\pm$1.5	$\pm$0.4
DT	69.5	$\pm$2.1	$\pm$0.40
DT (3σ E_d cut)	70.6	$\pm$1.2	$\pm$0.35

A.1.4 Additional DT Cut Efficiency Check

To investigate the DT efficiency dependence on the number of accidentals, we applied a prompt energy threshold of $E_p \geq 3.5$ MeV, largely reducing the number of accidentals in the selection and placing more emphasis on the IBDs (Fig. A.12(a)-(b)). Fig. A.12 provides a comparison of before and after this increased E_p threshold is applied. Though the spread in the efficiency curves is reduced once the threshold is implemented, the efficiencies are not hugely affected. The uncertainty, on the other hand, is significantly reduced after applying the prompt energy threshold.

Table A.2: Comparison of the DT cut efficiency with and without the $E_p \geq 3.5$ MeV threshold cut. The DT cuts used were the standard for the time, 800 mm cut. The uncertainties are the calculated as half the difference between the largest and smallest efficiencies. The prompt energy threshold increases the efficiency while reducing the uncertainties as the percentage of IBDs in the sample is increased significantly.

Method	Efficiency (%)	Uncertainty (%)	Near-Only Uncertainty (%)
DT	70.6	$\pm$1.2	$\pm$0.35
DT ($E_p \geq 3.5$ MeV)	71.3	$\pm$0.2	$\pm$0.12

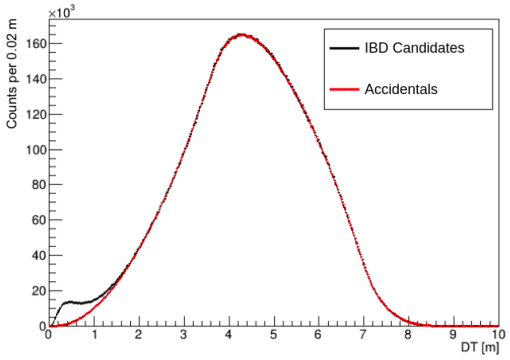

(a) DT Spectra without $E_p \geq 3.5$ MeV Threshold

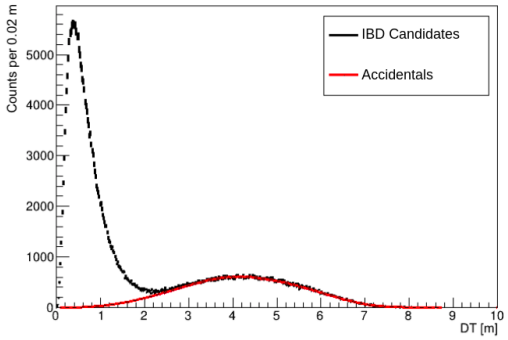

(b) DT Spectra with $E_p \geq 3.5$ MeV Threshold

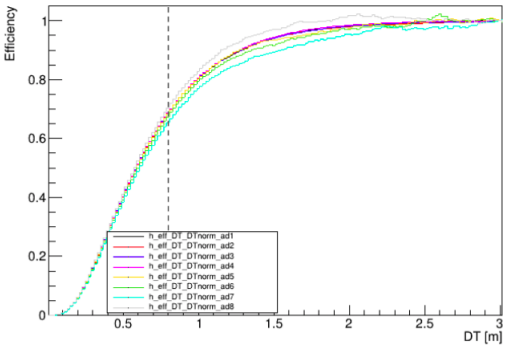

(c) DT Efficiencies without $E_p \geq 3.5$ MeV Threshold

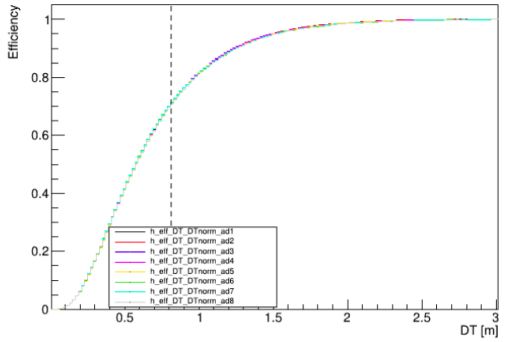

(d) DT Efficiencies with $E_p \geq 3.5$ MeV Threshold

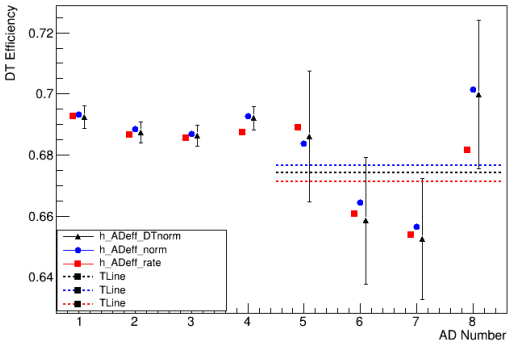

(e) DT Efficiencies at DT = 800 mm without $E_p \geq 3.5$ MeV Threshold

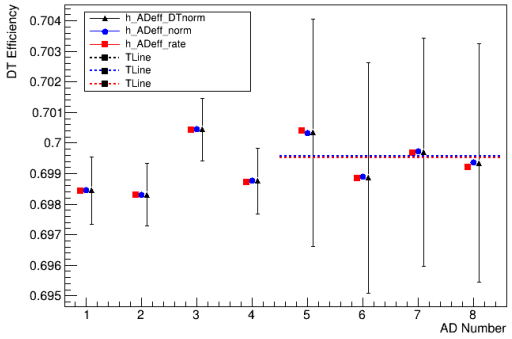

(f) DT Efficiencies at DT = 800 mm with $E_p \geq 3.5$ MeV Threshold

Figure A.12: $E_p \geq 3.5$ MeV threshold check on DT Efficiency: (a) and (b) are the DT spectra of EH1 AD1 before and after applying the prompt energy threshold to compare signal to background ratios. (c)-(d) compare the efficiency curves before and after, the spread is largely reduced after the prompt energy threshold; (e)-(f) show the efficiencies with the DT = 800 mm cut value. The dotted lines indicate the far AD average. Note the scales are different between (e) and (f).

A.2 Delayed Energy Cut Efficiency Checks

As shown in Fig. 4.18, a near-far difference was observed in the delayed energy cut efficiencies. To understand the source of this difference, several studies were conducted; most of these checks used the average of the near ADs vs the average of the far. The results of these studies are presented here.

The first approach compared the shapes of the near and far spectra. After averaging the ADs into near and far, the spectra were fit to obtain proper values of μ and σ. The spectra were then normalized by the $\mu \pm 3\sigma$ range, shown in Fig. A.13(a). In addition to some shape differences in the tails, the far ADs peak at slightly higher energy than the near ADs. In Fig. A.13(b), the extended range for the far ADs was adjusted to account for the shifted peak energy relative to the near ADs. The near-far difference remained essentially unchanged, indicating the shift in peak energy is not the cause of the E_d near-far difference.

As for the difference in tail shapes, variations on the extended range were implemented, as outlined by Fig. A.14, where (a) is the standard definition, (b) and (c) look at only the

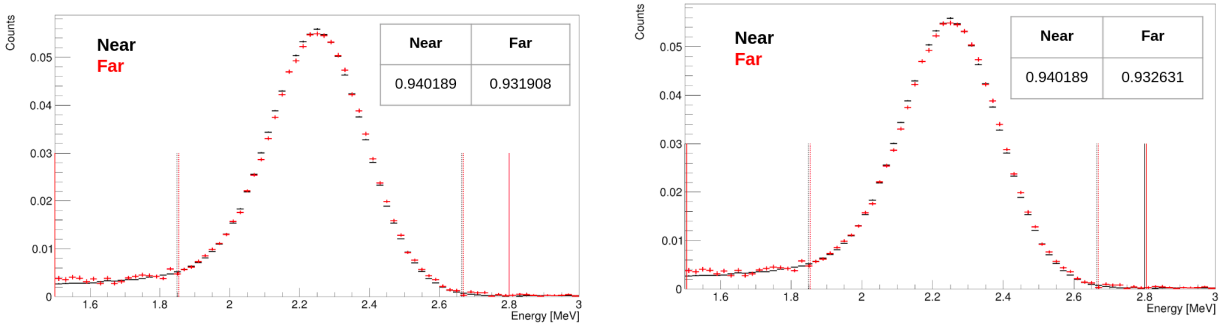

(a) Before shifting extended range for far hall

(b) Shifted extended range for far hall

Figure A.13: Delayed Energy Spectra comparison for near and far halls, normalized to the $\mu \pm 3\sigma$ range, indicated by the dotted lines. Solid lines mark the bounds of extended range. Notice tail shapes differ slightly, as well as the far ADs peak at slightly higher energy. (a) compares the normalized spectra using the same bounds for the extended range (1.5-2.8 MeV) for both near and far, while in (b), the extended range is shifted for the far hall to account for the difference in peak energy value. Near-far difference in efficiency remains.

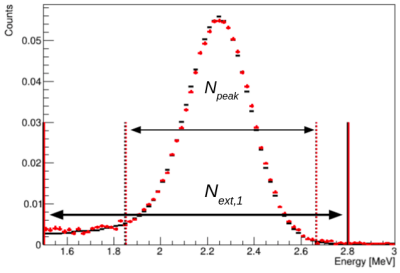

(a) Standard extended range

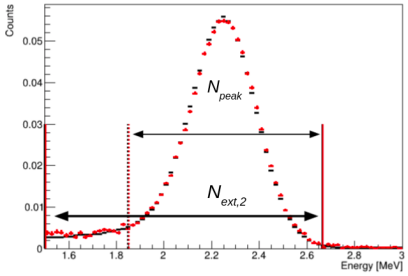

(b) Low energy tail only

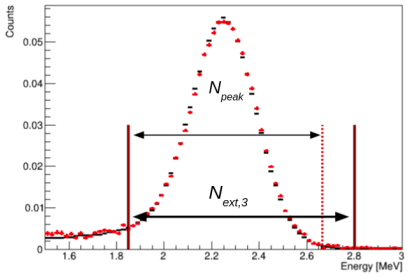

(c) High energy tail only

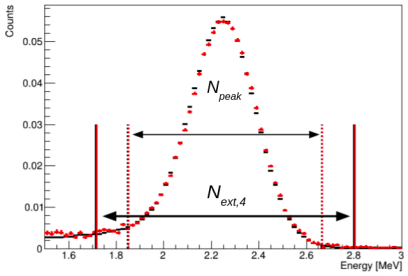

(d) $\mu \pm 4\sigma$ as extended range

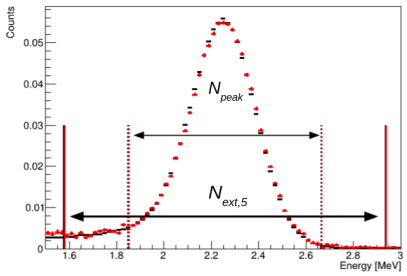

(e) $\mu \pm 5\sigma$ as extended range

Figure A.14: Diagrams for redefining the extended range in investigating the near-far difference: (a) standard definition (1.5 - 2.8 MeV), (b) only including the low energy tail (1.5 - $\mu + 3\sigma$ MeV), (c) only including the high energy tail ($\mu - 3\sigma$ - 2.8 MeV), (d) $\mu \pm 4\sigma$, (e) $\mu \pm 5\sigma$. Results presented in Tab. A.3.

low and high energy tails, respectively, and (d) and (e) are redefined based on the values of σ. The results are summarized in Tab. A.3. The standard definition of the extended range presents the largest near-far difference. Compared to the high energy tail only results, the low energy tail only contributes significantly more to the near-far difference observed by the standard definition. The results from the $\mu \pm 4\sigma$ and $\mu \pm 5\sigma$ extended regions confirm this conclusion: the near-far difference for both cases are less than the standard definition since neither includes all of the low energy tail, regardless of the increase in the high energy bound.

Table A.3: Delayed energy cut efficiency results using various definitions of the extended range, outlined in Fig. A.14. Near-far difference coming largely from the low energy tail differences.

Extended Range Definition	Near $\epsilon_{\text{delayed}}$	Far $\epsilon_{\text{delayed}}$	Percent Difference (%)
Standard	0.940189	0.932631	-0.80389
Low Energy Tail Only	0.942412	0.935985	-0.68189
High Energy Tail Only	0.997498	0.996172	-0.132928
$\mu \pm 4\sigma$	0.969762	0.966411	-0.34549
$\mu \pm 5\sigma$	0.948161	0.943824	-0.457401

The following two checks were aimed at the accidental backgrounds. The first check applied a prompt energy threshold ($E_p \geq 3.5$ MeV) to the selection, which reduced the accidental background. Figure A.15 shows the resulting spectra and efficiencies compared to the standard selection without the prompt energy threshold. The spectral shapes agree noticeably better with the threshold, leading to much less difference between near and far ADs.

Further checking the accidental background, the accidentals scaling was manually adjusted to determine if the scaling was done improperly. For the results shown in Fig. A.16, all three subtraction methods are included on the plots, however only the rate-corrected and distance normalized points were adjusted, so that the DT normalized (black points) were left as reference. Originally, this check was designed to determine how sensitive the delayed energy cut efficiency was to slight changes in the accidental subtraction: the accidentals were re-scaled by $\pm 0.03\%$ as that was roughly the size of the systematic uncertainty in the accidentals scaling methods for this selection. This resulted in very minor changes compared to the original scaling, see Fig. A.16(a)-(b). The accidentals were then re-scaled to the degree necessary to remove the near-far difference altogether. For this instance, shown in Fig. A.16(c), the re-scaling would need to increase the accidentals by 0.9%. This would be a large enough difference that it would have been noticed in previous results.

The next set of checks investigated the regional dependence of the events within the detector on the near-far difference. This check could indicate a source of the bias. Three versions of

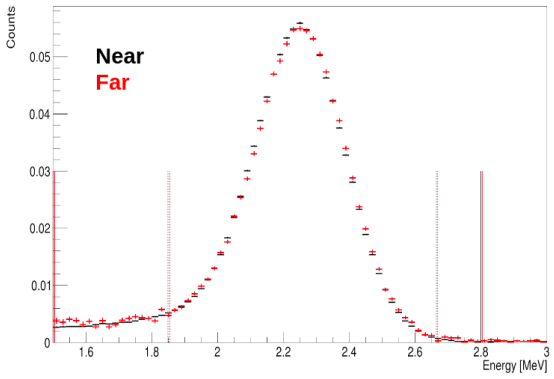

(a) Delayed Spectrum: No E_p Threshold

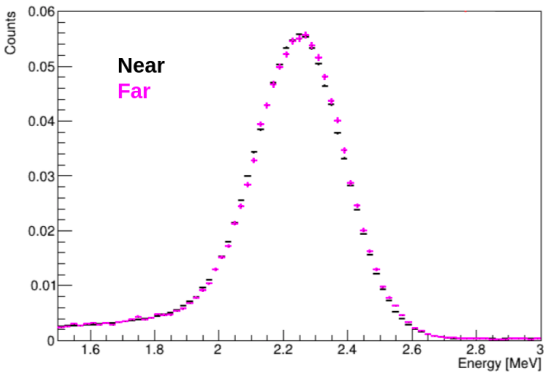

(b) Delayed Spectrum: $E_p \geq 3.5$ MeV Threshold

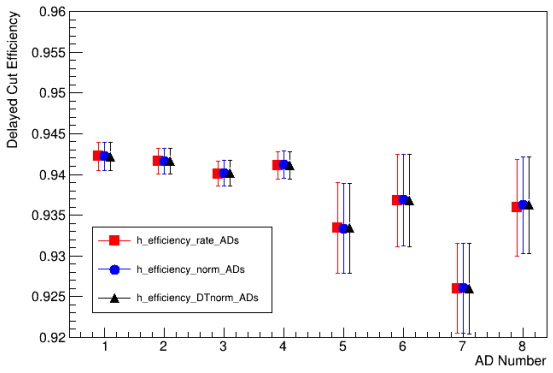

(c) Efficiencies: No E_p Threshold

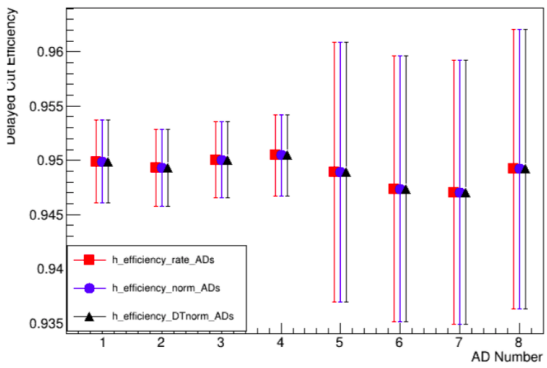

(d) Efficiencies: $E_p \geq 3.5$ MeV Threshold

Figure A.15: $E_p \geq 3.5$ MeV Threshold Check: Applied a prompt energy threshold to see how reducing accidentals affects the delayed energy cut efficiency and the near-far difference. (a)-(b) Delayed energy spectra before and after applying the prompt energy threshold, respectively, both normalized to the number of counts within $\mu \pm 3\sigma$; (c) Delayed energy cut efficiencies without prompt energy threshold for comparison; (d) Delayed energy cut efficiencies with the prompt energy threshold. Near-far differences in the shapes and the efficiencies are noticeably reduced when the prompt energy cut efficiency is applied.

this check were conducted: slices in z, slices in r^2, and z-vs-r^2 voxels. For each, the diagrams defining the numbering of the regions is provided in the left column of Fig. A.17 with the corresponding results in the right column. All ADs express the same general trends where the edges of the AD have lower efficiency than the center. The near-far difference is observed throughout the detector, as shown most clearly in Fig. A.17(f). This indicates that the near-far difference is not tied to a position dependent source, such as the ^{241}Am-^{13}C background for example.

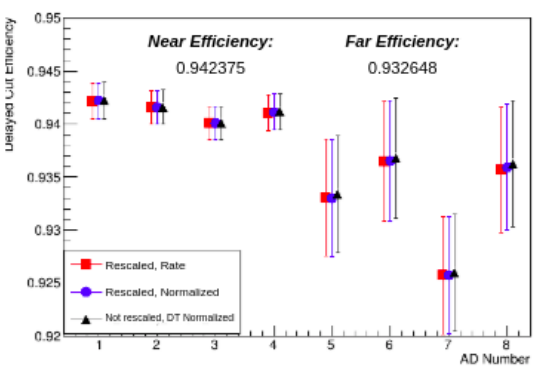

(a) 0.03% Fewer Accidentals

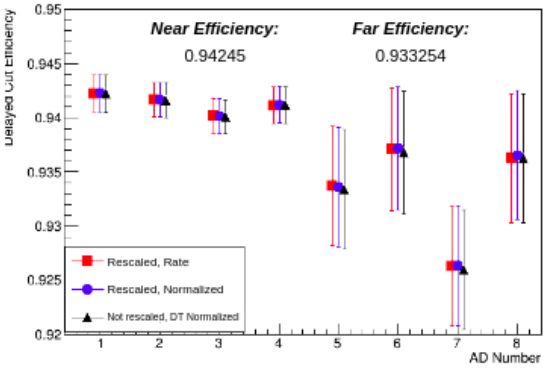

(b) 0.03% More Accidentals

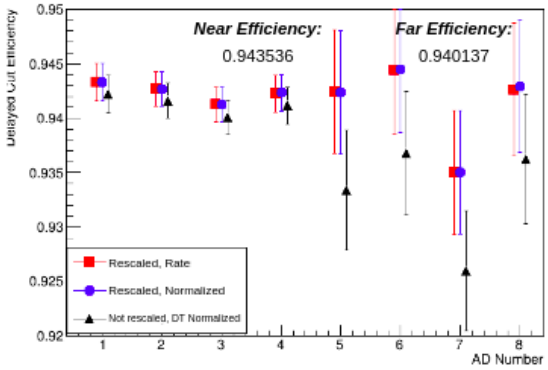

(c) 0.9% More Accidentals

Figure A.16: Manually re-scaling accidentals: Manually re-scaled the accidentals in the rate-corrected and normalized subtraction methods to compare the sensitivity to the accidentals subtraction on the delayed energy cut efficiency, DT normalized is left unchanged for comparison. (a) and (b) re-scale by $\pm 0.03\%$ as this is the uncertainty on the accidentals scaling, though the efficiencies (and near-far difference) remain essentially unchanged. c) To remove the near-far difference, accidentals need to be increased by 0.9%, a difference that would have been noticed if this was the cause of the near-far difference.

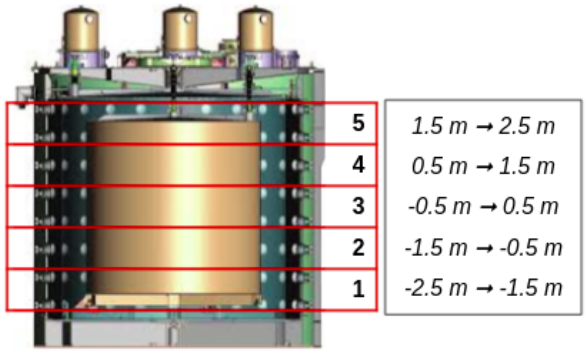

(a) z-slices

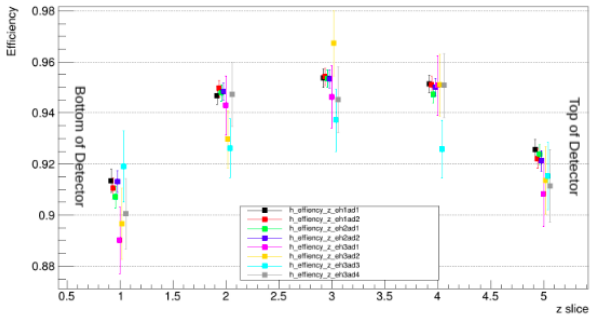

(b) z-slice Results

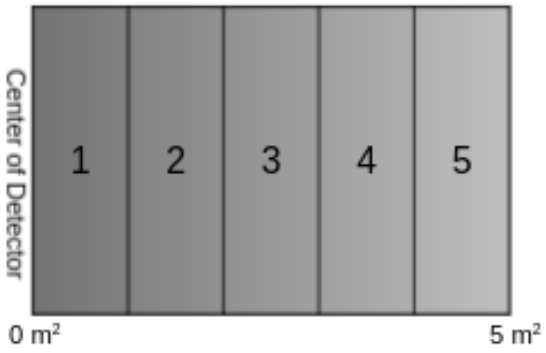

(c) r^2-slices

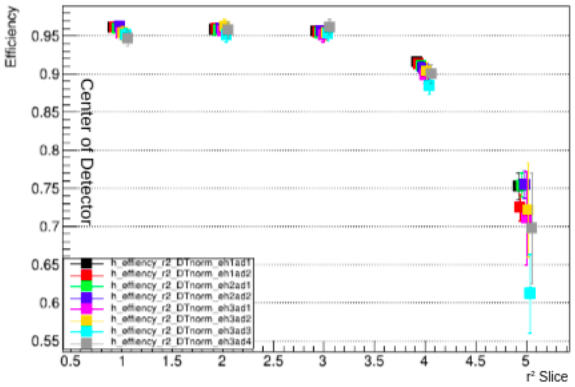

(d) r^2-slice Results

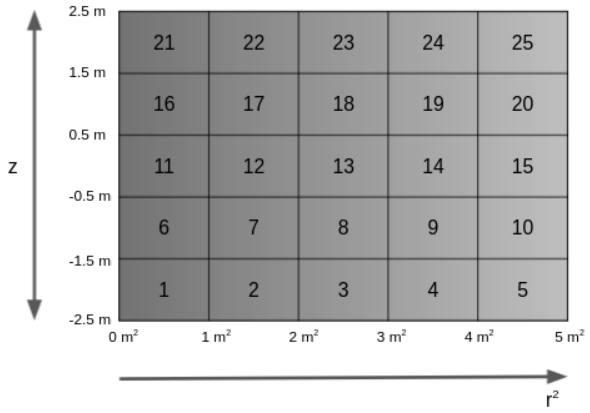

(e) Voxel

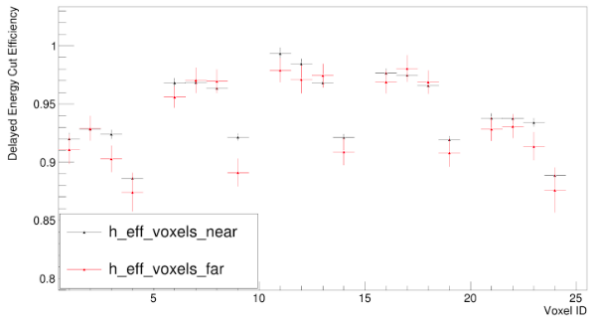

(f) Voxel Results

Figure A.17: Diagrams and results for checks on spacial dependence of the delayed energy cut efficiency. Slices in z-space defined in (a) and corresponding efficiencies in (b). r^2-slice definitions and results shown in (c) and (d). (e) and (f) define the voxels in z-vs-r^2 space and show the resulting efficiencies. Trends in z- and r^2- slices are identifiable in the voxel results, where efficiencies decrease at edges of the detector. Near-far difference is seen throughout the regions of the detector.

A final check specifically targeted the ^{212}Bi background. As seen in Fig. A.18(a), the ^{212}Bi spectrum resides almost entirely below the 1.5 MeV low energy cut. To ensure all of these events were removed, the extended range of the delayed energy cut efficiency was altered such that the lower bound was raised to 1.6 MeV. The efficiencies for the standard definition and this altered definition are provided in Fig. A.18(b) and (c): the results are inconclusive as the near-far difference is reduced, but still existent in the new case. This could be caused by the removal of the ^{212}Bi background, or simply by removing some of the low energy tail which has been identified as a contributing source of the near-far difference.

The results of the delayed energy cut efficiency calculations are summarized in Tab. A.4. The uncertainties here are defined as half the difference between the largest and smallest values. After these checks on the delayed energy cut efficiencies, the near-far difference remains, though this could be due to the un-subtracted correlated backgrounds in the data. As described in Sec. 4.4.5, the SPN data provided the cleanest sample and returned similar average efficiencies to the standard process, but improved the uncertainty, and was therefore used in the final fit.

Table A.4: Results of the delayed energy cut efficiency calculations using various methods to validate. The uncertainty is calculated as half the difference of the largest and smallest efficiencies. Providing the cleanest sample, the SPN selection calculates an efficiency similar to the the standard calculation but with uncertainties similar to the E_p threshold results, still more conservative than the near-only uncertainty of the standard. Therefore, the SPN results, 93.4±0.2%, are used in the analysis.

Method	Efficiency (%)	Uncertainty (%)	Near-Only Uncertainty (%)
Standard	93.7	±0.8	±0.1
SPNs (fitted)	93.4	±0.2	±0.04
$\mu \pm 5\sigma$	94.7	±0.5	±0.1
$E_p \geq 3.5$ MeV	94.9	±0.2	±0.05
^{212}Bi	95.2	±0.4	±0.1

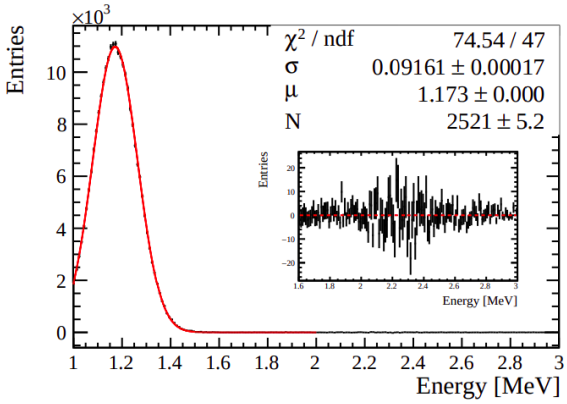

(a) ^{212}Bi Spectrum

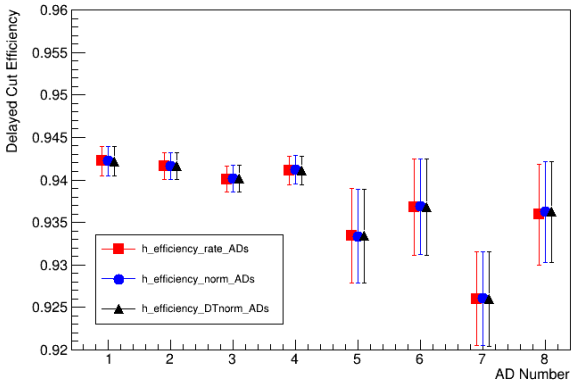

(b) Standard Extended Range

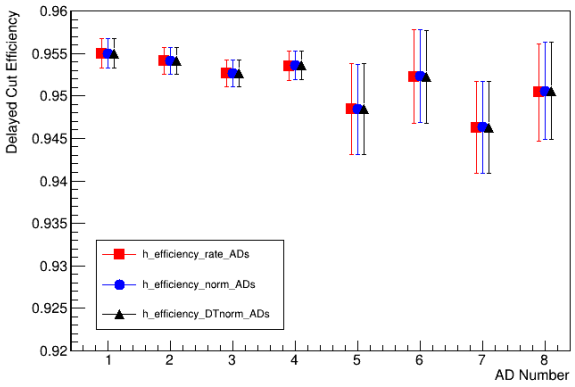

(c) Extended Range 1.6-2.8 MeV

Figure A.18: ^{212}Bi Check: Taken from [61], (a) is the spectrum of ^{212}Bi which could be the cause of the near-far difference. Efficiencies of the 8 ADs are shown in (b) and (c), where (b) uses the standard extended range, and (c) raises the lower bound to 1.6 MeV to ensure these events are removed. The spread of the efficiencies after raising the lower bound is about half of the spread with the standard extended range. While the difference is reduced, the results are inconclusive: near-far difference is not entirely removed, could be due to removing the ^{212}Bi background or simply that this removes a part of the low energy tail which was previously identified as a difference between the near and far halls.